DEVELOPMENT OF MICRO – MACHINED PLANAR MANIPULATORS

by

Yongjun Lai

Submitted
in partial fulfilment of the requirements
for the degree of

DOCTOR OF PHILOSOPHY

Major Subject: Mechanical Engineering

at

DALHOUSIE UNIVERSITY

Halifax, Nova Scotia   December, 2003

Canadä

Dalhousie University
Faculty of Engineering

Mechanical Engineering

The undersigned hereby certify that they have examined, and recommended to the Faculty of Graduate Studies for acceptance, the thesis entitled "Development of Micro - Machined Planar Manipulators" by Yongjun Lai in partial fulfillment of the requirements for the degree of Doctor of Philosophy.

Dated: Dec. 23. 2003

Supervisor:

Dr. Marek Kujath

External Examiners:

Dr. Roger Boudreau

Université de Moncton

Examiners:

Dr. Ted Hubbard

Dr. Geoff Maksym

Dalhousie University

Faculty of Engineering

DATE: ~~Dec. 23, 2003~~

AUTHOR: Yongjun Lai

THESIS: Development of Micro - Machined Planar Manipulators

MAJOR SUBJECT: Mechanical Engineering

DEGREE: Doctor of Philosophy

CONVOCATION: May, 2004

Permission is herewith granted to Dalhousie University to circulate and to have copied for non-commercial purposes, at its discretion, the above thesis upon the request of individuals or institutions.

                                         _____

                                          Signature of Author

The author reserves other publication rights, and neither the thesis nor extensive extracts from it may be printed or otherwise reproduced without the author's written permission.

The author attests that permission has been obtained for the use of any copyrighted material appearing in this thesis (other than brief excerpts requiring only proper acknowledgement in scholarly writing), and that all such use is clearly acknowledged.

TABLE OF CONTENTS

List of Tables

List of Figures

List of Abbreviations and Symbols

A	Area
a	Length
a_i	i-th entry in a Jacobian matrix, lower boundary of search area.
A_c	Cross-sectional area
b	Width of a cantilever beam, length
b_i	i-th entry in a Jacobian matrix, upper boundary of search area.
C	Center of the platform, damping matrix
ccw	Counter clockwise
c_i	i-th entry in a Jacobian matrix
CMC	Canadian Micro-Electronics Corporation
CM2	Chip name: compliant mechanism 2
CM3	Chip name: compliant mechanism 3
CM4	Chip name: compliant mechanism 4
CM5	Chip name: compliant mechanism 5
CMOS	Complementary metal oxide semiconductor
COR	Center of rotation
cw	Clockwise
DAC	Digital to Analog Converter
DAQ	Data Acquisition Card
df	Increment output force
diag	Diagonal matrix
Disp	Displacement
dl	Net expansion
DOF	Degree Of Freedom
dTA	Delta thermal actuator
dx	Deflection, output displacement

e	Distance between the center lines of hot and cold arms of sTA; original offset of hot arms in chevron actuator
E	Young's modulus
e_i	Term in a Jacobian matrix
Er	Rotation matrix
err	Error
Exp.	Experimental
F	Force vector, point force
f	Frequency; force
FEA	Finite Element Analysis
FEM	Finite Element Model
f_i	Term in a Jacobian matrix
f_{out}	Output force
FRF	Frequency response function
f(t)	Force vector
$F(\omega)$	Fourier transform of a forcing vector
G.A	Geometric advantage
GD	Golden division optimum method
GPa	1×10^9 Pa
h	Thickness of a cantilever beam, step
$H(\omega)$	FRF matrix
$H_{ij}(\omega)$	FRF relating motion at DOF i resulting from the force applied at DOF j
i	Index
I	Node in beam element
I_p	Platform's mass moment of inertia about mass center with taking account of added masses
IP	In-plane mode, in-phase mode
I_{p0}	Platform's mass moment of inertia about mass center without

	taking account of added masses
I_{ta}	Mass moment of inertia of motor about motor pivot with added mass from S-joint
I_{ta_c}	Mass moment of inertia of motor about mass center without added mass from S-joint
I_{ta_p}	Mass moment of inertia of motor about pivot without added mass from S-joint
J	Node in beam element, Jacobian matrix
K	Mass matrix for a vibration system
k_a	Axial stiffness of a S-joint
k_β	In-plane rotational stiffness of a S-joint
k_i	Coefficient of the integral block
k_s	Lateral stiffness of a S-joint
k_p	Coefficient of the proportional block
k_θ	In-plane rotational stiffness of a motor
L	Length, LaGrange function
l	Length from pivot to pin in the yoke
L_c	Length of cold arm of delta thermal actuator
L_{mc}	Distance between the dTA mass center to its pivot
l_0	The length of hot arm of unpowered TA
M	Mass matrix of a vibration system
M.A.	Mechanical advantage
MEMS	Micro Electro Mechanical Systems
Mi	The i-th motor
micron	1 μm or 1 x 10^{-6} m
MIMO	Multiple input and multiple output
MT2	Chip name: Micro Tools 2
M_{ta}	Mass of dTA without added mass from S-joints
M_p	Mass of platform with added mass from S-joints

M_{p0}	Mass of platform without added mass from S-joints
MUMPs	Multi User MEMS Process
n	Multiply factor
NA	Not applicable
N_{bi}	Nodes with boundary conditions
NI	National Instruments
N_{pi}	Nodes with external loads
OP	Out-of-plane mode, out-of-phase mode
OPT	Optimum method
P	Distributed load
PTP	Point to point control
Q	Damping factor
r	Platform's radius
rad	radian
R_L	Radius of the larger arc of S-joint
r_p	Distance between the added mass center to the center of platform
Rs	Radius of the smaller arc of S-joint
rTA	Ring Thermal Actuator
SEM	Scanning Electron Microscope
SF	Success/Fail optimum method
s_i	Displacement of S-joint in axial direction
SI	International System of Units
sTA	Standard thermal actuator
T	Temperature difference, kinetic energy
t	time
TA	Thermal Actuator
TA1	Chip name: Thermal Actuator 1
U	Potential energy
V	Voltage

v	Voltage
x	X axis in a coordinate system, displacement in x direction
X(t)	Displacement vector
x_{out}	Output displacement
y	y axis in a coordinate system, displacement in y direction
YC2	Chip name: Yeast Clamp 2
z	z axis in a coordinate system,
x, y, z	Rectangular coordinates

Greek Symbols

α	Angle; damping constant in a proportionally damped system
β	Angle; damping constant in a proportionally damped system
$\delta x, \delta y$	Derivative displacement in x, y direction
$\delta\varphi, \delta\theta,$	Derivative rotation
ϕ_r	The r-th normal model of an undamped system
Φ	Modal matrix
$\overline{\Phi}$	Mass normalized modal matrix
φ	Angle
θ	Angle
ν	Poisson's ratio
ρ	Density
ω_r	The r-th natural frequency
ζ_i	The i-th damping ratio
μm	1×10^{-6} meter
μSI	International System of Units for micro systems
Δx	Deflection

Acknowledgements

My deep appreciation goes out to those great people who helped me with this thesis. I want to thank Dr. Marek Kujath, my supervisor, and Dr. Ted Hubbard, for introducing me to MEMS. I want to thank them for their advice, financial & technical support, and for helping me get used to the new environment and making my research such an enjoyable and memorable experience.

Also, many thanks go to Dr. Jimmy Chuang, and Dr. Anastasis Georgiades, Dr. Heiko Fettig and Ryan Hickey, of their technical support and advice; to all Dalhousie MEMS Lab members: Neil Ellerington, Dan Sameoto, James MacDonald, for helping me with measurement and reading my thesis draft; Jeongkwan Lee, Lisa Hunt for providing me assistance and advice.

I thank Peter Jones and Greg Jollimore for their technical support.

I have many words of thank you for my family for their love and encouragement, for their inspiring me to continue exploring.

I thank you my wife, Kongying, for all of her encouragement, praise and support.

Last but not the least, thank you goes to my daughter, Joy, for her bringing so much fun to our family.

Abstract

Study of micro scale manipulators is challenging because of the microscopic scale. This thesis investigates the kinematic and dynamic behavior of planar polysilicon MEMS 3-DOF manipulators. The manipulators consist of three evenly distributed legs and one centrally located platform. Each leg is supported by an elastic spring, which is called S-joint, and is powered by a thermal actuator.

A rigid body kinematic model has been developed to study the work envelope of the manipulators and to facilitate automatic control. Experimental results were compared with predictions based on this model. Using the developed kinematic model, the geometry of manipulators has been optimized to obtain large work envelopes. The optimization included: radius of the platform and stroke of S-joints. Corresponding design guidelines have been provided as well. The largest measured work envelope, of the designed manipulators, is an area of approximately 20 μm in diameter.

A finite element model and a discrete spring-mass model of the manipulator have been developed. The numerical results of the spring-mass and the finite element models application revealed special properties of the manipulator such as, modes with repeated resonant frequencies, in-phase modes and out-of-phase modes, etc. The simulated results were compared with the experimental results and they agreed with each other.

Developed motion control algorithms included point to point and path control. They utilized vision system for feedback. The algorithms were applied successfully in experiments with 1-DOF and 3-DOF devices and resulted in errors of less than 0.3 μm.

1 Introduction

This chapter will provide a general introduction to MEMS including: scaling laws, fabrication of MEMS, joints, thermal actuators, and manipulators. Also, the state of the art for such devices will be presented.

1.1 Scope of the Thesis

In this study, attention was focused on the development of micro-machined manipulators which have three degrees of freedom: two translational and one rotational. Due to the important role that actuators play in driving a manipulator, investigations of thermal actuators were discussed. Kinematic and dynamic models are developed to analyze the performance of the manipulators. Based on the models, image processing technology was employed to obtain feedback information for automatic control of the manipulators.

This thesis does not consider the out-of-plane behavior of the manipulators. It also only considers the performance of devices in air.

1.2 Objectives of the Thesis

The objectives of the thesis were as follows:

(1) To review the published studies about compliant mechanisms and micromanipulators.

(2) To design and improve planar micro-machined manipulators using MEMS technology.

(3) To investigate kinematic and dynamic properties of the manipulators by analytical and numerical models, as well as experimental testing.

(4) To apply automatic control to the manipulators to achieve path tracking.

1.3 Major contributions of the thesis

The major contributions of this thesis are as follows:

1. In the author's opinion, the thesis is the first report on a systematic study of compliant parallel planar micromanipulators including: design, modeling, testing, and automatic feedback control.

2. The author has developed a kinematic model for the designed micromanipulators. The model simplified the study of the manipulators' components, such as springs, actuators, and provided a deep insight into the kinematic properties of the manipulators.

3. The author has developed a spring-mass dynamic model for the designed micromanipulators. The model demonstrates a way to characterize a micro system by simplifying its components. Experimental results confirmed the accuracy of simulations of the spring-mass dynamic model.

4. The author introduced the concept of toggle into the analysis of thermal actuators. This analysis leads to the development of design guidelines for other researchers.

5. The author designed two novel bidirectional thermal actuators, which can produce reversing force and motion.

1.4 The sizes of MEMS devices

The name MEMS, is an acronym derived from the term Micro-Electro-Mechanical-Systems. The MEMS devices are fabricated on silicon wafers and the structural material is polysilicon. These devices are both mechanical and electrical, because they have mechanical properties such as moving parts, mechanical resonant frequencies, elasticity, etc., and they exhibit electrical properties such as conductance, and capacitance. The components of MEMS are normally at a scale of 10 to 100 microns. Their feature sizes can be as small as 1 micron. As a comparison, the diameter of a human hair is normally about 100 microns. Comprised of multiple thin structural layers, the thickness of MEMS (few microns) is very small compared to their width, therefore most of MEMS structures are considered planar.

1.5 Effects caused by size

According to scaling laws, when the size of a device decreases, the response frequency increases. The smaller the object, the faster the response. Using this advantage, a variety of microsensors have been developed [1, 2]. As far as force is concerned, body forces such as gravity force and inertial force are proportional to the volumes (L^3) of the objects, while surface forces such as surface tension force, hydrogen bonding force, etc., are proportional to the surface (L^2). As the dimensions decrease, non-volume forces such as surface force, electrostatic forces or van der Waals forces become dominant. As humidity, temperature, and the surrounding medium change, the effect of the adhesive forces varies. In humid air, the adhesive forces typically are: van der Waals force, surface tension force (capillary condensation of water), and electrostatic force [3]. In such conditions, devices such as thermal actuators, motion amplifiers, gears, etc., could stick to the substrate and may not work. Also, they could get attached to operating probes due to electric static forces. These forces described below, make manipulation of microscopic objects much more difficult. During experiments, it was observed that microscopic objects are easy to catch but difficult to release. There are several effective ways to address this [3]: a sharply edged projection is effective in reducing the electrostatic force; a rough surface is good for reducing the van der Waals force; a thermal treatment at about 200 °C and a hydrophobic treatment of the surface are effective in reducing the surface force.

Generally speaking, there are two types of micromanipulation: contact and noncontact. The studied manipulation devices, such as manipulators and micro-grippers, belong to contact manipulation.

1.6 Fabrication of MEMS devices

Macro scale machining uses tools such as drills, lathes and grinding machines. The processes are physical. But for the two MEMS manufacturing processes, surface micro-

machining and bulk micro-machining, micro machining is a physical-chemical process. Vaporization and deposition are physical processes; photolithography and etching are chemical processes.

Surface micro-machining uses a layering process. Several polysilicon layers are separated by glass sacrificial layers. Photolithography is used to create specific shapes. More details about this process can be found in [4].

MUMPs is the process used to fabricate the devices studied in this thesis. MUMPs (Multi-User MEMS Process) is a surface micro-machining process provided by Cronos (JDS Company). Figure 1.1 shows the layers and their thickness used by MUMPs. The total thickness is less than 10 µm. The maximum thickness of a single layer is 2 µm. There are three polysilicon structural layers (Poly0, Poly1, and Poly2) separated by oxide phosphosilicate glass (PSG) sacrificial layers. Poly0 layer is deposited to a silicon nitride layer directly that is used as electrical isolation between the polysilicon and the substrate [5]. A structure of polysilicon layer is patterned by photolithography, a process that includes the coating of the wafers with photoresist, exposure of photoresist with the appropriate mask, and developing the exposed photoresist to create the desired etch mask for subsequent pattern transfer into the underlying layer. After patterning, a PSG sacrificial layer is then deposited by LPCVD (Low Pressure Chemical Vapor Deposition). At the end of the process, sacrificial layers are removed to free structural layers which are attached to substrate eventually through anchors. The final deposited layer is a 0.5 mm metal layer (gold) that provides for probing, bonding, electrical conductive wires, and reflective mirror surfaces.
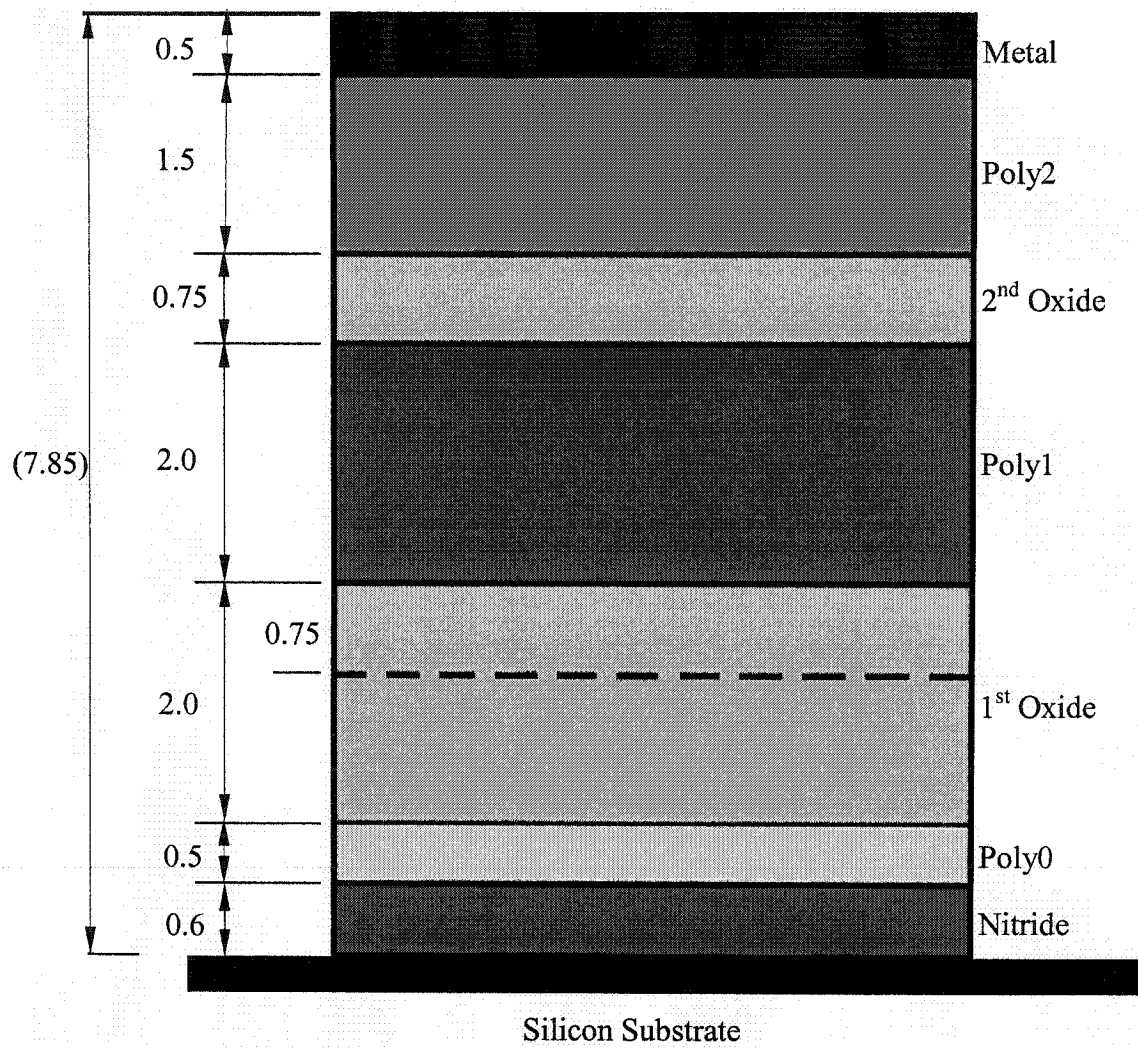
Figure 1.1 MUMPs Layers (units are in μm) [5].

Five MUMPs chips used in this research were designed by the author. The chips are labeled YC2, CM2, CM3, CM4, CM5, and their corresponding full names are Yeast Clamp 2, Compliant Mechanism 2, Compliant Mechanism 3, Compliant Mechanism 4, and Compliant Mechanism 5. In addition, one other chip was used in this research: TA1, Thermal Actuator 1, but it was not designed by the author.

1.7 Basic Operation of the manipulators

Figure 1.2 shows a compliant parallel manipulator. It has the basic structure of the manipulators studied in the thesis. They consist of one centrally located platform and three identical legs evenly distributed around the platform. Each leg is driven by a thermal actuator or a group of thermal actuators. The whole structure is suspended 2 μm above the substrate (the thickness of the removed sacrificial layer) and the anchors, located at the ends of the thermal actuators, attach it to the substrate. The minimum feature size of the manipulator components is 2 μm, while the overall size for the whole manipulator is about 1000 μm.

The following reasons determined the manipulator design. First of all, to move an object freely in a plane, three controlled DOF (two translational and one rotational) are required for operation. Thus, the system should be powered by three independent actuators. Secondly, the limitation of the MUMPs technology prevents users from making a powered serial manipulator, e.g., a motor cannot be mounted on a link powered by another motor. Therefore, parallel manipulators are the only logical choice. The platform is connected with legs by elastic S-joints. To assure a large work envelope of the platform, the S-joint should be flexible for axial and rotary motion.

Electric-current bimorph thermal actuators drive the manipulators. The platform can translate in two DOF and rotate in the plane as well. Depending on the power of the thermal actuators, the work envelope of the platform can be approximated by a circular area of 6 to 20 μm in diameter.
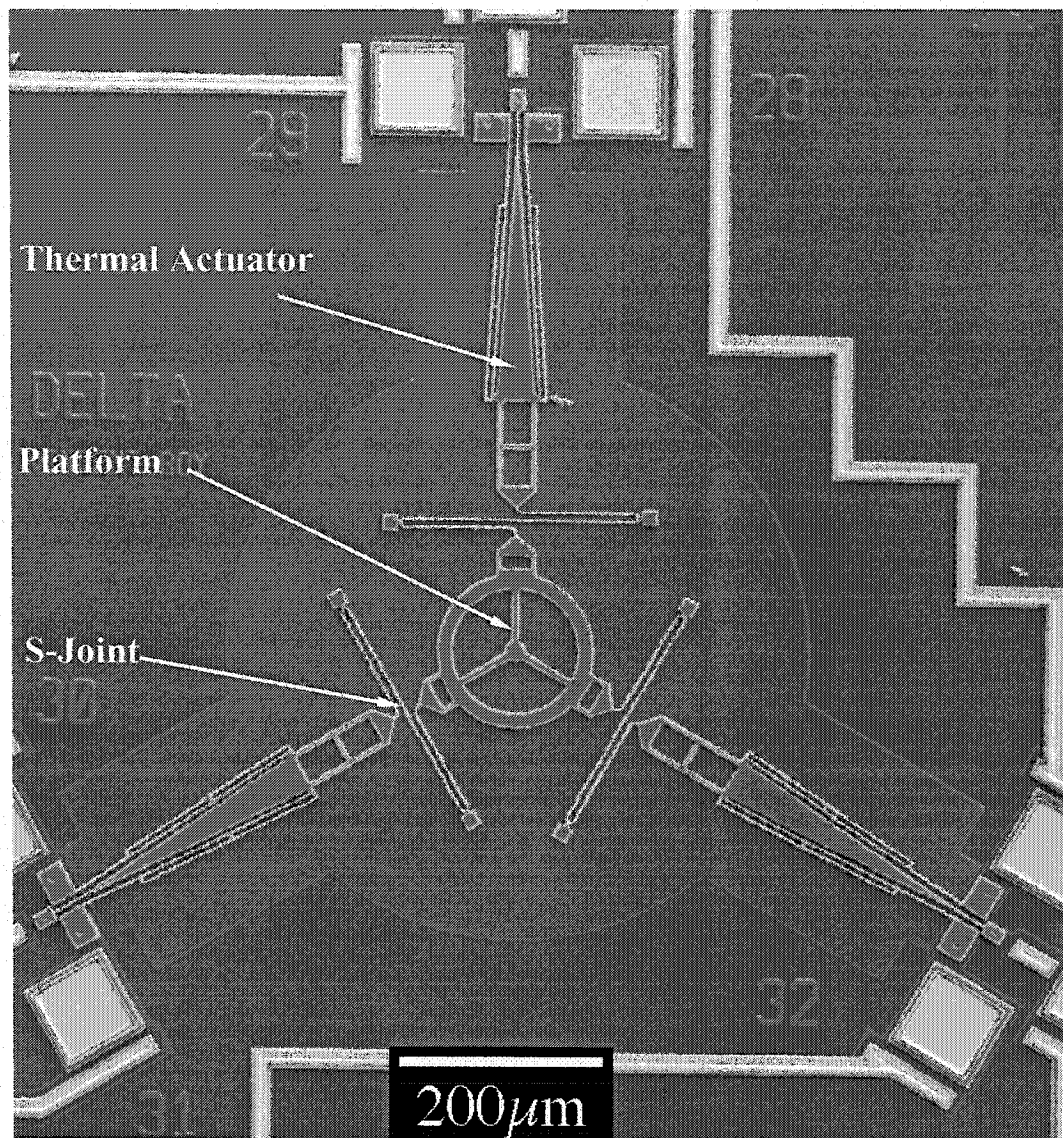
Figure 1.2 A manipulator on the CM2 chip.

1.8 Joints

Joints are essential parts in mechanical devices. When classic surface-contact joints were fabricated [6] with MUMPs technology, minimum gaps of 2 μm are mandatory to separate the two contacting surfaces during fabrication. These gaps caused backlash within the mechanisms. The effect of the backlash from the 2 μm gaps cannot be ignored. The clearance in joints may cause significant problems such as chaotic behavior [7]. To

avoid such negative effects, compliant flexures were selected to replace the surface-contact joints. The flexures are long and thin beams folded into specific shapes. Flexures of different shapes have different selective compliances [8]. Their in-house names reflect their shapes, e.g., I-joint and S-joint. The characteristic of an S-joint is that it is soft for in-plane translation in the axial direction and for rotation, while it is stiff against transverse deformation.
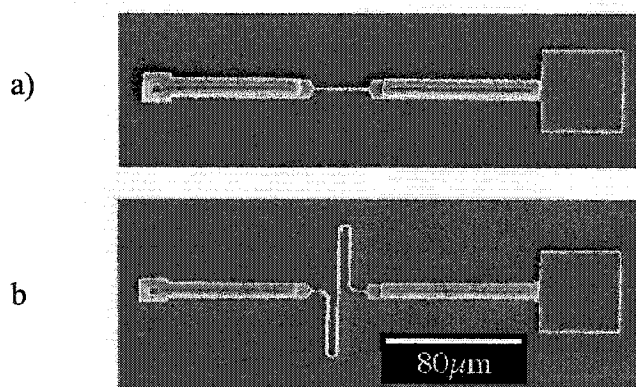
Figure 1.3 Micromachined flexures: a) I-joint, b) S-joint.

1.9 Thermal Actuators

The development of micro actuators plays a key role in the development of microelectromechanical systems. There are two kinds of well-known micro actuators: comb-driven electrostatic actuators [9] and thermal actuators [10, 11]. The former actuators provide only about 1µN of driving force and they require high voltages to operate. Since they consume practically no current, from the energy point of view, they are very efficient. However, their high working voltage makes their integration with standard electronics challenging. The bimorph thermal actuators described in [11] can offer about 10 µN forces and about 10 µm deflections or more [12, 13, 14]. Thermal actuators called chevrons [10, 15, 16] can provide driving forces from 100 to 800 µN depending on their geometry. Comparing the bimorph actuators with the chevron

actuators, the latter can produce 10 to100 times larger driving force with about 5 times smaller deflection. Thermal actuators will be discussed more fully in a later section.

1.10 State of the Art

The concept of compliant mechanism design has been developed for several decades including the design of flexure hinges [17, 18], flexible mechanisms [19], etc. Recent publications [20-23] indicate that compliant mechanism design continues attracting attention from researchers. Such research on compliant mechanisms has traditionally focused on macro scale mechanisms. However, as micro scale fabrication technology has been developed, more and more attention has been drawn to micro compliant mechanisms. Sigmund stated that compliant mechanisms are well-suited for MEMS [24] and he demonstrated it using topology optimization methods to design MEMS devices such as compliant micro grippers and micro thermal actuators. Furthermore, other micro compliant devices were investigated using topology optimization, such as micro structures with negative Poisson's ration by Sigmund [25], motion amplification systems by Canfield *et al* [26] and Kota *et al* [27]. Fettig *et al* conducted an investigation on MEMS compliant joints [17] and provided design guidelines of compliant joints. Similar micro compliant joints were used by Huang et al [28] and Chen et al [29] for designing microsystems. For example, a scratch drive actuator (SDA) is a single-flexure micro compliant structure, which was first presented in a paper by Akiyama et al [30] and optimized by Linderman et al [31] and Hunt et al [32]. Other recent published applications of micro compliant mechanisms include RF switches by Plotz et al [33], and micro tweezers by Jericho [34], etc.

Micromanipulation is also an attractive topic which includes manipulations of cells, bacteria and other micro organisms. From available publications, most of the manipulators developed for micromanipulations are comprised of compliant mechanisms. For example, Tanikawa [35] established a compliant micromanipulation system with a two-fingered micro hand based on a strategy of using chopsticks and then realized the manipulation of micro objects, such as 2 μm diameter latex balls, glass sticks, red blood

cells, etc, with associated errors of less than 0.1 μm. Goldbarb *et al* designed a three degree-of-freedom manipulator for micromanipulation by using split-tube flexure joints in order to minimize the surface effect [36]. Zou *et al* demonstrated a manipulator for cell manipulations [37], using conventional compliant notched joints to deliver desired micro motions. The overall size of the micro motion manipulator is macro scale. In addition, more and more researchers are using MEMS technology to develop manipulators for micromanipulations. State-of-the-art micromanipulators [38, 39], depending on surface contact joints to fulfill force and motion transmission, and are thus not well-suited to achieve high precision performance because of their inevitable behavior such as friction, backlash that is caused by the surface forces and the mandatory minimum spacing between adjacent parts. For example, joint clearances influence the singular configurations of a planar parallel manipulator [40]. The merits of compliant mechanisms, such as no backlash, suitable for small motions, etc, are summarized by Chen *et al* [41], and demonstrated by micro xy-stages for precision positioning reported by Kim *et al* [42, 43]. A two degree-of-freedom manipulator, similar to the xy-stage, was reported by Sun et al using Deep Reactive Ion Etching (DRIE) on Silicon-On-Insulator (SOI) wafer [44]. The manipulator, suspended on pairs of flexure beams, was actuated by two pairs of orthogonally oriented comb drives with approximately 5 μm of movement and 0.1 μm of accuracy. Recently, some multi-axis micromanipulation stages have also been developed based on compliant mechanisms [45 - 47] that are powered by non-MEMS actuators and are able to provide spatial motion: 90 nm translation and 5 μradians rotation.

Kinematic analysis is always an integral part of manipulator research. Gosselin [48] investigated parallel manipulators including such design criteria as workspace, singularity, dexterity in 1988. Wang and Gosselin [49] reported their research on singularity of 3-RRR manipulators. Gallant and Boudreau (2002) published a synthesis of planar parallel manipulators with prismatic joints for an optimal and singularity-free workspace [50]. Afterwards, Arsenault and Boudreau (2003) reported a synthesis of planar parallel manipulators with revolute joints (3-RRR) for an optimal and singularity-

free workspace [51]. Since the dimensions of a mechanism have no effect on its kinematic analysis, all kinematic methods applied to macro scaled mechanisms can be generalized to micro scaled mechanisms.

It is believed that the future for applications of microscopic actuated mechanisms is bright [52]. However, industrial applications are still rare. One of the obstacles is the difficulty of controlling such micro mechanisms accurately. In the 1980s, progress in computer and electronics made it possible to improve the performance of motion control. In the late 1980s and the early 1990s, several motion control theories were put into application [53-57], and motion control is now recognized as an important area in mechatronics [58]. Benefiting from current electronic technology, sensors can be integrated to MEMS devices, which makes feedback control for MEMS devices possible [59], at the cost of making systems more complex. Finally, high speed computers with strong vision processing software provide another possible way for feedback control in MEMS devices without integrated sensors [60, 35].

2 Thermal Actuators

The devices studied in this research were driven entirely by thermal actuators. Therefore this chapter will describe several kinds of actuators that have been developed. Central to their design is the use of geometric constraints to amplify motion from thermal expansion. Motion amplification is necessary since the thermal expansion of the active element is small (less than a micron). Several rigid-body kinematic models, that were developed to demonstrate the motion amplifications, are described in this chapter.

2.1 Toggle Mechanisms

A rigid-link four-bar mechanism is said to be a toggle when two of its moving and jointed links are collinear. The toggle configuration occurs when: the links of the toggle pair are folded side by side (the angle between the two links is zero degrees, as in Fig. 2.1 described below) or the toggle pair is open and the links are fully extended (the angle between the two links is 180 degrees). Making use of the high geometric advantage of toggle mechanisms, a thermal actuator can transform sub-micron expansion to the output deflection of several microns or even more.

2.1.1 Folded Toggle Mechanisms

A standard Thermal Actuator (sTA) shown in Figure 2.1 is based on a folded toggle and is comprised of two parallel arms of different cross- sectional areas [13]. The arms are connected to each other at one end, and attached to the ground at the other. When an electric current is passed through the loop, the arm with the smaller cross sectional area (called the hot arm) will become hotter than the thicker arm (called the cold arm) because the thinner arm provides higher resistance to the current. This will cause the hot arm to expand more than the cold arm. The net expansion between the hot and cold arms will drive the actuator motion. The basic components are shown in Figure 2.1.
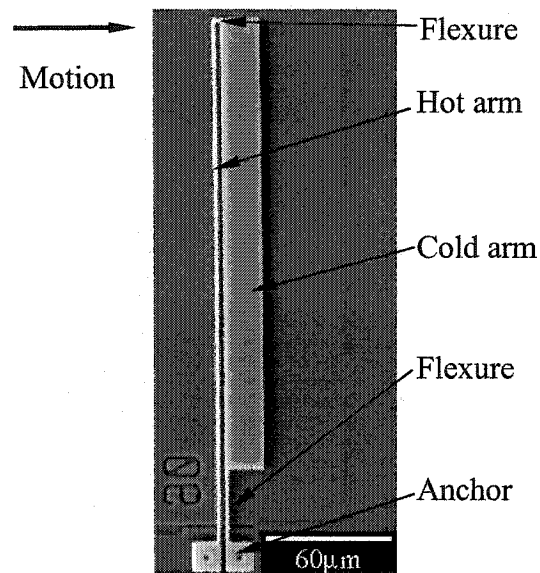
Figure 2.1 Standard Thermal Actuator.

The tip of the actuator moves in the direction of the cold arm. The exact center of rotation of the actuator is difficult to determine analytically. However, the rotation centers are close to the anchors at the ends of the cold arms. The standard thermal actuators can be modeled by the folded four-bar mechanism shown in Figure 2.2.
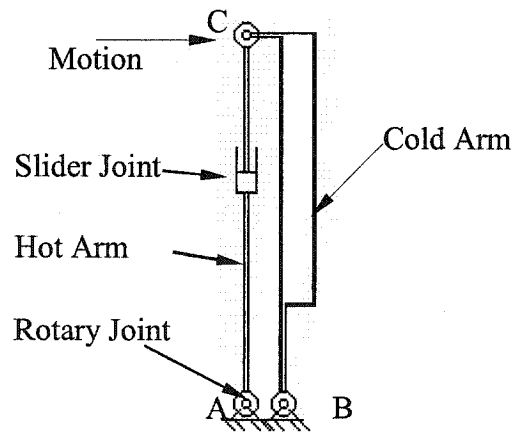
Figure 2.2 Rigid link model for sTA.

In Figure 2.2, the expansion phenomenon of the hot arm is modeled as a slider joint and the flexures are modeled as rotary joints. Limited by the MUMPs technology, a

mandatory minimum 2 μm feature size and 2 μm space between two separate components are required. Between the center lines of the hot arm and flexure in the cold arm there is a 4 μm distance. Compared with the length of the hot arm which is 200 μm, 4 μm is small enough to make the hot and cold arms close to the toggle position that is the arms are nearly colinar. The kinematic model shown in Figure 2.3 has been developed to calculate the approximate magnification for the sTA, including non-colinear links.
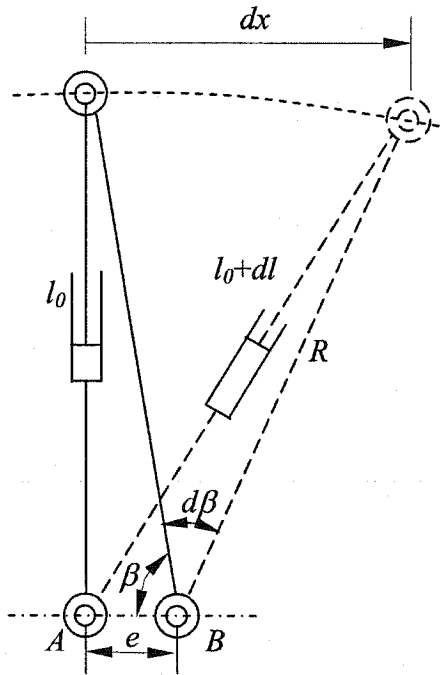
Figure 2.3 Kinematic model of a sTA.

In Figure 2.3, the varying length of the hot arm and the actuator's output displacement are labeled l_0+dl and dx respectively. The symbol R represents the constant length of the cold arm. The symbol e denotes the constant distance between the center lines of the hot and the cold arms. The angle β gives the original rest position of the cold arm. For a net expansion dl, the gain of the output motion can be calculated as follows: starting with a trigonometric relation

$$l^2 = R^2 + e^2 - 2 \cdot R \cdot e \cdot \cos \beta \qquad (2.1)$$

a differential relation can be obtained

$$l \cdot dl = \cdot R \cdot e \cdot \sin \beta \cdot d\beta \tag{2.2}$$

Assuming $l = R \sin\beta$ and $dx = R \, d\beta$, the magnification will be found as:

$$\frac{dx}{dl} = \frac{R}{e} \tag{2.3}$$

Equation 2.3 provides a useful estimate for the motion amplification of the folded toggle mechanism. For example, the motion amplification for a 200 μm long sTA with $e=$ 4 μm is approximately 50. Before buckling occurs in the hot arm, the net expansion of the sTA reaches approximately 0.2~0.3 μm. The experimentally measured output of 10~15 μm deflection confirms the prediction of equation (2.3) [61].

2.1.2 Versions of Folded Toggle Mechanisms

When a toggle mechanism is activated, it will either get closer to the toggle alignment or it will move away from it. A mechanism with the former property will be called an approaching toggle mechanism and the latter will be called a departing toggle mechanism.

a)   *b)*
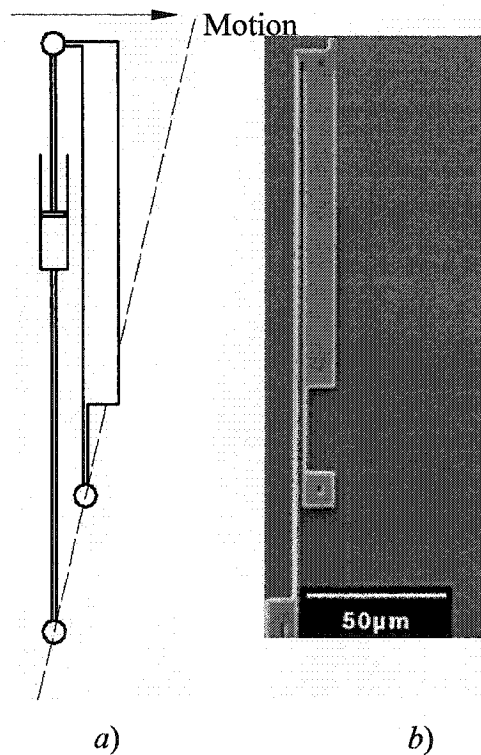
Figure 2.4 Approaching thermal actuator: a) rigid body model, b) SEM image.
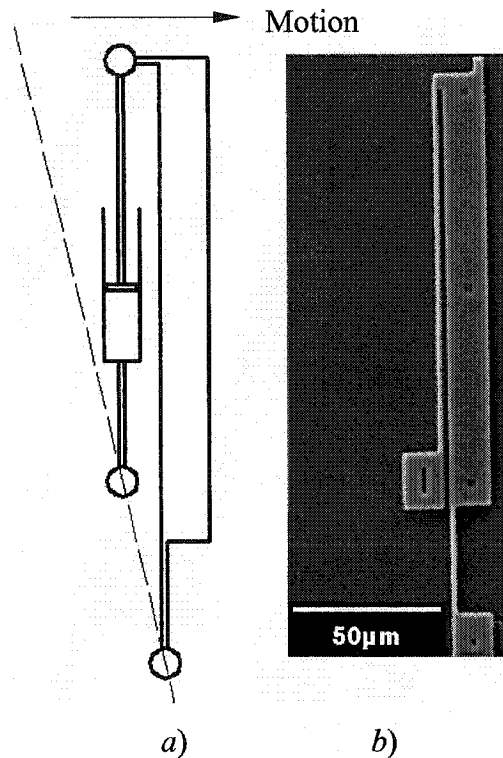
Figure 2.5 Departing thermal actuator: a) rigid body model, b) SEM image.

The arrows in Figure 2.4 & Figure 2.5 show the direction of motion. If all three rotary joints, represented by circles, were to lie on the dashed line, the device would be in toggle. Analyzing the rigid body model, it is very easy to determine whether the thermal actuators go into or out of toggle.

2.1.3 Open Toggle Mechanisms

The design of chevron actuators is based on the open toggle. They have two pairs of hot arms that expand towards one another. The actuator in Figure 2.6 has eight toggle pairs. Since the two hot arms are close to an open toggle configuration, small thermal expansions result in significant output motion at the middle tip where the arms are connected. For chevron actuators, the toggle alignment is the dashed line connecting

the two bases of the hot arms (see Figure 2.7). Since a chevron actuator can only move away from its ideal toggle, it is always a departing toggle mechanism.
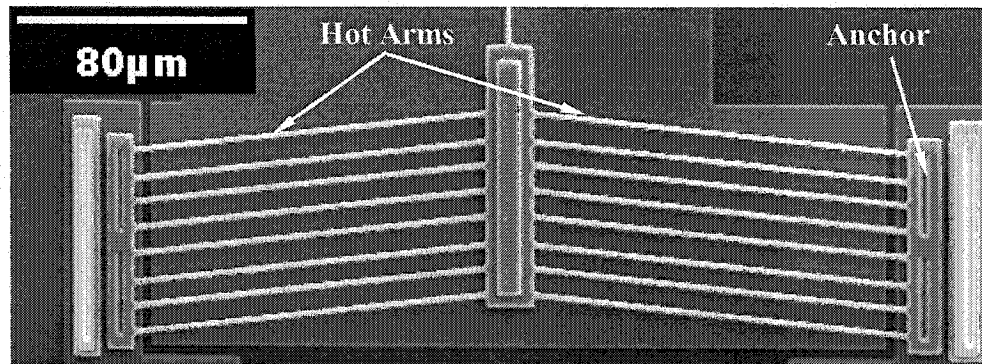
Figure 2.6 Chevron Thermal Actuator.

The expansion of the hot arms can be modelled as a sliding joint shown in Figure 2.7.
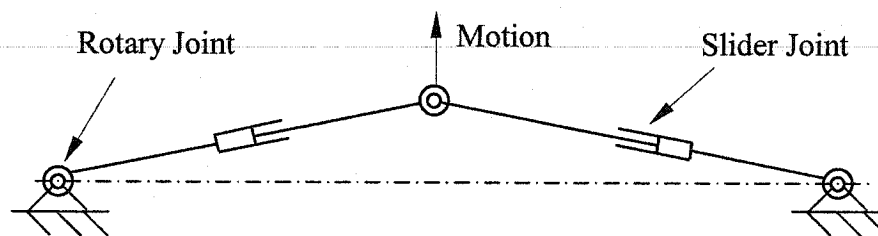
Figure 2.7 Rigid body model of a chevron actuator.

The rigid-body model of a chevron TA is a five-bar mechanism which has 2 controlled degrees of freedom. The two hot arms in the chevron TA are driven by the same current and produce the same amount of expansion. Figure 2.8 shows the geometric relation of a moving chevron TA.
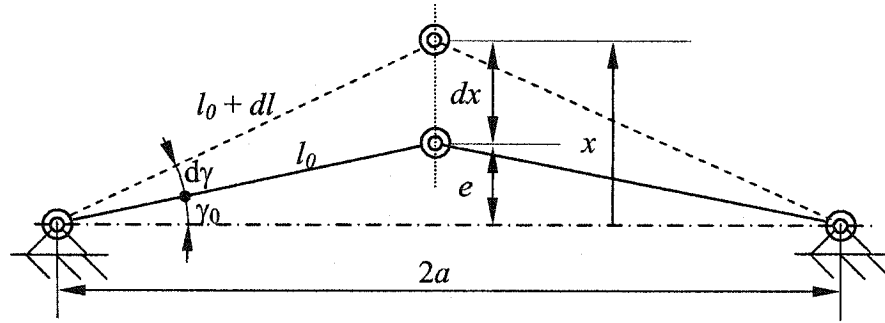
Figure 2.8 Geometric relations for a chevron TA.

Differentiating the trigonometric relations $x = l \cdot \sin \gamma$ and $a = l \cdot \cos \gamma$, where: a is constant, and $\gamma = \gamma_0 + d\gamma$, then rearranging them, the following relation can be found when $d\gamma$ is small:

$$\frac{dx}{dl} = \frac{a}{e} \qquad (2.4)$$

The motion amplification for a chevron actuator with 200 μm long arms and a 6° offset angle is approximately 10. When $\gamma = 6°$, then $e \approx 20$ μm, for a 200 μm long polysilicon hot arm with a 2x2 μm cross sectional area, the thermal expansion is normally less than 0.4 μm and it produces a maximum 4 μm output displacement. This was confirmed by measurements.

2.1.4 Force and displacement measurement

In order to measure forces on the micro-Newton scale, a micro force probe was constructed [62]. The device consists of an acupuncture needle mounted on the end of a rigid cantilever beam. The needle is positioned by three positioning stages (x, y, and z). The x positioning stage has a digital micrometer. The acupuncture needle and the MEMS device act as two springs in series with the total stiffness:

$$k_{total} = \frac{k_{needle} \cdot k_{TA}}{k_{needle} + k_{TA}} \qquad (2.5)$$

They experience the same force:

$$f = k_{needle} \cdot \Delta x_{needle} = k_{TA} \cdot \Delta x_{TA} \qquad (2.6)$$

Here k_{needle}, k_{TA}, Δx_{needle} and Δx_{TA} are the stiffnesses and deflections of the needle and thermal actuator.

When making a force measurement, it is important to choose an acupuncture needle that has approximately the same stiffness as the device to be tested [62]. Typical needles are 120 μm to 160 μm in diameter and 15 mm to 25 mm long. The resulting stiffnesses are in the range of 0.3 μN/μm to 3 μN/μm.

Needle deflections are measured by comparing the displacement of the needle tip with respect to the needle base: $\Delta x_{needle} = \Delta x_{base} - \Delta x_{image}$. The displacement of the needle base Δx_{base} is measured using the digital micrometer on the micro force probe. The displacement of the needle tip Δx_{image} is measured by taking a series of pictures of the needle tip (see Figure 2.9). These pictures are analyzed by a computer and the motion of the needle tip is measured in terms of pixels and then converted to microns with a resolution of approximately 0.5 μm. Figure 2.10 shows measured force and deflection for a sTA for 3, 4 and 5 volts. As expected, it was found that the forces decreased linearly with deflection. The 0 μm deflection is the position of the actuator when it is receiving no power or external force. Negative deflection values mean that the device was pushed back past its unpowered position.
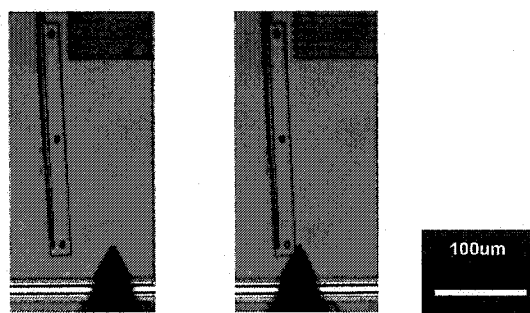
Figure 2.9 Acupuncture needle tip before and after contacting Thermal Actuator.
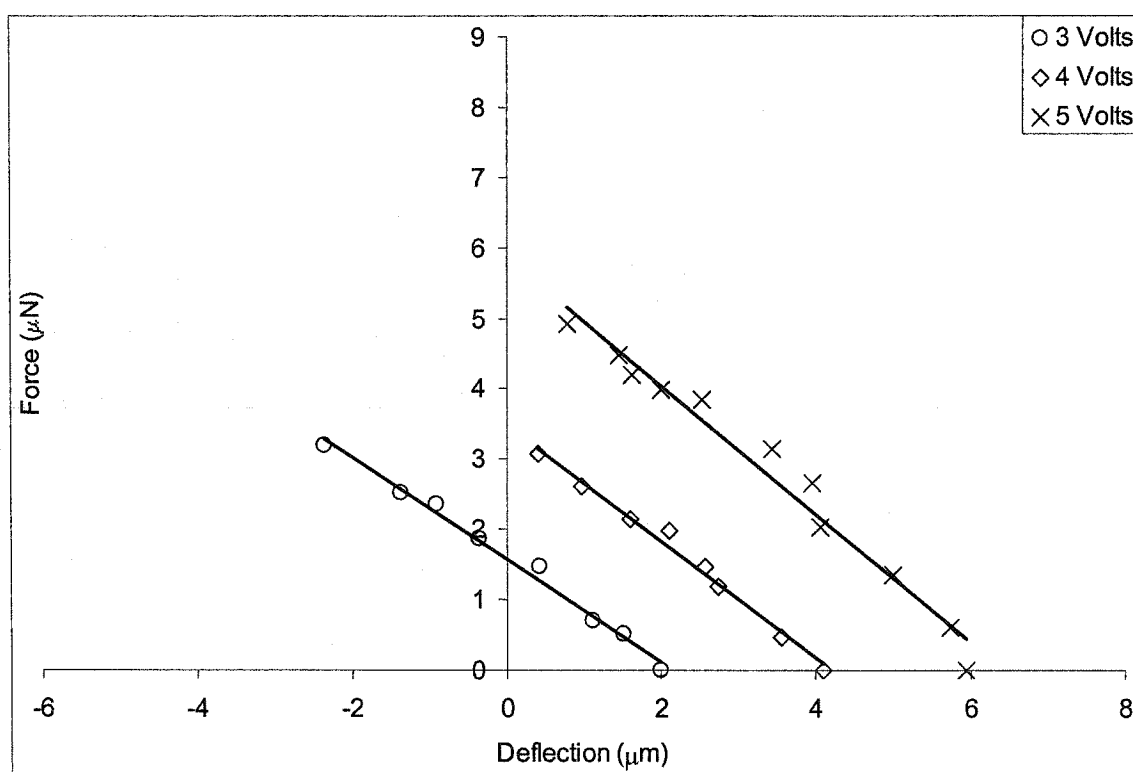
Figure 2.10 Force vs. deflection for a sTA (see Figure 2.1).
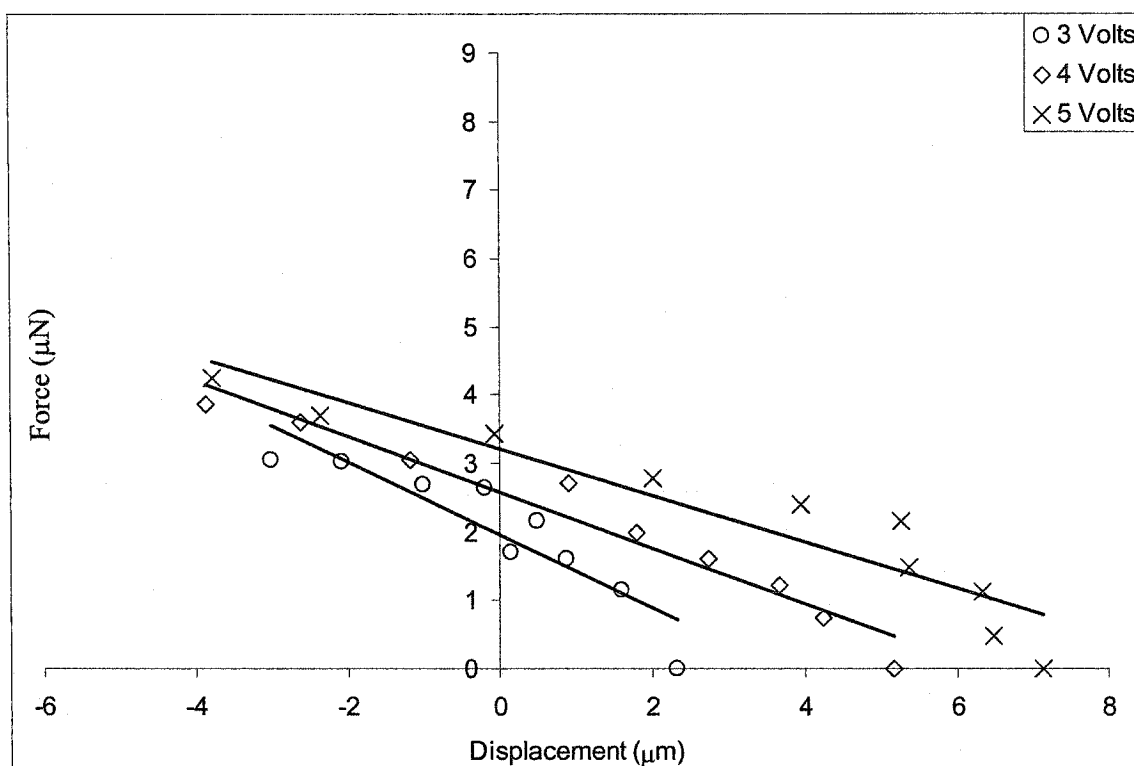
Figure 2.11 Force vs. deflection for an approaching toggle TA (see Figure 2.4).

Figure 2.11 shows the measurement results for the approaching toggle TA (see Figure 2.4b). Figure 2.12 gives the results for the departing toggle TA (see Figure 2.5b). As expected, Figure 2.11 shows that the TA approaching toggle had a larger range of motion but generated smaller forces than a sTA. Also, as the input voltage gets higher, the slope gets less steep. A departing toggle TA performed in an opposite way (see Figure 2.12).
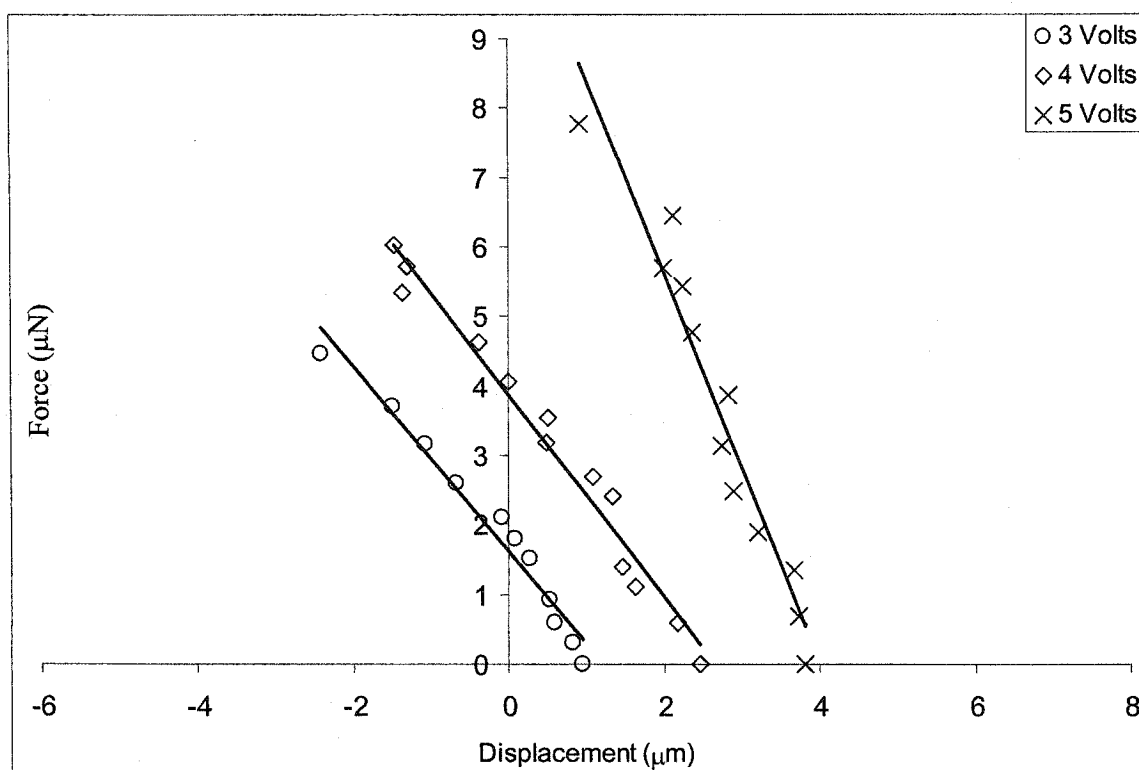
Figure 2.12 Force vs. deflection for a departing toggle TA (see Figure 2.5).

Figure 2.11 shows that the TA moving away from toggle had smaller deflections but generated larger forces. Moreover, the slope gets steeper when input voltage increases. A chevron TA with 8 pairs of hot arms can provide over 100 μN of force (see Figure 2.13), which is more than ten times the force that a sTA can develop, but they produce only 3 μm of motion when powered by 8 volts, while a single sTA generates 5 μN of force with 6 μm.
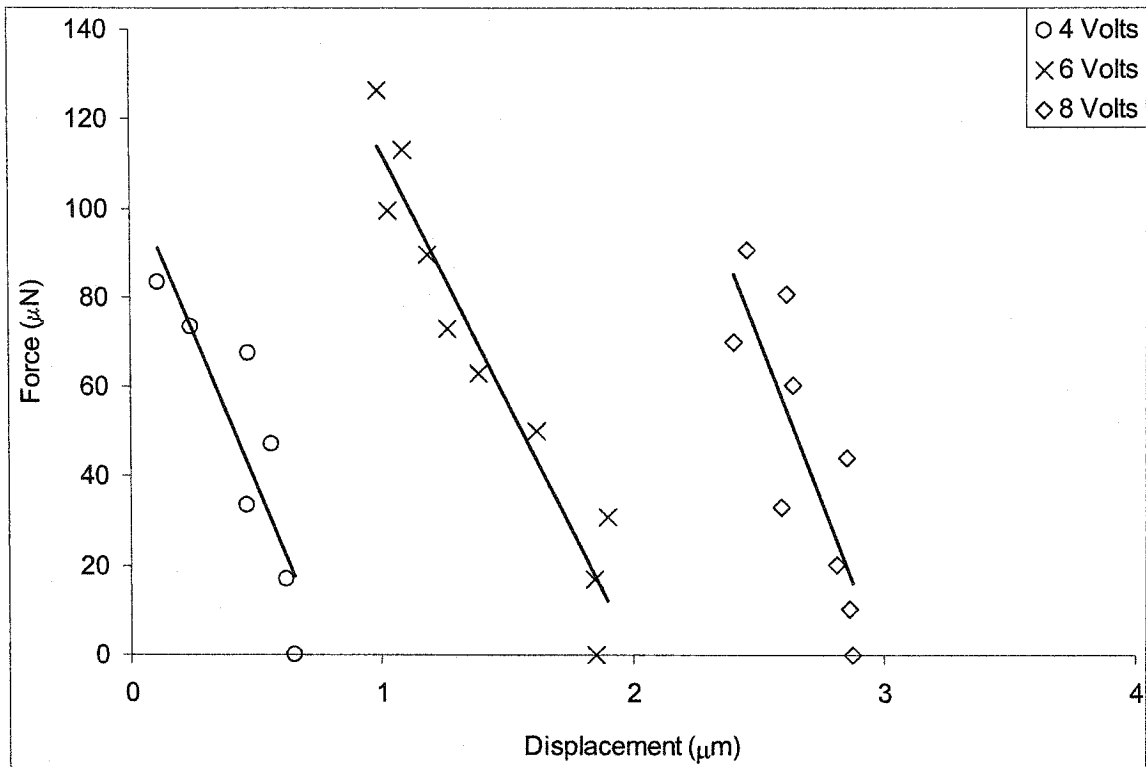
Figure 2.13 Force vs. deflection for the chevron TA (see Figure 2.6).

2.2   Bidirectional Thermal Actuators

The thermal actuators studied above were unidirectional. Unidirectional thermal actuators cannot satisfy all purposes, so bidirectional thermal actuators were developed. Bidirectional thermal actuators designed by R. Cragun can move 6 μm in both directions [14]. We wanted to develop actuators with greater range of motion.

2.2.1   Delta Thermal Actuator (dTA)

A delta thermal actuator consists of a central cold arm and a hot arm on each side. This arrangement creates two circuits and therefore bidirectional motion is possible. Its name comes from its shape which looks like an up-side-down delta sign (Figure 2.14a). The hot arms are 200 microns long with cross sections of 2x2 microns. A single hot arm and the

cold arm comprise a circuit. To move the actuator, power is applied to only one circuit or is alternated between the circuits.
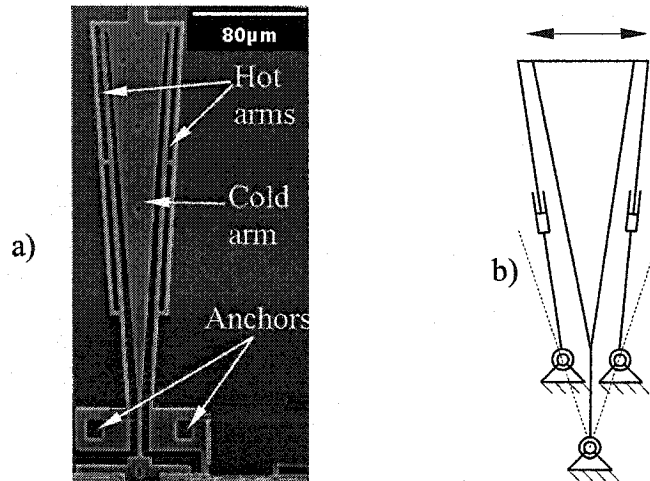
Figure 2.14 Delta Thermal Actuator (dTA): a) SEM image, b) kinematic model.

When one circuit is powered, there is no current go through the hot arm in the other circuit. The kinematic model for the delta TA comprises of two four-bar mechanisms which have a common output rocker linkage (Figure 2.14b). The dashed lines are the toggle positions for the two four-bar mechanisms. When one four-bar mechanism goes out of toggle the other four-bar mechanism goes into toggle. Figure 2.15 shows force vs. deflection for the delta TA (see Figure 2.14a).
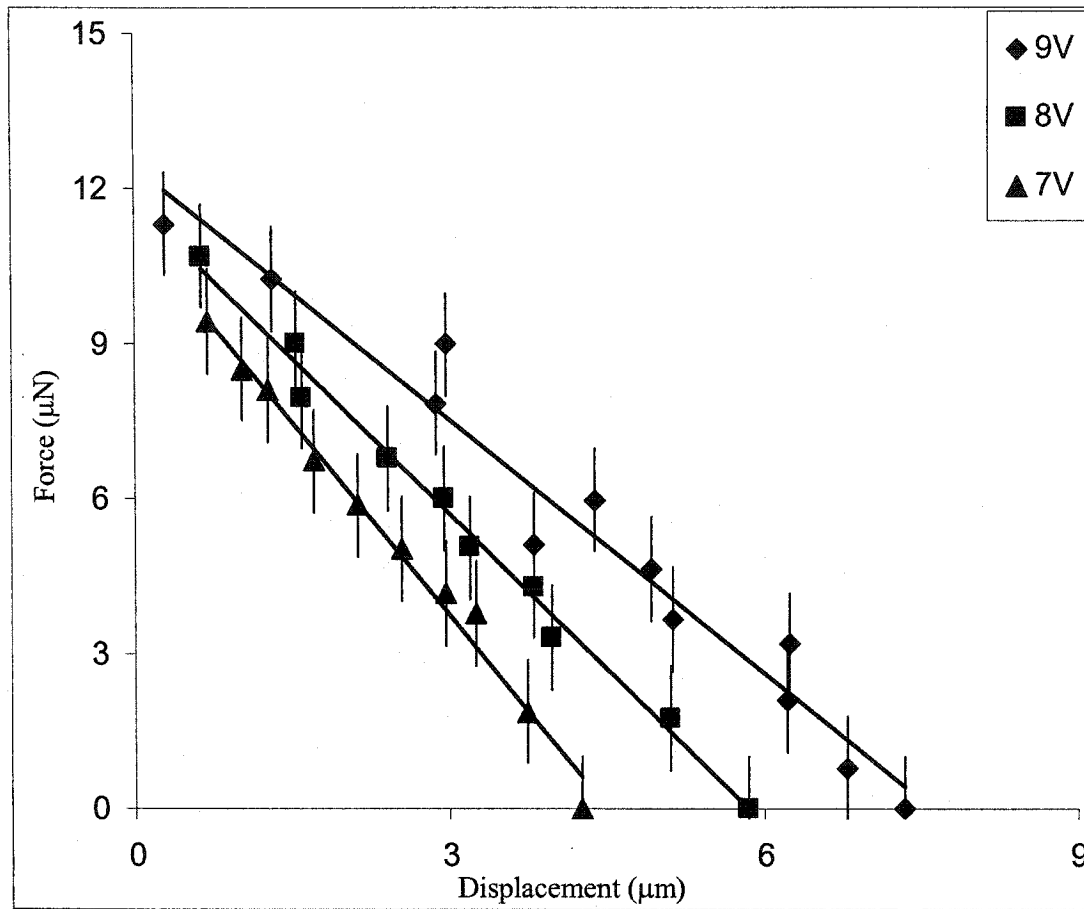
Figure 2.15 Force vs. Displacement of a delta Thermal Actuator.

The measurement results presented so far demonstrate that a sTA gives reasonable displacement with weak force while chevron actuators produce a strong force with small output motion. There are two methods to provide a thermal actuation with acceptable output motion and force. One method is to link a group of sTAs together by flexures to form a TA bank (see Figure 2.16a). The other method is to use a passive toggle amplifier to enlarge the deflection of a chevron actuator (see Figure 2.16b).
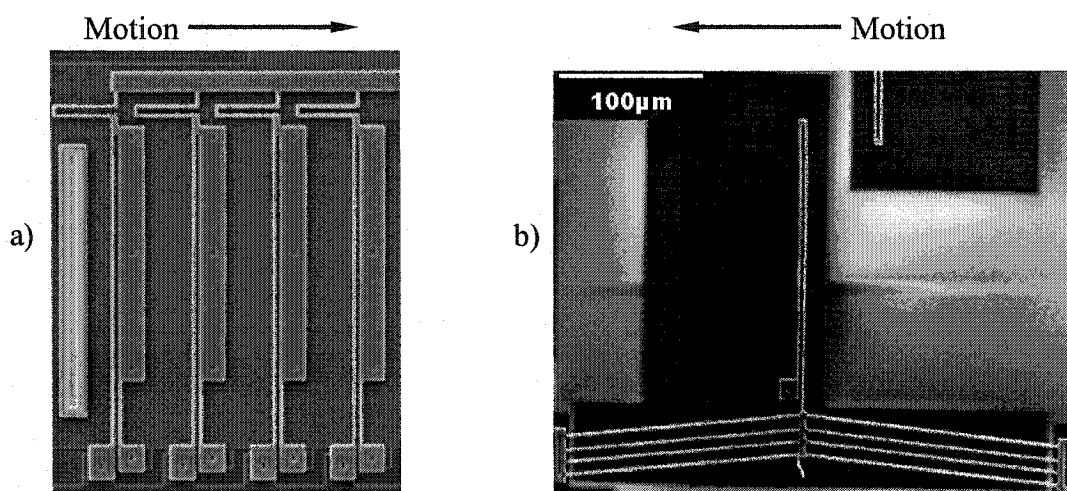
Figure 2.16 Modified thermal actuators a) sTA bank, b) Chevron TA with amplifier.

Since both methods involve deforming extra flexures, some of the energy produced by the actuators is stored in the flexures and that decreases the efficiency of the arrangement. Figure 2.17 compares the data at 5V for a sTA and a bank of five sTAs. The sTA bank produces much more force than a single sTA, but its output motion range decreases significantly.
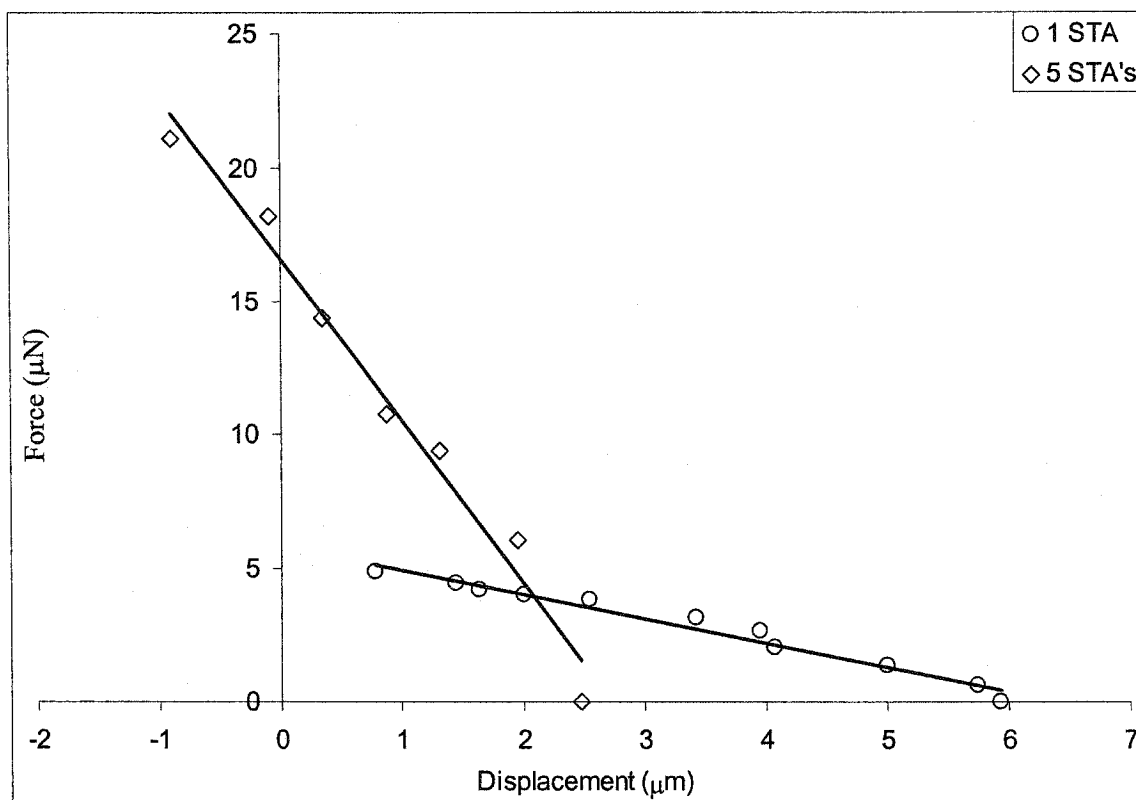
Figure 2.17 Comparison for sTA and five-sTA bank.

Figure 2.18 shows that a chevron actuator with an amplifier can produce a maximum displacement of 20 μm at 8V and approximately 3 μN maximum force.
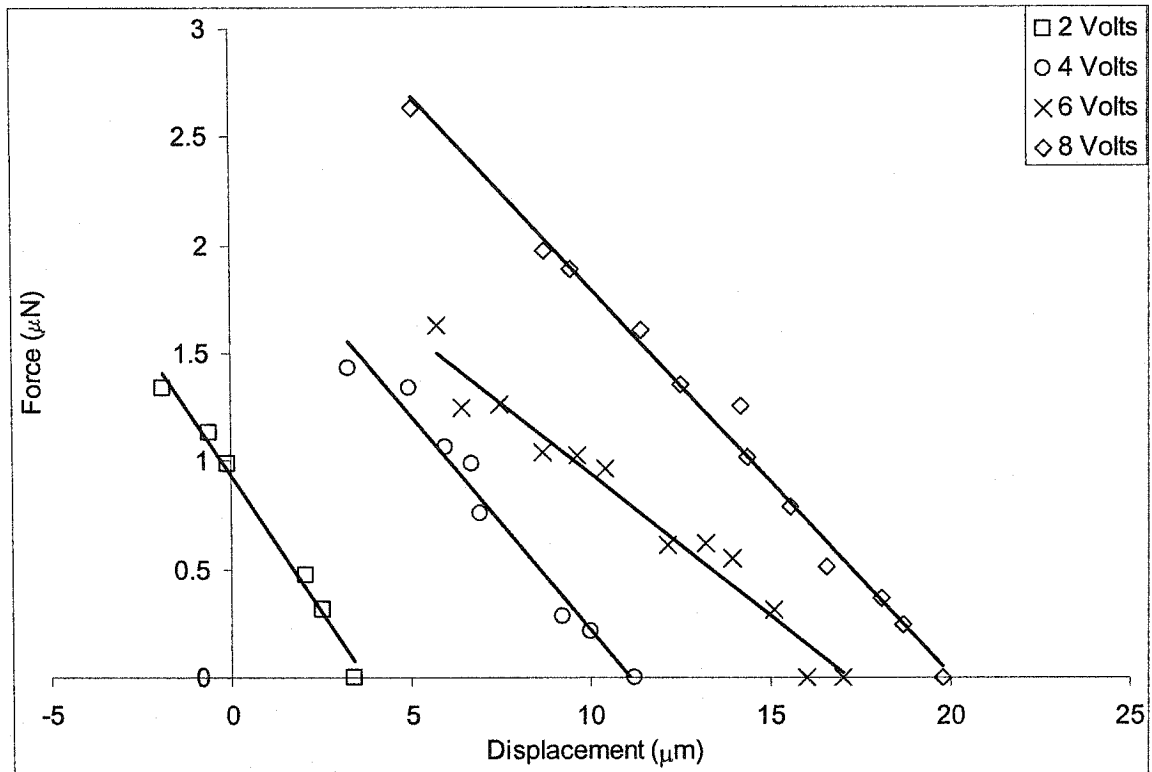
Figure 2.18 Force vs. displacement of a chevron TA with an amplifier (see Figure 2.16b).

2.2.2 T-motor

Four delta TAs (dTAs) were used to form a motor bank driving a T-shaped amplifier (see Figure 2.19). The whole assembly is referred to as a T-motor. The four dTAs work cooperatively rotating the T-structure about its instantaneous Center-Of-Rotation (COR) which is shown in Figure 2.19. The delta TAs in the T-motor were divided into two groups. Each group has two delta TAs driving to the same direction (see Figure 2.19). One group pushes the T-shaped structure while the other group pulls it. The driving forces form a force couple that rotates the T-structure. It was observed that the instantaneous COR moves very little (no more than 1 micron).
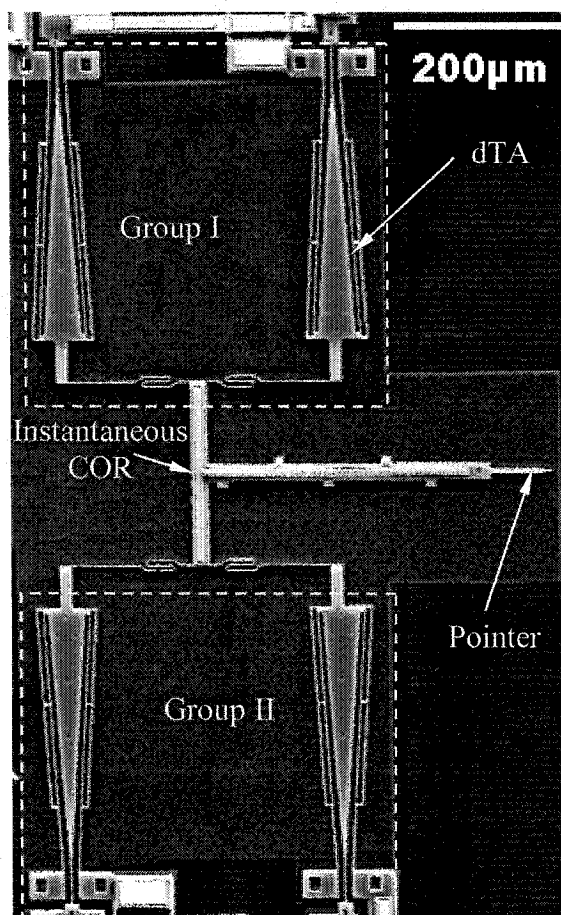
Figure 2.19 T-motor: T-shaped amplifier driven by 4 dTAs.

The pointer is the part that provides the output force and displacement. Figure 2.20 shows the force and displacement of the T-motor under specific voltages. At 11 volts, the T-motor can generate approximately 15 μN force or 15 microns displacement.
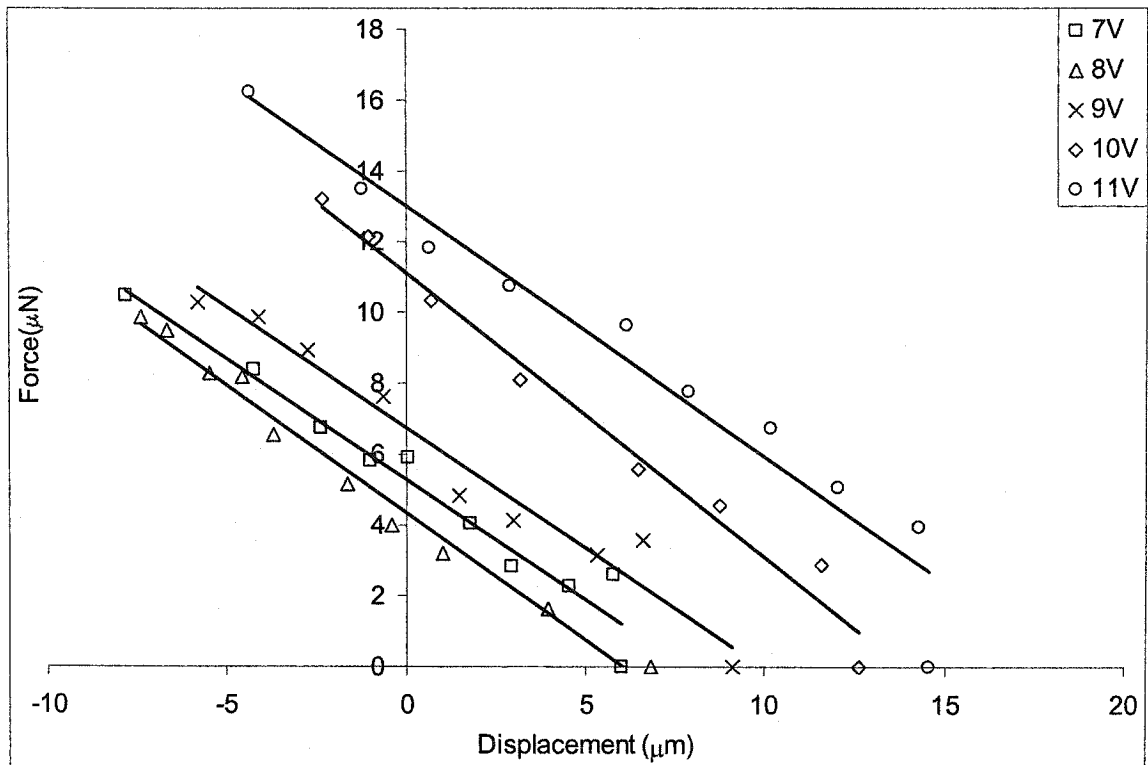
Figure 2.20 Force vs. deflection of T-motor.

2.2.3 Ring Thermal Actuator (rTA)

In addition to the two methods described above (T-motor and chevron with amplifier), a novel third design of a thermal actuator was developed by the author. A T-motor is not compact and occupies a large area, and a chevron with amplifier outputs small force. Therefore, a new compact and powerful TA was desired. Analyzing the rigid-body models of the sTA and dTA, we can see that the rotation centers are located at the bases of the cold arms. Several delta actuators can be arranged radially and they can share a single cold arm anchor. These actuators will rotate around the same point. Connecting all delta actuators, a rigid ring will output the motion and force. The ring has eliminated the cold arm flexures and the parasitic storage of elastic energy. Due to the limitation of MUMPs technology, the space available for wiring and anchors in the center is limited. This restricts the number of dTAs that can be added to the rTA. For a design purpose of

symmetry to form force couples, four dTAs were used to form a rTA. Figure 2.21 shows an SEM image of a rTA on CM5 chip. There are eight labeled arms, placed almost radially with an offset distance of $r_d = 4$ microns measured from the ring's center to the arm's axes. Figure 2.21b shows that the center-lines of the hot arms are tangent to this circle. When a rTA is activated, its arms either are compressed or expanded. The arms are 200 μm long and have 2 x 2 μm cross-sectional areas. Each arm is modeled as two rigid linkages with two rotary joints and a slider joint. The two rotary joints are located at the ends of the arms (see Figure 2.21b).

a) *b)*
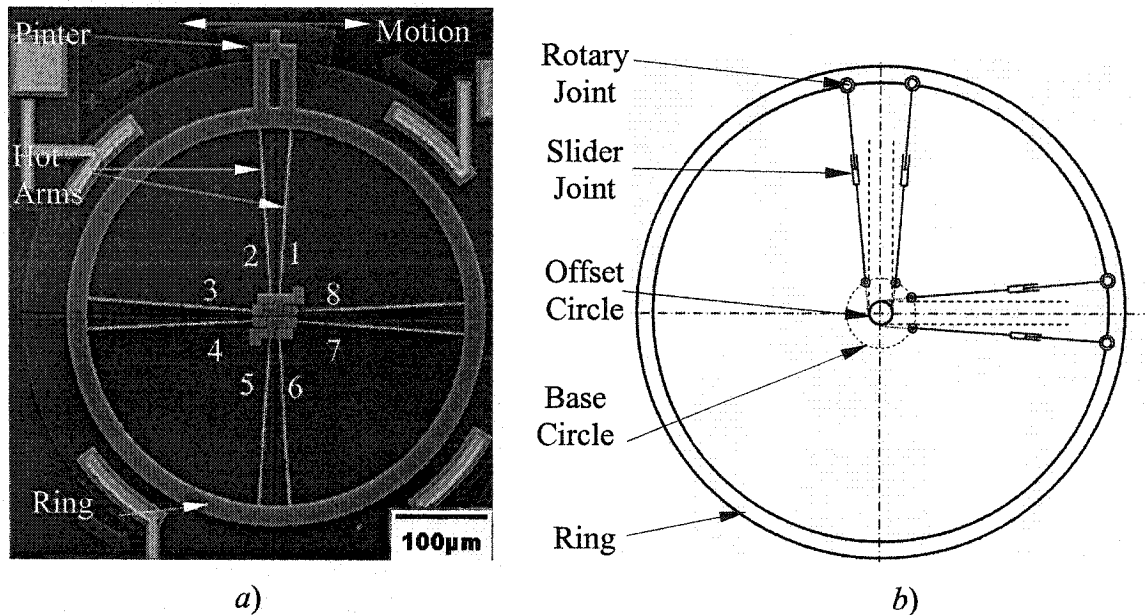
Figure 2.21 Ring Thermal Actuator (rTA) based on dTAs

a) SEM image, b) simplified kinematic model.

Due to the minimum separating space demanded in MUMPs fabrication, the ends of the hot arm could not be connected to their anchors at their tangential point on the offset circle. Instead, they are located at a dashed line circle in Figure 2.21b. This circle was concentric with the offset circle, was 54 μm in diameter, and was called base circle. The four arms were offset to the right with respect to the center line of each dTA, form one group. The other four arms were offset to the left and form another group. When one

group is powered, the arms of the other group idled without any current going through them. For example, when the current goes through the four arms offset to the right, they drive the wheel counterclockwise.

The active arms close the electric circuit in pairs. The simple electric connections for left drive (AA group) and right drive (BB group) are shown in Figure 2.22a. The symbols R_a and R_r in Figure 2.22 are resistances of the arms and the ring, respectively. For example, the TA drives counter clockwise if the right offset arms (arm 1, 3, 5, and 7) are activated. The anchors of arm-1 & arm-3 are connected by poly1, arm-5 and arm-7 as well (see Figure 2.22b). The anchors of arm-2 & arm-8, arm-4 & arm-6 are connected by poly0 which are underneath of poly1. Within the rTA, a driving current starts from the anchors of the arms 1 & 3, enters the ring, and ends at the anchors of the arms 5 & 7. Since the ring has far less resistance, it expands very little compared with the hot arms. Further, the rTA is a central symmetric structure and the driving forces are also distributed central symmetrically, therefore, the ring rotates about its center. The performance of the rTA will be described below following the description of an alternative rTA design.
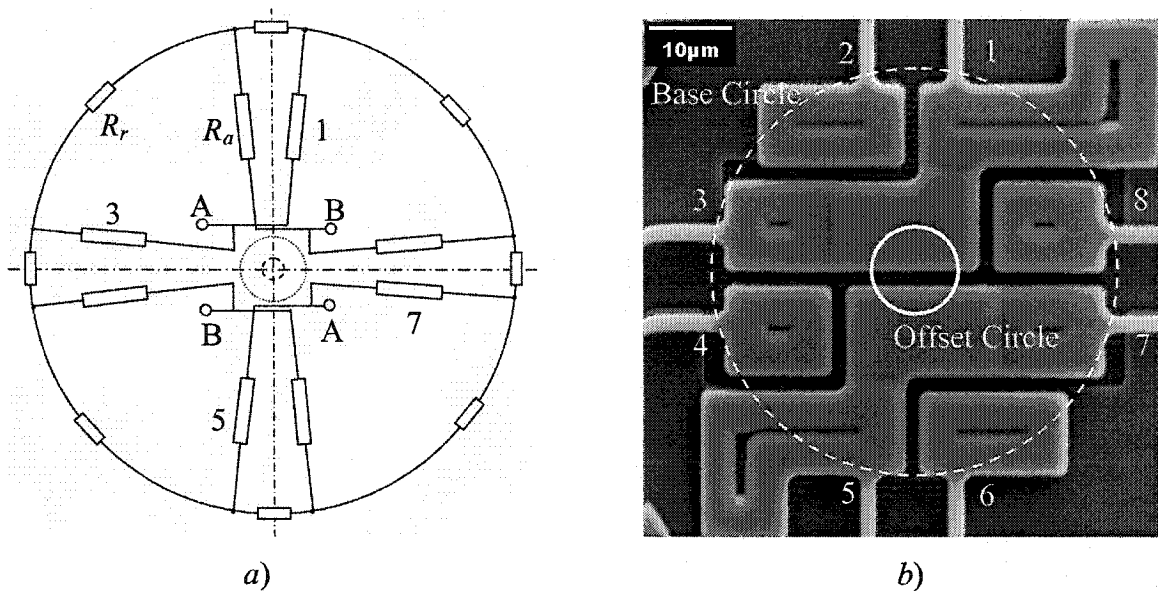
Figure 2.22 Electric connections of close circuits:

a) Electric connections,　　*b*) close-up of anchors

Similarly, instead of using delta TAs, four couples of TAs were used to design another bidirectional ring TA. Figure 2.23 shows the arrangement of the hot arms. The arrangement of the ends of the hot arms is the same as the rTA based on delta TAs (see Figure 2.22b). The two adjacent arms are parallel to each other, and are tangential to its offset circle whose radius r_s is 6 μm. The base circle of this rTA is 54 mm in diameter. Its electric connections are the same as the former rTA shown in Figure 2.22. Figure 2.23b shows the simplified kinematic model of the rTA based on sTAs.
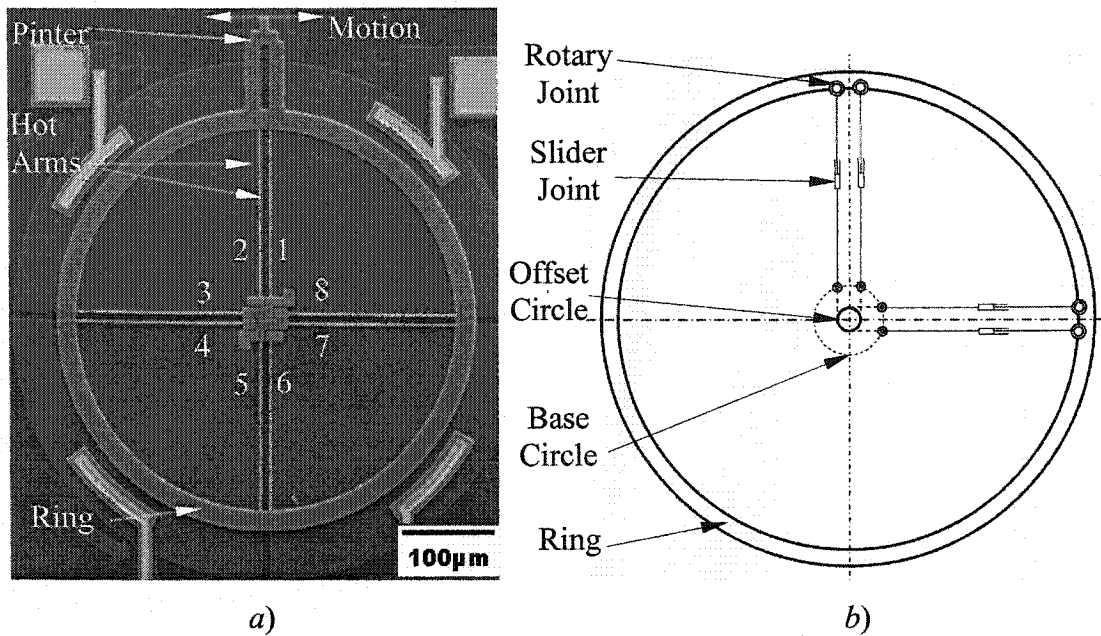
Figure 2.23 Ring TA based on standard TA (sTA):

a) SEM image, *b*) simplified kinematic model.

Since the structure of sTAs are central symmetric, forces form pure force couples turning the ring about its geometric center. In kinematic analysis, it is reasonable to add a virtual link connecting a rotary joint on the ring to a rotary joint at the center of the ring. Figure 2.24 explains the kinematic models for an arm within rTAs. The models are four-bar toggle mechanisms. Also, Figure 2.24 shows that the rTA based on dTAs (*a*) works closer to its ideal toggle position than the rTA based on sTAs (*b*) does. Therefore, the former is expected to produce larger rotation and smaller force than the latter does. The displacement of the rTAs in Figures 2.25 and 2.26, were measured at the outer edge of the ring.

a) rTA based on dTAs   b) rTA based on sTAs
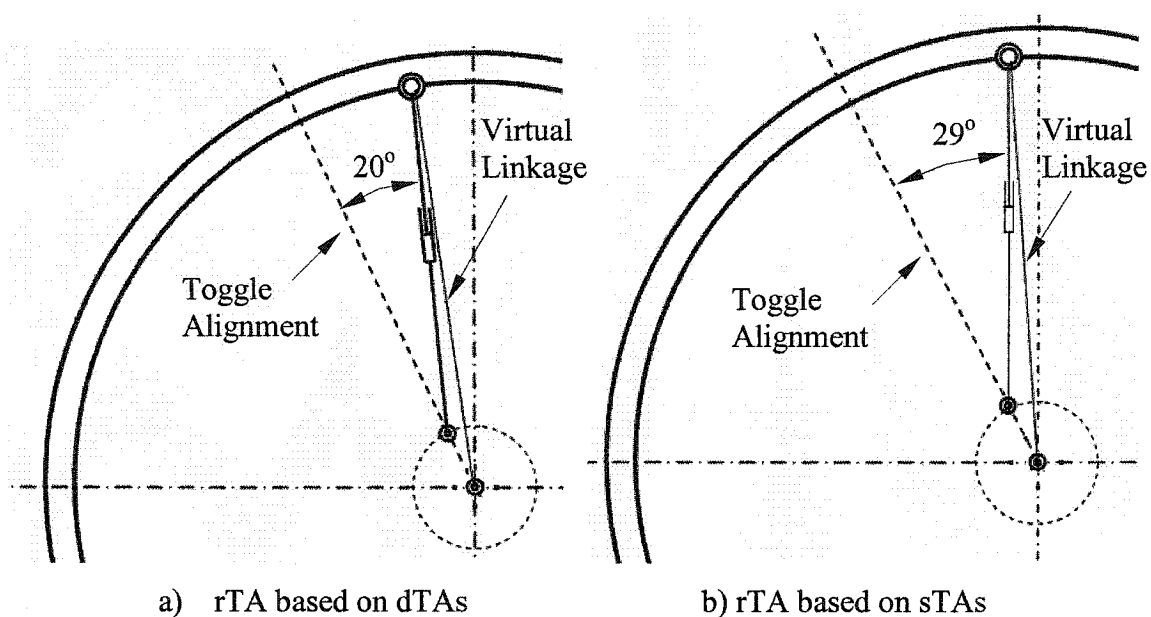
Figure 2.24 Diagrams of Toggle mechanisms for rTAs.
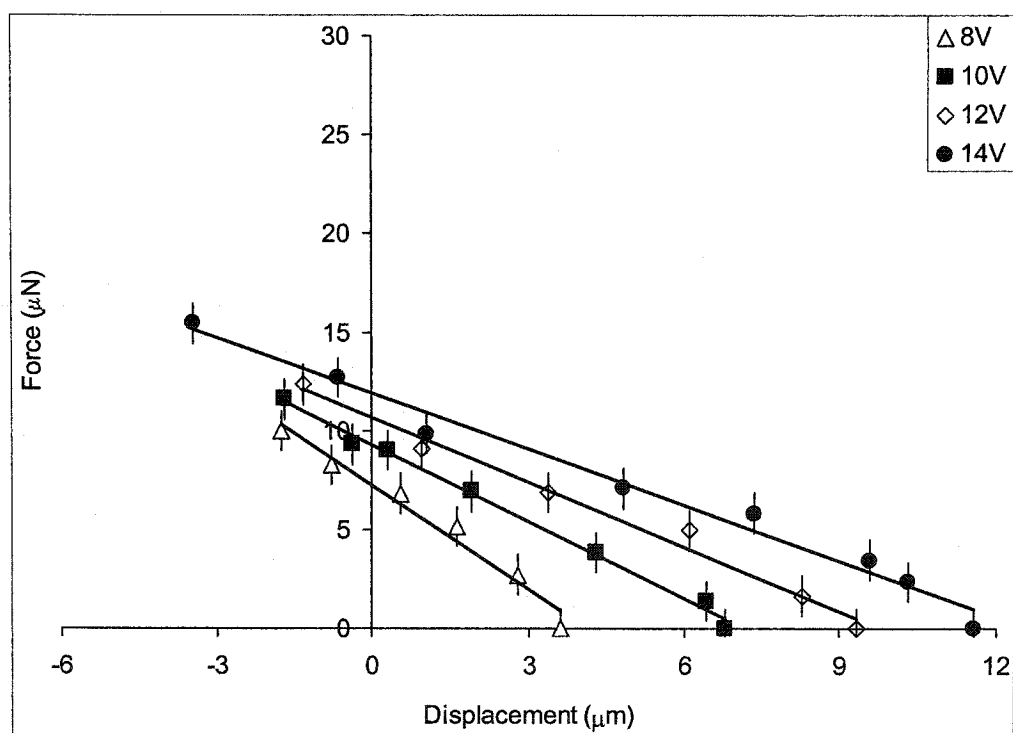
Figure 2.25 Force vs. displacement for ring TA based on dTAs.
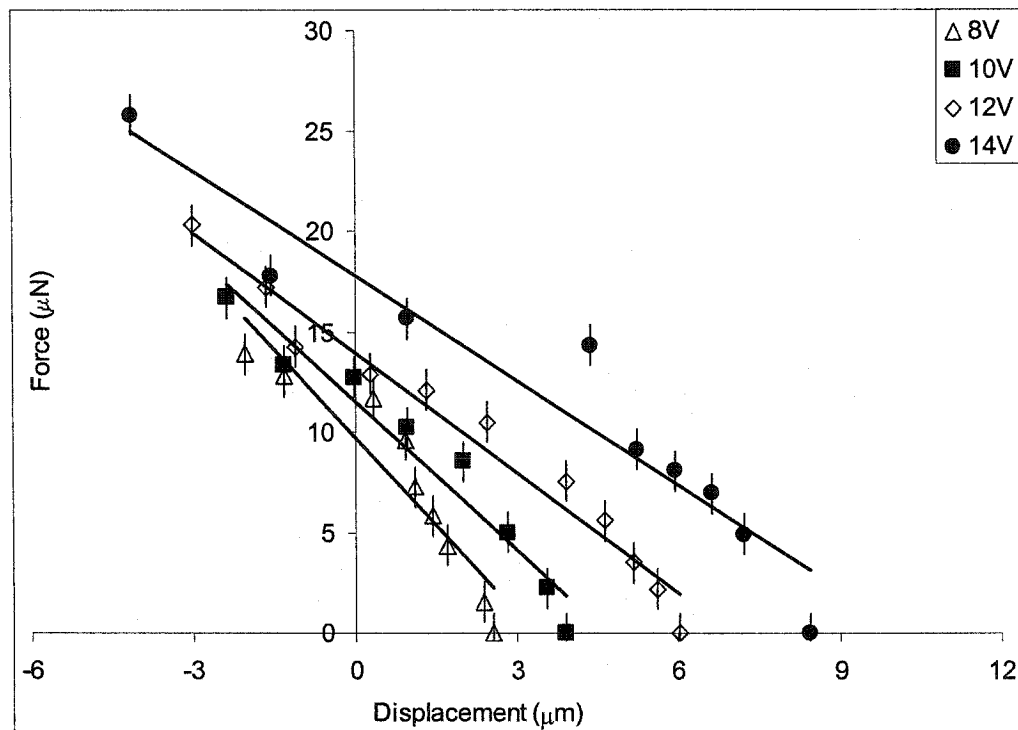
Figure 2.26 Force vs. displacement for ring TA based on sTAs.

Figures 2.25 and 2.26 show the measured forces vs. displacement for the ring TAs based on dTAs and sTAs, respectively. The four-bar mechanisms depart from their toggle alignment. Because of unpowered complex flexures, the rTAs demonstrate a similar property as that of an approaching toggle TA (see Fig. 2.11 vs. Fig. 2.25 and Fig. 2.26), the ring TAs experience higher voltages; and their slopes of force vs. displacement curves become less. Further, Figures 2.25 & 2.26 confirm that the rTA based on dTAs produces larger displacement and smaller force than the rTA based on sTAs does.

In addition, compared to a five sTA bank (see Figure 2.16a), the rTAs produce similar force, and much larger displacement. Further, compared to an amplifier powered by a chevron TA (see Figure 2.16b), the rTAs can produce about 20 μm totally, which is close to the amplifier's. However, maximum 3 μN force, which can be provided by the amplifier, is much smaller than the forces generated by the rTAs.

A third design of a ring TA is unidirectional (Figure 2.27). All of the spokes are hot arms and driving the ring in the same direction. Since there are no inactive arms in this unidirectional rTA, all energy produced by the hot arms drive the ring, and storage of elastic energy is minimized.

a)   b)
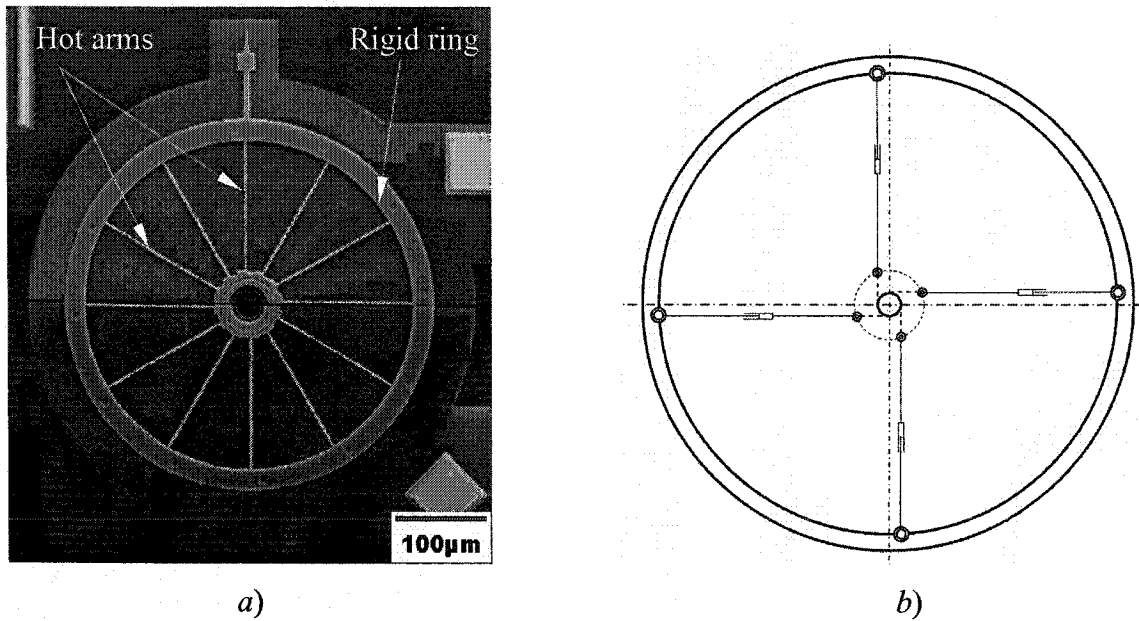
Figure 2.27 Unidirectional rTA: a) SEM image, b) Simplified kinematic model.

Figure 2.28 explains the electric wiring for the unidirectional rTA. The hot arms are divided into two groups by the horizontal center line of the ring. The anchor of one group of arms is connected to electric ground; the anchor of the other is connected to the positive polarity. A driving current will go through one group of arms, enter the ring, then go through the other group and close the circuit.
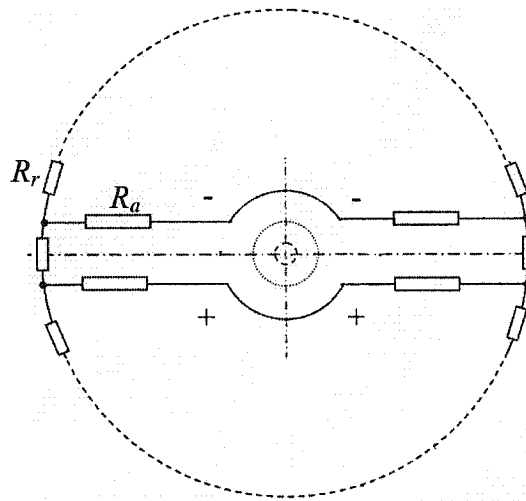
Figure 2.28 Electric connections of unidirectional rTA.

Unfortunately, the author found that the pointer attached to the unidirectional rTA is too flexible to measure its output force. Therefore, the performance of force vs. displacement is not provided here.

2.3 Summary

This chapter investigated Thermal Actuators (TAs) and developed a new conceptual wheel TA. Also the concept termed a "toggle" was introduced to classify TA types.

Compared to a departing toggle TA with the same size cold arm, an approaching toggle TA produces a larger displacement but a smaller force.

Comparisons among sTAs, sTAs bank, dTAs, chevron TAs with an amplifier and rTAs were done. The following conclusions can be drawn and can be used as a guideline for actuators selection.

    1) A chevron TA was the best force-producing actuator.

    2) A sTA bank worked inefficiently when flexures are used to connect single sTA together.

    3) dTAs and T-motor (4 dTA bank) are able to produce force and displacement in reversing directions. The efficiency of a dTA is lower than sTA's, because a cold arm and an idling hot arm in the dTA store energy generated by active hot arm.

4). rTAs produce the largest work with relatively large force and displacement in reversing directions. Considering this, rTAs are a better choice than others.

3 Kinematic Model for Micromanipulators

This chapter will examine the kinematic properties of several micromanipulators. The analysis is based on classic kinematics. After the analysis of the kinematic properties, a set of guidelines will be provided for the manipulator design.

3.1 Kinematic Modeling

To develop a kinematic model for Three Degree-Of-Freedom (3-DOF) manipulators, it is necessary to establish models of the components. All manipulators designed for this research have trisymmetric shapes. They are powered by different types of actuators. The actuators' motion can be treated as rotation about their centers of rotation, and therefore, a kinematic model of an actuator can be a simple pivoting beam.

All studied manipulators have a central platform supported and driven by flexures called S-joints (see Figure 3.1). The cross sections of these flexures are 2 × 2 μm. S-joints are compliant axially and in planar rotation but are designed to be stiff in the lateral direction. The actuators are only expected to produce forces that drive the platform only in the plane. Therefore, the S-joints' out-of-plane degrees of freedom were not taken into account in the model developed here. An S-joint will be modelled as a compound pin-and-slot joint (Prismatic & Revolute –PR joint) which allows both linear and rotary motions (see Figure 3.2). The axial translation of the S-joint depends on its stiffness and the footprint size. To make a softer S-joint, a longer unfolded length of its beam would be required.
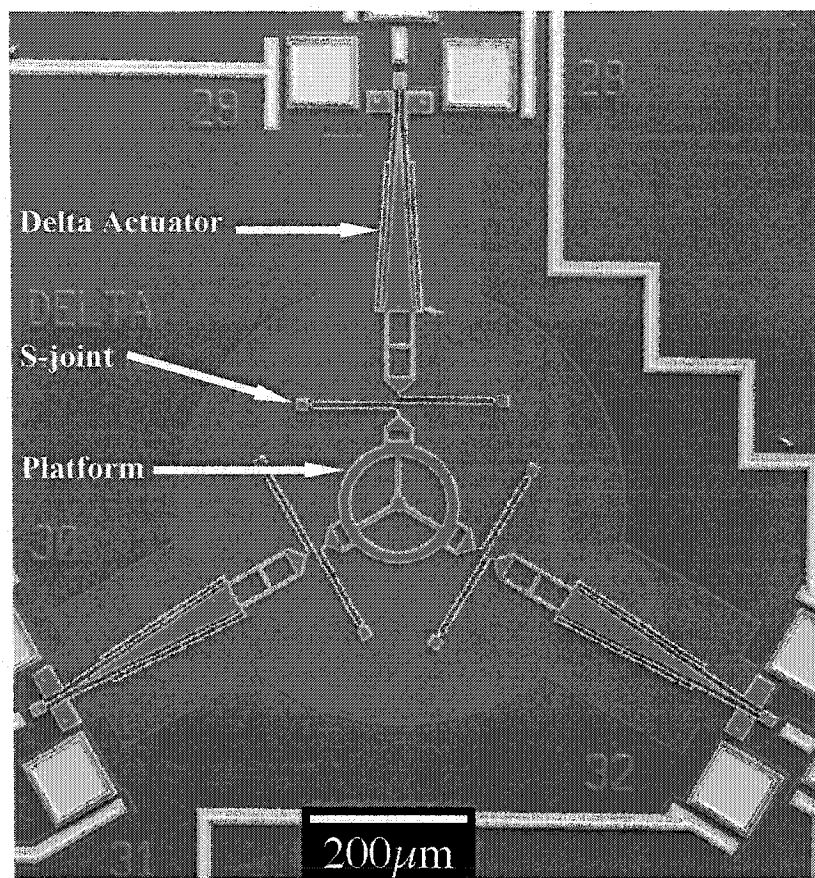
Figure 3.1 SEM image of a manipulator driven by delta TAs.

a)   *b)*
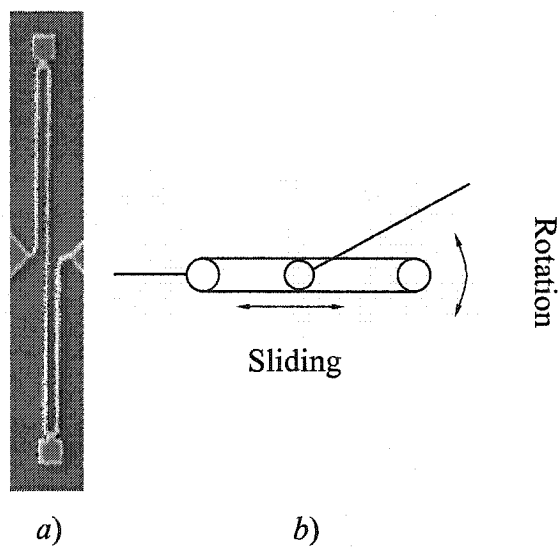
Figure 3.2 S-joint: *a)* SEM image, *b)* kinematic model- two DOF PR-joint.

The distance that the S-joint can be compressed & stretched is equal to the stroke of the pin-and-slot joint. Here, it is assumed that the S-joint compression and stretching strokes are equal. The pin of the S-joint model is originally located in the middle of the slot. The platform of the manipulator was modeled as a rigid disk. Figure 3.3 demonstrates the rigid body kinematic model of the manipulator.
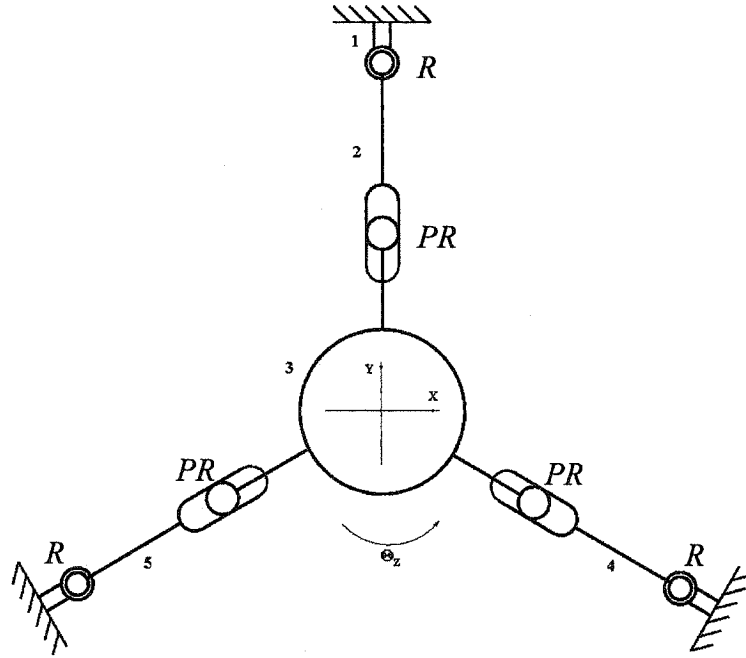
Figure 3.3 Kinematic model of manipulators: R – Revolute joint; PR – compound Prismatic & Revolute joint.

The kinematic model has five links and they are labeled in Figure 3.3 from 1 to 5. Link 1 is the frame. Links 2, 4, and 5 are motors; link 3 is the platform. There are three 1-DOF revolute (R) joints and three 2-DOF pin-and-slot (PR) joints. The mobility m for planar mechanisms can be calculated from the following equation [63]:

$$m = 3(L-1) - 2J_1 - J_2 \qquad (3.1)$$

Where L is the number of links in the mechanism, J_1 & J_2 denote the numbers of joints with 1 DOF and 2 DOF, respectively. In the case of the manipulator of Figure 3.3, L=5, J_1 =3 & J_2 =3. The mechanism has m = 3 DOF. Driven by the three motors, the platform

can translate in the x & y directions and rotate about the z axis (perpendicular to the x-y plane) as shown in Figure 3.3.

3.2 Work envelope

To study the manipulator's work envelope, a moving Cartesian coordinate system is attached to the platform at its center (C). At the neutral position, center C overlays the origin (o) of the coordinate system of the frame (Figure 3.4). The motor pivot positions M_i (i=1, 2, 3) are defined by coordinates (x_{0i}, y_{0i}). The dashed line in Figure 3.4b traces the new position of the platform subjected to rotation φ_p and translations x_c and y_c. The angles between line segments CP_i and the x axis are represented by φ_i, whose initial values are φ_{0i} (only φ_3 & φ_{303} are displayed in Figure 3.4b). The radius of the platform is defined by r, which is equal to CP_i. Positions of pin P_i are described by (x_{pi}, y_{pi}). The original length of the distance $(MP)_i$ is L_{i0}. The symbols $L_{(i)ext}$ and $L_{(i)comp}$ represent the stretching and compression strokes for the i-th S-joint. The maximum and minimum lengths of the distance $(MP)_i$ are $L_{i0} + L_{(i)ext}$ and $L_{i0} - L_{(i)comp}$, respectively.
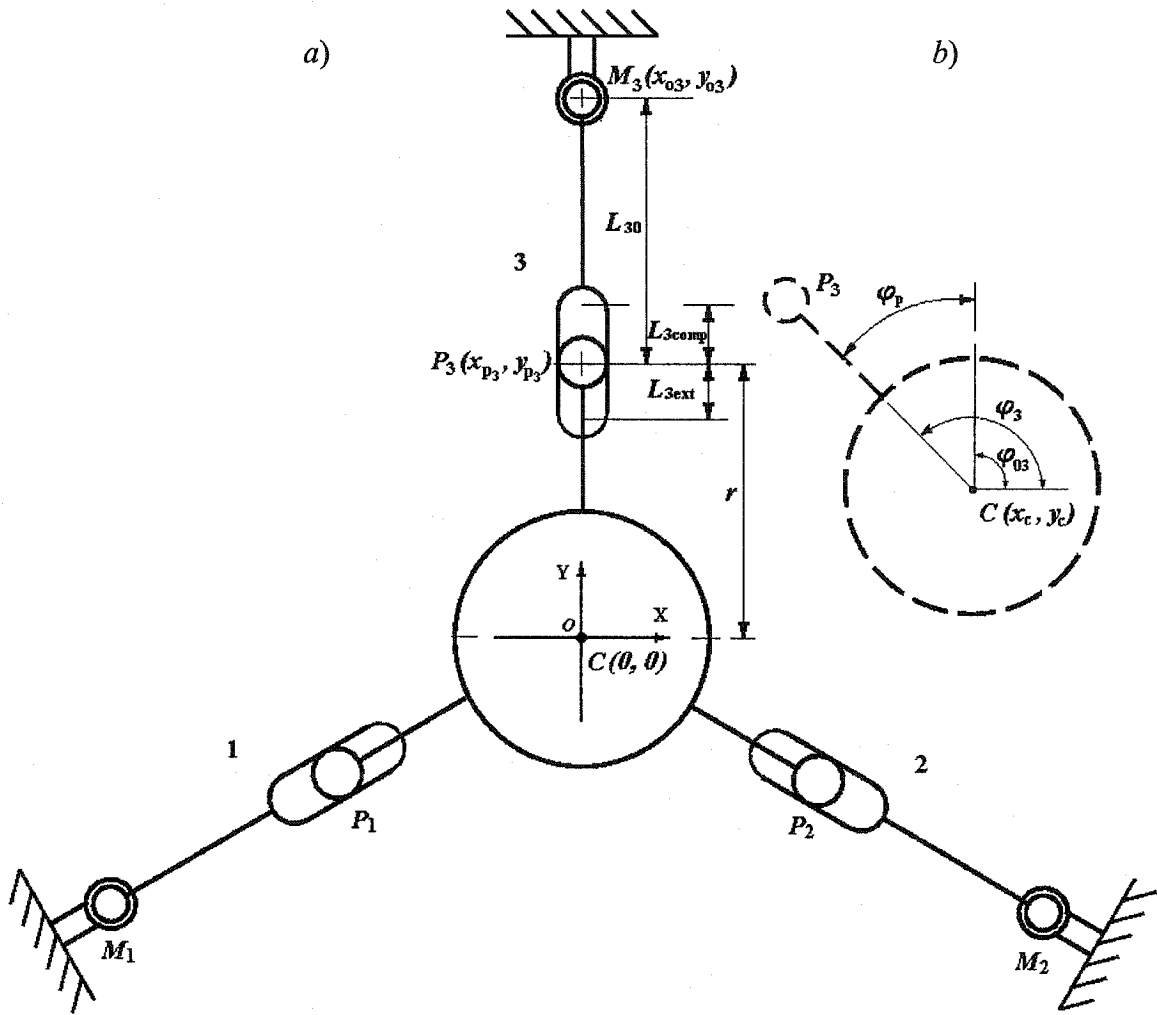
Figure 3.4 Coordinate system for the kinematic model:

a) neutral position, *b)* new position.

Taking into consideration only the third leg, pin P_3 of the platform can move anywhere within the following annular region (ring):

$$L_{3\min}^2 \leq (x_{p3} - x_{03})^2 + (y_{p3} - y_{03})^2 \leq L_{3\max}^2 \qquad (3.2)$$

Further, pin P_3 can be expressed by the position and orientation of the platform itself from the geometric relationships:

$$x_{p3} = x_c + r \cdot \cos\varphi_3$$

$$y_{p3} = y_c + r \cdot \sin\varphi_3 \tag{3.3}$$

The angle φ_3 is equal to the summation of φ_p and φ_{30} (see Figure 3.4b), where φ_{03} is constant. Substituting equations (3.3) into equation (3.2), the possible position and rotation of the platform (x_c, y_c, φ_p) are obtained in the following form:

$$L_{3\min}^2 \le [x_c + r \cdot \cos(\varphi_p + \varphi_{03}) - x_{03}]^2 + [y_c + r \cdot \sin(\varphi_p + \varphi_{03}) - y_{03}]^2 \le L_{3\max}^2 \tag{3.4}$$

With a specific rotation φ_p, the center of the platform (x_c, y_c) should be located in the area formed by the two concentric circles. The radii of these circles are $L_{3\max}$ and $L_{3\min}$, respectively (see Figure 3.5). Their co-center O_3 is located at:

$$[x_{03} - r \cdot \cos(\varphi_p + \varphi_{03}), y_{03} - r \cdot \sin(\varphi_p + \varphi_{03})] \tag{3.5}$$

Since the mechanism is tri-symmetric, another two similar equations can be obtained when only the motor 1 or the motor 2 is under consideration. A generalized equation, which defines work envelopes of the platform, is obtained for all three equations:

$$L_{i\min}^2 \le [x_c + r \cdot \cos(\varphi_p + \varphi_{03}) - x_{0i}]^2 + [y_c + r \cdot \sin(\varphi_p + \varphi_{03}) - y_{0i}]^2 \le L_{i\max}^2 \tag{3.6}$$

$$i = 1, \ 2, \ 3$$

where $\varphi_{01} = \dfrac{7\pi}{6}$, $\varphi_{02} = \dfrac{11\pi}{6}$ and $\varphi_{03} = \dfrac{3\pi}{6}$.

The constrained work envelope of the platform with a rotation of φ is demonstrated in Figure 3.5. The envelope is the common area, a polygon labeled *ABCDEF*, of the three rings. The locus of the co-centers O_1, O_2 and O_3 are the dashed line circles as shown in Figure 3.5 when rotation of the platform φ_p varies from 0 to 2π. The radius of the circles is the same as the radius of the platform r.
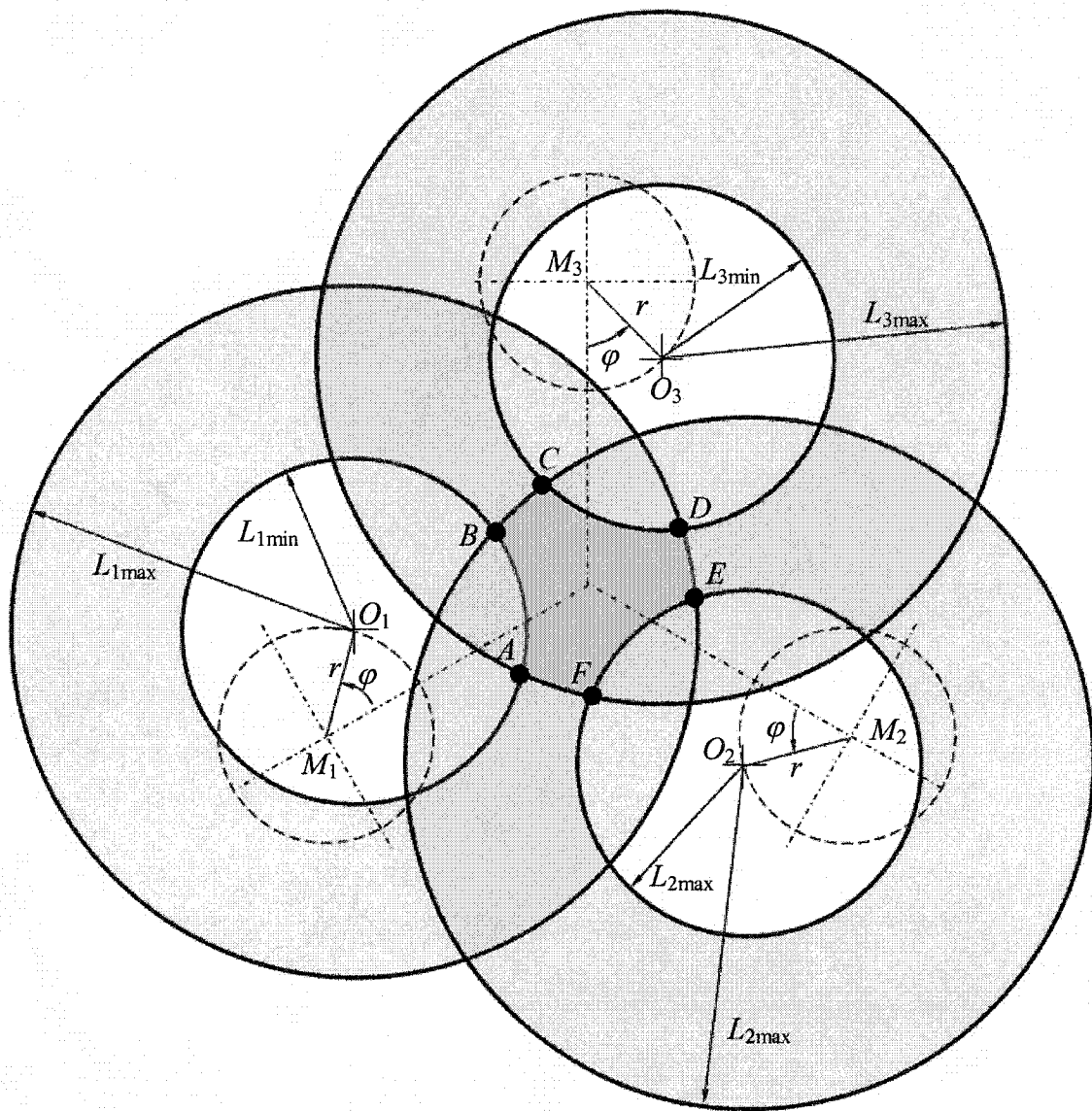
Figure 3.5 Construction of a constrained work envelope (ABCDEF) with the fixed platform rotation of $\varphi_p = \varphi$.

Samples of simulated shapes of the constrained work envelopes of a manipulator with a specific platform rotation angle are shown in Figures 3.6 and 3.7. The sides of the polygons are arc with relatively large radii (compare with Figure 3.5) so the arc curvatures are hardly noticeable.

The maximum rotation angle that the platform can achieve is found when the shaded area ABCDEF becomes zero in Figure 3.5. At that point, three circles with radius of L_{imax} have one common cross point which is at the center of the manipulator. The distance from the center of the manipulator to the base of the i-th motor is $r + L_{i0}$. Their trigonometric relation can be described as:

$$L_{i\,max}^2 = r^2 + (r + L_{i0})^2 - 2 \cdot r \cdot (r + L_{i0}) \cdot \cos\varphi_{p\,max} \tag{3.7}$$

The maximum rotation range $[-\varphi_{pmax}, \varphi_{pmax}]$ of the platform can then be obtained from the following equation:

$$\varphi_{p\,max} = \min\{\cos^{-1}\left(\frac{r^2 + (r + L_{i0})^2 - L_{i\,max}^2}{2 \cdot r \cdot (r + L_{i0})}\right)\}, i = 1, 2, 3. \tag{3.8}$$

For example, the parameters for the kinematic model of the manipulator driven by delta actuators in CM2 (see Figure 3.1) are: $r = 101$ μm, $L_{ext} = 8.2$ μm, $L_{comp} = 5.2$ μm, $L_{i0} = 292$ μm and $L_{imax} = 300.2$ μm ($i = 1, 2, 3$). The maximum rotation angle φ_{max} then is 20°, which means the platform can rotate from -20° to 20°. Using the above parameters, the platform constrained work envelope with a specific fixed rotation angle φ_p can be obtained by respectively applying equation (3.6). Figure 3.6 shows the constrained work envelopes with the fixed platform rotations of -15 and 15 degrees. Figure 3.7 shows the constrained work envelope with zero platform rotation.
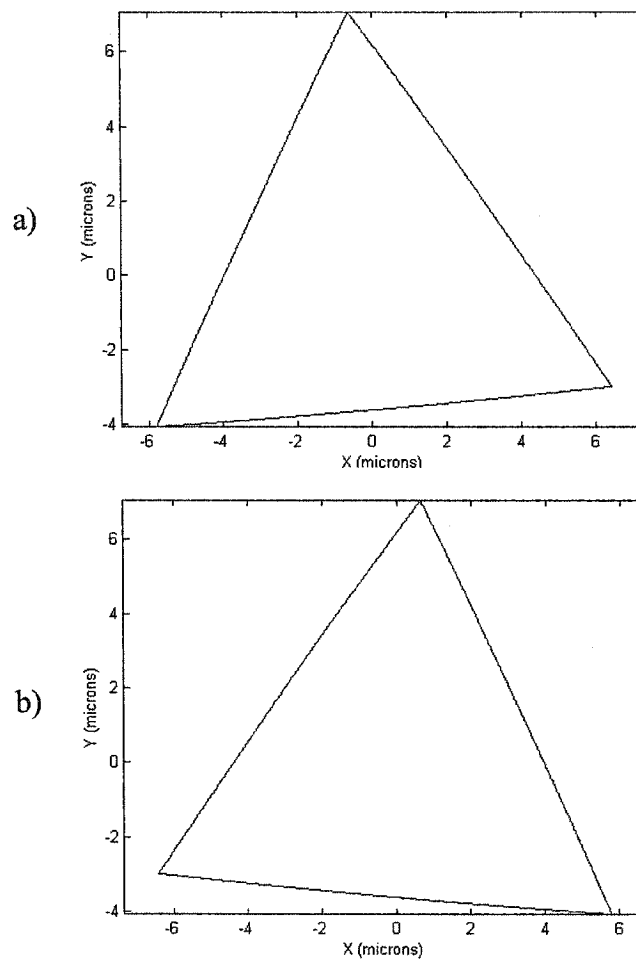
Figure 3.6 Simulated constrained work envelope of the manipulator on CM2 (see Figure 3.1) with platform rotation of   a) $\varphi_p = -15\,^{\circ}$ b) $\varphi_p = 15\,^{\circ}$.
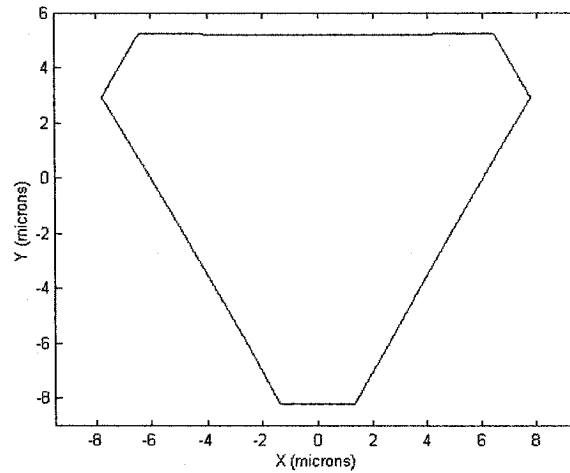
Figure 3.7 Simulated constrained work envelope of the manipulator driven on CM2 (see Figure 3.1) with platform rotation of $\varphi_p = 0$ °.

The entire work envelope for a planar manipulator is the area that contains all constrained work envelopes when the platform rotates from $-\varphi_{pmax}$ to φ_{pmax}. Figure 3.8a shows the simulated multiple constrained work envelopes with the platform rotating from −20 degrees to 20 degrees with a step size of 4 degree. The outline of these shapes forms the approximate entire work envelope of the manipulator (Figure 3.8b).
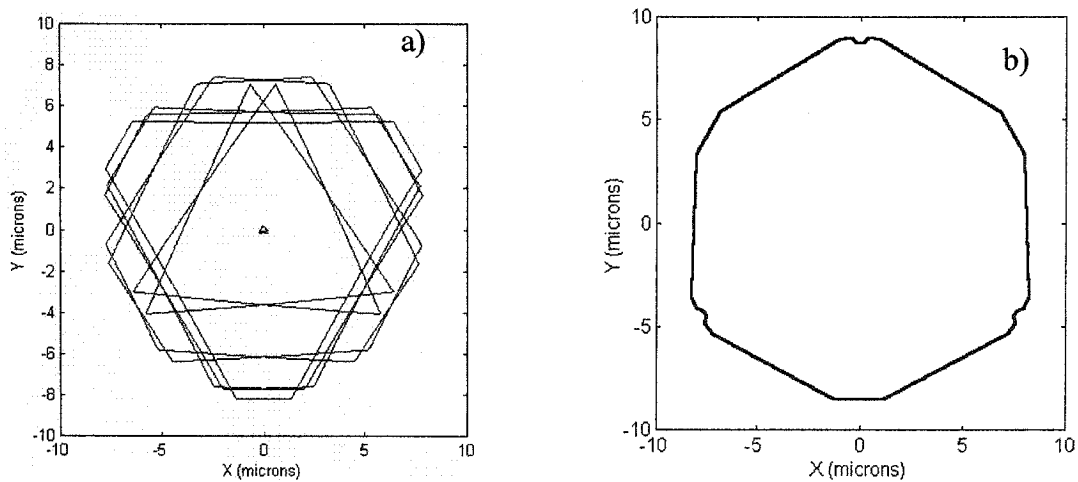
Figure 3.8 Simulated multiple constrained work envelopes form the entire work envelope for the manipulator on CM2 (see Figure 3.1): a) multiple constrained work envelope at steps of 4 degrees, b) resulted entire work envelope.

Combinations of three motors were actuated to experimentally find the work envelope. Figure 3.9 shows the simulated and experimental entire work envelope (maximum voltage is 6.5 volts) for the manipulator driven by delta TAs on CM2 (see Figure 3.1).

The experimental work envelope in Figure 3.9 is approximately a circle with a radius of 5 μm. There are several possible reasons for the asymmetry of the measured work envelope. The reported work envelope was a combination of measurements of six sections. Each section was measured for different combination of motor inputs. Measurement of each section required a new setup including re-wiring and re-focusing: this could produce some alignment errors. Also, electric current leakages between the bonding wires and the wires on the chip could affect the measured results. Furthermore, during testing, S-joints were observed sticking to the substrate that phenomenon could lead to the asymmetry of the tested work envelope as well. This stiction could have been avoided by design, for example, by adding dimples. The electric current leakage could have been reduced by design as well: using an exclusive bonding pad for each wire.
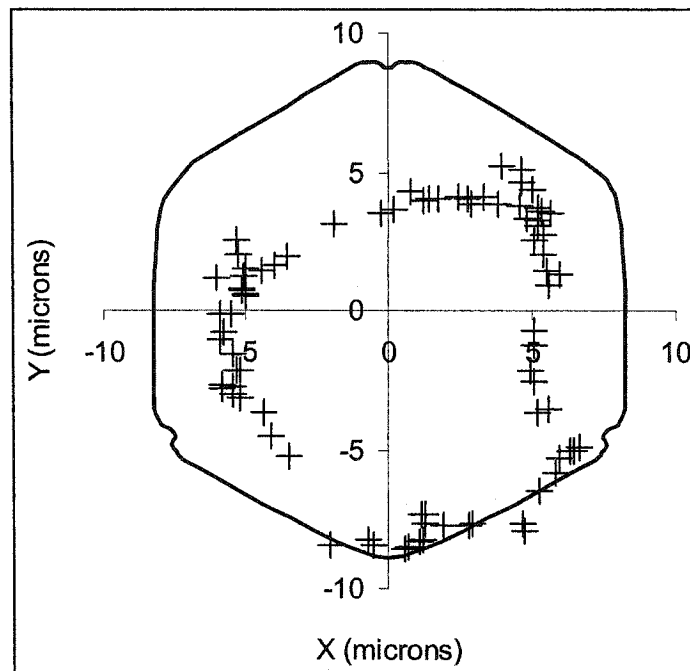
Figure 3.9 Simulated and tested (+) entire work envelopes of the manipulator on CM2

(see Figure 3.1).

Another manipulator on CM2 with similar parameters for the kinematic model was tested (see Figure 3.10 a).

a) SEM
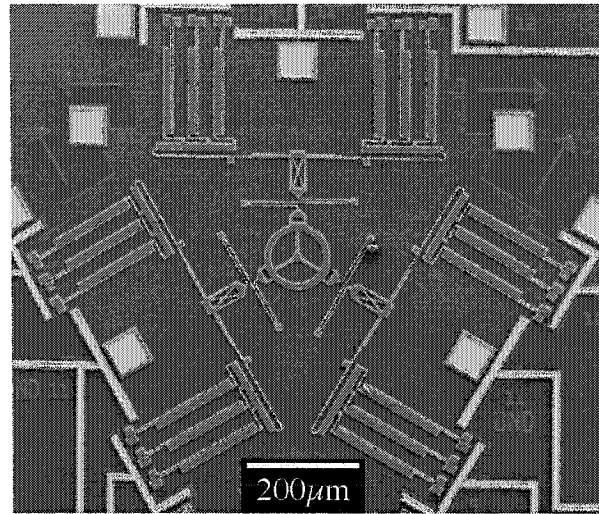
b) Work space
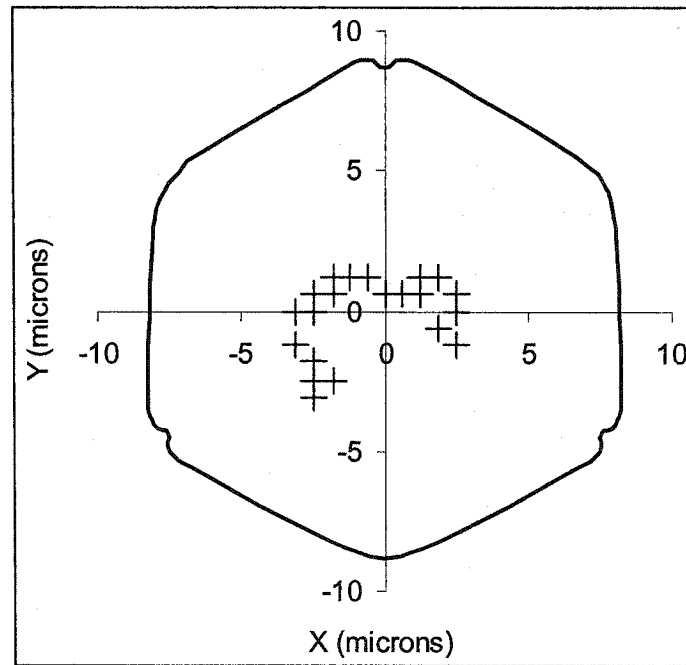
Figure 3.10 Manipulator driven by bi-directional sTA banks and its simulated & experimental (+) work envelope.

In this manipulator, the motors consist of two sTA banks which move in the opposite directions. Therefore, when one sTA bank works, the other acts as a parasitic spring and stores energy from the active sTA bank. Even though the actuators for this

manipulator are ideally stronger than a single delta actuator, the measured entire work envelope of this manipulator (see Figure 3.10 b) under the same maximum voltage is smaller than the experimental work envelope of the manipulator driven by delta actuators. The reason for this is that the inactive sTA bank and the flexures connecting two sTA banks must be deformed, which decreases the energy available to drive the platform. The tested data did not form a closed loop because one of the sTA banks did not work.

3.3   How geometric parameters affect the entire work envelope

The application of the kinematic model of Figure 3.3 provides a tool for predicting the entire work envelopes of a manipulator. Figure 3.11 demonstrates the change of the size of the areas of the constrained work envelope with different platform rotation angles. The constrained work envelope reaches its maximum when $\varphi_p = \pm 8°$. The constrained work envelope size for $\varphi_p = 0°$ is slightly smaller than the maximum possible values. The actuators in the prototype can only rotate the platform a few degrees ($< 4°$) (see Figure 3.11). Due to the small rotation of the platform, there are no significant changes (less than 4%) between the entire work envelope and the constrained work envelope at $\varphi_p = 0°$. Therefore, the constrained work envelope at $\varphi_p = 0°$ was used to represent the entire work envelope of the manipulator.
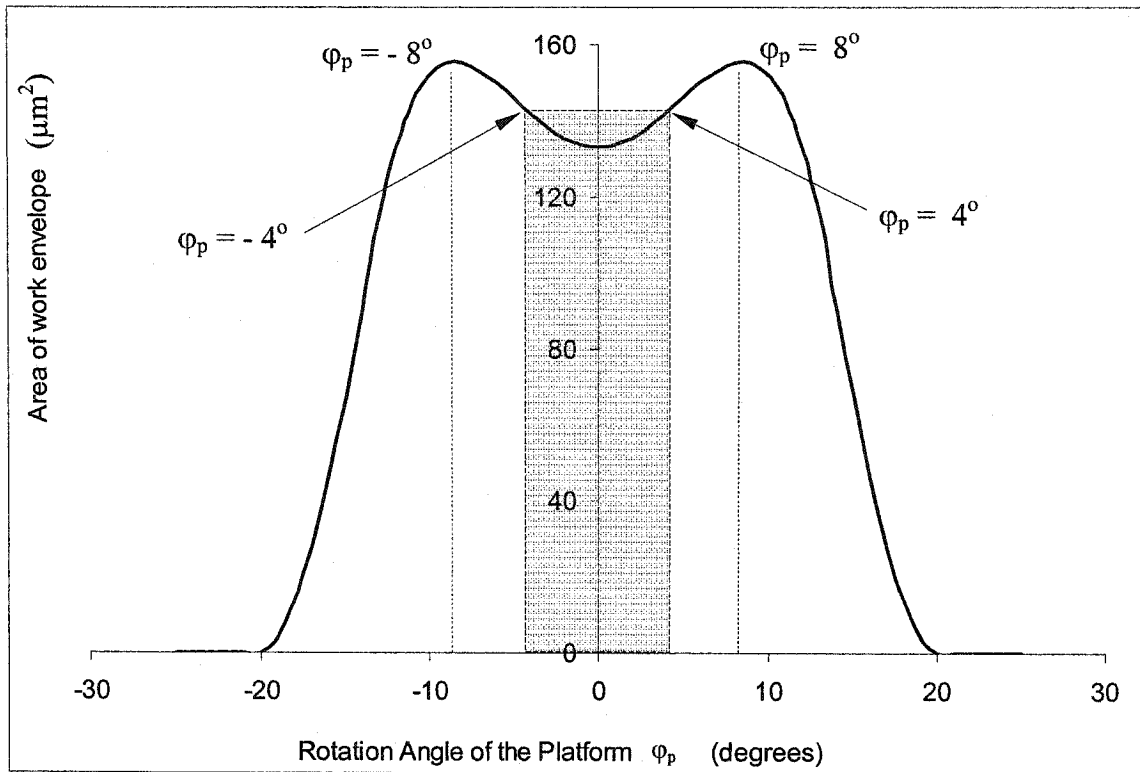
Figure 3.11 The area of constrained work envelopes vs. rotation angle of the platform φ_p for the manipulator on CM2 (see Figure 3.1).

Using the constrained work envelope of $\varphi_p = 0°$ as the entire work envelope of the prototypes, the kinematic model also provides information on how the structural parameters affect the entire work envelope. Variation of the platform's radius, while the overall size of the manipulator remains the same, has minimal effect on the entire work envelope (see Figure 3.12).
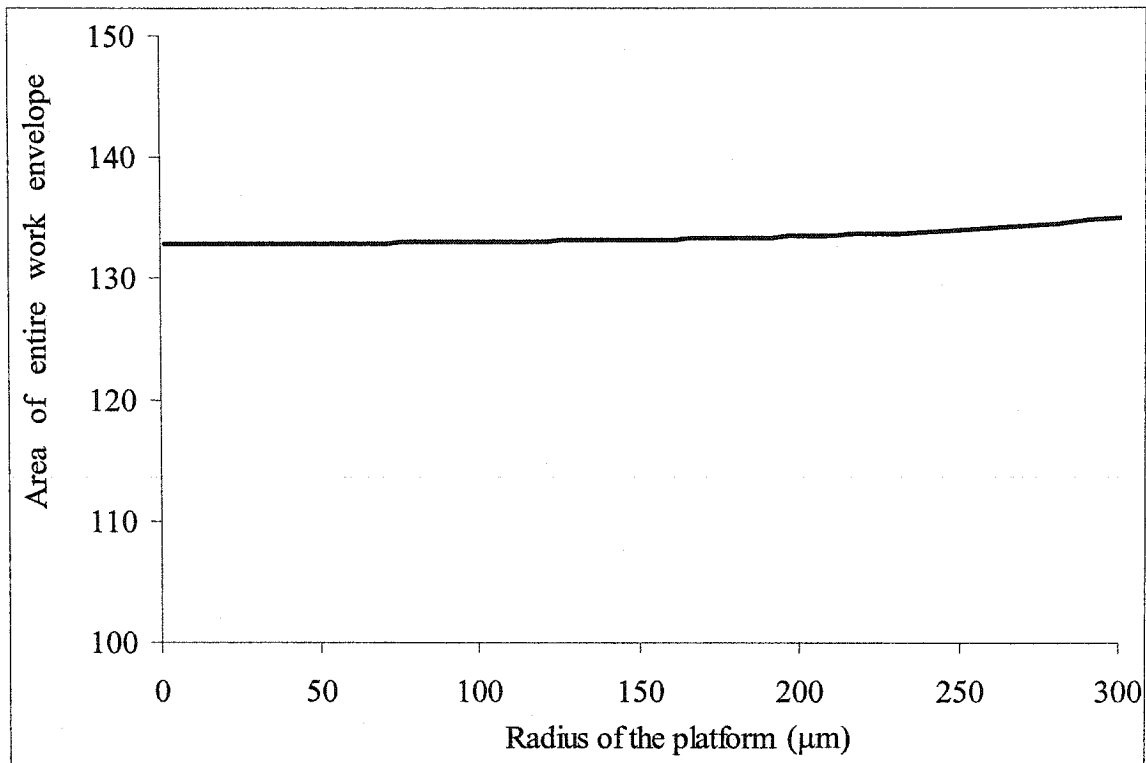
Figure 3.12 Area of entire work envelopes vs. radius of the platform based on the prototype of the manipulator on CM2 (see Figure 3.1).

Even though the radius of the platform varies from 1 μm to 300 μm, the areas of the work envelopes change less than 3 percent. Therefore, the radius of the platform does not affect the prototype's entire work envelope significantly.

In practice, the motors can provide a small angle of rotation which is different from the assumption used to produce cycle rotations in the kinematic model. Based on his experiments, the author found that, for a similar type of motor, the output power is proportional to a motor's size. Since the simulated results in Figure 3.12 demonstrated that the size of the platform is not critical, for a given overall size, a manipulator with a small platform and large motors will have a large entire work envelope.

The S-joints' compression and extension strokes may affect the entire work envelope. To study this effect, a simulation was performed based on the same prototype

on CM2 as above. Preserving all parameters except the S-joints' strokes which range from 1 µm to 10 µm, the entire work envelopes were simulated (see Figure 3.13).
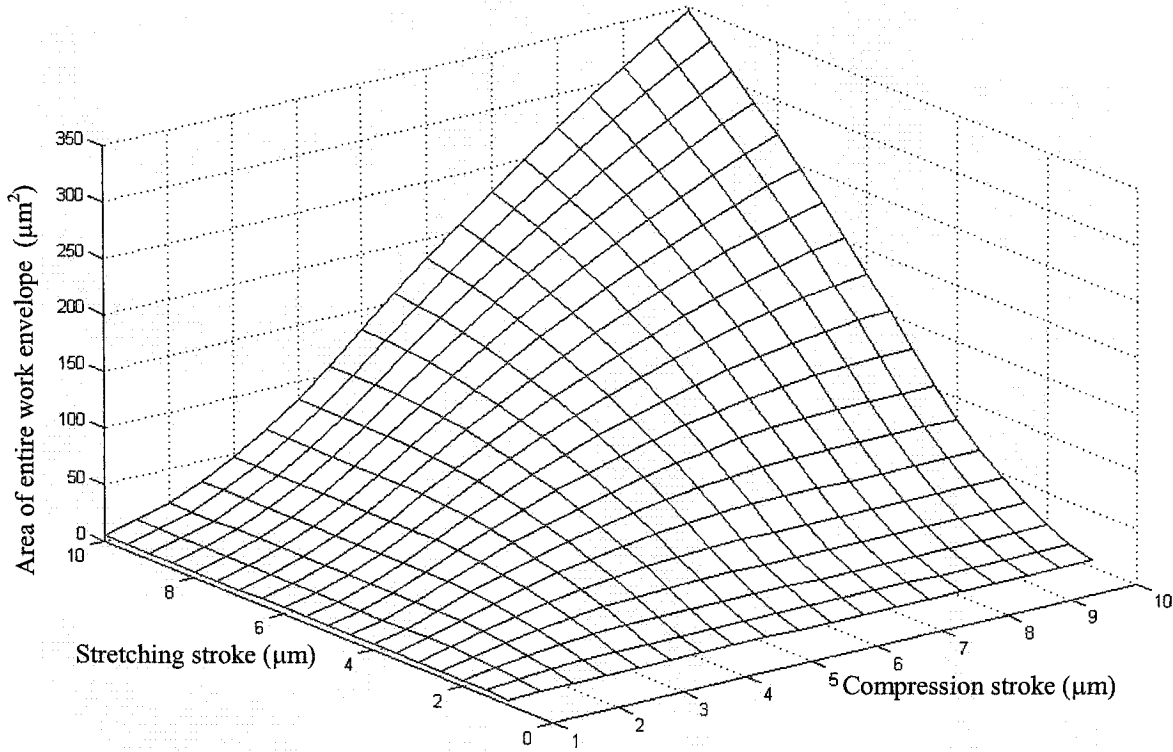
Figure 3.13 The entire work envelope vs. compression and stretching stroke of the S-joints based on the prototype of the manipulator on CM2 (see Figure 3.1).

The x & y axes in Figure 3.13 represent the compression & extension stroke sizes, respectively. The simulated results demonstrate that as the compression and extension strokes increase, the size of the entire work envelope increases.

In the compliant manipulator, the larger the displacement of the S-joints, the more energy will be stored in the S-joints. The S-joints can therefore be designed to supply sufficient compression and extension for a desired work envelope, but the lateral stiffness of the S-joints decreases when the stroke increases which decreases accuracy and therefore increases error relative to the simulation. This is because the lateral stiffness of the S-joints in the kinematic model is assumed to be infinite.

Generally, to design a manipulator with an acceptable entire work envelope, the following criteria need to be considered:

1) Actuators (motors) should provide enough power (both higher output displacement and higher force, the better);

2) If the actuators (motors) work as a group, they should work cooperatively (not against each other) and efficiently (spending as less power as possible to deform motors themselves);

3) The S-joints are to supply compression and extension strokes that are as large as possible. However, increasing strokes will decrease the lateral stiffness of the S-joints which is not desirable. An optimum S-joint for each manipulator with different motors can be found experimentally if fabrication is not an issue, though it is difficult to determine theoretically.

4). To achieve a design of a manipulator with a large entire work envelope, the platform size of a manipulator should be small, and the size of the motors should be large.

3.4   Summary

In this chapter a rigid body 3-DOF kinematic model has been developed for the planar compliant manipulators. Experimental work envelopes were compared to the simulated results for the manipulators. Based on the kinematic model, the effects on the work envelope of the geometric parameters were investigated and guidelines for designing a manipulator with a large entire work envelope were provided.

4 Finite Element Model of a Micromanipulator

This chapter will use the finite element method to develop a model for simulation of the dynamic behavior of a delta TA and a selected micromanipulator.

4.1 Introduction

The finite element method is a very powerful and popular method for solving problems that cannot be solved analytically. The basic concept of the finite element method for analysis of solid structures is based on the division of a domain (Ω) of a continuum structure into finite substructures which are called *elements*.

The finite element method was originally developed for solving static structural problems [64]. However, it is applied to solve a variety of problems in science and engineering including heat transfer, fluid mechanics, acoustics, electromagnetics, dynamics, modal analysis, etc. ANSYS, popular software for finite element analysis, was used to conduct static and dynamic analysis.

4.2 Units

The units used in ANSYS can not be specified. To get correct results, SI units must be used for the numeric input values. However, using SI units during simulations of MEMS devices, some of the matrix entries will be very small numbers leading to computational challenges. This could make the solutions unreliable or their convergence difficult. To avoid these disadvantages, SI units were partially modified to a new μSI system [65]: the basic length, force and pressure units were changed to 1μm, 1μN and 1MPa respectively; other units were kept the same as the corresponding units in SI. Table 4.1 shows the basic & derived units and their relationship with SI units.

Table 4.1 Units conversion from SI to μSI*

Variables	SI Units	Dimensions	Multiplication Factors	μSI Units	Dimensions
Length	m	m	10^6	μm	m
Mass	kg	kg	1	kg	kg
Force	N	kg · m/s^2	10^6	μN	kg · μm/s^2
Time	s	s	1	s	s
Young's Modulus	Pa	kg/(m · s^2)	10^{-6}	MPa	kg/(μm · s^2)
Density	kg/m^3	kg/m^3	10^{-18}	kg/μm^3	kg/μm^3

* See [8] ch.4.3.2

For example, the material properties for polysilicon provided by W. Sharp [66], which the devices studied are made from, are listed as follows:

Young's Modulus:
$$E = 169 \times 10^9 \, Pa = 169 \times 10^3 \, \frac{\mu N}{\mu m^2} \qquad (4.1)$$

Poisson's Ratio
$$v = 0.22 \qquad (4.2)$$

Density
$$\rho = 2330 \frac{kg}{m^3} = 2.33 \times 10^{-15} \frac{kg}{\mu m^3} \qquad (4.3)$$

Using the μSI units, the outputs from the simulation will be in the same units, for example, force is in μN and displacement is in μm.

4.3 Delta TA

The delta TA was described in section 2.2.1. Simple finite element modal analysis, which provides mode vectors and resonant frequencies, can provide some characteristics of this kind of actuator. Since the devices studied were fabricated through MUMPs technology, with 2 μm thickness, they can be regarded as planar thin films or shell structures. According to this geometry, an ANSYS element Shell63 (see Appendix B for more

details) was used to model the delta actuator. Figure 4.1 shows the meshed layout of the delta TA.
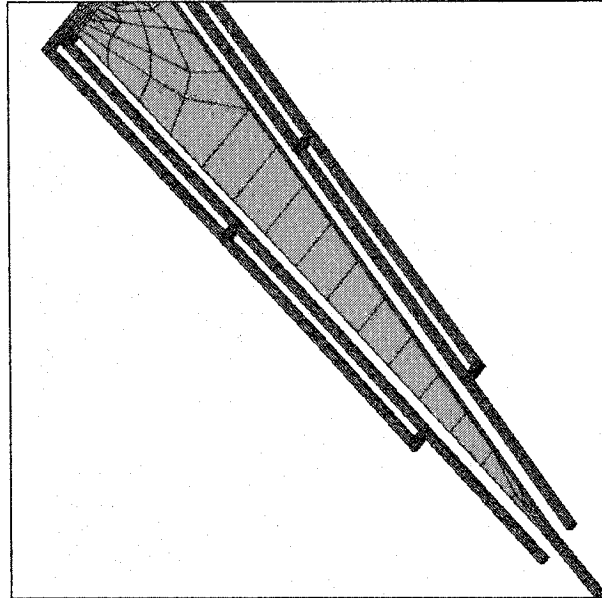
Figure 4.1 Meshed delta actuator.

Figure 4.2 shows three modes of the delta TA from modal analysis. The shaded white shapes are the neutral position of the delta actuator; the black solid shapes are the modes from the simulation. The simulated dTA had a length of 230 μm. The first mode of the delta actuator is bending out of plane with a corresponding frequency of 32 kHz. The second mode is rotating in the plane at 74 kHz. The third mode is a higher order bending out of plane mode at 270 kHz.

a) Out-of-plane, 32 kHz

Rotating about the *y* axis
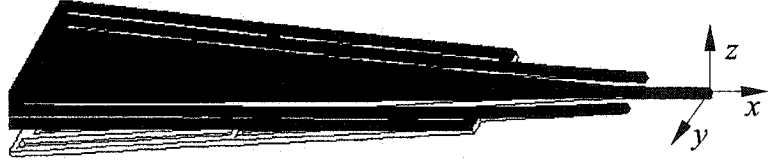
b) In-plane, 74 kHz

Rotating about the *z* axis
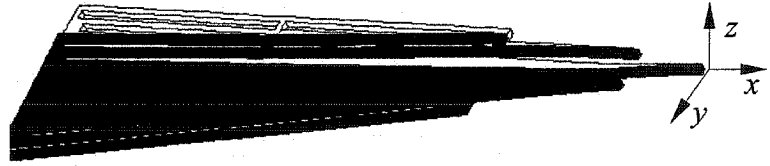
c) Out-of-plane, 270 kHz

Buckling about the *y* axis
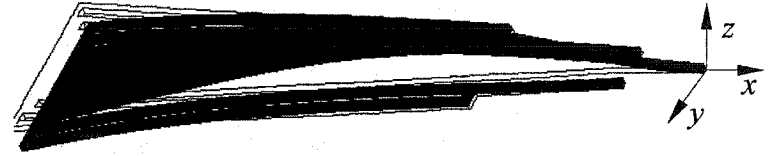
Figure 4.2 Modes of vibration for delta TA.

Assuming the kinematic Center-Of-Rotation (COR) is located at or near the base of the cold arm, the stiffness can be calculated using force divided by displacement. For example, to determine the stiffness of in-plane rotation, a sample in-plane load F (μN) is applied to the node on the central line of the actuator farthest from the cold arm base and the displacement ds (μm) is recorded. Using L to denote the distance (μm) from the loaded node to the COR, the in-plane stiffness can be calculated by

$$k_\theta = \frac{F \cdot L^2}{ds} \quad \mu N \mu m \, / \, rad \qquad (4.4)$$

The in-plane rotation stiffness of the delta TA was calculated as 83300 μN·μm / rad.

4.4 Modal analysis of a manipulator

Since all manipulators studied have similar trisymmetric geometric shapes, they should have similar dynamic behaviors. The finite element analysis for one manipulator can then be generalized to others. The manipulator selected for finite element analysis is shown in Figure 4.3.
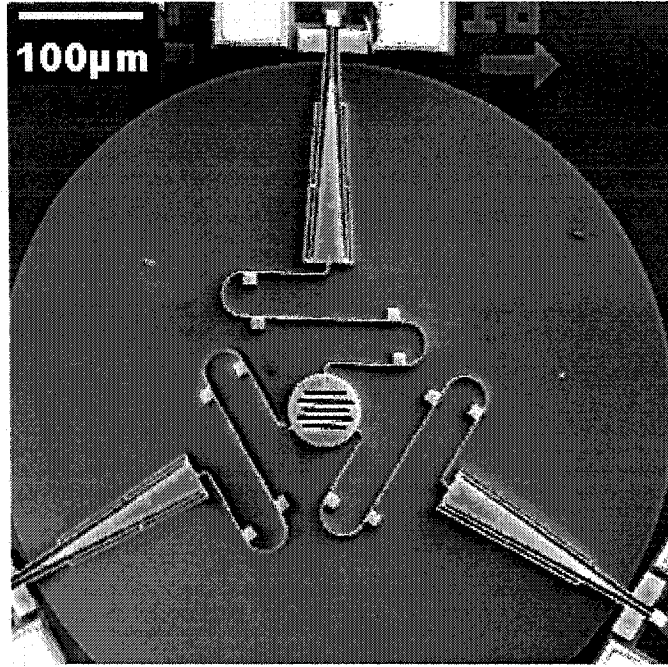
Figure 4.3 SEM image of the manipulator on the YC2 chip.

The ANSYS element Shell63 was used for three delta TAs and the central platform. In an S-joint, the beam is mostly subjected to bending. Therefore, an ANSYS Beam4 element was used. The global coordinate system is set up as follows: the origin o is located at the center of the platform of neutral position; the xy plane is the central plane of the whole manipulator; the y axis starts from the origin and points to the base point on the central line of the top delta TA; the x axis points to the right horizontally; the z axis is perpendicular to the xy plane and points out of the plane which can be determined by the right-hand rule (see Figure 4.4).
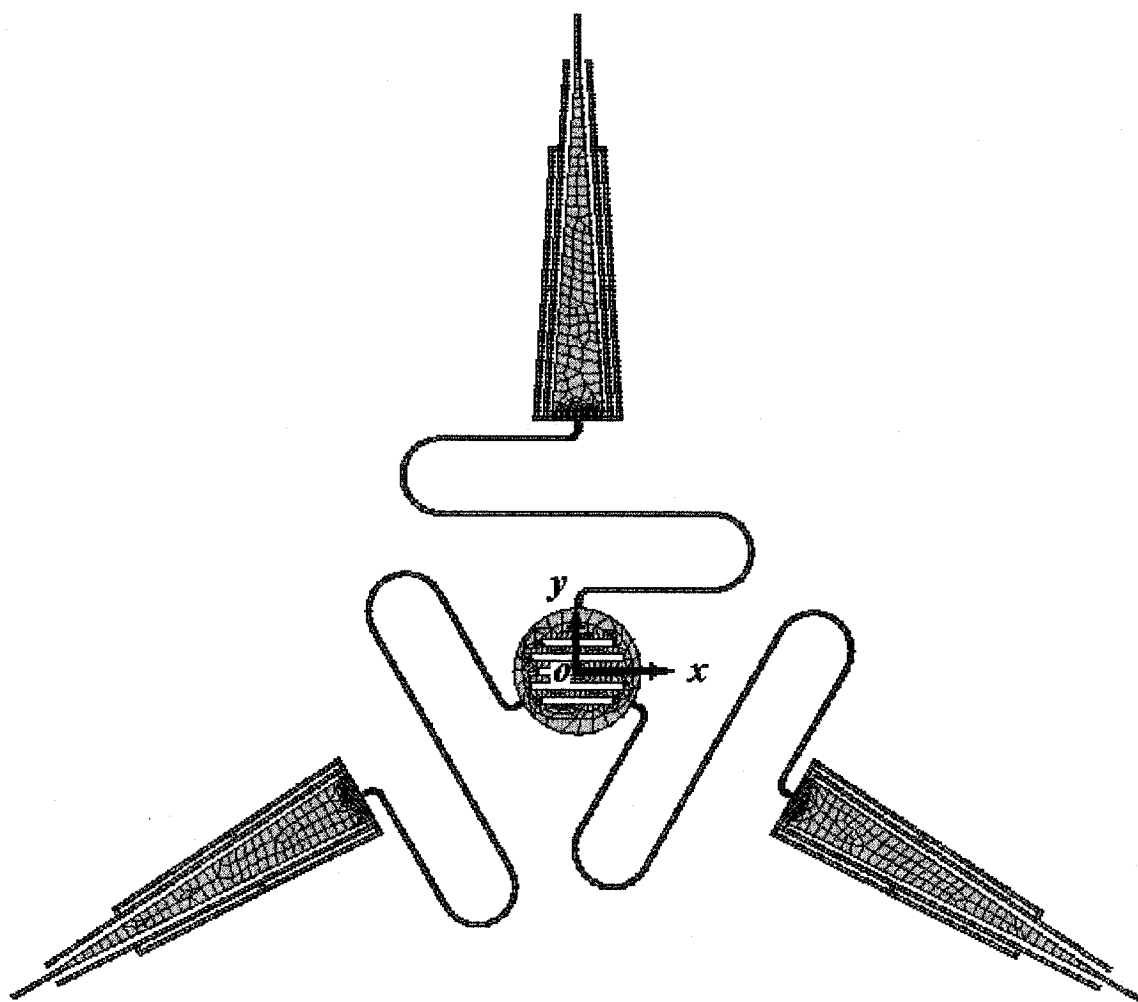
Figure 4.4 View of the finite elements and the global coordinate system xy.
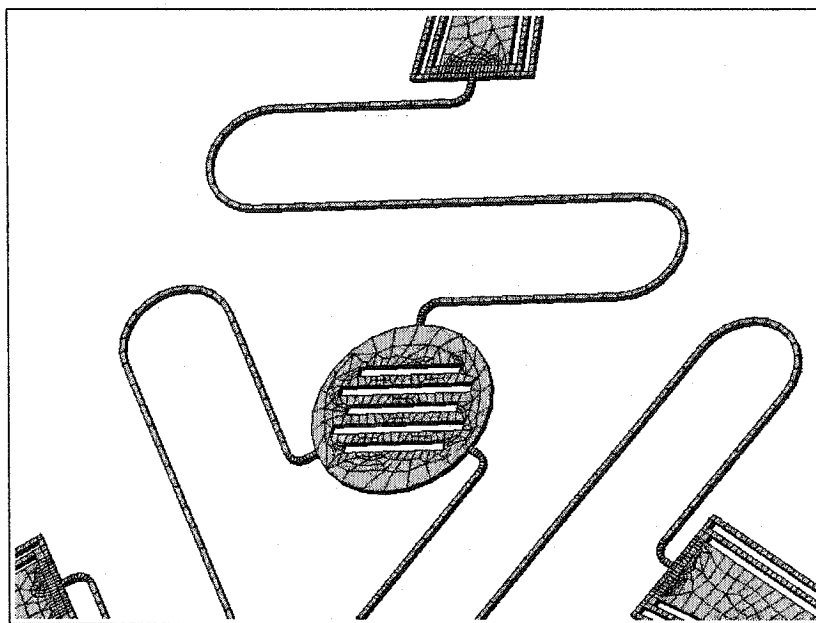
Figure 4.5 Close-up of the element layout of Figure 4.4.

Figure 4.5 is a close-up view for the mesh layout of Figure 4.4. Ten free vibration modes from the finite element analysis will be demonstrated.
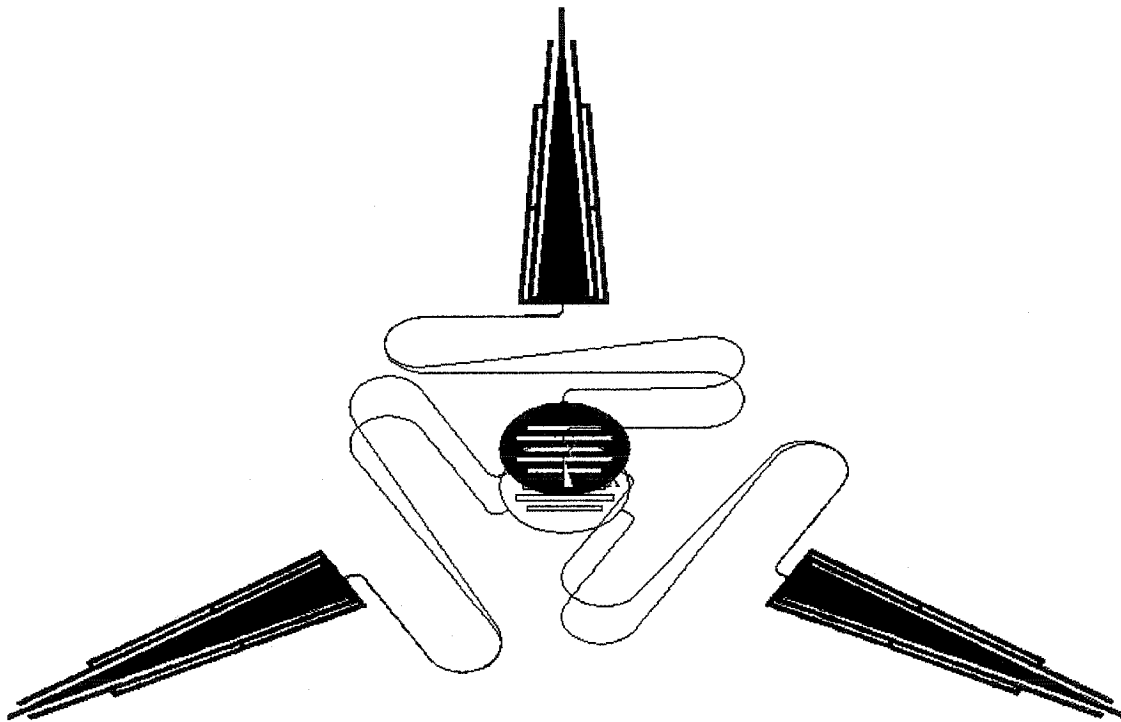
Figure 4.6 The first mode of the manipulator (out-of-plane translation, 19 kHz).

Figure 4.6 is the view of the first mode of the manipulator from the point (0, 1, 1). The platform moves out of the *xy* plane and the S-joints bend out of the *xy* plane at 19 kHz. Compared to the out-of-plane motions of the platform and S-joints, the magnitude of out of plane motion of three delta TAs (first mode of the delta actuators) is insignificant.
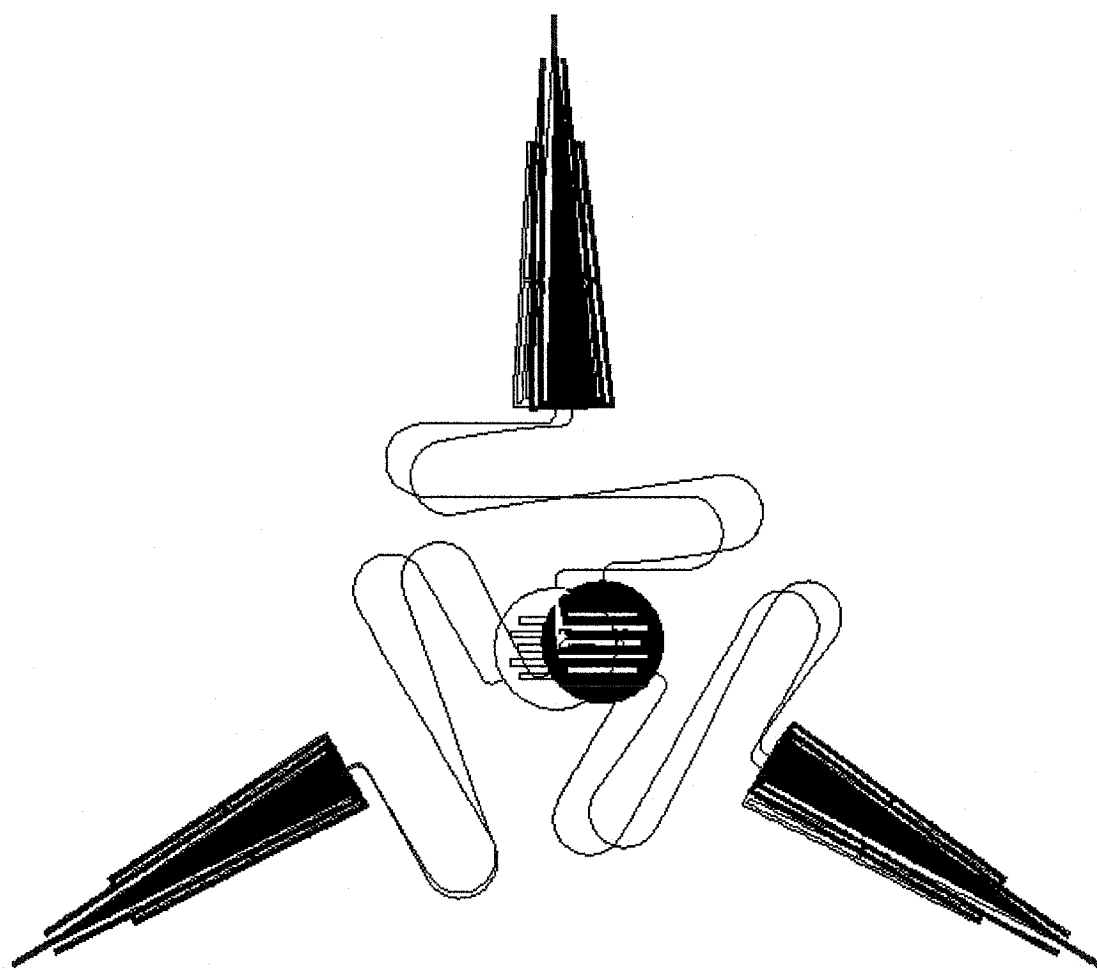
Figure 4.7 The second mode of the manipulator (in-plane translation, 38 kHz).
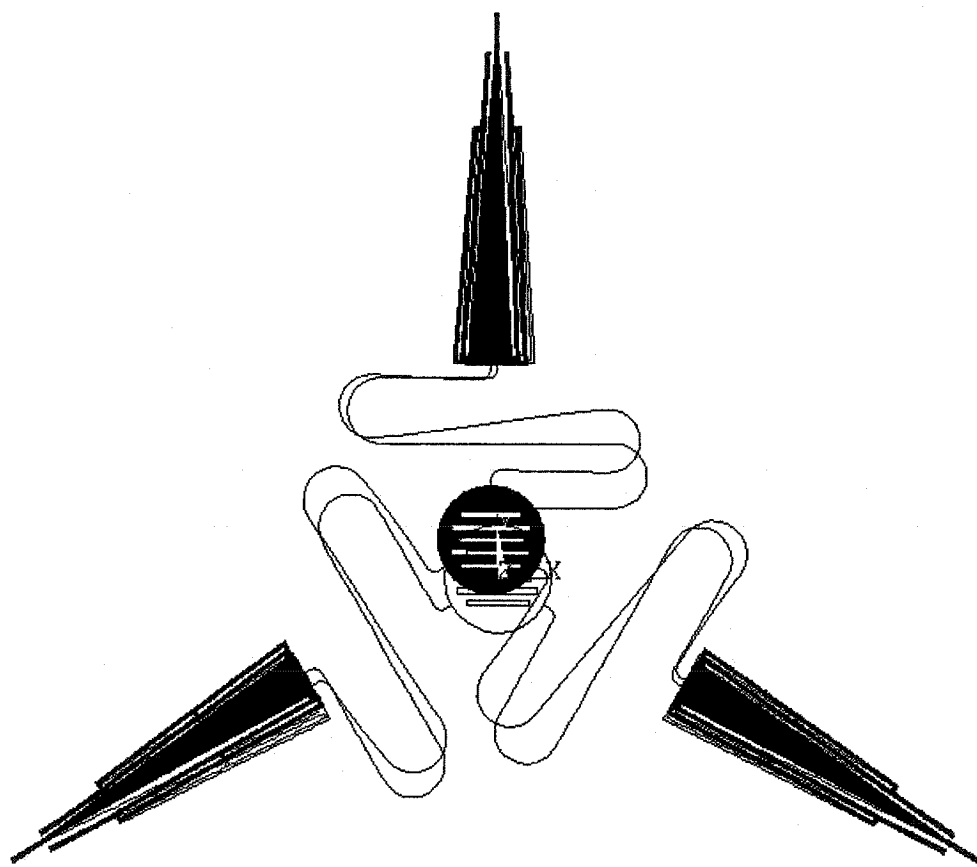
Figure 4.8 The third mode of the manipulator (in-plane translation mode at 38 kHz).
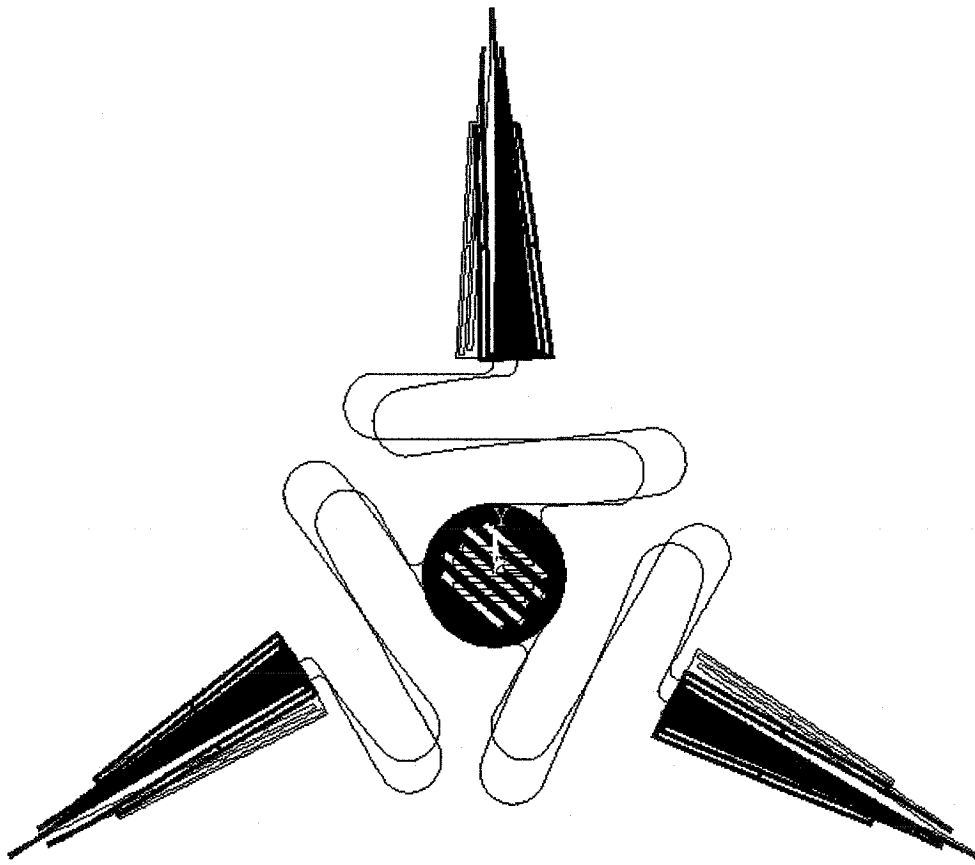
Figure 4.9 The fourth mode of the manipulator (in-plane rotation, 50 kHz).

Figures 4.7-4.9 show three modes in the xy plane from viewpoint (0, 0, 1). Furthermore, in these four modes (from 1st to 4th) the platform's moving direction was observed to be following the actuators' driving direction. In this case, the modes are called in-phase modes.
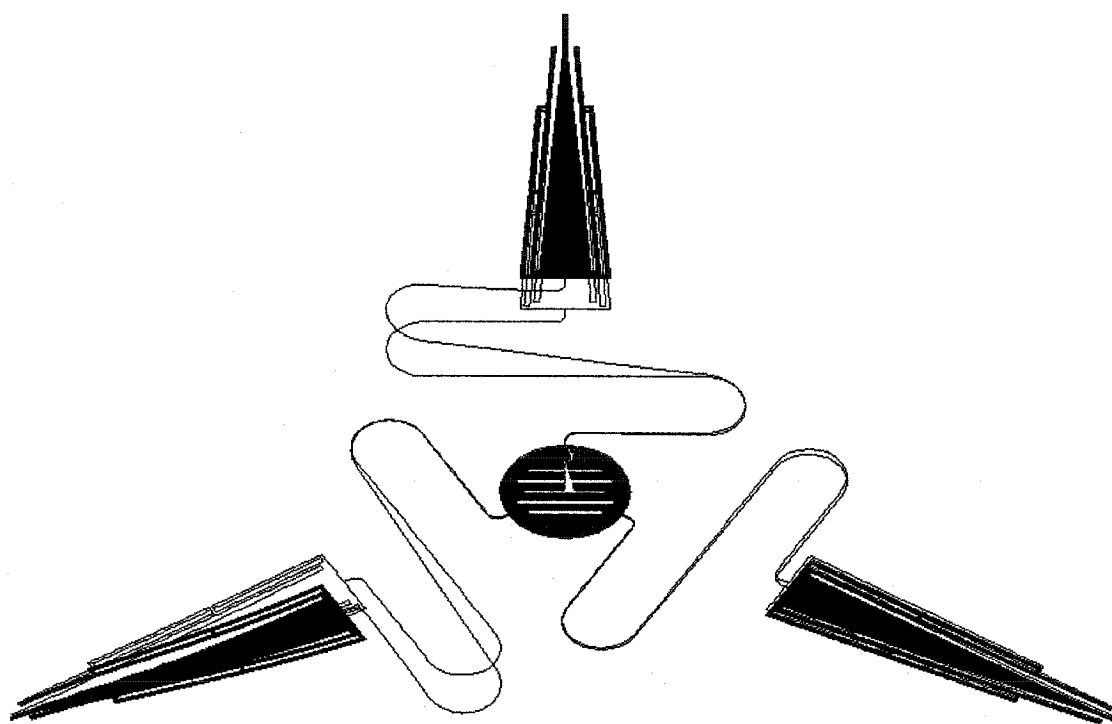
Figure 4.10 The fifth mode of the manipulator (out-of-plane tilting, 56 kHz).
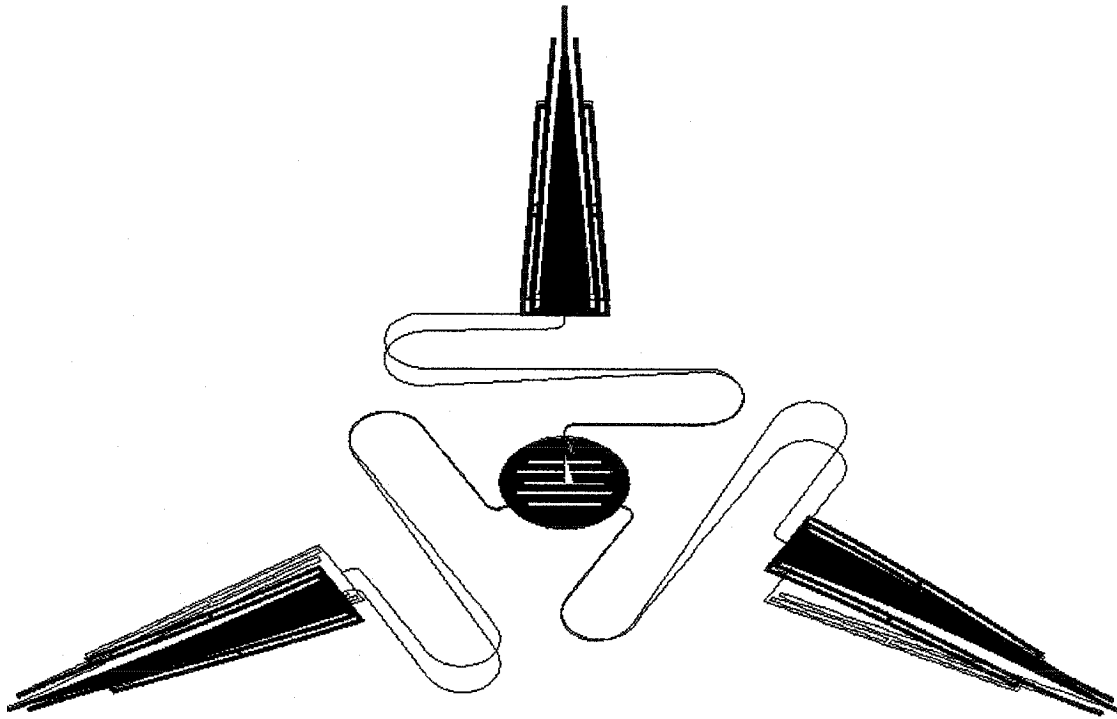
Figure 4.11 The sixth mode of the manipulator (out-of-plane, 56 kHz).

Figures 4.10 and 4.11 are the out-of-plane tilting modes at 56 kHz (viewed from point [0,-1, 1]). In these two modes, two TAs move upwards out-of-plane, the third TA moves downwards out-of-plane. Compared to the motions of the S-joints and motors, these two modes show that the platform's movement is very small and negligible.
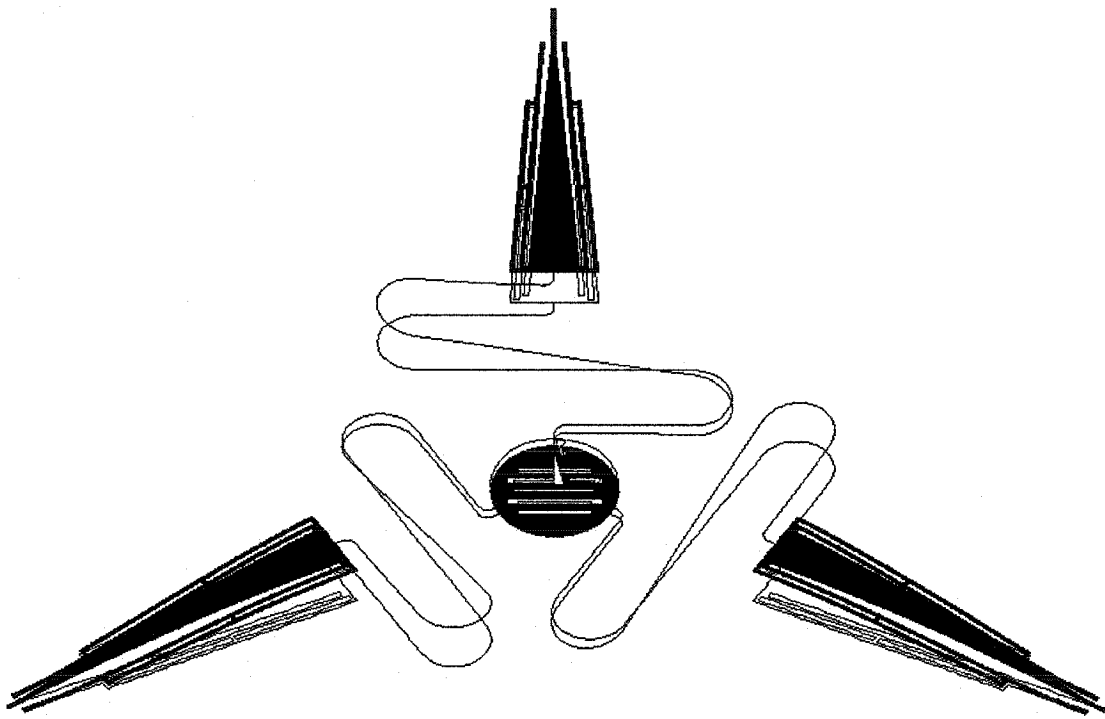
Figure 4.12 The seventh mode of the manipulator (out-of-plane translation, 56 kHz).

Figure 4.12 is the view of the seventh mode from point (0, -1, 1). This mode shows that the platform, S-joints and actuators are moving out of the xy plane. However, in this mode, the three delta actuators move in a positive (negative) direction about the z axis, while the platform moves in the opposite direction (out-of-plane).
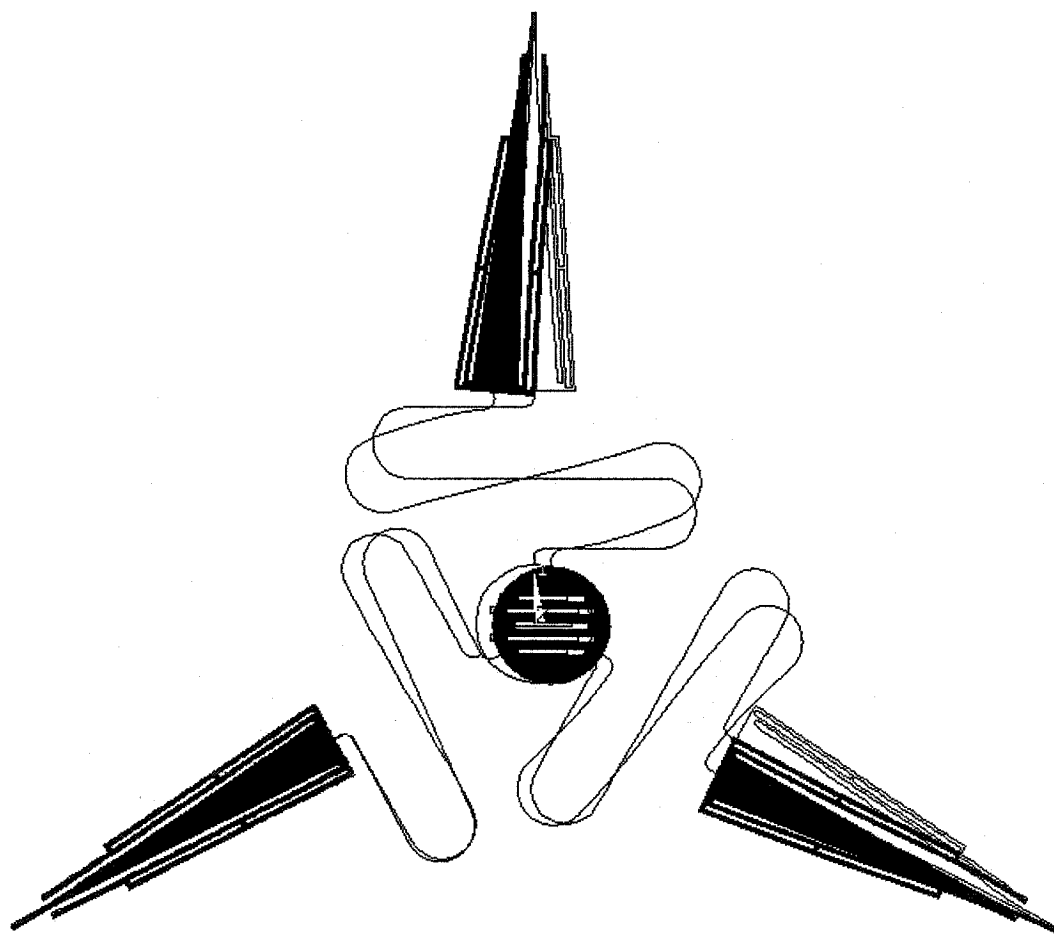
Figure 4.13 The eighth mode of the manipulator (in-plane translation, 83 kHz).
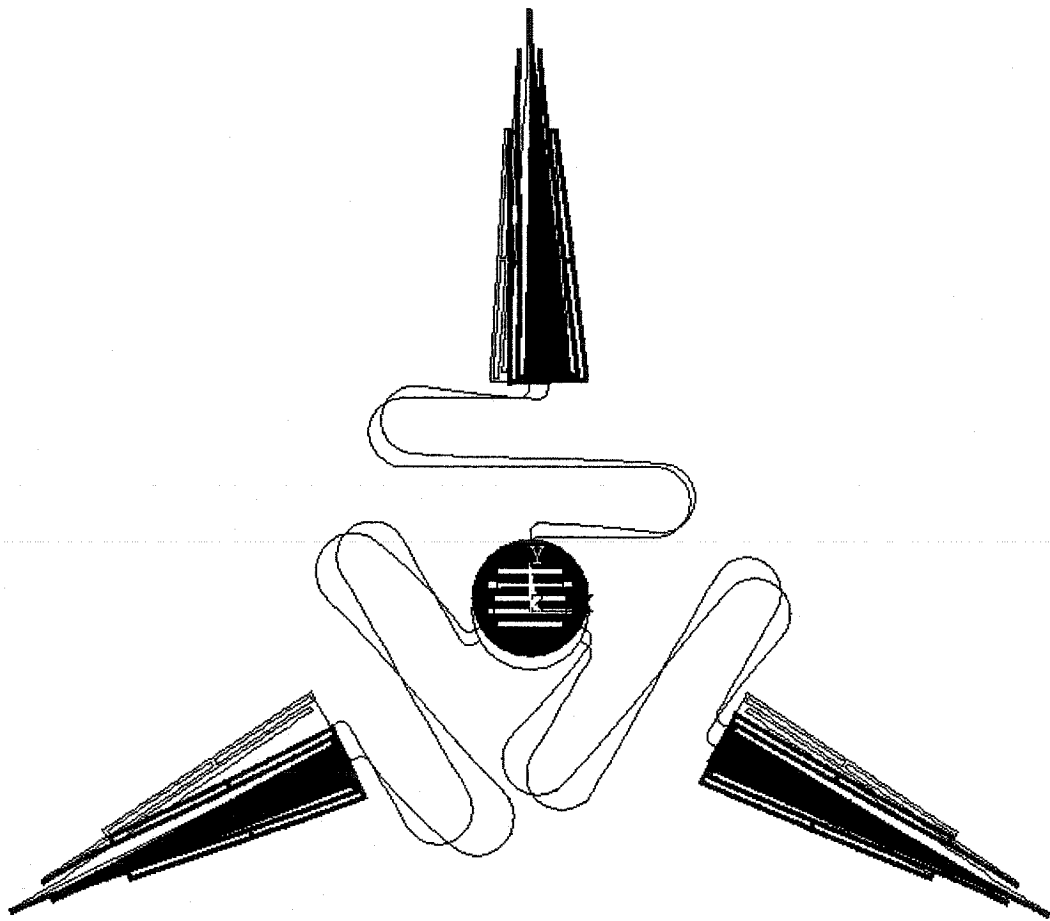
Figure 4.14 The ninth mode of the manipulator (in-plane translation, 83 kHz).

Figure 4.13 and Figure 4.14 are two repeated modes in the xy plane. The corresponding frequency is 83 kHz. In these two modes, the platform translates in the plane with negligible rotation.
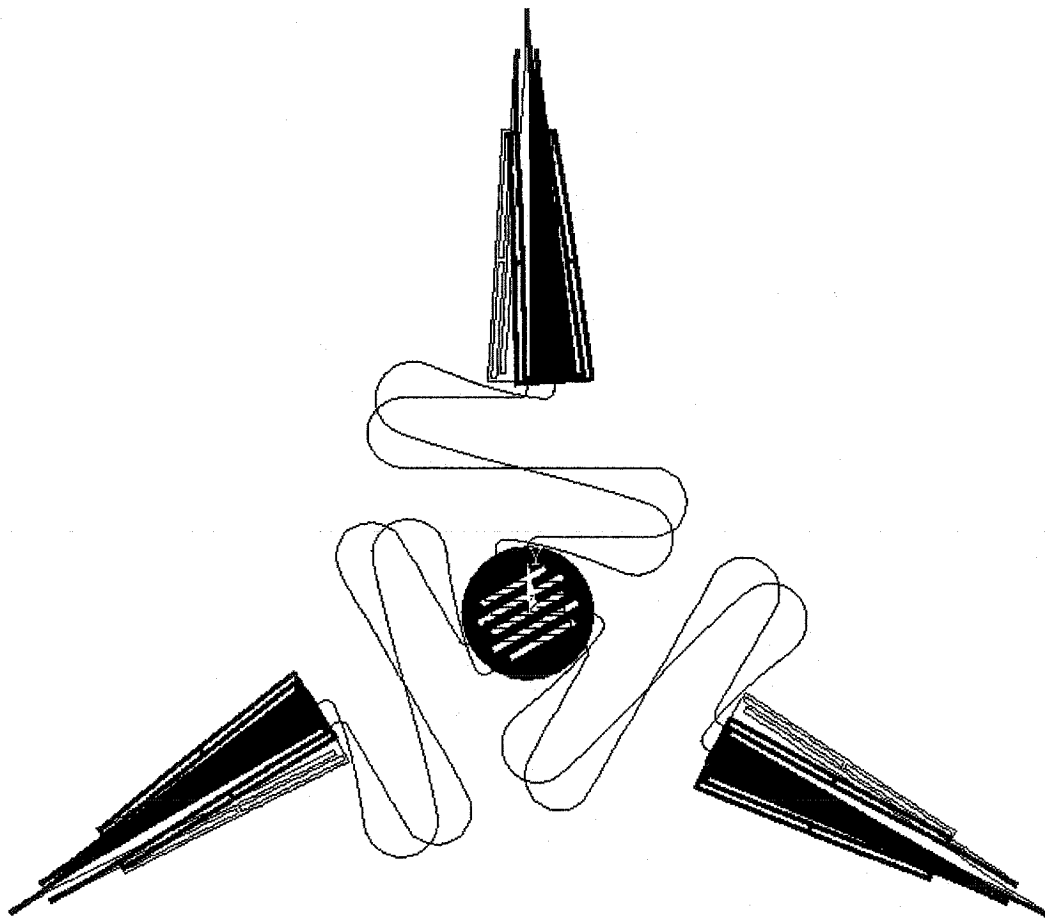
Figure 4.15 The tenth mode of the manipulator (in-plane rotation, 91 kHz).

Figure 4.15 is the view of the tenth mode from point (0, 0, 1). The mode shows that the manipulator moves in the xy plane at a resonant frequency of 91 kHz. The platform in this mode rotates around its center with a negligible translation.

Two types of elastic modes are observed: in-phase and out-of-phase. These terms refer to the relative motion of the platform and the motors. If the oscillating platform moves as if it was driven by the motors in a rigid body mode, the elastic mode is referred to as an in-phase mode, e.g., all the motors rotate simultaneously clockwise and the platform rotates counterclockwise: the system is said to be in an in-phase rotation mode. When the oscillating platform moves in the opposite direction as the rigid body motion would suggest: the elastic mode is described as out-of-phase.

4.5 Summary

The ten modes from finite element analysis were demonstrated above. The results are summarized in Table 4.2 and will be compared to the experimental results in later chapters. The adjacent repeated translation modes have the same modal frequency because of the structural symmetry in the xy plane.

Table 4.2 Results from finite element analysis

Modes:	Frequency (kHz)	Type	Plane	Phase	Notes
1	29	Translation	Spacial	In-phase	
2	38	Translation	Planar	In-phase	Repeated mode
3	38	Translation	Planar	In-phase	Repeated mode
4	50	Rotation	Planar	In-phase	
5	56	Tilting	Spacial	NA	The Platform does not move. Repeated mode
6	56	Tilting	Spacial	NA	The Platform does not move. Repeated mode
7	56	Translation	Spacial	Out-of-phase	
8	83	Translation	Planar	Out-of-phase	Repeated mode
9	83	Translation	Planar	Out-of-phase	Repeated mode
10	91	Rotation	Planar	Out-of-phase	

5   Spring-Mass Models for a Micromanipulator

In Chapter 4, a finite element model was developed for a micro manipulator. One of the advantages of finite element analysis is that it produces much more information than spring-mass models do. However, FEM deeply depends on the geometry of the prototype. Any slight geometry differences of the prototype require remodelling. Developing a finite element model is time consuming work. Compared to FEM, spring-mass modeling is simpler and more easily modified for any changes. The computational effort is less, and most of all it does not require an expensive simulation software. Additionally, spring-mass models give intuitive insight into the governing dynamics because of their low number of mass elements. This chapter presents the dynamic modeling of the compliant micro manipulator studied in Chapter 4. Two discrete spring–mass models were developed. Simulations from both dynamic models were compared with the finite element model and the experimental results.

5.1   Introduction

Spring-mass models are commonly used in vibration studies. The method is to carefully, though arbitrarily, divide the system into lumped masses and massless springs that connect them. Where to divide the mass amongst the parts is critical. A mass matrix and a stiffness matrix are then obtained from this simplified model. The material used is polysilicon with modulus of elasticity $E=169$ GPa, Poisson's ratio $v=0.22$ and the density $\rho=2330$ kg/m^3 [66], and the mass matrix and stiffness matrix can be computed from the specific geometries.

Even though the first modes of the manipulator and the delta actuators are out of plane modes, the manipulator is expected to move in-plane only since only in-plane driving forces can be produced by the delta TAs. Therefore, the spring-mass models used are planar.

The first spring-mass model developed has only three degrees of freedom (x, y and φ) which represent the platform of the manipulator as it translates along x and y axes and rotates around the z axis. Lagrange's equations were used to acquire the system dynamic equations. The Jacobian matrix obtained in a later section is employed to relate the dependent variables to the three independent variables (x, y and φ).

The second spring mass model has six degrees of freedom (x, y, φ for the platform and θ_1, θ_2 & θ_3 for the three delta actuators).

5.2   Jacobian Matrix

A Jacobian matrix reflects the relation between the velocities of the manipulator input and output variables. Figure 5.1 shows a single linkage rotating about a point B with an angular velocity of $\vec{\omega}$. The linear velocity of the point A is $\vec{v}$ which can be divided into two parts: radial and transverse. The link can be represented by the vector $\vec{r}$ in the global coordinate system xy. The velocity $\vec{v}$ [67] is:

$$\vec{v} = \frac{d\vec{r}}{dt} = \frac{d}{dt}(r \cdot \vec{e}_r) = \dot{\vec{r}}_r + \vec{\omega} \times \vec{r} \tag{5.1}$$

In plane, the second term on the right hand side in equation (5.1) could be written in:

$$\vec{\omega} \times \vec{r} = \begin{bmatrix} 0 & -\omega \\ \omega & 0 \end{bmatrix} \cdot \vec{r} = \omega \cdot \begin{bmatrix} 0 & -1 \\ 1 & 0 \end{bmatrix} \cdot \vec{r} = \omega \cdot E_r \cdot \vec{r} \tag{5.2}$$

here,

$$E_r = \begin{bmatrix} 0 & -1 \\ 1 & 0 \end{bmatrix} \tag{5.3}$$
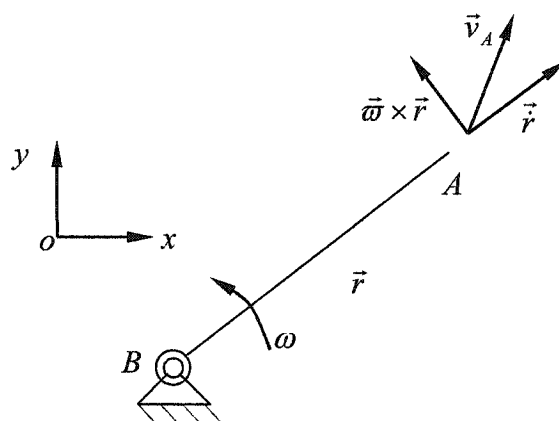
Figure 5.1 Illustration of equation (5.1).
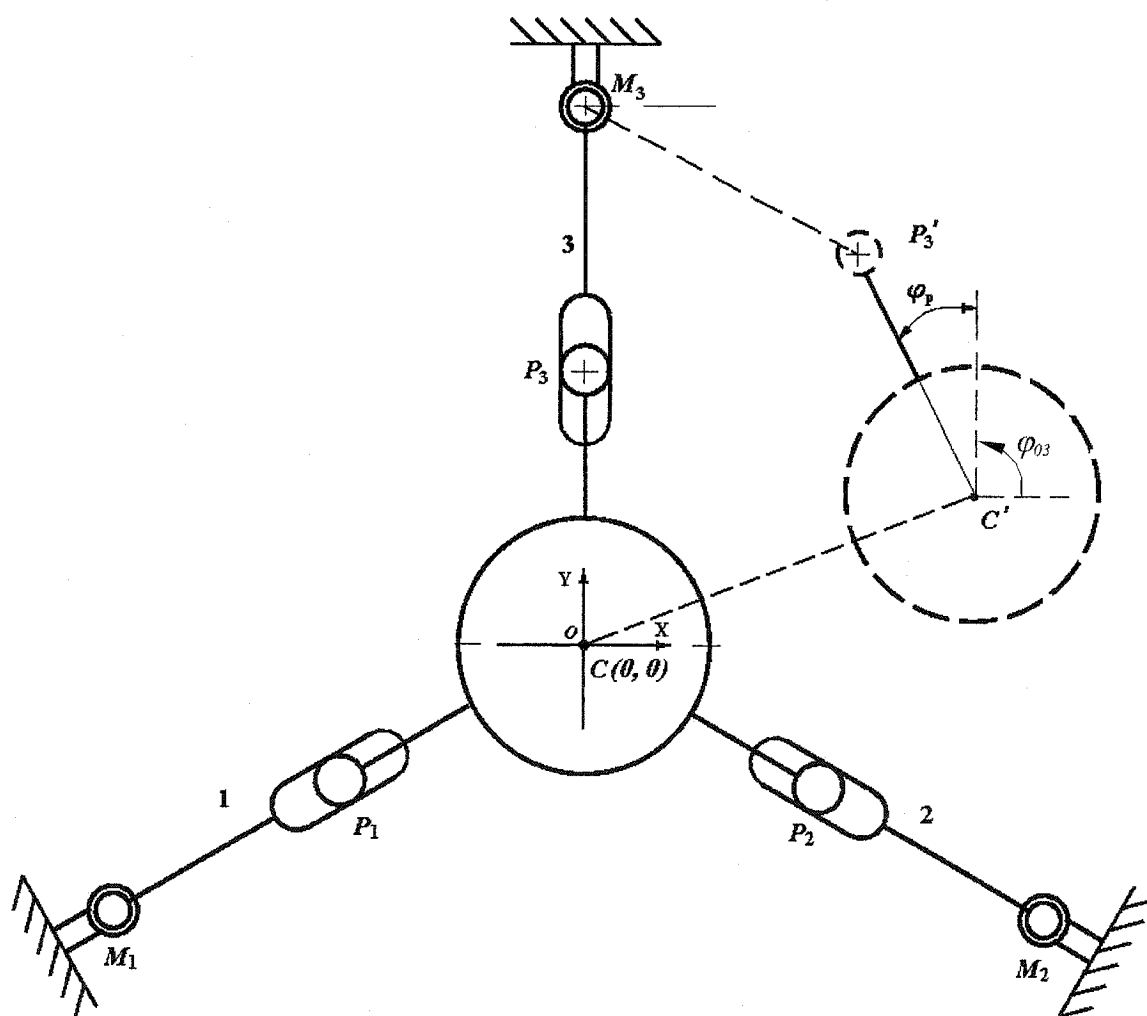
Figure 5.2 The layout of the manipulator for calculating the Jacobian matrix.

Using the procedure described above, the Jacobian matrix for the kinematic model of 3-DOF manipulators can be derived. The dashed line platform in Figure 5.2 is an arbitrary new position. Figure 5.2 shows a geometric closed loop M_3-P_3-o-C'-P_3'-M_3. In this loop, the following geometrical relations are found:

$$\overrightarrow{oP_3'} = \overrightarrow{oM_3} + \overrightarrow{M_3P_3'} \tag{5.4}$$

$$\overrightarrow{oP_3'} = \overrightarrow{oC'} + \overrightarrow{C'P_3'} \tag{5.5}$$

Differentiating equations (5.4) and (5.5) with respect to time, two expressions for the velocity of the point P_3 can obtained. The expression derived from equation (5.4) connects input variable (θ_3) with the velocity of P_3; the expression derived from equation (5.5) associates output variables (x_c, y_c, φ_p) with the velocity of P_3. Through these two expressions for the velocity of the point P_3, the relationship between input and output variables can be found (see Appendix A):

$$l_3\dot{\theta}_3 = -\dot{x}_c \sin(\theta_{03} + \theta_3) + \dot{y}_c \cos(\theta_{03} + \theta_3) + r_3\dot{\varphi}_p \cos(\theta_{03} + \theta_3 - \varphi_{03} - \varphi_p) \tag{5.6}$$

where l_3 is the distance M_3P_3, r_3 is the distance $C'P_3'$, φ_{03} is the initial angle between CP_3 and the x axis.

Similar results can be obtained from studying the points P_1 and P_2.

$$l_1\dot{\theta}_1 = -\dot{x}_c \sin(\theta_{01} + \theta_1) + \dot{y}_c \cos(\theta_{01} + \theta_1) + r_1\dot{\varphi}_p \cos(\theta_{01} + \theta_1 - \varphi_{01} - \varphi_p). \tag{5.7}$$

$$l_2\dot{\theta}_2 = -\dot{x}_c \sin(\theta_{02} + \theta_2) + \dot{y}_c \cos(\theta_{02} + \theta_2) + r_2\dot{\varphi}_p \cos(\theta_{02} + \theta_2 - \varphi_{02} - \varphi_p). \tag{5.8}$$

Written in matrix form, equations (5.6), (5.7) and (5.8) are changed to the following equation.

$$\begin{pmatrix} l_1 & 0 & 0 \\ 0 & l_2 & 0 \\ 0 & 0 & l_3 \end{pmatrix} \begin{bmatrix} \dot{\theta}_1 \\ \dot{\theta}_2 \\ \dot{\theta}_3 \end{bmatrix}$$

$$= \begin{pmatrix} -\sin(\theta_{01} + \theta_1) & \cos(\theta_{01} + \theta_1) & r_1\cos(\theta_{01} + \theta_1 - \varphi_{01} - \varphi_p) \\ -\sin(\theta_{02} + \theta_2) & \cos(\theta_{02} + \theta_2) & r_2\cos(\theta_{02} + \theta_2 - \varphi_{02} - \varphi_p) \\ -\sin(\theta_{03} + \theta_3) & \cos(\theta_{03} + \theta_3) & r_3\cos(\theta_{03} + \theta_3 - \varphi_{03} - \varphi_p) \end{pmatrix} \begin{bmatrix} \dot{x}_c \\ \dot{y}_c \\ \dot{\varphi}_p \end{bmatrix} \tag{5.9}$$

The terms r_i are constants in this case, and their values are equal to the r defined in Figure 3.4. The terms l_i represent the distances between P_i and M_i, which can not be equal to zero. Therefore, the diagonal matrix in the left hand side of equation (5.9) always has an inverse. When left multiplied by this inverse matrix, equation (5.9) is simplified to the form below.

$$\begin{bmatrix} \dot{\theta}_1 \\ \dot{\theta}_2 \\ \dot{\theta}_3 \end{bmatrix} = \begin{pmatrix} \dfrac{-\sin(\theta_{01}+\theta_1)}{l_1} & \dfrac{\cos(\theta_{01}+\theta_1)}{l_1} & \dfrac{r\cos(\theta_{01}+\theta_1-\varphi_{01}-\varphi_p)}{l_1} \\ \dfrac{-\sin(\theta_{02}+\theta_2)}{l_2} & \dfrac{\cos(\theta_{02}+\theta_2)}{l_2} & \dfrac{r\cos(\theta_{02}+\theta_2-\varphi_{02}-\varphi_p)}{l_2} \\ \dfrac{-\sin(\theta_{03}+\theta_3)}{l_3} & \dfrac{\cos(\theta_{03}+\theta_3)}{l_3} & \dfrac{r\cos(\theta_{03}+\theta_3-\varphi_{03}-\varphi_p)}{l_3} \end{pmatrix} \begin{bmatrix} \dot{x}_c \\ \dot{y}_c \\ \dot{\varphi}_p \end{bmatrix} \qquad (5.10)$$

The Jacobian matrix J_1 between the velocities of the input variables θ_i and the velocities of the output variables x_c, y_c and φ_p is defined as the 3 by 3 matrix in equation (5.10).

Since the radial velocity of P_i (along the M_iP_i) denotes the velocity of the S-joints in axial compression and stretching, it is useful to obtain the Jacobian matrix for these velocities and the output variables. The relation between the radial velocities of P_i and the velocities of the output variables is:

$$\begin{bmatrix} \dot{l}_1 \\ \dot{l}_2 \\ \dot{l}_3 \end{bmatrix} = \begin{pmatrix} \cos(\theta_{01}+\theta_1) & \sin(\theta_{01}+\theta_1) & r_1\sin(\theta_{01}+\theta_1-\varphi_{01}-\varphi_p) \\ \cos(\theta_{02}+\theta_2) & \sin(\theta_{02}+\theta_2) & r_2\sin(\theta_{02}+\theta_2-\varphi_{02}-\varphi_p) \\ \cos(\theta_{03}+\theta_3) & \sin(\theta_{03}+\theta_3) & r_3\sin(\theta_{03}+\theta_3-\varphi_{03}-\varphi_p) \end{pmatrix} \begin{bmatrix} \dot{x}_c \\ \dot{y}_c \\ \dot{\varphi}_p \end{bmatrix} \qquad (5.11)$$

The Jacobian matrix J_2 between the velocity $\dot{l}_i$ and output variables x_c, y_c and φ_p is defined as the 3 by 3 matrix in equation (5.11). The angles θ_{0i} in the J_1 and J_2 have the constant values:

$$\theta_{01} = \pi/6, \ \theta_{02} = 5\pi/6, \theta_{03} = 3\pi/2. \qquad (5.12)$$

The angles φ_{0i} in the J_1 and J_2 are given in equation (3.6). Therefore, the two Jacobian matrices are simplified as:

$$J_1 = \begin{pmatrix} \dfrac{-\sin(\theta_{01} + \theta_1)}{l_1} & \dfrac{\cos(\theta_{01} + \theta_1)}{l_1} & \dfrac{-r\cos(\theta_1 - \varphi_p)}{l_1} \\[2ex] \dfrac{-\sin(\theta_{02} + \theta_2)}{l_2} & \dfrac{\cos(\theta_{02} + \theta_2)}{l_2} & \dfrac{-r\cos(\theta_2 - \varphi_p)}{l_2} \\[2ex] \dfrac{-\sin(\theta_{03} + \theta_3)}{l_3} & \dfrac{\cos(\theta_{03} + \theta_3)}{l_3} & \dfrac{-r\cos(\theta_3 - \varphi_p)}{l_3} \end{pmatrix} \qquad (5.13)$$

$$J_2 = \begin{pmatrix} \cos(\theta_{01} + \theta_1) & \sin(\theta_{01} + \theta_1) & -r\sin(\theta_1 - \varphi_p) \\ \cos(\theta_{02} + \theta_2) & \sin(\theta_{02} + \theta_2) & -r\sin(\theta_2 - \varphi_p) \\ \cos(\theta_{03} + \theta_3) & \sin(\theta_{03} + \theta_3) & -r\sin(\theta_3 - \varphi_p) \end{pmatrix} \qquad (5.14)$$

5.3 Flexure joints

5.3.1 Stiffness

The dimensions of the S-joints used in the manipulator are shown in Figure 5.3. The neutral length of the S-joint, measured in the axial direction, is denoted by L_4. The S-joint geometry includes two identical semicircles with radius R_L and arcs with radius of R_s. The total tuning length of the S-joint beam is:

$$L_{total} = 2 \cdot L_1 + 2 \cdot L_2 + L_3 + 2 \cdot \pi \cdot R_L + \pi \cdot R_s \qquad (5.15)$$

here $L_1 = 4$ μm, $L_2 = 70$ μm, $L_3 = 152$ μm, $L_4 = 104$ μm, $R_s = 6$ μm, $R_L = 21$ μm resulting in the total length of 451 μm.
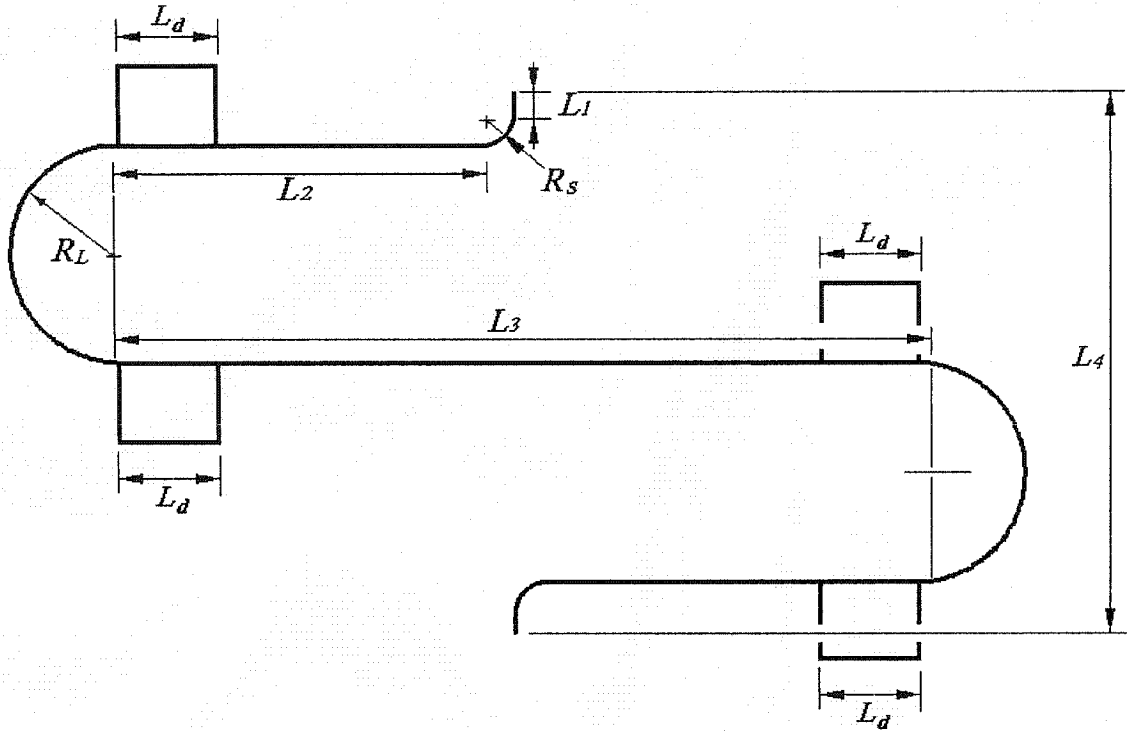
Figure 5.3 Structure of the S-joint.

The S-shaped joint allows stretching and compression in the axial direction, a small transverse motion, and rotation simultaneously. The in-plane rotational and axial stiffnesses of the S-joint can be computed from H. Fettig's formulas as following [8]:

$$k_\beta = 900 \frac{\mu N \mu m}{rad} (\frac{250 \mu m}{L_\beta})$$ (5.16)

$$k_a = 0.83 \frac{\mu N}{\mu m} (\frac{250 \mu m}{L_\alpha})^{3.19}$$ (5.17)

where L_α and L_β are effective lengths for calculating axial stiffness and in-plane rotation stiffness.

The maximum compression stroke for the S-joint is approximately 80 μm (= $4R_L$). In order to keep an S-joint free of stiction, four tabs with dimples are added to the S-joint. The addition of tabs is needed because the S-joint width is too narrow to place a dimple directly on it. Since the four dimple tabs (at L_d, Fig. 5.3) stiffen the S-joints, their lengths are subtracted from the total length when calculating the axial linear stiffness and in-

plane rotation stiffnesses. Similarly, the lengths of the two small arcs R_s are subtracted. In this case, the length subtracted from the total length is $4L_d + \pi R_s = 52 + 19 = 71\,\mu m$. The semicircles in the S-joints are not deformed significantly for axial compression and stretching. Therefore, arbitrarily, half of the length of the arcs R_L was subtracted from the total beam length when calculating the axial stiffness. So, the effective length L_β for calculating the in-plane rotational stiffness of the S-joint is:

$$L_\beta = L_{total} - 4 \cdot L_d - \pi \cdot R_s \approx 380\ \mu m \qquad (5.18)$$

The effective length L_α for calculating the axial stiffness of the S-joint is:

$$L_\alpha = L_{total} - 4 \cdot L_d - \pi \cdot R_s - \pi \cdot R_L \approx 320\ \mu m \qquad (5.19)$$

Inputting $L_\beta = 380$ μm to equation (5.16), the in-plane rotation stiffness is:

$$k_\beta = 900 \frac{\mu N \mu m}{rad} \left(\frac{250 \mu m}{380 \mu m}\right) \approx 592 \frac{\mu N \mu m}{rad} \qquad (5.20)$$

Inserting $L_\alpha = 320$ μm into equation (5.17) produces the axial stiffness:

$$k_a = 0.83 \frac{\mu N}{\mu m} \left(\frac{250 \mu m}{320 \mu m}\right)^{3.19} \approx 0.378 \frac{\mu N}{\mu m} \qquad (5.21)$$

Since the transverse motion is related to the axial length of the S-joint (joint's footprint), when calculating the transverse stiffness k_t, the S-joint can be treated as a cantilever beam (see Figure 5.4) with approximate length L_4 of the footprint.
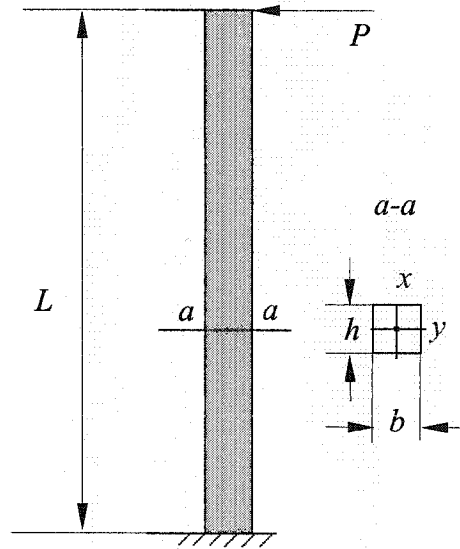
Figure 5.4 Cantilever beam.

The displacement of the cantilever beam with a point load P at its free end is [68]:

$$dx = -\frac{PL^3}{3EI_x} \qquad (5.22)$$

here dx is the displacement; L is the length of the cantilever beam; E is the elastic modulus of the material; I_x is the moment of inertia of the cross section of the beam computed about the neutral axis x. The equivalent stiffness can be obtained from equation (5.22):

$$k_t = \frac{3EI_x}{L^3} \qquad (5.23)$$

The moment of inertia I_x is [68]:

$$I_x = \frac{hb^3}{12} \qquad (5.24)$$

here h and b are the thickness and width of the beam respectively. Inputing $b = h = 2$ μm, $L = 100$ μm to equations (5.23) and (5.24), the transverse stiffness is obtained as $k_t = 0.67$ μN /μm.

5.3.2 Dynamic model of the S-joint

Stiffness and mass distribution play key roles in dynamic modeling. Figure 5.5 shows the mass distribution and three massless springs: two linear and one spiral. The model springs, individually, have the same stiffness as to the S-joint's k_a, k_t and k_β. The computed mass of the S-joint including the four dimples is $M_s = 6.7 \times 10^{-3}$ μg. The mass M_s was arbitrarily divided into two equal parts at the two ends of the S-joint.
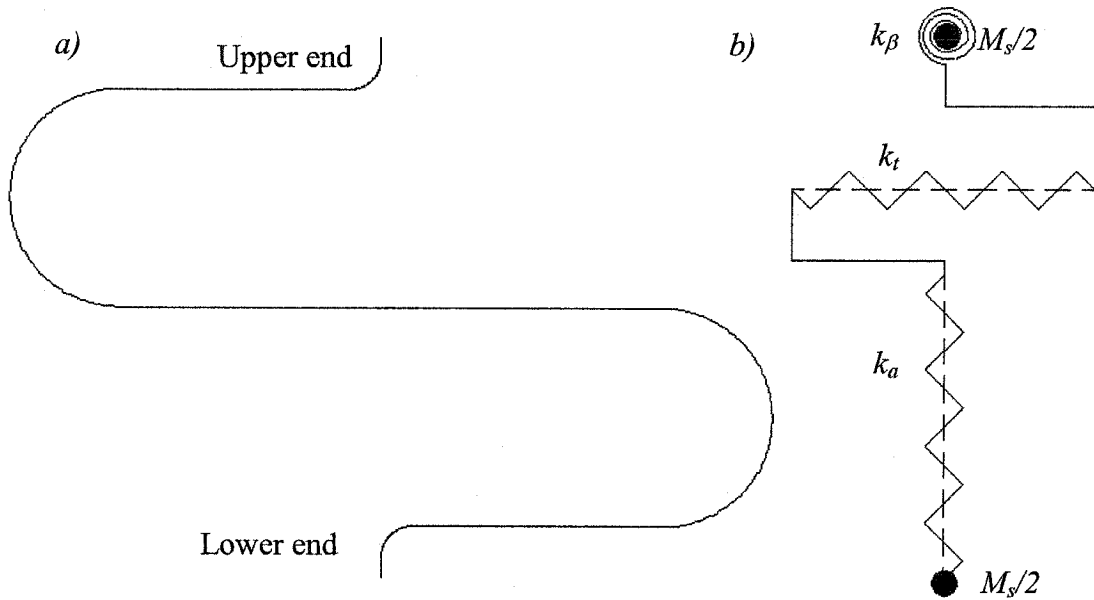
Figure 5.5 S-joint a) and its model b).

The linear spring k_a is assigned to the end of the actuator and moves along the center line of the actuator; the linear spring k_t accommodates the small transverse motion that is perpendicular to the center line of the actuator; the spiral spring k_β, located at the edge of the platform, allows rotation. Ideally, the transverse stiffness k_t should be infinite and the axial and rotational stiffnesses should be zero.

5.4 Actuators

The detailed delta TA geometry was demonstrated in Chapter 4. According to the specific geometry of the delta TA and the physical properties of the material, the mass, mass center location and moment of inertia around the mass center were found. The mass center is located, on the center line, 181 μm away from the cold arm base (see Figure 5.6). The symbol L_{mc} denotes the distance from the Mass Center to the base of the cold arm. The mass of the delta motor computed from its volume and density is $M_{ta} = 2.08 \times 10^{-2}$ μg. The computed motor's moment of inertia about the Mass Center is $I_{ta\_c} = 61.5$ (μg)(μm)^2. Therefore, the moment of inertia about the base of the cold arm, which is assumed to be a ground pivot, can be calculated as follows:

$$I_{ta\_p} = I_{ta\_c} + M_{ta} \cdot L_{mc}^2 = 61.5 + 2.08 \cdot 10^{-2} \cdot 181^2 \approx 750(\mu g)(\mu m)^2 \qquad (5.25)$$
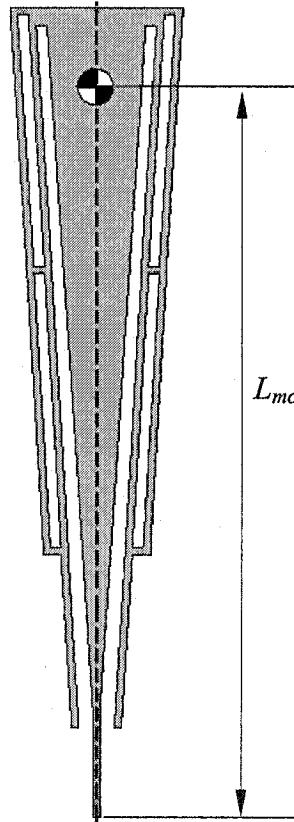
Figure 5.6 Mass Center location of delta actuator.

The mass of the S-joint is $M_s = 6.7 \times 10^{-3}$ µg. Half of the S-joint mass was assigned to the motor located at the end of the center line of the cold arm: $L_c = 230$ µm away from the cold arm base. This added mass contributed moment of inertia to the motor pivot.

$$I_{ta} = I_{ta\_p} + M_s / 2 \cdot L_c^2 = 750 + 3.35 \cdot 10^{-3} \cdot 230^2 = 927(\mu g)(\mu m)^2 \qquad (5.26)$$

5.5 Platform

A detailed geometry of the platform was described in Chapter 4. The mass center is located at its geometric center. The computed mass of the platform is $M_{p0} = 1.35 \times 10^{-2}$ µg; the moment of inertia about the z axis is $I_{p0} = 9.28$ µg·µm². The platform is connected to the three S-joints and in the dynamic model; halves of the masses of the S-joints are added to the platform. The model effective platform mass M_p and moment of inertia I_p can be calculated as following:

$$M_p = M_{po} + 3 \cdot (M_s / 2) = 1.35 \cdot 10^{-2} + 3 \cdot 3.35 \cdot 10^{-3} = 2.36 \cdot 10^{-2} \mu g \qquad (5.27)$$

$$I_p = I_{p0} + 3 \cdot (M_s / 2) \cdot r_p^2 = 9.28 + 3 \cdot 3.35 \cdot 10^{-3} \cdot 35^2 = 21.59(\mu g)(\mu m)^2 \qquad (5.28)$$

where r_p represents the radius of the platform.

5.6 3-DOF spring-mass model

A 3-DOF dynamic model can simulate the platform's in-plane behavior such as in-plane modes and corresponding frequencies. Since this model only focuses on the platform behavior, an S-joint is simply modeled by two springs: an axial linear spring and a spiral spring; which means that the transverse stiffness is infinitely large.

5.6.1 Modeling

Figure 5.7 shows a 3-DOF dynamic model of the manipulator. The manipulator is modeled as a rigid link mechanism with 9 springs. There are 6 spiral springs and 3 linear springs. The linear springs are assigned to the actuators; the three spiral springs from the S-joints are assigned to the platform at a fixed radius r measured from the platforms

center and spread 120° apart. The platform is treated as a rigid ternary link. In the model, r is equal to r_p, which represents that a spiral spring is located at the edge of the platform.
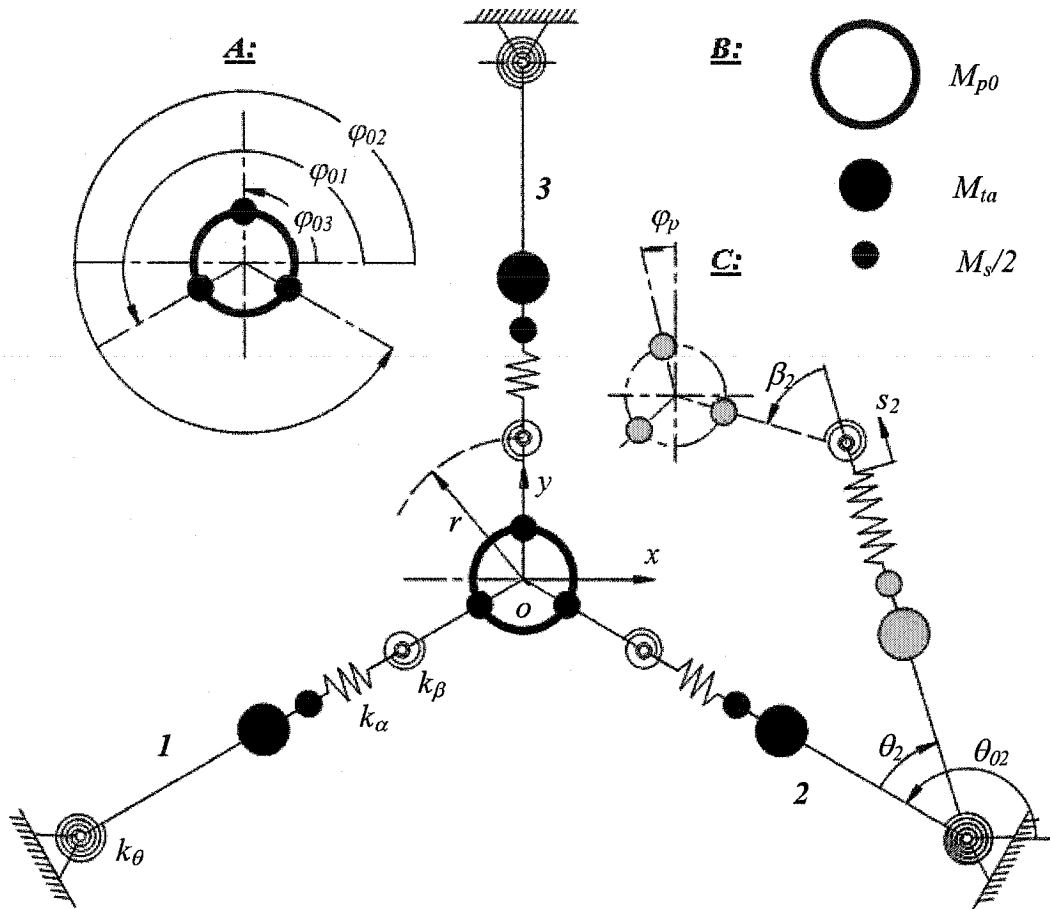
Figure 5.7 3-DOF dynamic model of the manipulator.

Three motion variables x, y and φ_p were chosen as the micromanipulator's 3 independent DOF. They describe the position and posture of the platform in the global coordinate system xoy. Three dependent variables are defined as follows: θ_i is the incremental angle of rotation of the motor with respect to its neutral position, s_i is the length increment of the actuator along its center line with respect to its neutral length, and β_i is the relative angle between the platform's arm and the actuator's center line.

Figure 5.7 shows the manipulator model components in the neutral position plus three details. Detail **A** illustrates the assignments of angles of the initial orientations ϕ_{i0} of the spiral springs with respect to the absolute coordinate system xoy; detail **B** shows the assignment of mass symbols: M_{po} is the platform mass, M_{ta} is the actuator mass, $M_s/2$ is half of the S-joint mass; detail **C** shows the assignment of the dependent variables: θ_i, β_i and s_i. In addition, detail **C** shows the assignment of the independent posture-variable φ_p and the neutral orientation of the leg θ_{0i} with respect to the global coordinate system xoy. The linear velocity relationships between dependent variables, θ_i, β_i, s_i and independent variables x, y, φ_p can be expressed by velocity Jacobians. Since the platform displacements are small during vibration, the deformations of the springs only insignificantly change the geometry of the manipulator. Thus these changes can be ignored and therefore, θ_i, β_i and s_i can be treated as zeros when calculating the corresponding Jacobian matrices. So the Jacobian matrix from equations (5.13) & (5.14) will be modified into equations (5.29) and (5.30):

$$
\begin{pmatrix} \dot{\theta}_1 \\ \dot{\theta}_2 \\ \dot{\theta}_3 \end{pmatrix} = J_1 \begin{pmatrix} \dot{x} \\ \dot{y} \\ \dot{\varphi}_p \end{pmatrix} = \begin{bmatrix} a_1 & b_1 & c_1 \\ a_2 & b_2 & c_2 \\ a_3 & b_3 & c_3 \end{bmatrix} \begin{pmatrix} \dot{x} \\ \dot{y} \\ \dot{\varphi}_p \end{pmatrix}
\tag{5.29}
$$

$$
\begin{pmatrix} \dot{s}_1 \\ \dot{s}_2 \\ \dot{s}_3 \end{pmatrix} = J_2 \begin{pmatrix} \dot{x} \\ \dot{y} \\ \dot{\varphi}_p \end{pmatrix} = \begin{bmatrix} d_1 & e_1 & f_1 \\ d_2 & e_2 & f_2 \\ d_3 & e_3 & f_3 \end{bmatrix} \begin{pmatrix} \dot{x} \\ \dot{y} \\ \dot{\varphi}_p \end{pmatrix}
\tag{5.30}
$$

here $a_i = -\sin\theta_{0i}/p_i$, $b_i = \cos\theta_{0i}/p_i$, $c_i = r\cos(\varphi_{0i} - \theta_{0i})/p_i$, $d_i = \cos\theta_{0i}$, $e_i = \sin\theta_{0i}$, $f_i = -r\sin(\varphi_{0i} - \theta_{0i})$, $i = 1, 2, 3$. The term p_i represents the distance between the two spiral springs of the i-th actuator. According to the assumption, the values of p_i will be replaced by the neutral length between the two coil springs of the i-th actuator which is 334 μm. Radius r is equal to the radius of the platform $r_p = 35$ μm. The values of the angles are the following:

$$\theta_{01} = \pi/6; \quad \theta_{02} = 5\pi/6; \quad \theta_{03} = 3\pi/2;$$

$$\varphi_{01} = 7\pi/6; \quad \varphi_{02} = 11\pi/6; \quad \varphi_{03} = \pi/2. \tag{5.31}$$

Inputing the specific parameter values to equations (5.29) and (5.30), leads to the following Jacobian matrices:

$$J_1 = \begin{bmatrix} -0.0015 & 0.0026 & -0.105 \\ -0.0015 & -0.0026 & -0.105 \\ 0.0030 & 0 & -0.105 \end{bmatrix} \quad (5.32)$$

$$J_2 = \begin{bmatrix} 0.866 & 0.5 & 0 \\ -0.866 & 0.5 & 0 \\ 0 & -1 & 0 \end{bmatrix} \quad (5.33)$$

For linear vibration, the Jacobian matrices J_1 & J_2 can be used to relate θ_i, β_i, and s_i to the three independent variables (x, y, φ_p):

$$\begin{pmatrix} \theta_1 \\ \theta_2 \\ \theta_3 \end{pmatrix} = J_1 \begin{pmatrix} x \\ y \\ \varphi_p \end{pmatrix} = \begin{bmatrix} a_1 & b_1 & c_1 \\ a_2 & b_2 & c_2 \\ a_3 & b_3 & c_3 \end{bmatrix} \begin{pmatrix} x \\ y \\ \varphi_p \end{pmatrix} \quad (5.34)$$

$$\begin{pmatrix} s_1 \\ s_2 \\ s_3 \end{pmatrix} = J_2 \begin{pmatrix} x \\ y \\ \varphi_p \end{pmatrix} = \begin{bmatrix} d_1 & e_1 & f_1 \\ d_2 & e_2 & f_2 \\ d_3 & e_3 & f_3 \end{bmatrix} \begin{pmatrix} x \\ y \\ \varphi_p \end{pmatrix} \quad (5.35)$$

The small angles β_i are the differences between φ_p and θ_i and they can be expressed in the following matrix form:

$$\begin{pmatrix} \beta_1 \\ \beta_2 \\ \beta_3 \end{pmatrix} = \begin{bmatrix} 0 & 0 & 1 \\ 0 & 0 & 1 \\ 0 & 0 & 1 \end{bmatrix} \begin{pmatrix} x \\ y \\ \varphi_p \end{pmatrix} - J_1 \begin{pmatrix} x \\ y \\ \varphi_p \end{pmatrix} = \begin{bmatrix} -a_1 & -b_1 & 1-c_1 \\ -a_2 & -b_2 & 1-c_2 \\ -a_3 & -b_3 & 1-c_3 \end{bmatrix} \begin{pmatrix} x \\ y \\ \varphi_p \end{pmatrix} = J_3 \begin{pmatrix} x \\ y \\ \varphi_p \end{pmatrix} \quad (5.36)$$

Similarly, the Jacobian matrix J_3 can be used for relating velocities $\dot{\beta}_i$ and ($\dot{x}, \dot{y}, \dot{\varphi}_p$):

$$\begin{pmatrix} \dot{\beta}_1 \\ \dot{\beta}_2 \\ \dot{\beta}_3 \end{pmatrix} = J_3 \begin{pmatrix} \dot{x} \\ \dot{y} \\ \dot{\varphi}_p \end{pmatrix} = \begin{bmatrix} -a_1 & -b_1 & 1-c_1 \\ -a_2 & -b_2 & 1-c_2 \\ -a_3 & -b_3 & 1-c_3 \end{bmatrix} \begin{pmatrix} \dot{x} \\ \dot{y} \\ \dot{\varphi}_p \end{pmatrix} \quad (5.37)$$

The value of the Jacobian matrix J_3 is:

$$J_3 = \begin{bmatrix} 0.0015 & -0.0026 & 1.105 \\ 0.0015 & 0.0026 & 1.105 \\ -0.0030 & 0 & 1.105 \end{bmatrix} \quad (5.38)$$

5.6.2 Dynamic equations:

Since the system moves in a plane, the gravity potential energy does not change. The kinetic energy T comes from the movements of the masses and the potential energy U comes from the deformations of the springs. The kinetic and potential energy can be calculated as follows:

$$T = \sum_{i=1}^{3} \frac{1}{2} I_{tai} \dot{\theta}_i^2 + \frac{1}{2} M_p \dot{x}^2 + \frac{1}{2} M_p \dot{y}^2 + \frac{1}{2} I_p^2 \dot{\varphi}_p^2 \quad (5.39)$$

$$U = \sum_{i=1}^{3} \frac{1}{2} (k_{\theta i} \theta_i^2 + k_{ai} s_i^2 + k_{\beta i} \beta_i^2) \quad (5.40)$$

here, term k_{ai} is the stiffness of the linear spring in the i-th actuator; terms $k_{\theta i}$ and $k_{\beta i}$ represent the stiffnesses of the spiral springs; term I_{tai} is the moment of inertia of the i-th actuator about its base. Since the manipulator is trisymmetric and $k_{a1} = k_{a2} = k_{a3} = k_a$, k_{ai} was replaced by k_a. Similar replacement was made for $k_{\theta i}$, $k_{\beta i}$ and I_{tai}.

The Lagrange equations have the following form:

$$\frac{d}{dt}(\frac{\partial L}{\partial \dot{q}_i}) - \frac{\partial L}{\partial q_i} = 0, \text{ here } L = T - U \quad (5.41)$$

Specifically, for the model considered, q_i (i = 1, 2, 3) are the independent variables: x, y and φ_p. The dynamic equation for the first independent variable x can be written as:

$$\frac{d}{dt}(\frac{\partial L}{\partial \dot{x}}) - \frac{\partial L}{\partial x} = 0 \quad (5.42)$$

The details of the dynamic equation can be developed in the following steps:

$$\frac{\partial L}{\partial \dot{x}} = M_p \dot{x} + I_{ta}(\dot{\theta}_1 \cdot \frac{\partial \dot{\theta}_1}{\partial \dot{x}} + \dot{\theta}_2 \cdot \frac{\partial \dot{\theta}_2}{\partial \dot{x}} + \dot{\theta}_3 \cdot \frac{\partial \dot{\theta}_3}{\partial \dot{x}}) \quad (5.43)$$

From equation (5.29), the partial derivatives are found constant:

$$\frac{\partial \dot{\theta}_1}{\partial \dot{x}} = a_1, \qquad \frac{\partial \dot{\theta}_2}{\partial \dot{x}} = a_2, \qquad \frac{\partial \dot{\theta}_3}{\partial \dot{x}} = a_3 \qquad (5.44)$$

Replacing $\dot{\theta}_1$, $\dot{\theta}_2$, $\dot{\theta}_3$ with $\dot{x}$, $\dot{y}$ and $\dot{\varphi}_p$ through Jacobian matrix J_l (see equation 5.29), the following result is achieved:

$$\frac{\partial L}{\partial \dot{x}} = (M_p + I_{ta} \cdot \sum_{i=1}^{3} a_i^2) \cdot \dot{x} + I_{ta} \cdot (\sum_{i=1}^{3} a_i b_i) \cdot \dot{y} + I_{ta} \cdot (\sum_{i=1}^{3} a_i c_i) \cdot \dot{\varphi}_p \qquad (5.45)$$

Differentiating equation (5.45) with respect to t, the second derivative is obtained:

$$\frac{d}{dt}\left(\frac{\partial L}{\partial \dot{x}}\right) = (M_p + I_{ta} \cdot \sum_{i=1}^{3} a_i^2) \cdot \ddot{x} + I_{ta} \cdot (\sum_{i=1}^{3} a_i b_i) \cdot \ddot{y} + I_{ta} \cdot (\sum_{i=1}^{3} a_i c_i) \cdot \ddot{\varphi}_p \qquad (5.46)$$

The second term in the left hand side of equation (5.42) is developed as follows:

$$\frac{\partial L}{\partial x} = k_\theta (\theta_1 \cdot \frac{\partial \theta_1}{\partial x} + \theta_2 \cdot \frac{\partial \theta_2}{\partial x} + \theta_3 \cdot \frac{\partial \theta_3}{\partial x})$$
$$+ k_a (s_1 \cdot \frac{\partial s_1}{\partial x} + s_2 \cdot \frac{\partial s_2}{\partial x} + s_3 \cdot \frac{\partial s_3}{\partial x}) + k_\beta (\beta_1 \cdot \frac{\partial \beta_1}{\partial x} + \beta_2 \cdot \frac{\partial \beta_2}{\partial x} + \beta_3 \cdot \frac{\partial \beta_3}{\partial x}) \qquad (5.47)$$

Using equations (5.34), (5.35) and (5.36), the component partial derivative terms are determined:

$$\frac{\partial \theta_1}{\partial x} = a_1, \qquad \frac{\partial \theta_2}{\partial x} = a_2, \qquad \frac{\partial \theta_3}{\partial x} = a_3$$

$$\frac{\partial s_1}{\partial x} = d_1, \qquad \frac{\partial s_2}{\partial x} = d_2, \qquad \frac{\partial s_3}{\partial x} = d_3 \qquad (5.48)$$

$$\frac{\partial \beta_1}{\partial x} = -a_1, \qquad \frac{\partial \beta_2}{\partial x} = -a_2, \qquad \frac{\partial \beta_3}{\partial x} = -a_3$$

Then equation (5.47) has the following form:

$$\frac{\partial L}{\partial x} = k_\theta (\theta_1 \cdot a_1 + \theta_2 \cdot a_2 + \theta_3 \cdot a_3)$$
$$+ k_a (s_1 \cdot d_1 + s_2 \cdot d_2 + s_3 \cdot d_3) - k_\beta (\beta_1 \cdot a_1 + \beta_2 \cdot a_2 + \beta_3 \cdot a_3) \qquad (5.49)$$

Substituting θ_i, β_i and s_i with x, y and φ_p, equation (5.47) is expressed in three independent variables:

$$\frac{\partial L}{\partial x} =$$

$$[(k_\theta + k_\beta) \cdot \sum_{i=1}^{3} a_i^2 + k_a \cdot \sum_{i=1}^{3} d_i^2] \cdot x + [(k_\theta + k_\beta) \cdot \sum_{i=1}^{3} a_i b_i + k_a \cdot \sum_{i=1}^{3} d_i e_i] \cdot y \qquad (5.50)$$

$$+ [(k_\theta + k_\beta) \cdot \sum_{i=1}^{3} a_i c_i + k_a \cdot \sum_{i=1}^{3} d_i f_i - k_\beta \cdot \sum_{i=1}^{3} a_i] \cdot \varphi_p$$

Similarly, the results for $\dot{y}$ and $\dot{\varphi}_p$ have been found as follows:

$$\frac{d}{dt}\left(\frac{\partial L}{\partial \dot{y}}\right) = I_{ta}(\sum_{i=1}^{3} a_i b_i) \cdot \ddot{x} + (M_p + I_{ta} \sum_{i=1}^{3} b_i^2) \cdot \ddot{y} + I_{ta}(\sum_{i=1}^{3} b_i c_i) \cdot \ddot{\varphi}_p \qquad (5.51)$$

$$\frac{\partial L}{\partial y} = [(k_\theta + k_\beta) \cdot \sum_{i=1}^{3} a_i b_i + k_a \cdot \sum_{i=1}^{3} d_i e_i] \cdot x + [(k_\theta + k_\beta) \cdot \sum_{i=1}^{3} b_i^2 + k_a \cdot \sum_{i=1}^{3} e_i^2] \cdot y$$

$$+ [(k_\theta + k_\beta) \cdot \sum_{i=1}^{3} b_i c_i + k_a \cdot \sum_{i=1}^{3} e_i f_i - k_\beta \cdot \sum_{i=1}^{3} b_i] \cdot \varphi_p \qquad (5.52)$$

$$\frac{d}{dt}\left(\frac{\partial L}{\partial \dot{\varphi}_p}\right) = I_{ta}(\sum_{i=1}^{3} a_i c_i) \cdot \ddot{x} + I_{ta}(\sum_{i=1}^{3} b_i c_i) \cdot \ddot{y} + (M_p + I_{ta} \sum_{i=1}^{3} c_i^2) \cdot \ddot{\varphi}_p \qquad (5.53)$$

$$\frac{\partial L}{\partial \varphi_p} = [(k_\theta + k_\beta) \cdot \sum_{i=1}^{3} a_i c_i - k_\beta \cdot \sum_{i=1}^{3} a_i + k_a \cdot \sum_{i=1}^{3} d_i f_i] \cdot x$$

$$+ [(k_\theta + k_\beta) \cdot \sum_{i=1}^{3} b_i c_i + k_a \cdot \sum_{i=1}^{3} e_i f_i - k_\beta \cdot \sum_{i=1}^{3} b_i] \cdot y \qquad (5.54)$$

$$+ [(k_\theta + k_\beta) \cdot \sum_{i=1}^{3} c_i^2 - k_\beta \cdot \sum_{i=1}^{3} c_i + k_a \cdot \sum_{i=1}^{3} f_i^2] \cdot \varphi_p$$

Written in a matrix form, equation (5.41) has the following form:

$$\overline{M} \begin{pmatrix} \ddot{x} \\ \ddot{y} \\ \ddot{\varphi}_p \end{pmatrix} - \overline{K} \begin{pmatrix} x \\ y \\ \varphi_p \end{pmatrix} = 0 \qquad (5.55)$$

here, $\overline{M}$ is the system mass matrix

$$\begin{bmatrix} M_p + \sum_{i=1}^{3} I_{ta} a_i^2 & \sum_{i=1}^{3} I_{ta} a_i b_i & \sum_{i=1}^{3} I_{ta} a_i c_i \\ \sum_{i=1}^{3} I_{ta} a_i b_i & M_p + \sum_{i=1}^{3} I_{ta} b_i^2 & \sum_{i=1}^{3} I_{ta} b_i c_i \\ \sum_{i=1}^{3} I_{ta} a_i c_i & \sum_{i=1}^{3} I_{ta} b_i c_i & I_p + \sum_{i=1}^{3} I_{ta} c_i^2 \end{bmatrix} \tag{5.56}$$

$\overline{K}$ is the system stiffness matrix

$$\begin{pmatrix} K_{11} & K_{12} & K_{13} \\ K_{21} & K_{22} & K_{23} \\ K_{31} & K_{32} & K_{33} \end{pmatrix} \tag{5.57}$$

The expressions of components of $\overline{K}$ are listed below:

$$K_{11} = \sum_{i=1}^{3} [a_i^2 (k_\theta + k_\beta) + d_i^2 k_a] \tag{5.58}$$

$$K_{12} = K_{21} = \sum_{i=1}^{3} [a_i b_i (k_\theta + k_\beta) + d_i e_i k_a] \tag{5.59}$$

$$K_{13} = K_{31} = \sum_{i=1}^{3} [a_i c_i (k_\theta + k_\beta) - a_i k_\beta + d_i f_i k_a] \tag{5.60}$$

$$K_{22} = \sum_{i=1}^{3} [b_i^2 (k_\theta + k_\beta) + e_i^2 k_a] \tag{5.61}$$

$$K_{23} = K_{32} = \sum_{i=1}^{3} [b_i c_i (k_\theta + k_\beta) - b_i k_\beta + e_i f_i k_a] \tag{5.62}$$

$$K_{33} = \sum_{i=1}^{3} [k_\theta c_i^2 + k_\beta (c_i^2 - c_i) + f_i^2 k_a] \tag{5.63}$$

Using μSI units and substituting the corresponding values into equations (5.56) & (5.57) leads to:

$$\overline{M} = \begin{pmatrix} 3.6 & -1.5 \times 10^{-16} & -5.0 \times 10^{-15} \\ -1.5 \times 10^{-16} & 3.6 & 5.3 \times 10^{-15} \\ -5.0 \times 10^{-15} & 5.3 \times 10^{-15} & 5210 \end{pmatrix} \times 10^{-11} \tag{5.64}$$

$$\overline{K} = \begin{pmatrix} 1.6 & -2.0 \times 10^{-16} & -4.0 \times 10^{-15} \\ -2.0 \times 10^{-16} & 1.6 & 5.4 \times 10^{-15} \\ -4.0 \times 10^{-15} & 5.4 \times 10^{-15} & 4910 \end{pmatrix} \qquad (5.65)$$

Note that these matrices are virtually diagonal. The eigenvalue function in Matlab software was used to solve for the eigenvalues and modes from equation (5.55). The off-diagonal terms are much smaller than the diagonal terms; therefore the off-diagonal terms were set to zero. The system natural frequencies are: $f_1 = 33$ kHz, $f_2 = 33$ kHz, $f_3 = 49$ kHz. Their corresponding modes are:

$$\begin{pmatrix} 1 \\ 0 \\ 0 \end{pmatrix} \qquad \begin{pmatrix} 0 \\ 1 \\ 0 \end{pmatrix} \qquad \begin{pmatrix} 0 \\ 0 \\ 1 \end{pmatrix} \qquad (5.66)$$

The first two modes are pure translation modes with the same frequencies. The third mode is a pure rotational mode. The number of elastic DOF is the same as the number of kinematic DOF of the rigid body, i.e., 3. This is a direct result of the fact that a 3-DOF dynamic model does not have redundant elastic degrees of freedom. Thus the leg variables θ_i, β_i and s_i are dependant on the platform variables x, y and φ. The relation between the dependent and independent variables is obtained via Jacobian matrices of Equations (5.29), (5.30), (5.34) - (5.37). The kinematic coupling of the actuators' motion to the platform, via the Jacobians, assures that the motor inertial properties and the compliance of the ground pivot are included in the system matrices of equation (5.55).

Furthermore, using Jacobian matrices, the corresponding modes of the actuators can be obtained through the platform modes. For example, corresponding to the pure rotation mode $(0, 0, 1)^T$ of the platform rotating about its center (Figure 5.7), the mode for the actuators is represented by the third column of the Jacobian matrix J_l, which is (-0.105, -0.105, -0.105)^T. The connection between the platform and actuator rotation can be explained as follows: to rotate the platform counterclockwise, the three actuators have to rotate clockwise by equal amounts.

5.7　6-DOF spring-mass model

The 3-DOF model studied previously can quickly provide the dynamic behavior of the platform; however, it doesn't include modes with motors. A 6-DOF model, which can produce modes with motors, was developed (see Figure 5.8) under the assumptions: a) the system vibration is in its linear range and it happens in the XY plane; b) the S-flexures are modeled by 3 separate springs which allow three planar independent motions: axial, transverse and in-plane rotation about the z-axis; the corresponding stiffnesses are k_a, k_t and k_β; c) the platform is a rigid body; d) one half of the S-springs' masses was assigned to the platform and one half to the motors; e) the motors rotate about their bases modeled as springs with stiffness k_θ.

The elastic motion independent variables are: two in-plane translations of the platform labeled by x and y; the platform's in-plane rotation about the z axis denoted by φ_p ; in-plane rotations for the three motors represented by θ_1, θ_2 and θ_3.
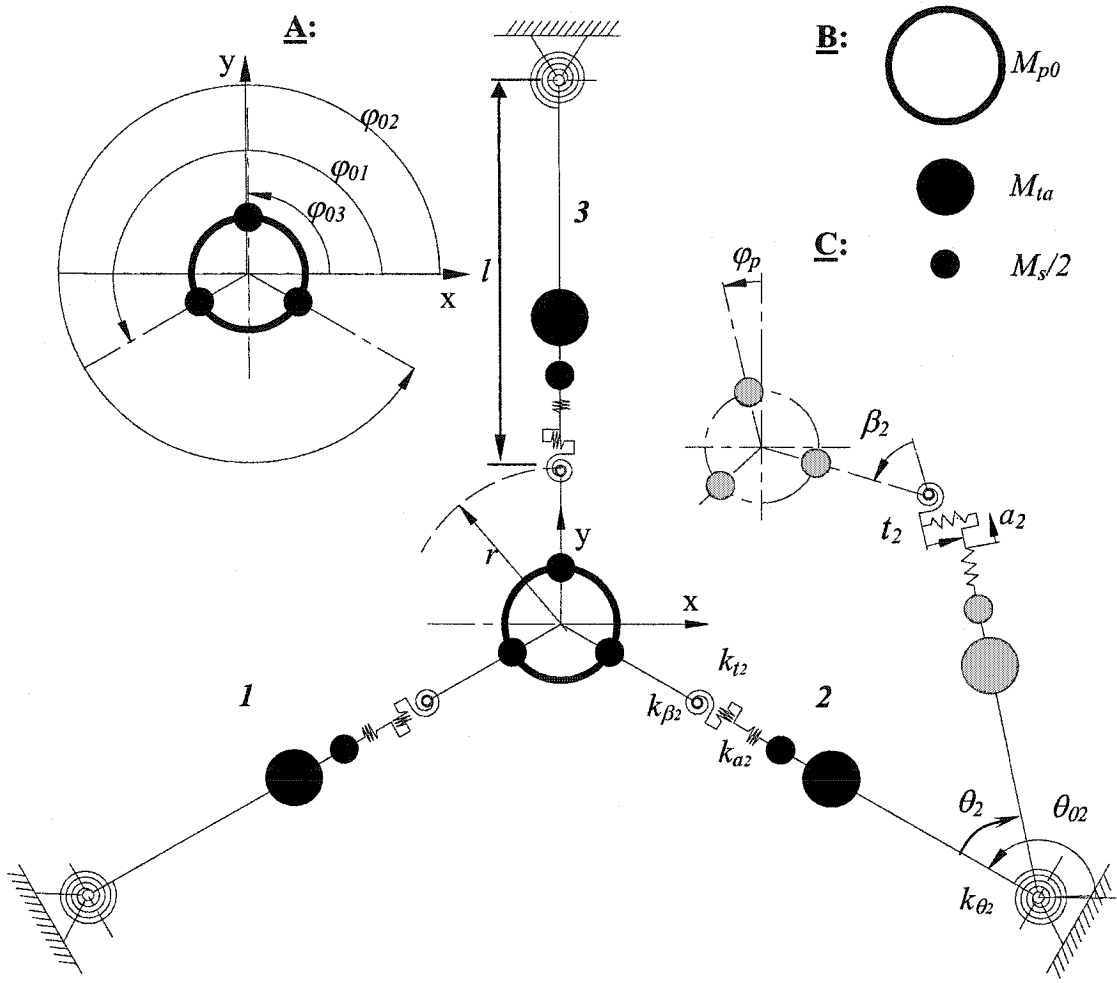
Figure 5.8 6-elastic-DOF spring mass model

Detail A: Motor angles; Detail B: Mass legends; Detail C: angle assignments.

For a free vibration system, the dynamic equation has the following form:

$$[M]_{6\times6}[\ddot{X}]_{6\times1} + [K]_{6\times6}[X]_{6\times1} = [0]_{6\times1} \tag{5.67}$$

where $[M]_{6\times6}$ is the inertia matrix, $[X]_{6\times1}$ is the displacement vector and $[K]$ is the stiffness matrix. The absolute motion coordinates are associated with masses and mass moment of inertia, therefore, the off-diagonal terms in the mass matrix $[M]$ are zeros, and the coordinates are coupled by the stiffness matrix $[K]$.

$$[M] = \begin{bmatrix} M_p & & & & & \\ & M_p & & & o & \\ & & I_p & & & \\ & & & I_{ta} & & \\ & o & & & I_{ta} & \\ & & & & & I_{ta} \end{bmatrix}, \quad [X] = \begin{bmatrix} x \\ y \\ \varphi_p \\ \theta_1 \\ \theta_2 \\ \theta_3 \end{bmatrix} \qquad (5.68)$$

According to Hooke's law, the system obeys the following equation:

$$[K]_{6\times6}[X]_{6\times1} = [F]_{6\times1} \qquad (5.69)$$

If the platform moves a single displacement unit in the x direction, the displacement vector will be:

$$[X]_{6\times1} = \begin{bmatrix} 1 & 0 & 0 & 0 & 0 & 0 \end{bmatrix}^T \qquad (5.70)$$

Substituting the displacement vector (5.70) into equation (5.69), the first column of the stiffness matrix will have the same value as the force vector which caused the unit displacement in the x direction [69]. A similar procedure can be applied to each of the remaining motion variables and the stiffness matrix of the system can thus be determined as follows:

$$\begin{bmatrix} \frac{3}{2}k_a & 0 & 0 & \frac{1}{2}k_t l & \frac{1}{2}k_t l & -k_t l \\ 0 & \frac{3}{2}k_a & 0 & \frac{\sqrt{3}}{2}k_t l & \frac{\sqrt{3}}{2}k_t l & 0 \\ 0 & 0 & 3(k_\beta + k_t r^2) & k_\beta + k_t lr & k_\beta + k_t lr & k_\beta + k_t lr \\ \frac{1}{2}k_t l & \frac{\sqrt{3}}{2}k_t l & k_\beta + k_t lr & k_\theta + k_\beta + k_t l^2 & 0 & 0 \\ \frac{1}{2}k_t l & \frac{\sqrt{3}}{2}k_t l & k_\beta + k_t lr & 0 & k_\theta + k_\beta + k_t l^2 & 0 \\ -k_t l & 0 & k_\beta + k_t lr & 0 & 0 & k_\theta + k_\beta + k_t l^2 \end{bmatrix} \qquad (5.71)$$

Where the distances l and r are defined in Figure 5.8: they are measured from the upper end (connecting to the platform) of the S-joint to the cold arm base of the motor and the platform center, respectively. The values for the terms in matrices (5.68) & (5.71) are:

$$k_a = 0.378 \ \mu N/\mu m,$$

$$k_\beta = 529 \ \mu N\mu m/rad,$$

$$k_t = 0.7 \ \mu N/\mu m,$$

$$k_\theta = 83320 \ \mu N \mu m/rad,$$

$$l = 334 \ \mu m,$$

$$r = 35 \ \mu m,$$

$$I_p = 21.59 \ (\mu g)(\mu m)^2,$$

$$I_{ta} = 927 \ (\mu g)(\mu m)^2,$$

$$M_p = 2.36 \ x \ 10^{-2} \ \mu g.$$

Substituting the parameter values to the system's mass and stiffness matrices then using Matlab's Eigenvalue function, the natural frequencies and the corresponding modes of the system were obtained as listed in Table 5.1:

Table 5.1 Simulated natural frequencies and modes.

Modes	1	2	3	4	5	6
Freq.	32kHz	32kHz	45kHz	72kHz	72kHz	87kHz
Description	In phase translation	In phase translation	In phase rotation	Out of phase translation	Out of phase translation	Out of phase rotation
x	−1.00	0.05	0	1.00	− 0.21	0
y	0	0.99	0	0	0.98	0
φ_p	0	0	− 0.98	0	0	0.99
θ_1	0.0009	0.0016	0.0983	0.0045	− 0.0086	0.0772
θ_2	0.0009	− 0.0017	0.0983	0.0045	0.0067	0.0772
θ_3	− 0.0019	0.0001	0.0983	− 0.0090	0.0019	0.0772

From Table 5.1, it can be observed that in modes 1, 2, 4 and 5 the platform translates in-plane with negligible rotation, while in modes 3 and 6 the platform rotates with negligible translation. As was found in Chapter 4, here two types of elastic modes are also identified: in-phase and out-of-phase. These terms refer to the relative motion of the platform and the motors. If the oscillating platform moves as if it was driven by the motors in a rigid body mode, the elastic mode is referred to as an in-phase mode, e.g., all

motors rotate simultaneously clockwise and the platform rotates counterclockwise. When the oscillating platform moves in the opposite direction as the rigid body motion would suggest: the elastic mode is described as out-of-phase. Mode-1 & mode-2 are in-phase translation modes; mode-4 & mode-5 are out-of-phase translation modes; mode-3 & mode-6 are in-phase and out-of-phase rotation modes, respectively. The modal vectors in Table 5.1 show that in the out-of-phase modes the coupling S-flexures are being deformed more significantly than in the in-phase modes. Some of the modes have repeated resonant frequencies because of the symmetry of the manipulator structure, e.g., mode-1 and mode-2 both have modal frequencies of 32 kHz.

5.8   Frequency Response Function (FRF)

For an n-DOF linear time-invariant system, the dynamic equation can be written in the following matrix form:

$$M\ddot{X}(t) + C\dot{X}(t) + KX(t) = f(t) \tag{5.72}$$

Where M, C, and K are $n \times n$ mass, damping, and stiffness matrices; $X(t)$ and $f(t)$ are $n \times 1$ displacement and exciting force vectors, respectively.

5.8.1   Mass-normalized Modes

The two elastic models studied above were undamped systems. To compare their frequency response with an experimental response, a proper damping model is needed. Once the analytical modes and the frequencies are obtained, the theoretical spectrum response can be calculated by [70]. This will be calculated here.

Symbols ω_r and ϕ_r denote the r-th natural frequency and normal mode of an undamped system, and they satisfy the following equation [70]:

$$M^{-1}K\phi_r = \varpi_r^2 \phi_r \tag{5.73}$$

An $n \times n$ modal matrix can be defined as

$$\Phi = [\phi_1, \phi_2, \cdots, \phi_n]. \tag{5.74}$$

This modal matrix satisfies the orthogonality conditions

$$\Phi^T M\Phi = diag[\overline{m}_1, \overline{m}_2, \cdots, \overline{m}_n];$$

$$\Phi^T K\Phi = diag[\overline{k}_1, \overline{k}_2, \cdots, \overline{k}_n].$$

(5.75)

here $diag[\overline{m}_1, \overline{m}_2, \cdots, \overline{m}_n]$ and $diag[\overline{k}_1, \overline{k}_2, \cdots, \overline{k}_n]$ are the modal-mass matrix and the modal-stiffness matrix, respectively. The normal modes can be mass-normalized using the modal-mass matrix as follows.

Let

$$\overline{\Phi} = \Phi diag[\frac{1}{\sqrt{\overline{m}_1}}, \frac{1}{\sqrt{\overline{m}_2}}, \cdots, \frac{1}{\sqrt{\overline{m}_n}}],$$

(5.76)

then

$$\overline{\Phi}' M \overline{\Phi} = I_{n \times n};$$

$$\overline{\Phi}' K \overline{\Phi} = diag[\varpi_1^2, \varpi_2^2, \cdots, \varpi_n^2],$$

(5.77)

here, $I_{n \times n}$ is a unit matrix, and $\overline{\Phi}'$ is the transposed matrix of $\overline{\Phi}$.

For the 3-DOF elastic model, the modal-mass matrix is

$$\begin{bmatrix} 3.6 & 0 & 0 \\ 0 & 3.6 & 0 \\ 0 & 0 & 5210 \end{bmatrix} \times 10^{-11}.$$

(5.78)

Using equation (5.76), the mass-normalized modal matrix of the system is calculated as

$$\begin{bmatrix} 166 & 0 & 0 \\ 0 & 166 & 0 \\ 0 & 0 & 4.4 \end{bmatrix} \times 10^3.$$

(5.79)

Using equation (5.75) and the normal modes from Table 5.1, the modal-mass matrix of the 6-DOF elastic model is

$$\begin{bmatrix} 2.9 & & & & & \\ & 2.9 & & & o & \\ & & 4780 & & & \\ & & & 14 & & \\ & o & & & 14 & \\ & & & & & 3780 \end{bmatrix} \times 10^{-11}. \tag{5.80}$$

Similarly, using equation (5.76), the corresponding mass-normalized modal matrix of the system is obtained

$$\begin{bmatrix} -1.873 & 0.092 & 0 & 0.854 & -0.181 & 0 \\ 0 & 1.870 & 0 & 0 & 0.835 & 0 \\ 0 & 0 & -0.045 & 0 & 0 & 0.051 \\ 0.002 & 0.003 & 0.004 & 0.004 & -0.007 & 0.004 \\ 0.002 & -0.003 & 0.004 & 0.004 & 0.006 & 0.004 \\ -0.004 & 0 & 0.004 & -0.008 & 0.002 & 0.004 \end{bmatrix} \times 10^5. \tag{5.81}$$

5.8.2 Damping of the systems

Assuming the systems are proportionally damped, the damping matrix C can be expressed by the mass matrix M and the stiffness matrix K:

$$C = \alpha \cdot M + \beta \cdot K, \tag{5.82}$$

where α and β are constant parameters.

The damping matrix of the system can be diagonalized by the system mass-normalized modes, i.e.,

$$\overline{\Phi}'C\overline{\Phi} = diag[2\zeta_1\varpi_1, \ 2\zeta_2\varpi_2, \cdots, \ 2\zeta_n\varpi_n], \tag{5.83}$$

$$\zeta_j = (\frac{\alpha}{\varpi_j} + \beta\varpi_j), j = 1, 2, \dots n \tag{5.84}$$

where ζ_j is called the j-th damping ratio.

From the reported research such as H. Zhang et al [71] and H. Fettig [72], for MEMS devices, the damping quality factor Q value varies from 6 to 18 resulting in 0.02 to 0.08 damping coefficient. Setting arbitrarily:

$$\alpha = 1.2 \times 10^3 \text{ and } \beta = 2 \times 10^{-8} \qquad (5.85)$$

the damping ratios for the 3-DOF model are calculated:

$$\zeta_1 = 0.0307,$$

$$\zeta_2 = 0.0307, \qquad (5.86)$$

$$\zeta_3 = 0.0226;$$

and the computed damping ratios for the 6-DOF model are:

$$\zeta_1 = 0.0318,$$

$$\zeta_2 = 0.0318,$$

$$\zeta_3 = 0.0241,$$

$$\qquad (5.87)$$

$$\zeta_4 = 0.0178,$$

$$\zeta_5 = 0.0178$$

$$\zeta_6 = 0.0165.$$

The damping ratios for the two models are close or within the range from 0.02 to 0.08, which means the two constant parameters α and β are reasonable for the system.

5.8.3   Frequency Response Function (FRF)[*]

The definition of the frequency response function matrix of a proportionally damped system is given by [70]

$$X(\varpi) = H(\varpi)F(\varpi) \qquad (5.88)$$

Where $X(\omega)$ is the Fourier transform of the displacement vector, $F(\omega)$ is the Fourier transform of the forcing vector, and $H(\omega)$ is the FRF matrix of the form:

$$H(\varpi) = [-M\varpi^2 + j\varpi C + K]^{-1}. \qquad (5.89)$$

---

[*] see [70] for more information.

The FRF relating motion of the i-th Degree of Freedom (DOF) and resulting from the force applied at the j-th DOF is given by

$$H_{ij}(\varpi) = \frac{X_i(\varpi)}{F_j(\varpi)} = \sum_{r=1}^{n} \frac{\bar{\phi}_{ir}\bar{\phi}_{jr}}{\varpi_r^2 - \varpi^2 + 2j\zeta_r\varpi_r\varpi}. \tag{5.90}$$

For an exciting force with specific frequency ω, the FRF matrix can be calculated from equation (5.90), and the corresponding displacements can be determined by equation (5.88). If a sweeping sinusoid wave force is applied to the DOF i, the theoretical response of the manipulator can be obtained through the FRF of the models.

For example, an exciting force $F = (0, 1, 0)$ is applied to the second DOF (the platform's motion in y direction) of the 3-DOF model with sweeping frequency from 20 kHz to 120 kHz, the corresponding displacement response of the second DOF in the frequency domain is demonstrated in Figure 5.9. Similarly, an exciting force $F = (0, 1, 0, 0, 0, 0)$ is applied to the second DOF of the 6-DOF model, the displacement response of the second DOF in the frequency domain is exhibited in Figure 5.10. Figure 5.10 showed that the manipulator has two resonances corresponding to two types of translation modes: in-phase and out-of-phase. The magnitude of the in-phase translation modes is about six times larger than the magnitude of the out-phase translation modes. The reason for that is that the out-of-phase modes occur at higher frequency.
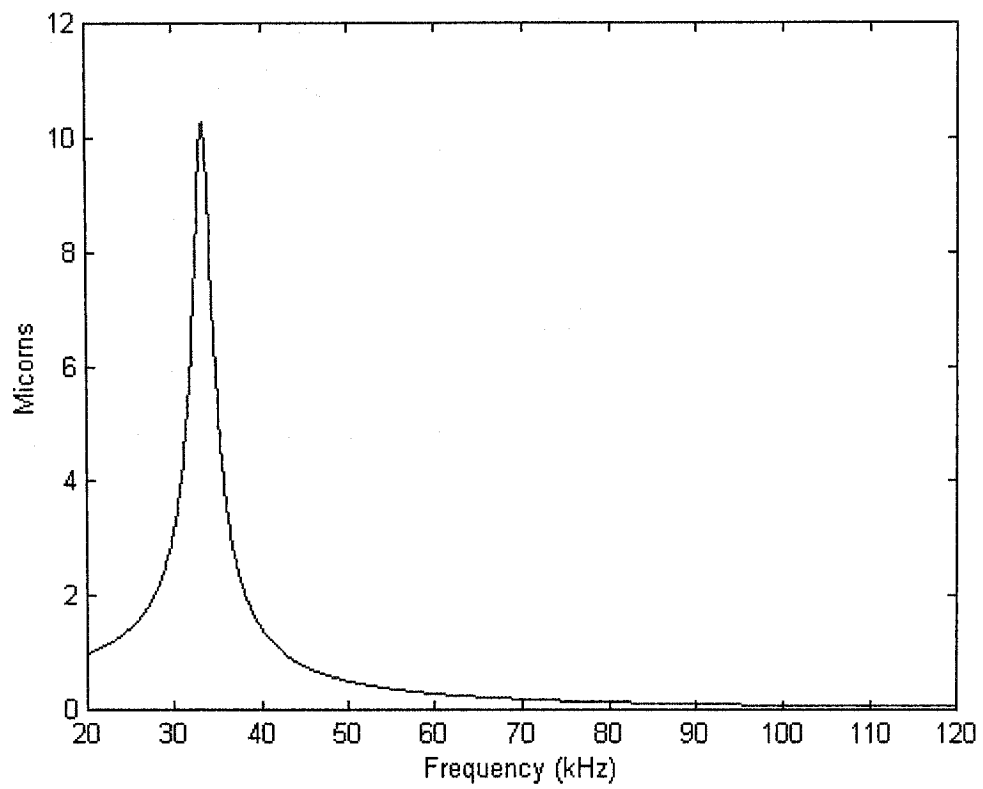
Figure 5.9 The simulated frequency response of the second DOF (y-axis) of the 3-DOF model excited by a force.
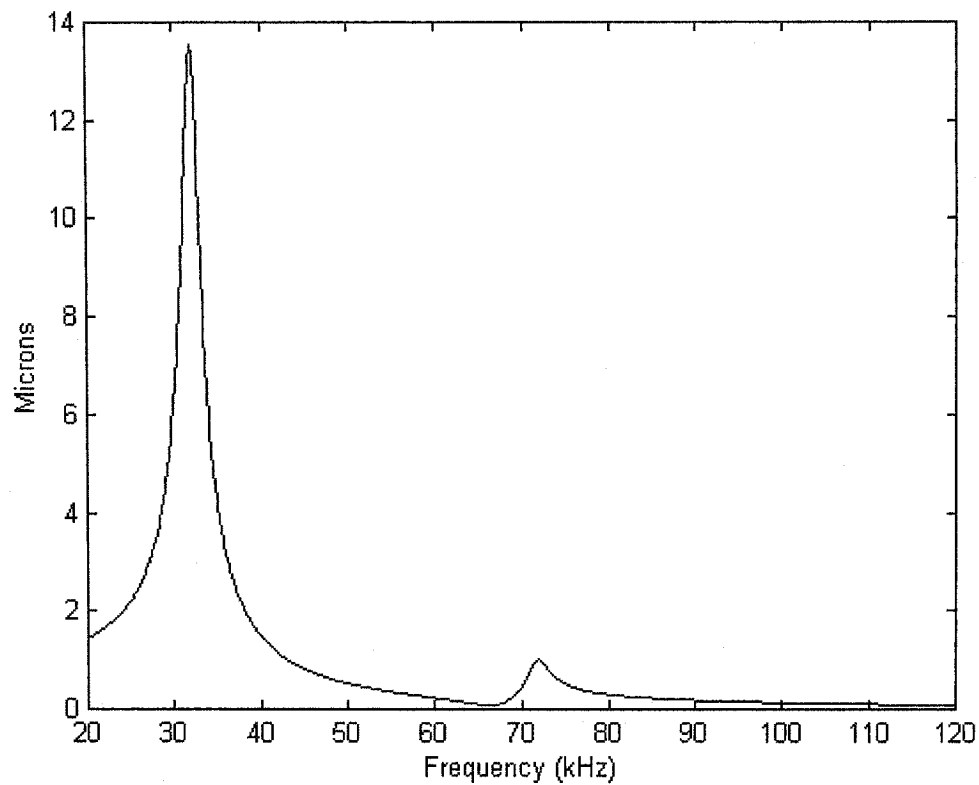
Figure 5.10 The simulated frequency response of the second DOF (y-axis)of the 6-DOF model excited by a force applied to the same DOF (see Figure 5.9).

5.9 Summary

This chapter investigated two kinds of spring-mass models for the manipulator: 3-DOF & 6-DOF. A frequency response function was computed for spectrum analysis. The results are similar to the FEM simulation described in Chapter 4. Two types of modes were identified: out-of-phase and in-phase. A discussion comparing the results is given following a description of the experiments in the next chapter, so that analytical, FEM, and experimental results can be compared together.

6 Comparison of simulated and experimental results

In this chapter, a comparison and analysis is given for the simulated results of the FEM, spring-mass models, and experimental results.

6.1 Experimental Setup

To detect the natural frequencies for MEMS devices, sensors for macro scale devices cannot be used because of their large size. In this research a non-contact laser probe and photodetector were used (Figure 6.1). This apparatus allowed measurements of in-plane resonant frequencies only. A red laser beam, emitted by a red diode, reaches a MEMS device through a beam splitter, red light reflector, and microscope. The laser beam is reflected back to a photodetector. The intensity of the reflected laser beam changes when the device moves. That change is detected by the photodector. The laser beam has a diameter of 10-40 μm (depending on the objective magnification) and it is stationary. The manipulator structure can be moved horizontally on an x/y table, allowing different sections of the manipulator to be exposed to the light of the laser beam. When the features of the oscillating manipulator cut through the laser beam, the reflectance properties change. The reflected laser light intensity is monitored by a photodetector located at the end of laser beam path. The measured response signal is roughly proportional to the amplitude of the modes and the resonance peaks can be clearly identified. In this study, the proportionality factor was not investigated. The described laser probe allows measurements of frequencies up to 200 kHz.
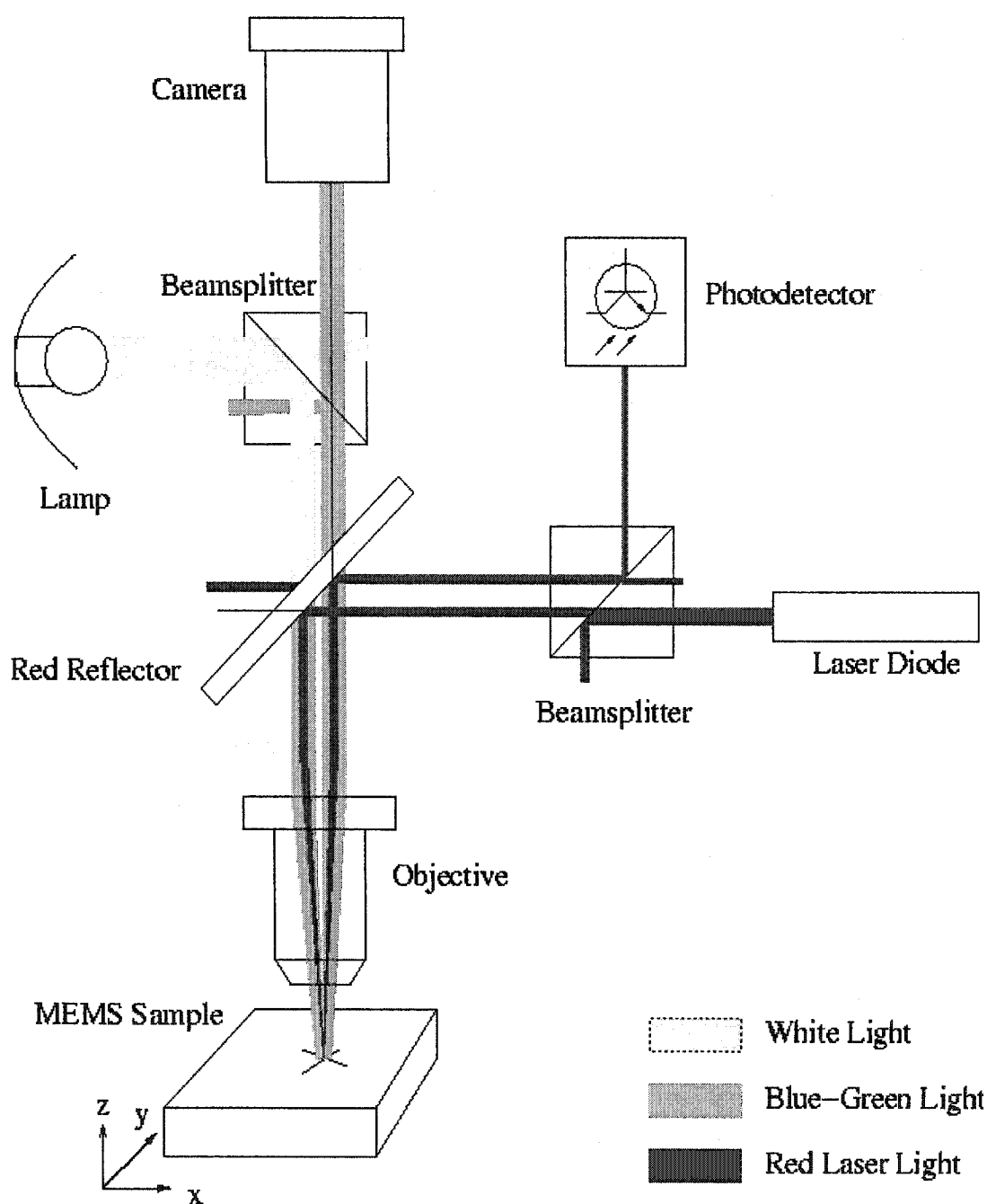
Figure 6.1 Schematic of laser probe microscope.

The response of the platform can be recorded and analyzed by a spectrum analyzer if the laser spot is set on the edge of the platform and a sinusoid voltage is applied to the motors. Figure 6.2 shows the manipulator's response when a sinusoid

voltage with magnitude of 0-5 volts (peak to peak: 5.0 volts + 2.5 volts DC offset) is applied to the actuator *3* (see Figure 5.8), and frequency is swept from 10 kHz to 110 kHz at sweeping speed of 16 kHz/s.
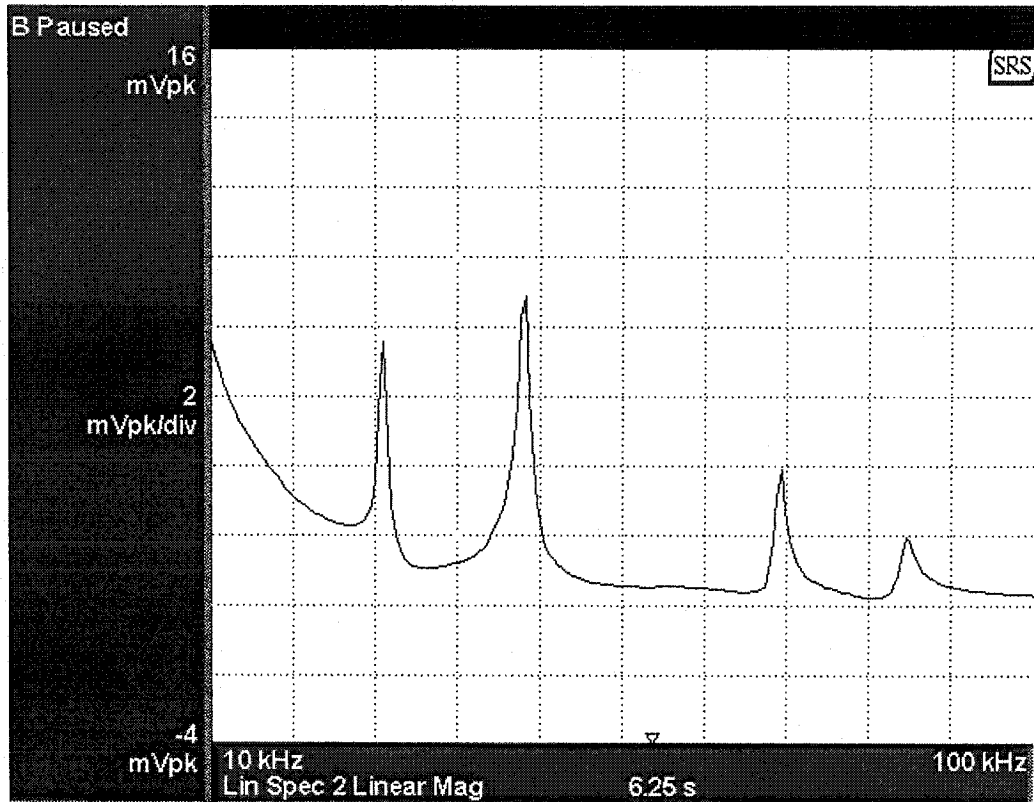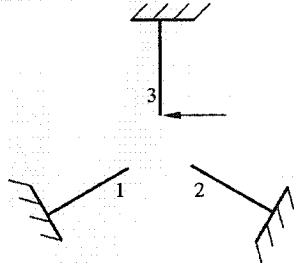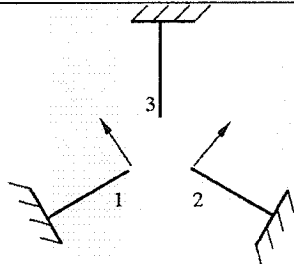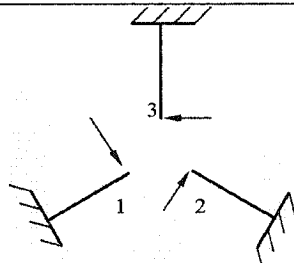
Figure 6.2 Spectrum response of the manipulator with a single actuator being excited (driving combination *3* in Table 6.1).

There are four resonant frequency peaks observed during the experiments. Four measured peaks from the experiments were at 28 kHz, 44 kHz, 72 kHz and 86 kHz.

When different driving combinations are used (see Table 6.1), the system produces different responses such as in Figures 6.3 & 6.4. More details and analysis are given in the following chapter.

Table 6.1 Different combination of exciting motors.

Label of the Driving Motors Combination	Driving Motor Layout (See Figure 5.8)
3	
12 (Translation)	
123 (Rotation)	
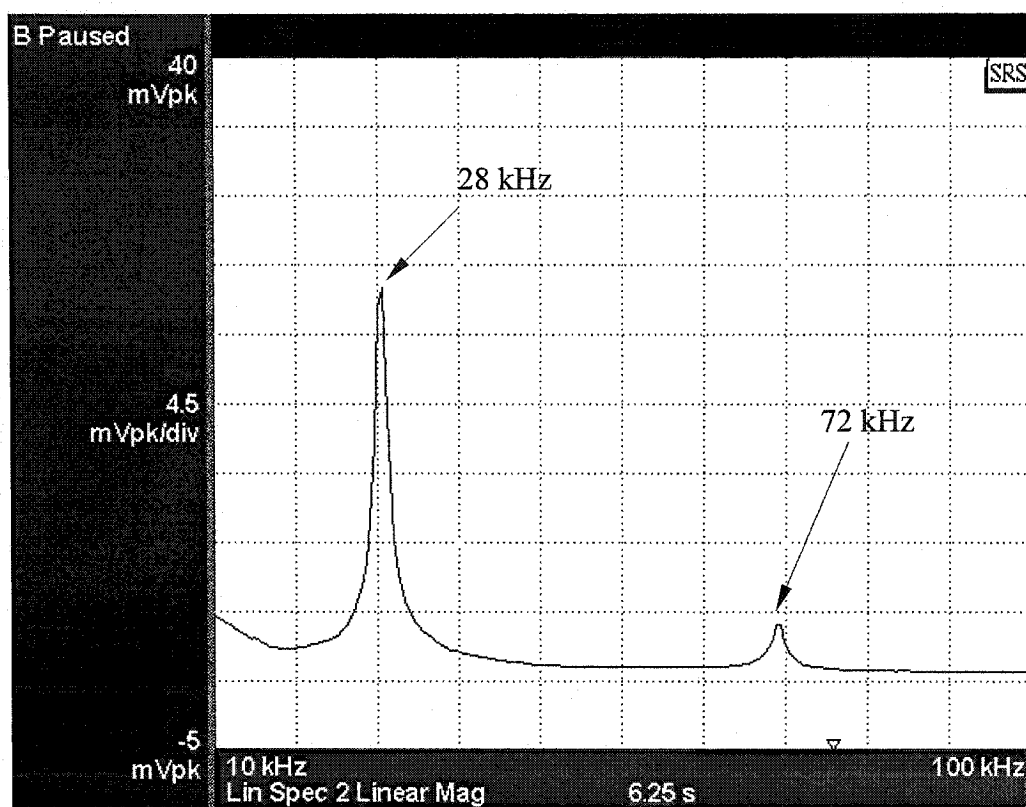
Figure 6.3 Spectrum response of the manipulator with two actuators active (translation driving combination 12 in Table 6.1).

Figure 6.4 Spectrum response of the manipulator with three actuators active (rotation driving combination *123* in Table 6.1).

6.2 Model Comparison

From the finite element model in Chapter 4, it was discovered that the manipulator had six in-plane modes (Out-of-plane motion will not be considered here since the spring-mass model used doesn't include the out-of-plane degree of freedom. Furthermore, the measurement system cannot observe the out-of-plane modes). These six modes and their modal frequencies agree with the simulated results from the 6-DOF spring-mass model. They have two pairs of repeated translation modes (mode-1 & mode-2, mode-4 & mode-5). Mode-1 & mode-2 are in-phase translation modes; mode-4 & mode-5 are out-of-phase translation modes. Mode-3 & mode-6 are in-phase and out-of-phase rotation modes. Since harmonic analysis for FEM is a time consuming work, the 6-DOF model was selected when comparing with the experimental testing.

Since the prototype can only be excited by its actuators, the simulated forces for 6-DOF spring-mass model are also applied to the corresponding degrees of freedom. Since only linear motion changes the density of the reflected laser beam, the rotation of the platform from the FRF is converted to linear motion by multiplying the radius of the platform r, (35 μm).

Three driving combinations were applied to the 6-DOF spring-mass model (see Table 6.1). Thus the driving force vectors for the 6-DOF spring-mass model are

$$F_3 \ = [0, \ 0, \ 0, \ 0, \ 0, \ 1]^T;$$
$$F_{12} = [0, \ 0, \ 0, \ 1, \ -1, \ 0]^T;$$
$$F_{123} = [0, \ 0, \ 0, \ 1, \ 1, \ 1]^T.$$

We know, from the analytical studies in Chapter 5, that the first and third peaks correspond to the pairs of translation modes (mode-1 & mode-2) at 32 kHz and (mode-4 & mode-5) at 72 kHz, respectively; the second and fourth peaks belong to the rotation modes: mode-3 at 45 kHz and mode-6 at 87 kHz, respectively (see Tables 5.1 and 6.2).
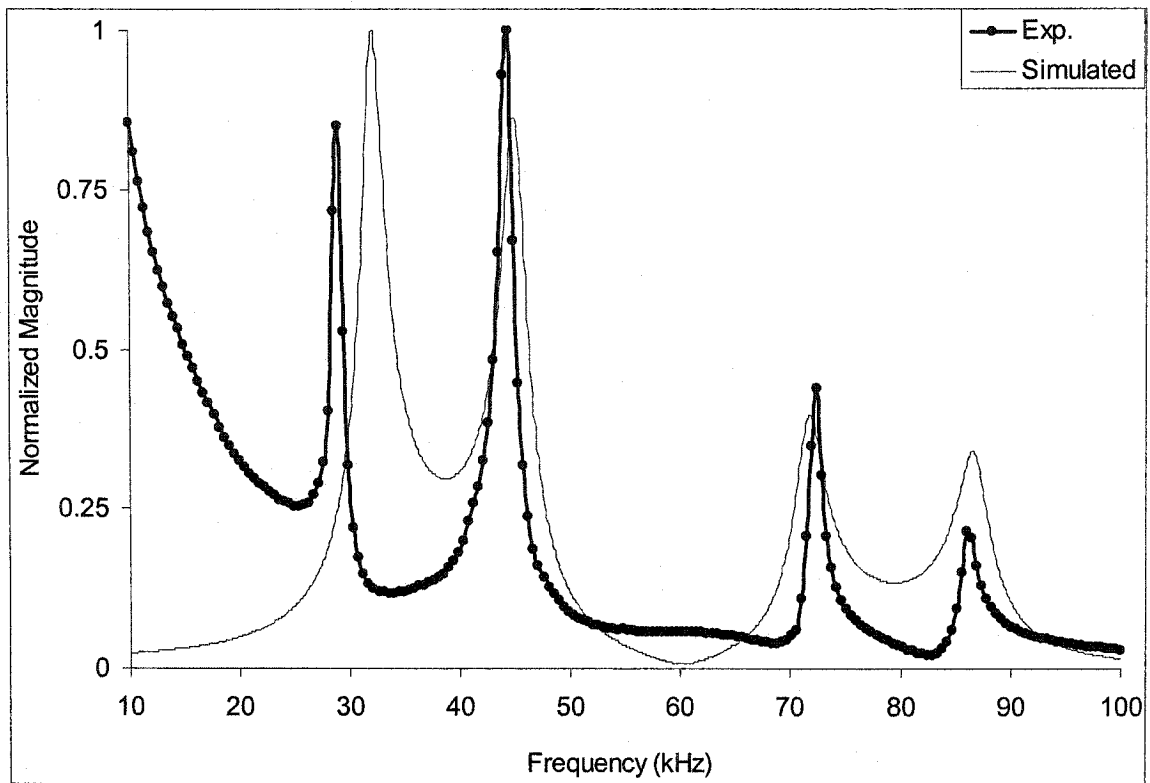
Figure 6.5 Frequency response spectrum generated by driving combination *3* from Table 6.1.

To verify that the four spectrum peaks in Figure 6.5 represent the simulated modes, another two driving combinations from Table 6.1 were applied to the prototype and the model. These two combinations are: 1) *12*-drive; 2) *123*-drive. Since the system has a tri-symmetric shape, the *12*-drive will excite the translation modes more intensely than the rotational modes. Therefore, the magnitudes of the spectrum peaks for the translation modes were expected to be higher than the rotational modes'. Figure 6.6 shows the results for the *12*-drive. There are only two spectrum peaks for the simulation results which represent translation modes at 34 kHz (mode-1 & mode-2) and at 73 kHz (mode-4 & mode-5). The rotation modes are not represented here at all. Similarly, the experiments revealed two peaks only as well, but at 28 kHz and 72 kHz. This confirms that the first and third spectrum peaks in Figure 6.5 represent the translation modes of the prototype.
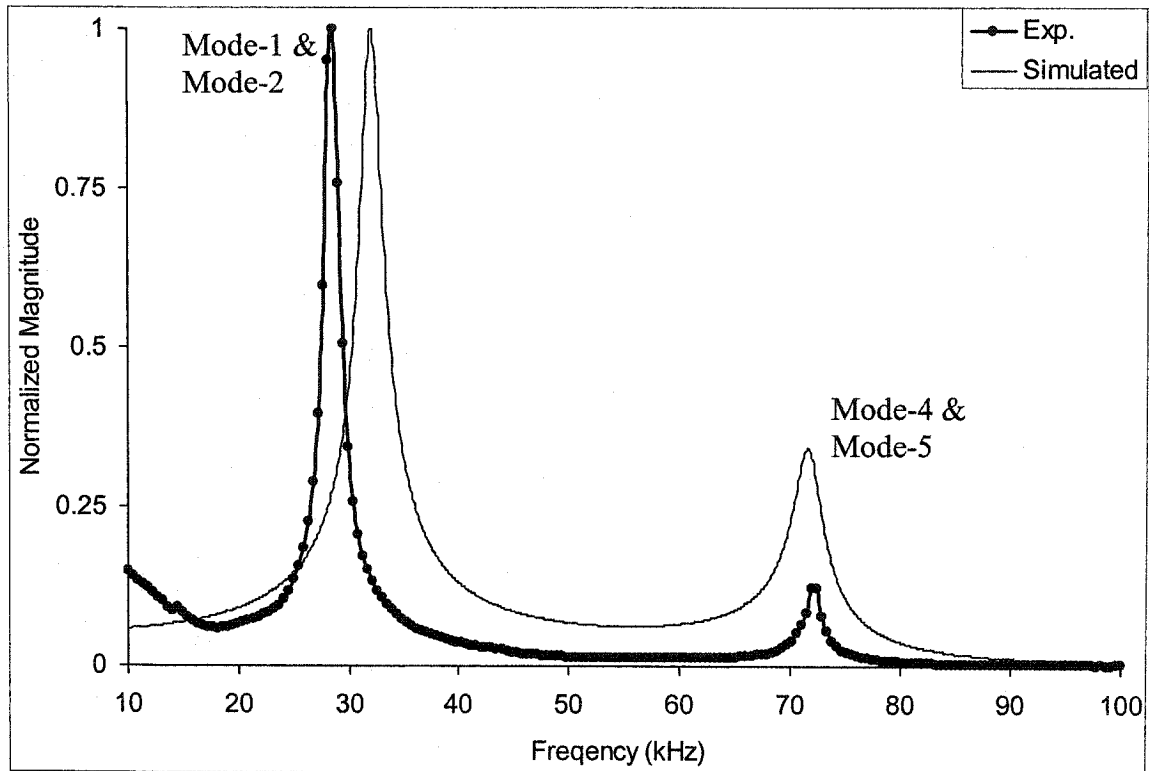
Figure 6.6 Frequency response spectrum excited by *12*-drive (translation modes only).

The driving combination *123* excites the rotational modes to a greater degree than the translational modes. Therefore, the magnitudes of the peaks for the rotational modes were expected to dominate the spectrum. Figure 6.7 shows the simulation and experiment results. There are only two spectrum peaks in the simulation results which represent rotational modes: at 48 kHz mode-3 and at 91 kHz mode-6. In the experimental results, even though there are four peaks, the two resonances at 44 kHz and 86 kHz dominate the spectrum. That confirms that the second and fourth spectrum peaks in Figure 6.5 represent the rotation modes and the first and the third peaks correspond to translation modes for the prototype.
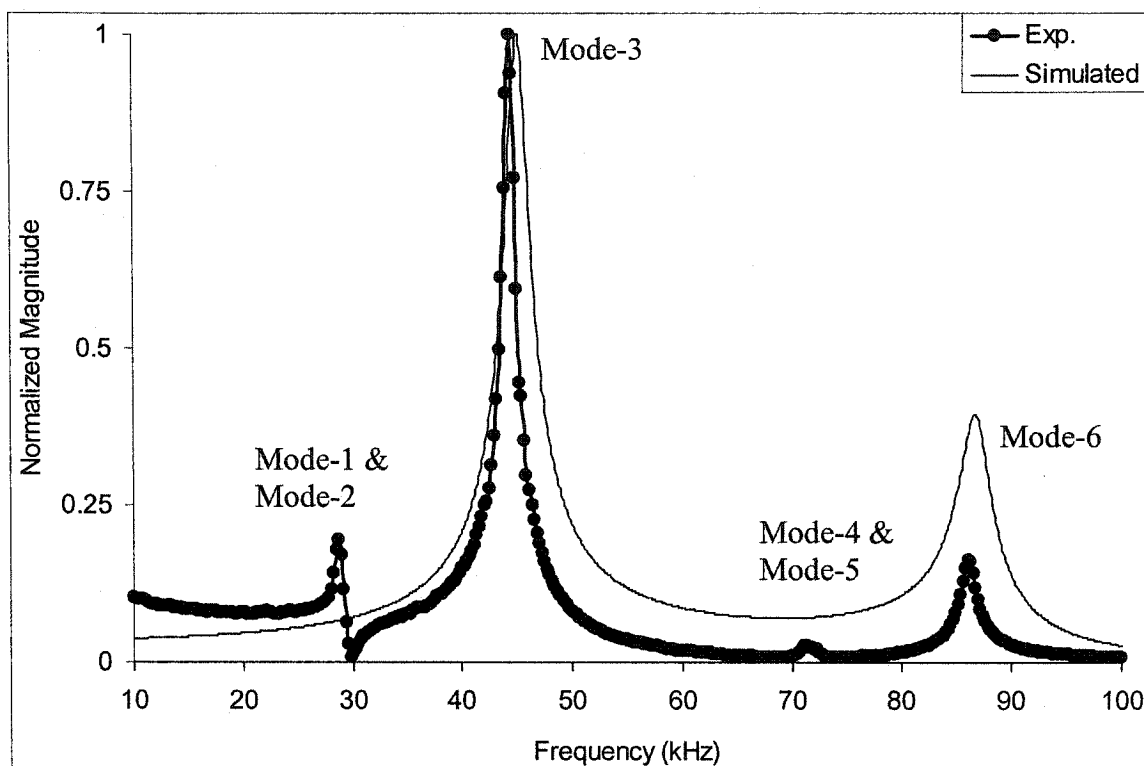
Figure 6.7 Frequency response spectrum excited by *123*-drive (rotation modes only).

The experimental resonant frequencies are lower than the results from the FEM and the spring – mass model (see Table 6.2). One reason for obtaining higher simulated frequencies is the imbedded assumption that the bases of the motors are fixed rigidly to the substrate. However, in reality, the fabricated anchors have a large but finite stiffness. Note also that the damping factors typically measured in MEMS ($\zeta = 0.1$, $Q = 5 \sim 20$) [10] decrease the resonant frequencies by less than 1%, thus damping is not a cause of the observed resonant frequency differences, in all likelihood.

Table 6.2 Experimental and simulated modal frequencies.

Modes	Frequency (kHz)			
	Experimental	Simulated		
	Prototype	3-DOF	6-DOF	FEM
1	28	33	32	38
2	28	33	32	38
3	44	49	45	50
4	72	-	72	83
5	72	-	72	83
6	86	-	87	91

Table 6.3 The relative errors of simulated results.

Modes	Relative Errors[*] (%)		
	3-DOF	6-DOF	FEM
1	18	14	36
2	18	14	36
3	11	2	14
4	-	0	15
5	-	0	15
6	-	1	6

* (Simulated – Exp.) / Exp. x 100%

6.3 Conclusion

The three models (3-DOF, 6-DOF, FEM) have successfully simulated the dynamic behavior of the planar manipulator. The analysis provides vibration modes and resonance frequencies for the system. The analytical results were verified by experiments for various excitation loads. The relative errors between the predicted and experimental natural frequencies are listed in Table 6.3. The 6-DOF model has the best prediction with less than 5% errors except for the lowest translation modes (14%). The FEM has the highest errors but it provides information about the out-of-plane modes.

7 1-DOF Device Control

This chapter explores control methods of a MEMS device with a single DOF. Optical hardware and software are employed to obtain feedback.

7.1 Introduction

Feedback controls on the MEMS devices are challenging because of the small sizes of MEMS devices. However advances in current electronic technology may make integrated feedback sensors possible in MEMS devices. However, this would complicate MEMS design. Another approach is to use high speed computer and vision processing software to obtain feedback control. Because the MEMS studied are planar, we used vision-based motion monitoring as a practical means for feedback control.

The hardware of the feedback loop consisted mainly of a microscope, a camera, and a computer (see Figure 7.1).
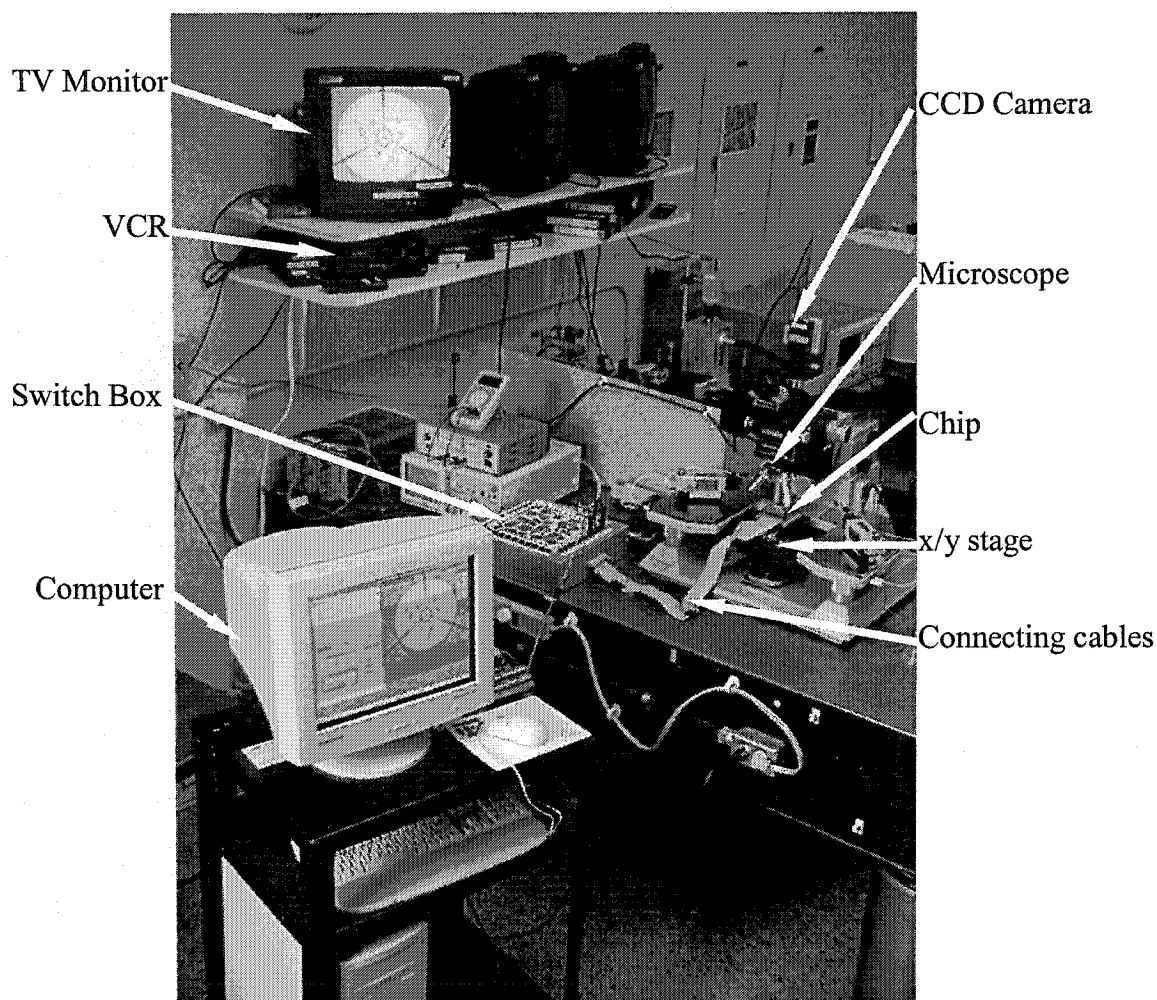
Figure 7.1 Feedback control loop setup.

The MicroZoom probe station was the main device for experiments. It was located on an air table to damp vibrations. An x/y stage, CCD camera and 3 different power microscope objectives were installed on the probe station. A 40 pin DIP socket holding the MEMS devices is attached to the x/y stage. The camera can take 30 pictures per second, i.e. the upper working frequency of the camera is 30 Hz. The images taken by the camera are sent to a control computer and a TV monitor equipped with a VCR. Basic setups of the computer are: 256 Mbytes memory, Pentium III 800 MHz CPU. This control computer has two *NI-DAQ PCI-6035E* boards and one *NI-IMAQ PCI* 1409 board. The *NI-DAQ* boards perform data acquisition; they can also output two separate analog

signals. In the studied research, the *NI-DAQ* boards work as two DAC's (Digital to Analog Converters) providing analog voltages (from -10 volts to 10 volts). The *IMAQ* PCI-1409 is a high-accuracy, monochrome video acquisition board. It features a 10-bit Analog-to-Digital Converter (ADC) that converts video signals to digital formats. The 40-pin switch box facilitates easy connections of the control circuit to the MEMS devices on the chip. The switch box is equipped with a copy of the chip layout of easy orientation of the experimenter.
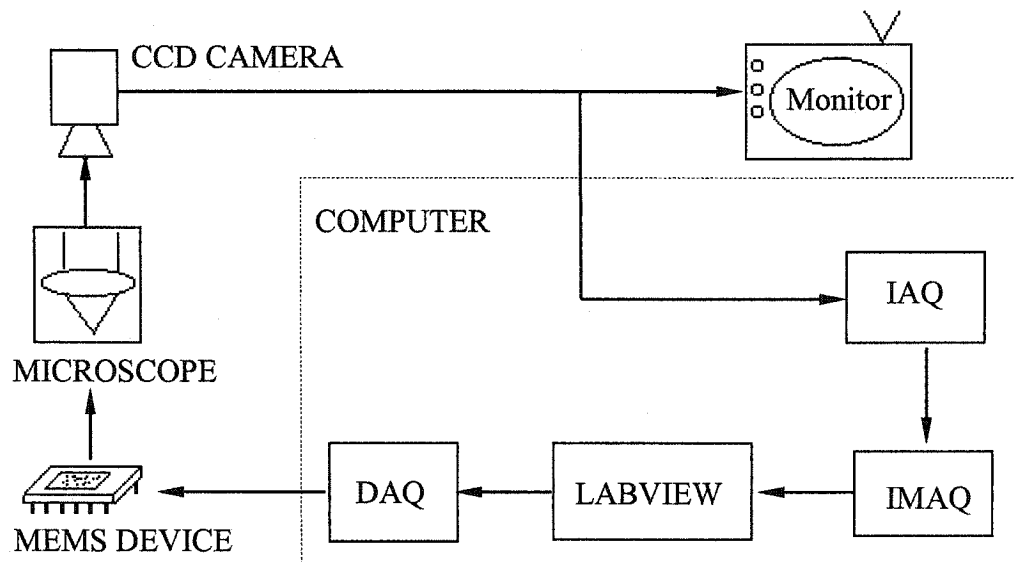
Figure 7.2 Flowchart of feedback control.

Figure 7.2 shows the flowchart of the feedback control loop. IAQ in figure is the *IMAQ PCI*-1409 card obtaining and digitalizing pictures from the CCD camera. The control program is based on the National Instrument Software *LabView*. When the program begins control, it first takes a picture with the neutral position of the device. Once a pattern and a Region Of Interest (ROI) are manually selected within the picture, the program follows the motion of the platform within the ROI. The measurement results

are recorded. The motion response of the device is obtained by continuously taking and measuring pictures and comparing the results to the first record.

In this chapter, two methods are demonstrated that show how 1-DOF devices were automatically controlled. A control scheme is also developed to keep the device stable after it moves to the appointed position.

For a standard Thermal Actuator (sTA), its response time measured by Hickey is about 300 μs [74]. Also, he pointed out that the sTA's break frequency, defined as the frequency at which the amplitude falls off by ~1%, is at about 200 Hz; the cut-off frequency, defined as the frequency at which the actuator becomes static to a sinusoid input signal, is at about 60 kHz. The highest control frequency of the optical feedback loop that author used was about 2 Hz, which is far below the limiting 200 Hz. Therefore, the sTA behaved as a kinematic system with no inertia.

A control scheme with PI controller shown in Figure 7.3 was applied to a sTA. The parameters k_p, k_i, are arbitrarily set to 0.1 and 0.001, respectively. An integral block with unit coefficient is used to accumulate the previous voltages. For example, the sTA is set to move 4 μm and maintain that position. The corresponding experimental result is demonstrated in Figure 7.4.
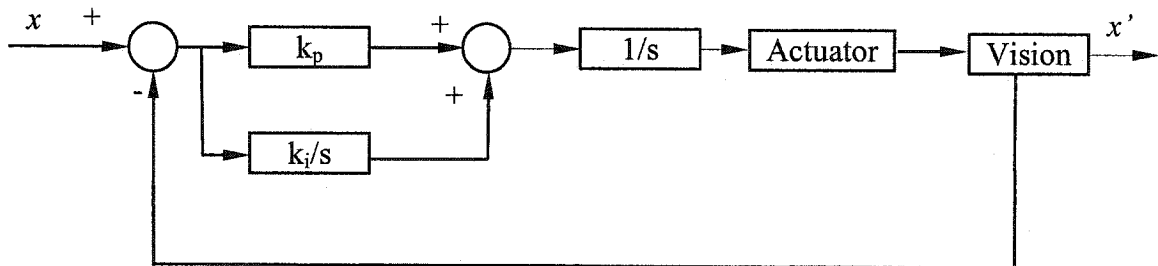
Figure 7.3 Control scheme with a PI controller.
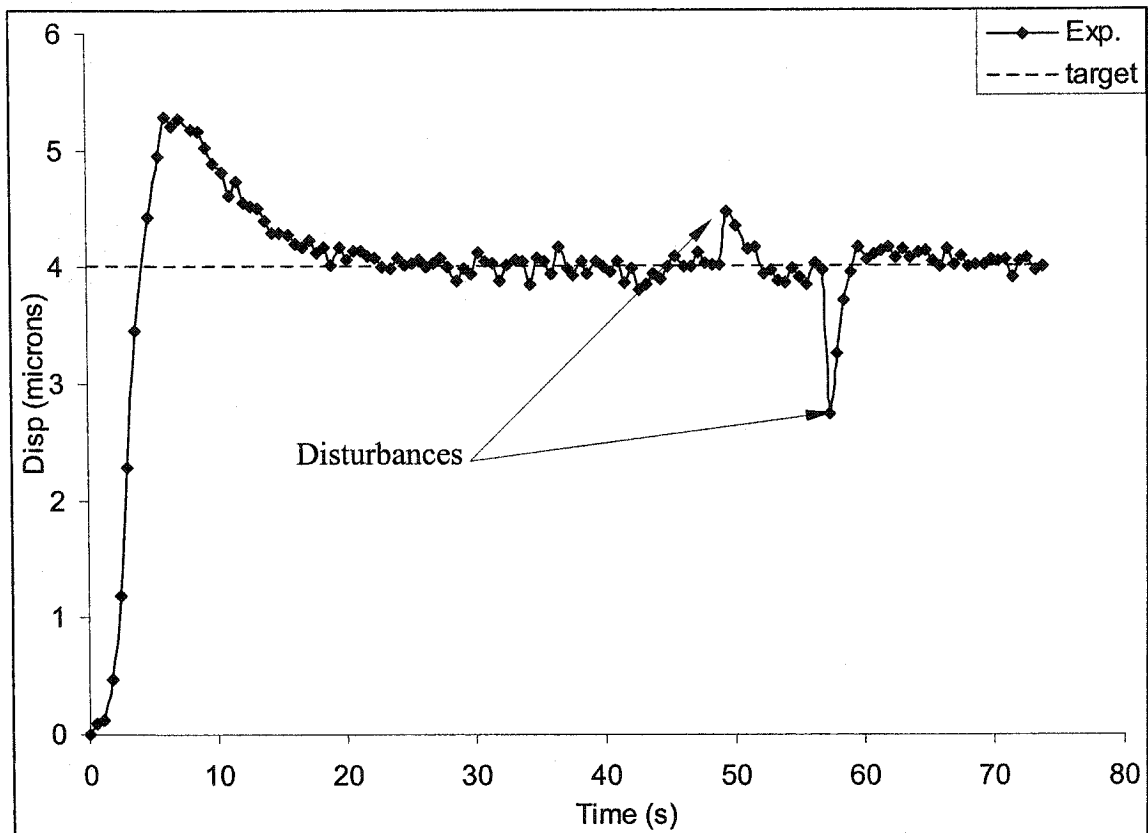
Figure 7.4 Response of a sTA under control of a PI controller.

Figure 7.4 shows that the response has approximately 30% overshoot, and it takes 20 seconds to reach steady state. The steady state error is approximately 0.2 micron. Also, it demonstrates that the system can go back to steady state after it is disturbed. Instead of using the above classic PI controller, two optimum controllers were also developed in the research which could reach steady state faster.

7.2   Success / Failure controller

In order to keep a MEMS device free of plastic deformation, driving voltages have to keep in a certain range. For example, for a sTA, the highest voltage is set to 6.5 volts. Knowing the range of the input variable, the Success / Failure (SF) controller [73] is applicable for most 1-DOF MEMS devices and normally works well.

The distance between the target position and current position is defined as an objective function $f(x)$. The variable x here is the voltage applied on the controlled device and it varies within the range of $[a, b]$. The SF controller can be described as a procedure of solving a mathematical minimum value problem for

$$\min_{a \le x \le b} f(x) \tag{7.2}$$

The method is explained as applied to the MEMS device. The following steps are used to drive the device to the target position x^*:

1) Set all output voltages to zero and take a picture with the CCD camera; select an area in the picture as a Pattern to be followed (Region of Interest); and measure the position of the Pattern and record it as the start position (neutral position);

2) Set the target position; the searching step h and the precision ε (greater than zero);

3) Set an initial value x_0 for the variable x, take a picture and measure the position of the pattern. Calculate $f(x_0)$, which is the value of the target position x^* minus current position x_0;

4) Set the next value of x: $x_1 = x_0 + h$;

5) Similar to step 3, get $f(x_1)$;

If $f(x_1)$ and $f(x_0)$ both are positive or negative and the absolute value of $f(x_0)$ is bigger than the absolute value of the $f(x_1)$, then the voltage x_1 is successful result (x_1 is closer to x^* than x_0 was); set $x_0 =: x_1$; $f(x_0) =: f(x_1)$; $h =: 2h$; go to step 4.

Otherwise, check the absolute value of h. If $|h| \ge \varepsilon$, then $h = - \frac{1}{4} h$, go to step 4. If $|h| \le \varepsilon$, then go to step 6.

6) Stop the program and assign x_0 to the final optimum output voltage.

Figure 7.5 shows the flowchart of an SF controller for 1-DOF device:
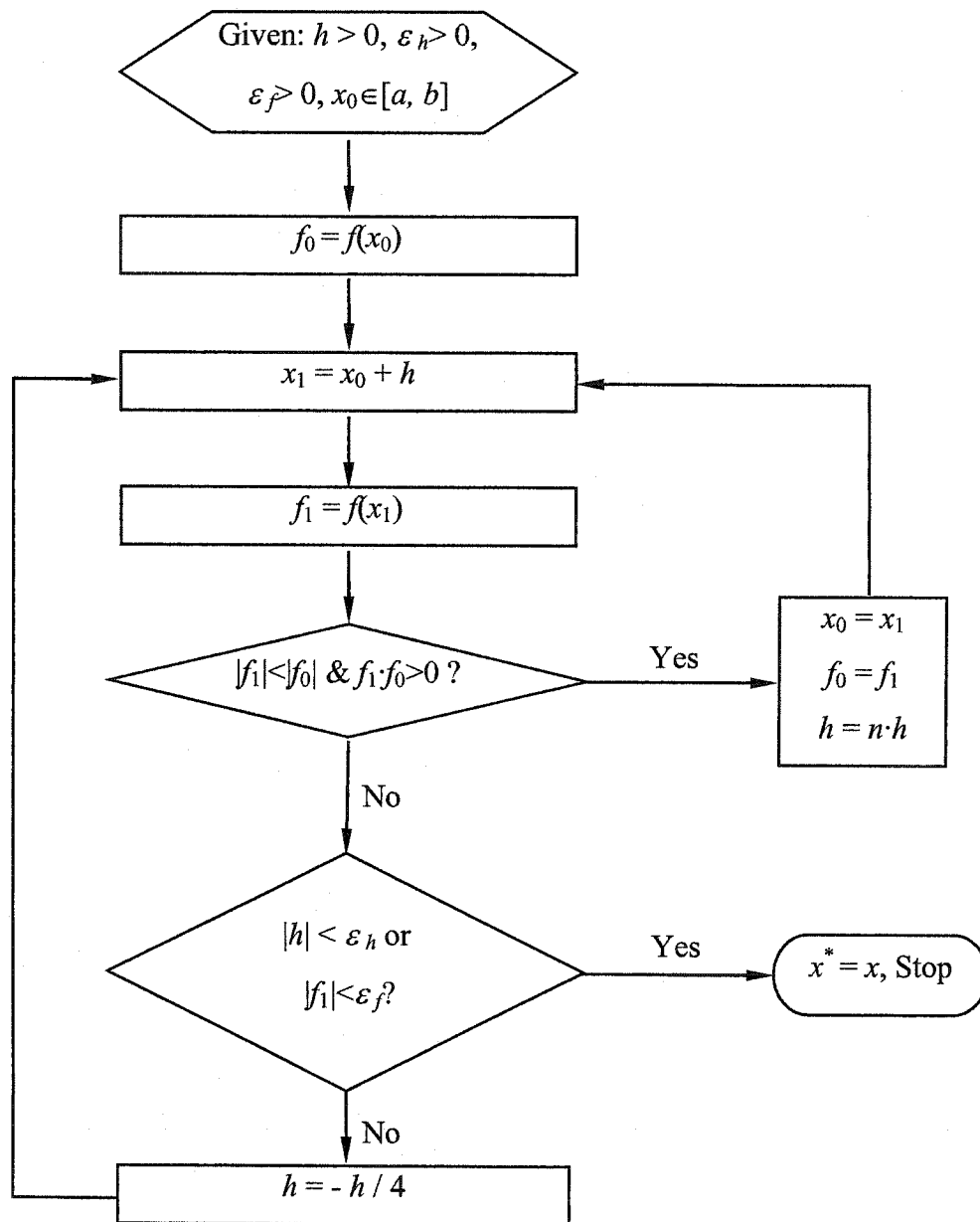
Figure 7.5 Flow chart of Success/Failure Controller.

The number n in Figure 7.5 is the multiplying factor for the search step h. According to the author's experience, h should not be too small, i.e., no less than 20% of the span of the searching range (b-a). The precision variables ε_h and ε_f are determined by the available experimental setup. The DAQ board (PCI-6040E, formerly called PCI-MIO-16E-4) features a 12-bit digital-to-analog converter (DAC). The corresponding

voltage varies from -10v to 10v resulting in a resolution of 0.005 volts per bit. The precision parameter ε_h was set to 0.05 volts. The precision ε_f is the criterion for the objective function measuring the distance. This criterion is related to the power of the microscope. If the conversion scale from pixel to micron is 3:1, then the half pixel width, which is 0.15 microns, is set as the criterion. When subpixel accuracy is selected during IMAQ pattern matching, the resolution is even higher.

For a demonstration, the SF controller was applied to two 1-DOF devices. One is a sTA (on TA1 chip) which is a basic device used in many other devices. The other one is a T-shaped amplifier (T-amp) driven by two cooperating delta actuators (see Figure 7.7) which is used as a motor in a manipulator (on CM3 chip). The task set for the sTA is that the end of the cold arm moves 2.67 μm. The task set for the T-amp is that the end of pointer moves 10 μm. The initial voltage x_0 and search setup h are set to $x_0 = 0$ and $h = 2$ volts. To check the response, 1.5 and 2 are assigned to n. In this case, it was observed that the criterion $\varepsilon_1 < 0.05$ volts was always satisfied early (less than 10 seconds).
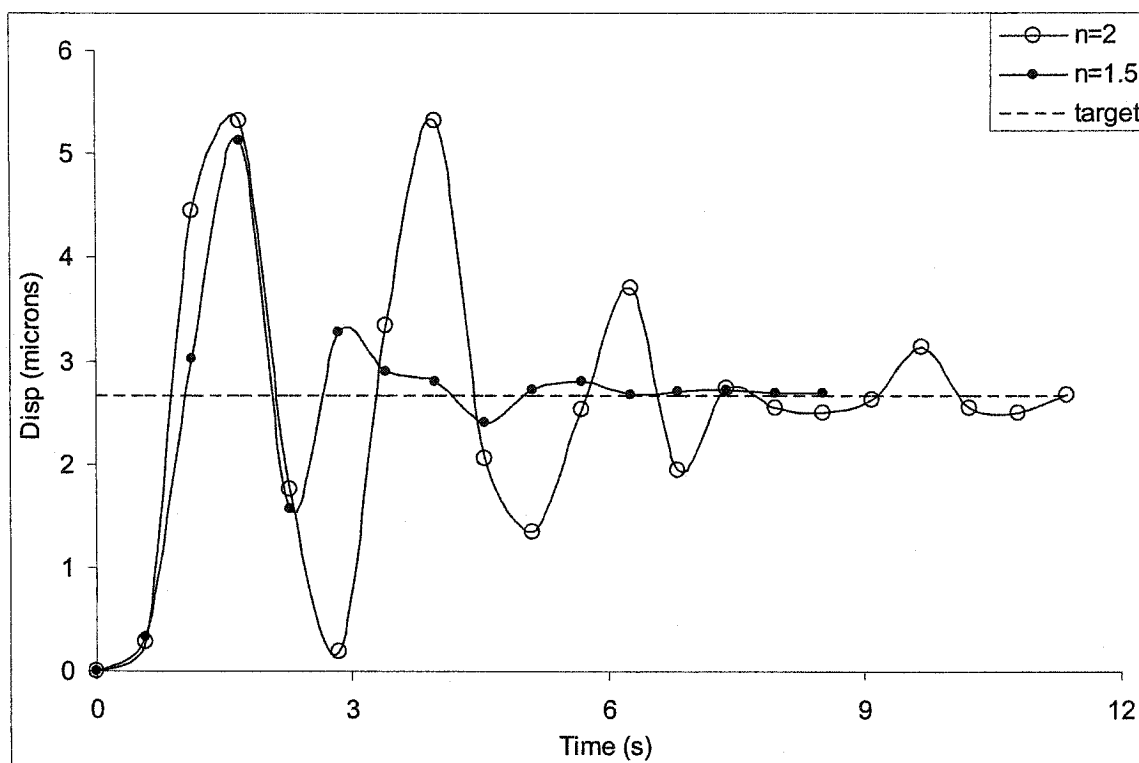
Figure 7.6 Response of a sTA controlled by a SF algorithm.

Figure 7.6 shows the responses of a sTA controlled by a SF controller.
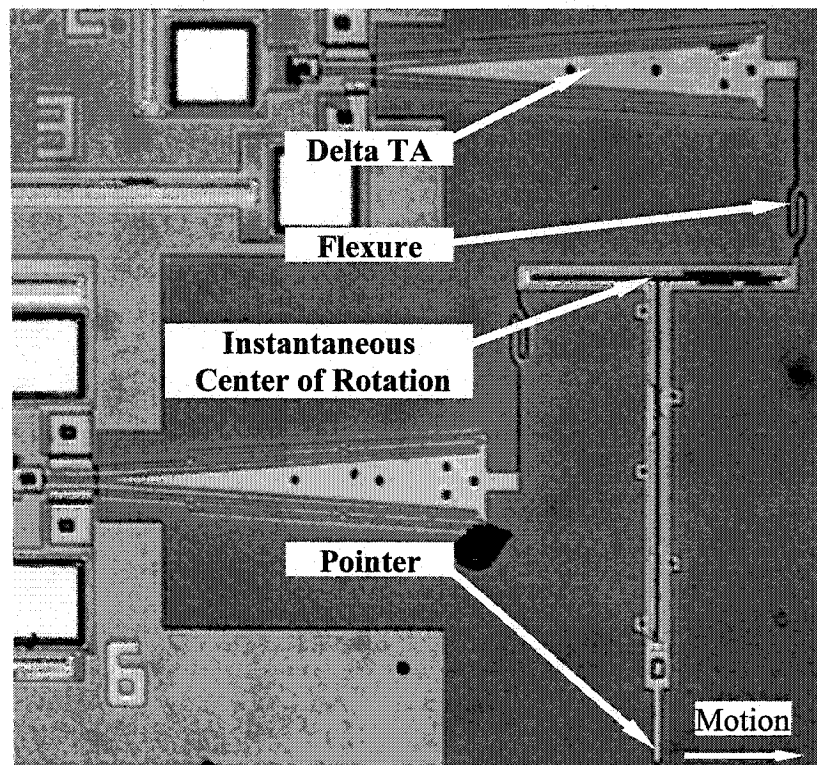
Figure 7.7 T-amplifier driven by two delta actuators on CM3 chip.

The T-amplifier shown in Figure 7.7 has two delta actuators. These delta actuators were connected to the T-shaped rigid structure by flexures. Driven in the opposite directions, these actuators rotate the T-shaped structure about its instantaneous center of rotation. The pointer in Figure 7.7 is the output part. When connected to other devices, the T-amplifier works as a rotary motor.
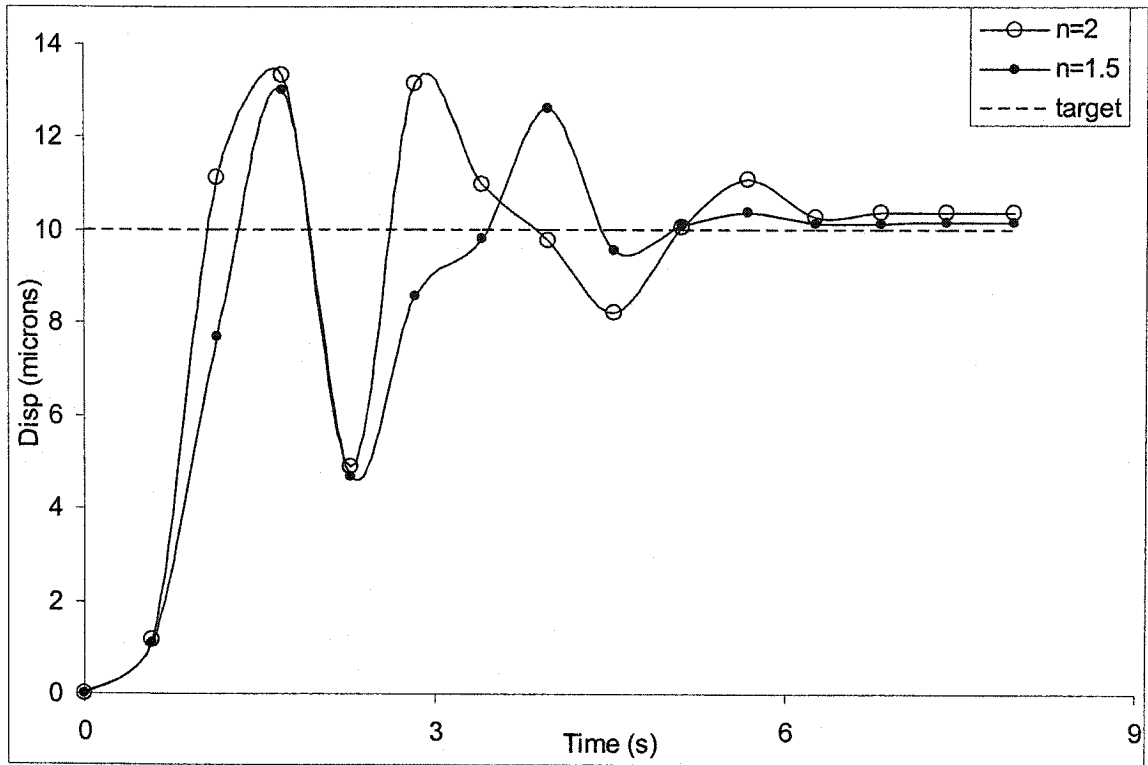
Figure 7.8 Response of the T-amplifier.

Figure 7.8 shows the responses of the T-amplifier controlled by the SF controller with $n = 1.5$ & 2. Figures 7.6 and 7.8 exhibited that the multiplication factor n affects the control property of the SF controller and when n=1.5 the performance of the controller was better. Also they show that it takes less than 10 seconds for the devices to reach the desired positions.

7.3 Golden Division controller

The Golden division controller is another optimal controller applicable to MEMS devices for which the relation between input voltages and output motion is not available. The same as in the SF controller, the distance between the target position and current positions is defined as an objective function $f(x)$; the variable x here is the voltage applied to the controlled devices; it is varying within the range of $[a_1, b_1]$. The main principle is

searching the optimum solution by concentrating the searching area. The details are listed as follows:

1) given: lower limit of x is a_1, upper limit of x is b_1, minimum span of the search range (precision) ε, target distance s, division parameter α (= 0.618);

2) Measure and record the neutral position $p(0)$, calculate the target position $p_t = p(0) + s$;

3) $\lambda_1 = a_1 + (1-\alpha)(b_1 - a_1)$; apply voltage at amount of λ_1; measure the position $p(\lambda_1)$ and calculate the $f(\lambda_1) = p_t - p(\lambda_1)$;

4) $\mu_1 = a_1 + \alpha(b_1 - a_1)$, apply voltage at amount of μ_1 and measure the position $p(\mu_1)$ and calculate $f(\mu_1) = p_t - p(\mu_1)$; counter $k = 1$;

5) if $b_k - a_k < \varepsilon$, then the optimum solution $x^* \in [a_k, b_k]$ and $x^* \approx 0.5(b_k + a_k)$, stop the searching; otherwise, if $f(\lambda_1) > f(\mu_1)$, go to step 6), or if $f(\lambda_1) \leq f(\mu_1)$, go to step 7).

6) $a_{k+1} = \lambda_k$, $b_{k+1} = b_k$; $\lambda_{k+1} = \mu_k$, $f(\lambda_{k+1}) = f(\mu_k)$; $\mu_{k+1} = a_{k+1} + \alpha(b_{k+1} - a_{k+1})$, apply voltage at amount of μ_{k+1} and measure the position $p(\mu_{k+1})$ and calculate $f(\mu_{k+1}) = p_t - p(\mu_{k+1})$; go to step 8).

7) $a_{k+1} = a_k$, $b_{k+1} = \mu_k$; $\mu_{k+1} = \lambda_k$, $f(\mu_{k+1}) = f(\lambda_k)$; $\lambda_{k+1} = a_{k+1} + (1-\alpha)(b_{k+1} - a_{k+1})$, apply voltage at amount of λ_{k+1} and measure the position $p(\lambda_{k+1})$ and calculate $f(\lambda_{k+1}) = p_t - p(\lambda_{k+1})$; go to step 8).

8) $k = k + 1$; go to step 5).

This controller was applied to the two control objects used in Section 7.2. The sTA was desired to move 4 microns, and the T-amp was expected to move 10 microns. The initial voltage searching ranges for the sTA and the T-amp were [0, 6.5v] & [0, 7.5v], respectively; the minimum span of the voltage searching range (precision) was set to 0.1 volts.

Figure 7.9 shows the response of the sTA moving 4 μm under the guidance of the GD and the SF (n=2) controller. The final errors of the GD and the SF controllers were about 0.2 μm and 0.4 μm, respectively.
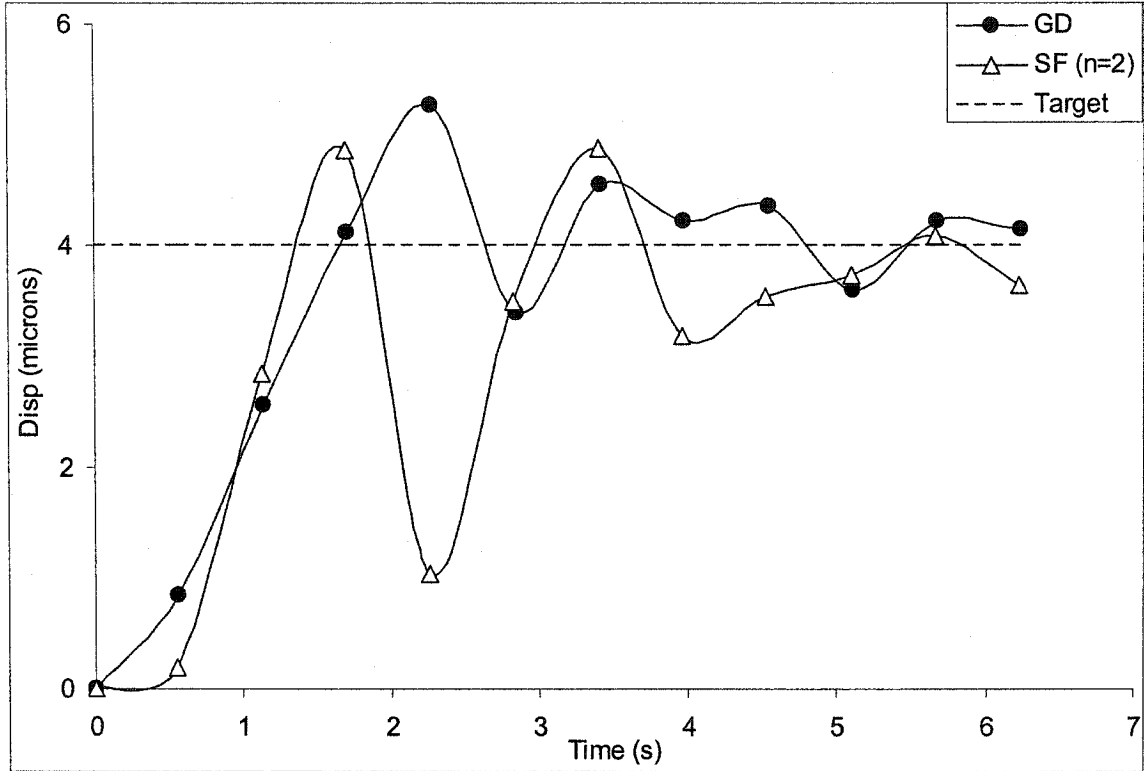
Figure 7.9 Response of the sTA under control of the GD controller.

Figure 7.10 displays the response of the T-amp moving 10 μm under guidance of the GD & the SF (n=1.5) controllers. The final errors of both controllers are 0.4 μm. Figure 7.11 shows the voltages determined by the GD controller for the sTA and T-amp. For both objects, it takes less than 10 seconds to reach the optimization goal. Figures 7.9 & 7.10 also exhibit that GD and SF controllers have a similar performance. Compared to the PI controlled results in Figure 7.4, the GD & SF controllers can reach the target point within less than half the time needed by the single PI controller. At the micro scale, the inertia force is not a dominant force any more. Furthermore, the speed of a MEMS device

responding to a step input is high and far beyond the controller speed. Therefore, a PID controller is not expected to be faster than a PI controller. Initial trials confirmed this observation.
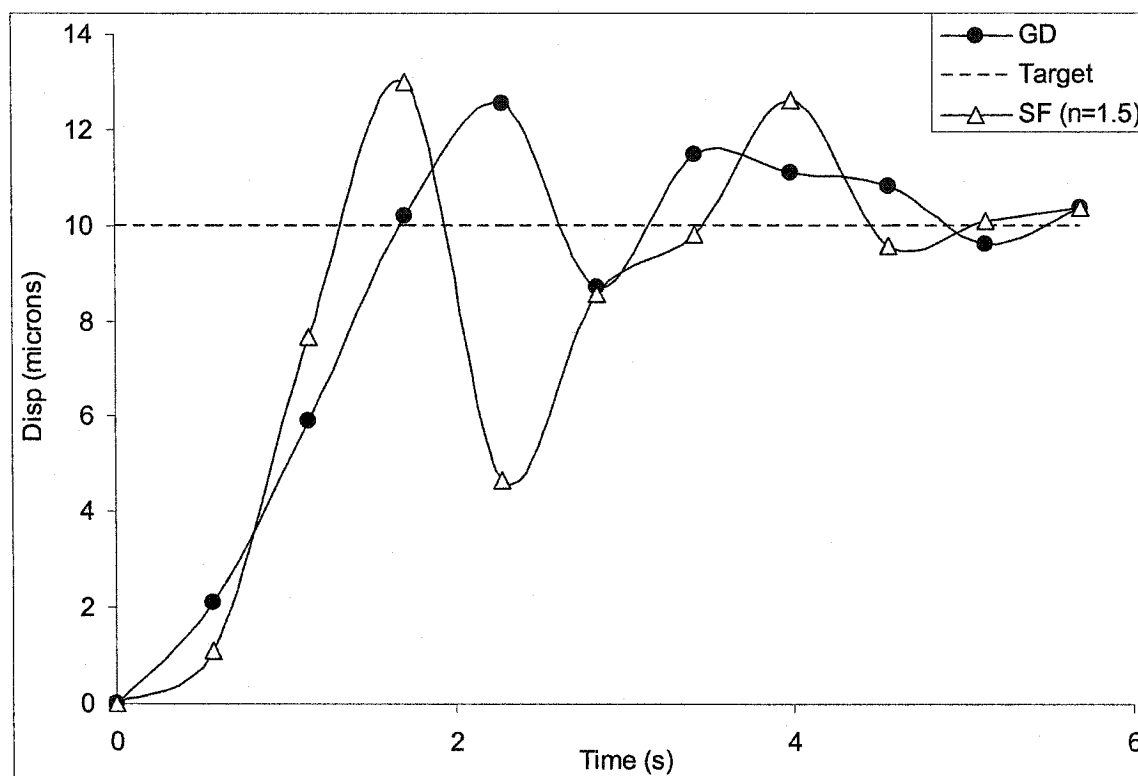
Figure 7.10 Response of T-amp under control of the GD & SF controllers.
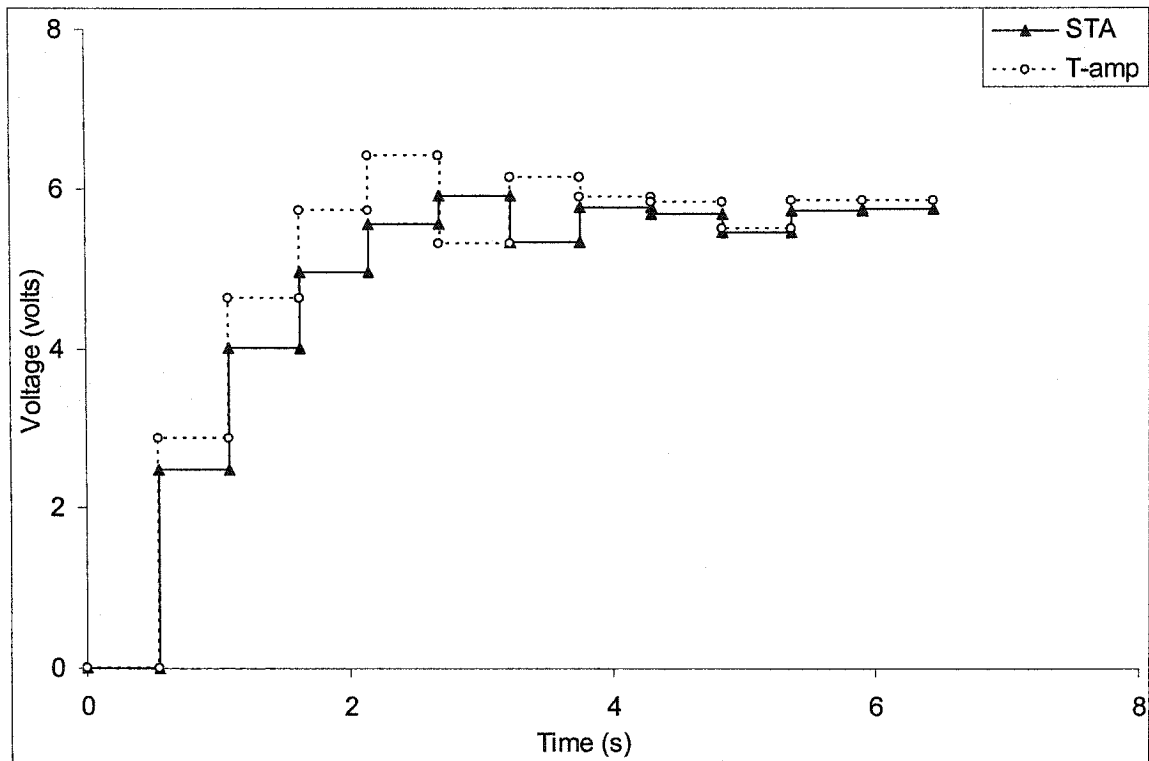
Figure 7.11 Voltages applied to the sTA and the T-amp.

7.4 PI compensator for disturbances

The two controllers SF & GD studied above provide a way to drive any 1-DOF devices to a specific distance faster than the classic PI controller. Furthermore, users do not need to tune the control parameters. However, the shortcoming of these two controllers is that they do not have the ability to control the disturbance after the optimum solution is found. To compensate for this disadvantage, a mixed controller comprised of a PI compensator and either a GD controller or an SF controller was considered.

A chevron amplifier (see Figure 7.12) is selected as the control object. Motion of the centre position of the pattern (the square area enclosed by the shaded line) is measured by the vision system. The displacement of this pattern center is treated as the feedback response.
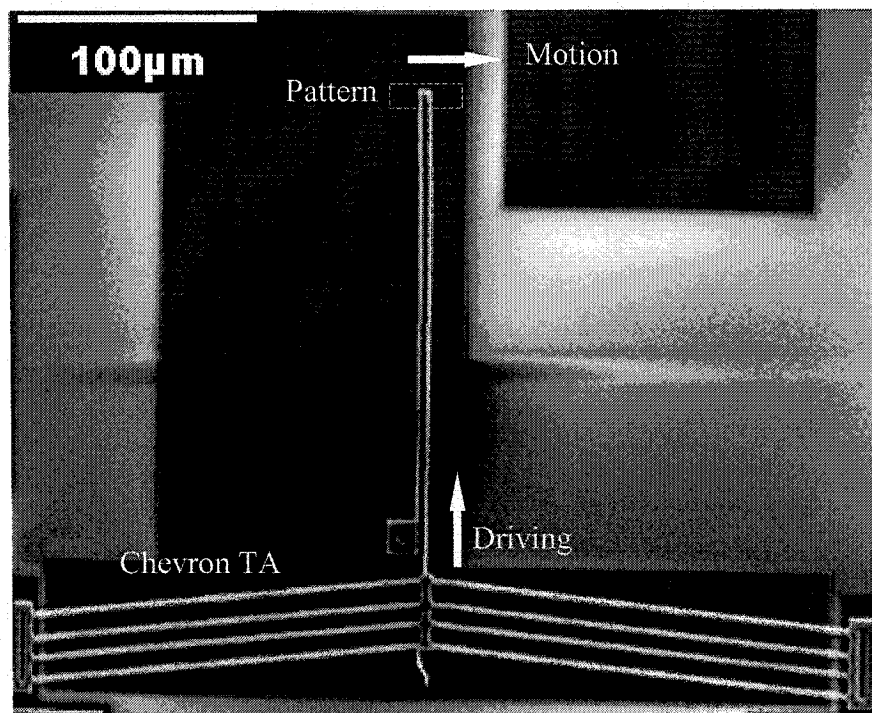
Figure 7.12 Chevron amplifier.

Figure 7.13 shows the response of the chevron amplifier without a PI compensator. Similarly to the sTA and the T-amp studied previously, it takes 10 seconds to get the optimum solution where the pattern moves 5 microns. Some disturbances (such as environmental vibrations) are added to the system after 10 seconds, and the system shows no ability to block the disturbance. A control scheme has been developed to overcome this shortcoming (see Figure 7.14).
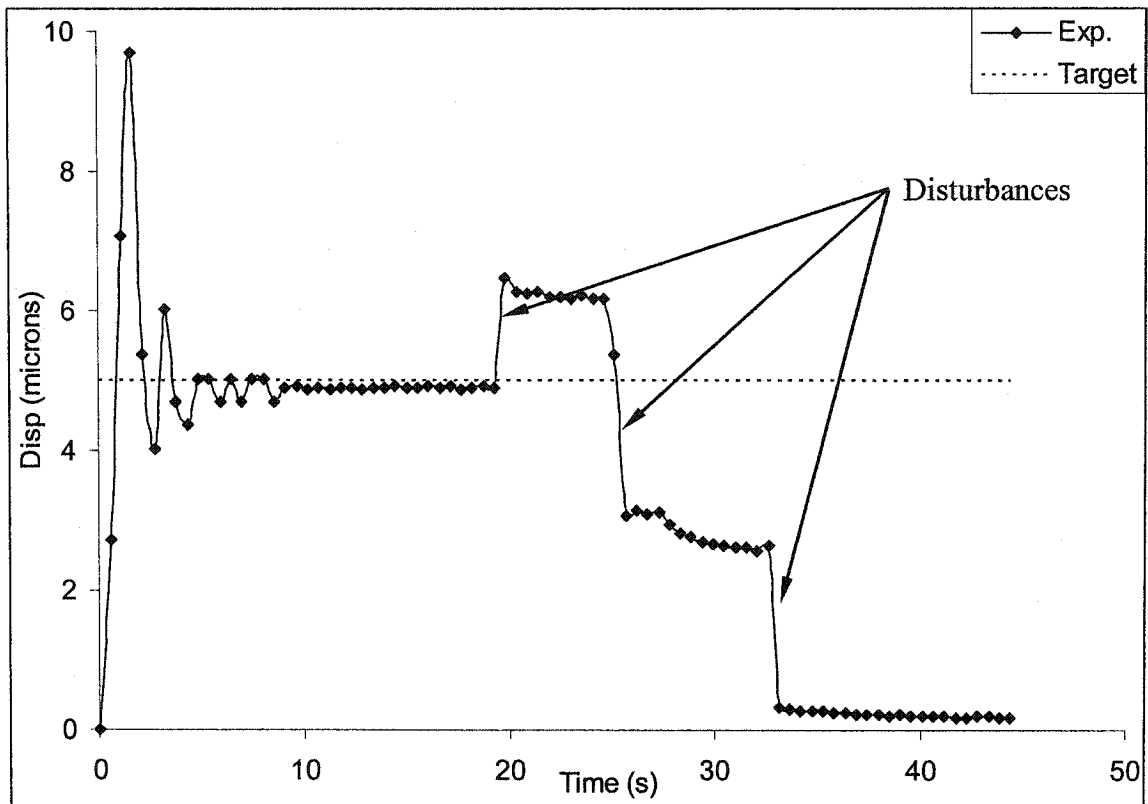
Figure 7.13 Response without a PI compensator.

The symbol x in Figure 7.14 is the target position, x' is the response position. The block OPT is an optimum controller that could be either a SF or a GD controller. The proportional and integral coefficients k_p and k_i are experimentally found to be the best when have values of 0.3 and 0.01 respectively.
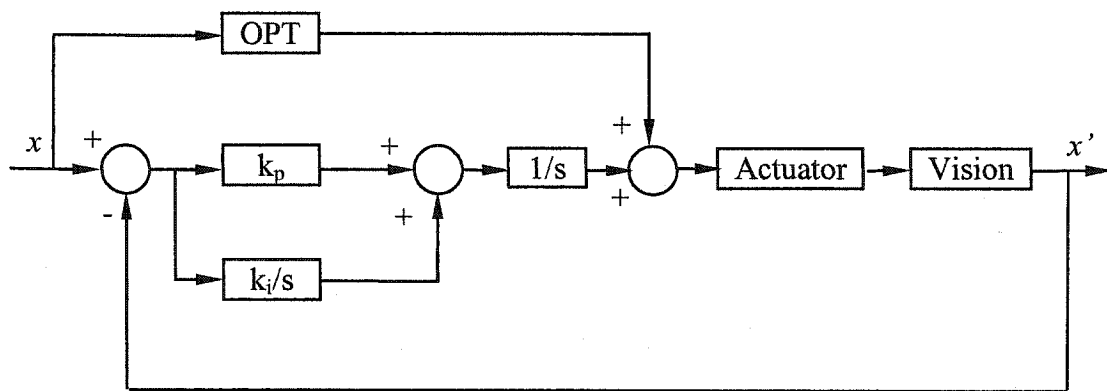
Figure 7.14 1-DOF control scheme.
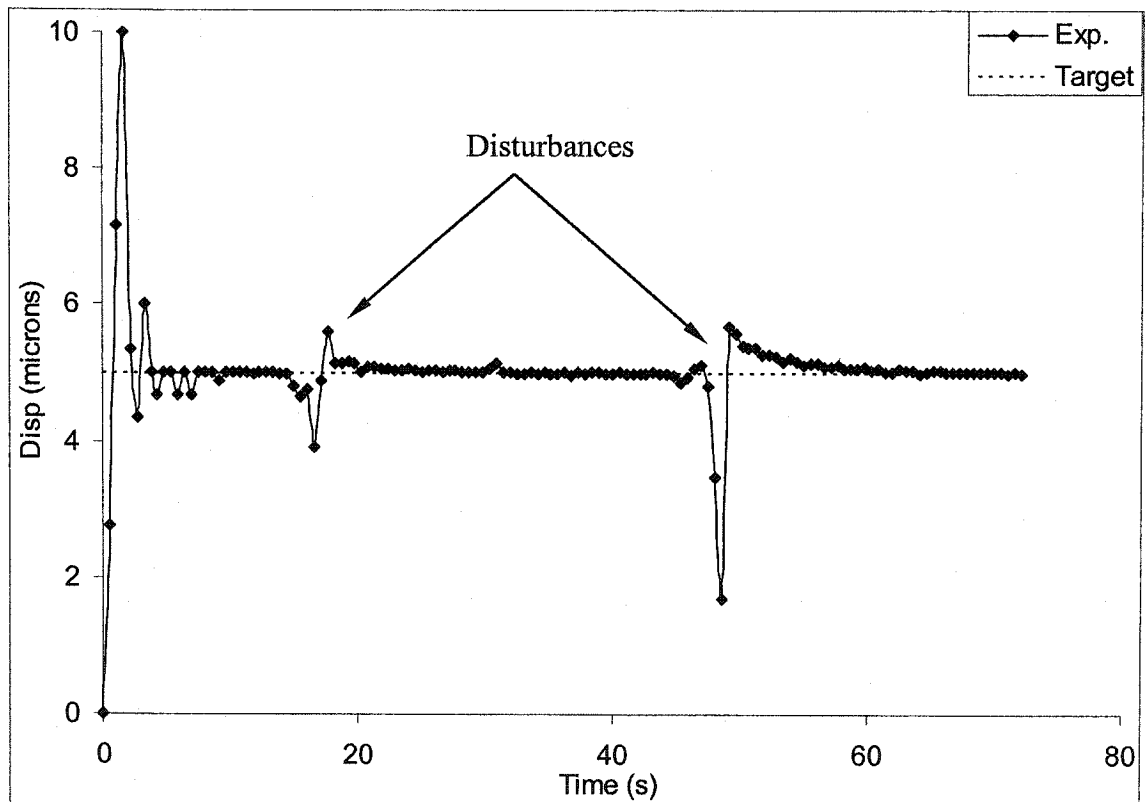
Figure 7.15 Response of GD controller with PI compensator.

Figure 7.15 shows the response of a chevron amplifier to disturbances after moving 5 µm and reaching to the target position. The GD is adopted in the OPT block. The searching area for GD here is from 0 volts to 7.5 volts. As demonstrated in this

figure, the control system with a PI compensator has the ability to restore the output to the target position when a disturbance occurs.

7.5 Summary

In this chapter, two optimal controllers have been developed for 1-DOF micro devices guidance. Compared to a conventional PI (Proportional & Integral) controller, these two optimal controllers required less time to reach steady states. Two hybrid controllers were comprised of a PI controller and the two optimal controllers individually. They were applied to different devices and they were found to be stable in the presence of disturbances.

8 3-DOF Device Control

This chapter investigates control of a compliant micro manipulator, with 3 kinematic DOF, which has been designed and fabricated from polysilicon using the MUMPs surface micromachining process.
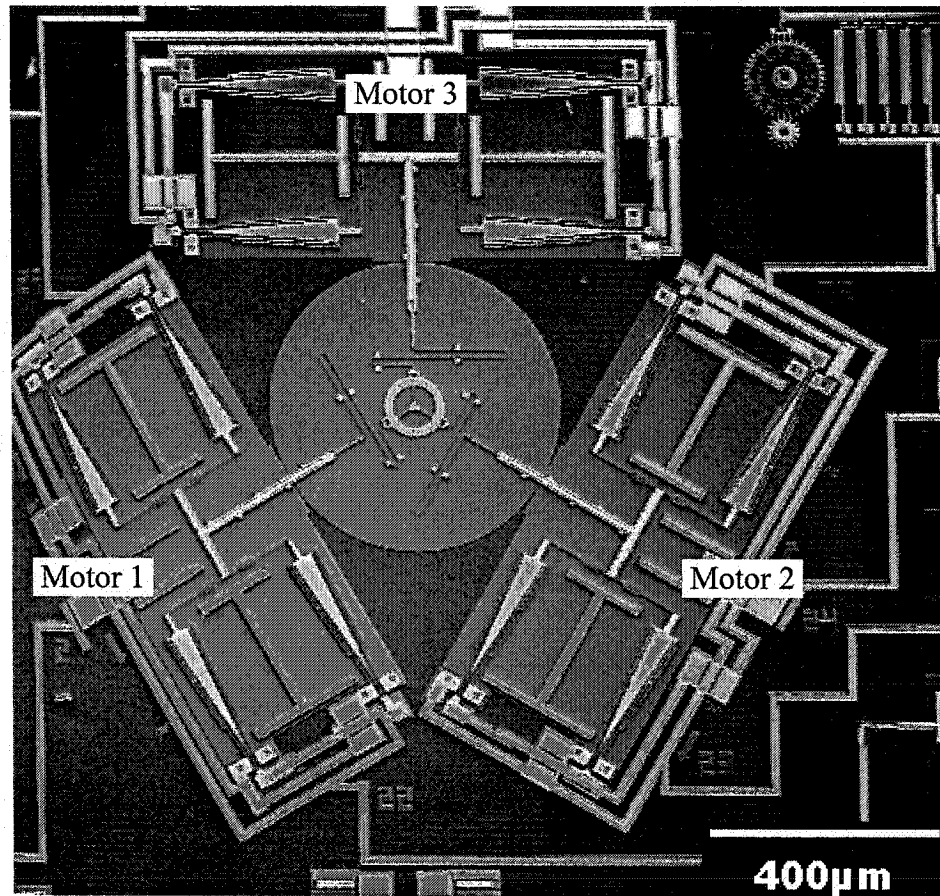
Figure 8.1 SEM of a compliant micro manipulator on CM4.

The kinematic model for this manipulator is the same as the kinematic models of all other manipulators studied in Chapter 3. The origin of the coordinate system is also located at the center of the platform at the neutral position (see Figure 3.4). The displacements of the platform in the x & y directions are labeled by x_c & y_c. The rotations of the platform and three motors are represented by φ and θ_1, θ_2, θ_3, respectively. The

platform center (x_c, y_c) is located at a distance r from the center of the yoke joint. The lengths from the leg ground pivots to the pins in the yokes are denoted by L_1, L_2 and L_3. The input and output variables are connected by a Jacobian matrix of the kinematic model, i.e., by equation (5.13) which has the following form:

$$\begin{bmatrix} \dot{\theta}_1 \\ \dot{\theta}_2 \\ \dot{\theta}_3 \end{bmatrix} = \begin{bmatrix} \dfrac{-\sin(\theta_{01}+\theta_1)}{L_1} & \dfrac{\cos(\theta_{01}+\theta_1)}{L_1} & -\dfrac{r\cos(\varphi-\theta_1)}{L_1} \\ \dfrac{-\sin(\theta_{02}+\theta_2)}{L_2} & \dfrac{\cos(\theta_{02}+\theta_2)}{L_2} & -\dfrac{r\cos(\varphi-\theta_2)}{L_2} \\ \dfrac{-\sin(\theta_{03}+\theta_3)}{L_3} & \dfrac{\cos(\theta_{03}+\theta_3)}{L_3} & -\dfrac{r\cos(\varphi-\theta_3)}{L_3} \end{bmatrix} \begin{bmatrix} \dot{x}_c \\ \dot{y}_c \\ \dot{\varphi} \end{bmatrix} \tag{8.1}$$

The above Jacobian matrix can be used to relate small input ($\delta\theta_1$, $\delta\theta_2$, $\delta\theta_3$) and output (δx_c, δy_c, $\delta\varphi_3$) small movements as well.

8.1 Motors

The motors used to power the manipulators are based on delta-Thermal-Actuators (dTA). To obtain larger force and displacement, each leg is operated by four dTAs assembled into a T-motor (see Figure 8.2).

The T-motor provides bidirectional driving and requires only three electrical wires: one for common ground and two wires for the two driving directions. As compared to the T-motor, a bidirectional rTA requires two separate wires for each direction. For example, when a bidirectional rTA is powered to rotate counterclockwise, the other two wires for clockwise direction have to be suspended: not connected to anything. For automatic control purposes, the T-motor is more convenient for wiring.
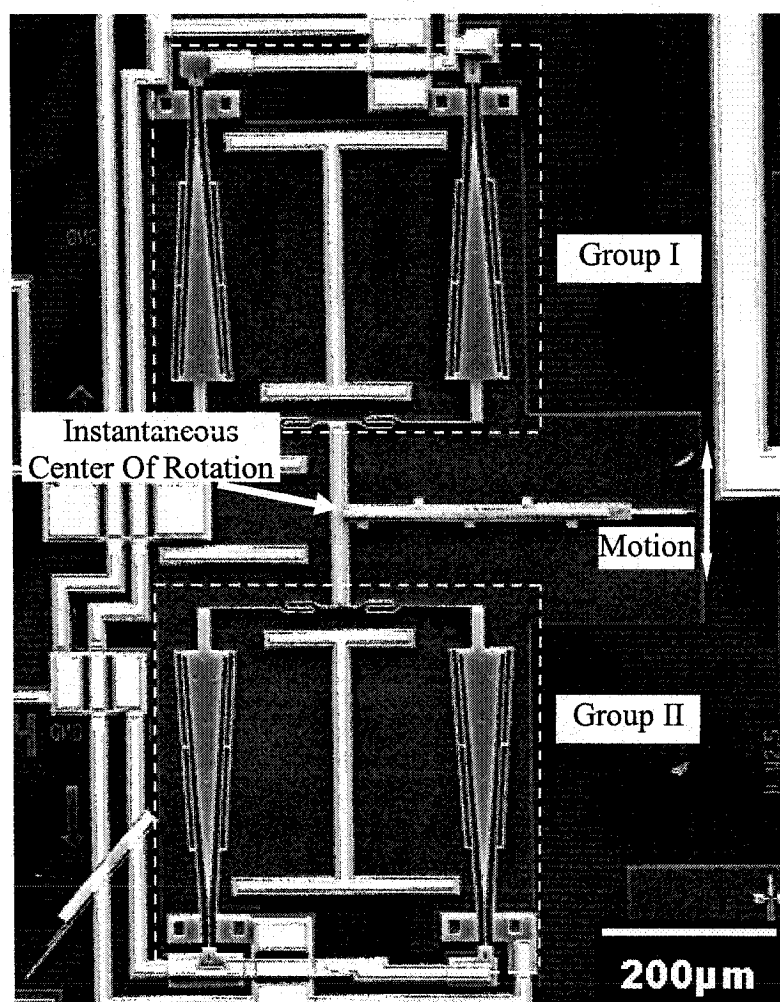
Figure 8.2 SEM of a T-shaped amplifier driven by 4 dTAs (T-motor).

To determine the relation between the driving voltages of the T-motors and their angular displacement, three sets of experiments were performed. Only a single motor, driving each manipulator leg, was powered at a time. Though the manipulator was not loaded externally, the manipulator flexures provided internal load. The total number of flexures is about 75, and each of them stores elastic energy when deformed. A single delta TA has 5 flexures alone: three are attached to the anchors and two are connecting the side hot arms to the central triangular cold arm. The performance of the three tested T-motors was almost identical for small displacements but different noticeably when the displacements were large. That was because the fabrication process and the material

properties introduced imperfections that distorted the performance symmetry for large displacements. Figure 8.3 shows the angular displacement vs. voltage characteristic for each motor.
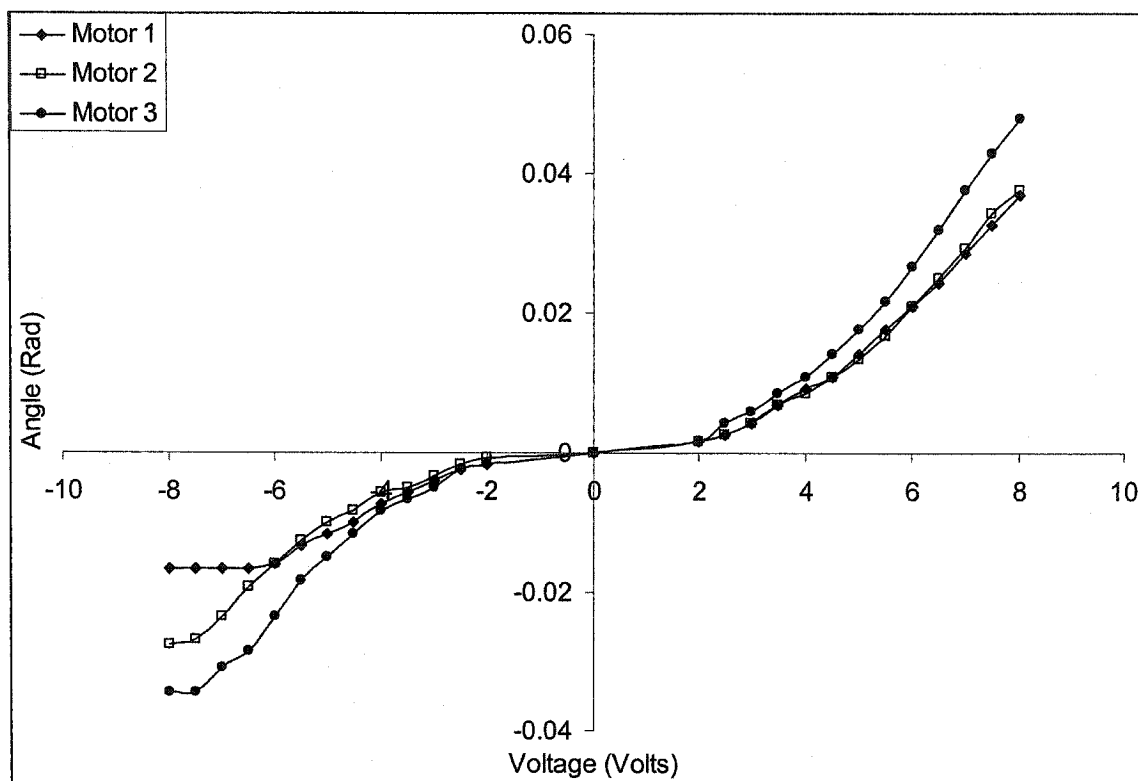
Figure 8.3 Measured rotation angle θ_i vs. input voltage for the T-motors.

Since the thermal actuators are current driven (I^2R), a change in the polarity of the voltage does not change the actuators' driving direction. To make delta actuators move in two directions using a single analog input, a voltage splitter was developed. It is comprised of two Ge diodes with gate voltage of 0.3 volts. They are arranged side by side with opposite polarities. Figure 8.4 shows how a single sine wave voltage drives a dTA.
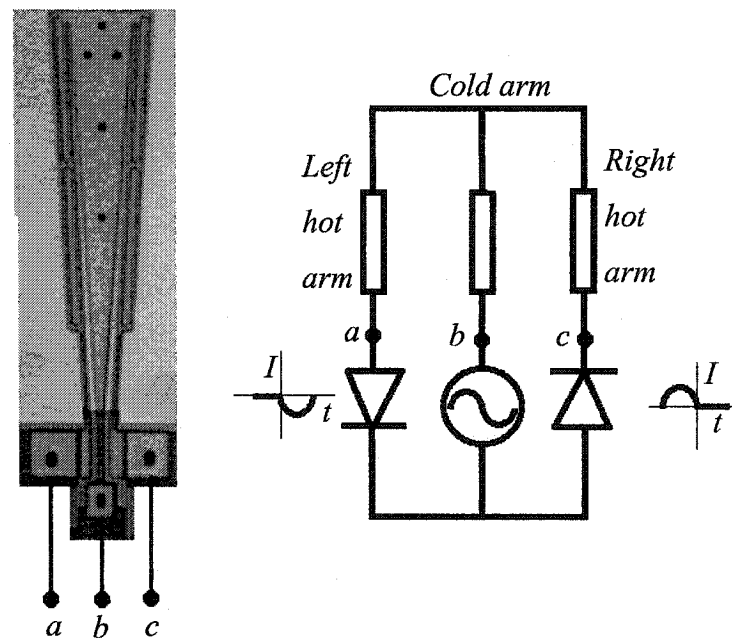
Figure 8.4 Electrical connection of a voltage splitter for a bidirectional actuator.

8.2   Control algorithm

There are three inputs and three outputs for this system. The input variables are the three voltages driving the three T-motors.   The output variables were the platform displacements in the x & y directions, and the platform rotation φ about the z axis. Since the *IMAQ* software encounters more noise when it measures a pattern that rotates, especially when the rotations are small and the pattern is symmetric, the measured platform rotation was not fed back to the system. Instead, the value for the rotation angle was set to zero during the whole control procedure no matter what measured rotation results were. Thus the control system had 3 inputs and was using only 2 outputs as feedback (x & y motion). A point to point controller and a path controller will be described below, in which the translations will be controlled.

8.2.1   Point to Point Control (PTP)

Figure 8.5 shows a block diagram for a point to point controller. The IKP block is the inverse kinematic problem solver which provides the initial rotation angles for the three

motors. The K_p block is a diagonal matrix arbitrarily set to Diag[0.25, 0.25, 0.25]. Some other settings such as Diag[0.05, 0.05, 0.05], Diag[0.1, 0.1, 0.1], Diag[0.3, 0.3, 0.3], and Diag[0.5, 0.5, 0.5] were tried. But Diag[0.25, 0.25, 0.25] was found to provide best control results. The J block uses the Jacobian matrix of equation (8.1) to convert the displacement errors (δx, δy, $\delta \varphi$) to the motor differential outputs ($\delta \theta_1$, $\delta \theta_2$, $\delta \theta_3$) and to update the Jacobian matrix itself. For the specific initial values $r = 82$ μm, $L_i = 430$ μm, $\theta_1 = \theta_2 = \theta_3 = \varphi = 0$, $\theta_{01} = \pi/6$, $\theta_{02} = 5\pi/6$, $\theta_{03} = \pi/2$, the initial Jacobian matrix is:

$$\begin{bmatrix} -0.012 & 0.02 & -0.191 \\ -0.012 & -0.02 & -0.191 \\ 0.024 & 0 & -0.191 \end{bmatrix} \tag{8.2}$$

a)
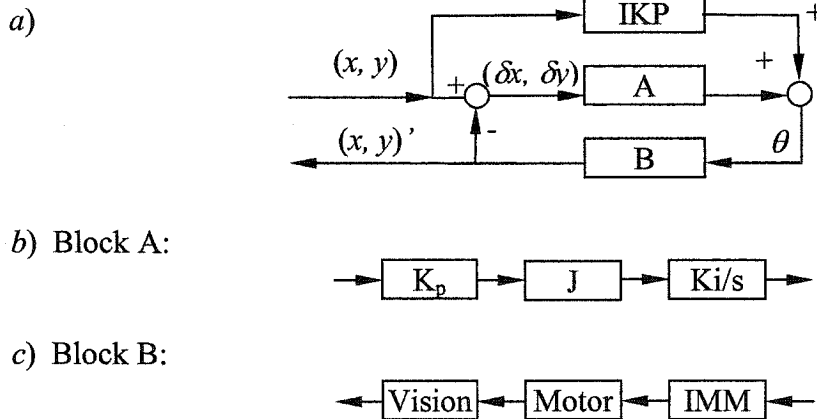
b) Block A:

c) Block B:

Figure 8.5 Block diagram for PTP control: *a)* the system, *b)* details of block A, *c)* details of block B.

The maximum control loop frequency is very low: 2 Hz. The key limiting factor is the image grabbing and digitalizing speed which is about 500 ms for an image. Since the control frequency is only 2 Hz and the TA's maximum operation frequency is 1500 Hz [74], the system can be considered kinematic (no inertia). The integrating block K_i/s

was introduced to compute the platform position for the differential inputs: $\delta\theta_1$, $\delta\theta_2$, and $\delta\theta_3$. The gain for this block is tuned to Diag[1, 1, 1]. The IMM block represents the Inverse Motor Model obtained experimentally from data in Figure 8.3.

Figure 8.6 shows the response of the platform under disturbances conditions during its motion from the neutral position to a point 3.3 μm along the x axis and 10 μm along the y axis with zero rotation. After 2.5 seconds from the start of the program, the platform reached the target position. Then disturbances were applied to the system. The response shows that the control scheme is stable.
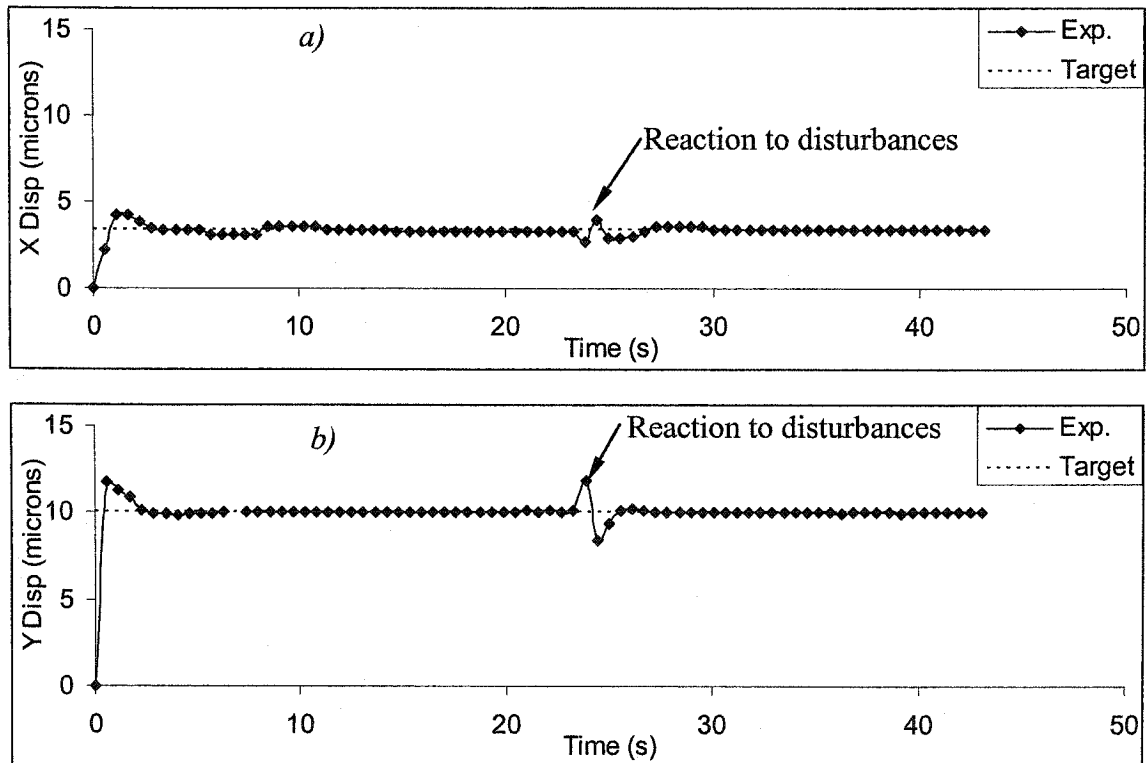
Figure 8.6 Response of PTP: $a)$ in x direction, $b)$ in y direction.

The disturbances were produced by impacting the probe station where the controlled MEMS device was hold. They had a form of step input form.
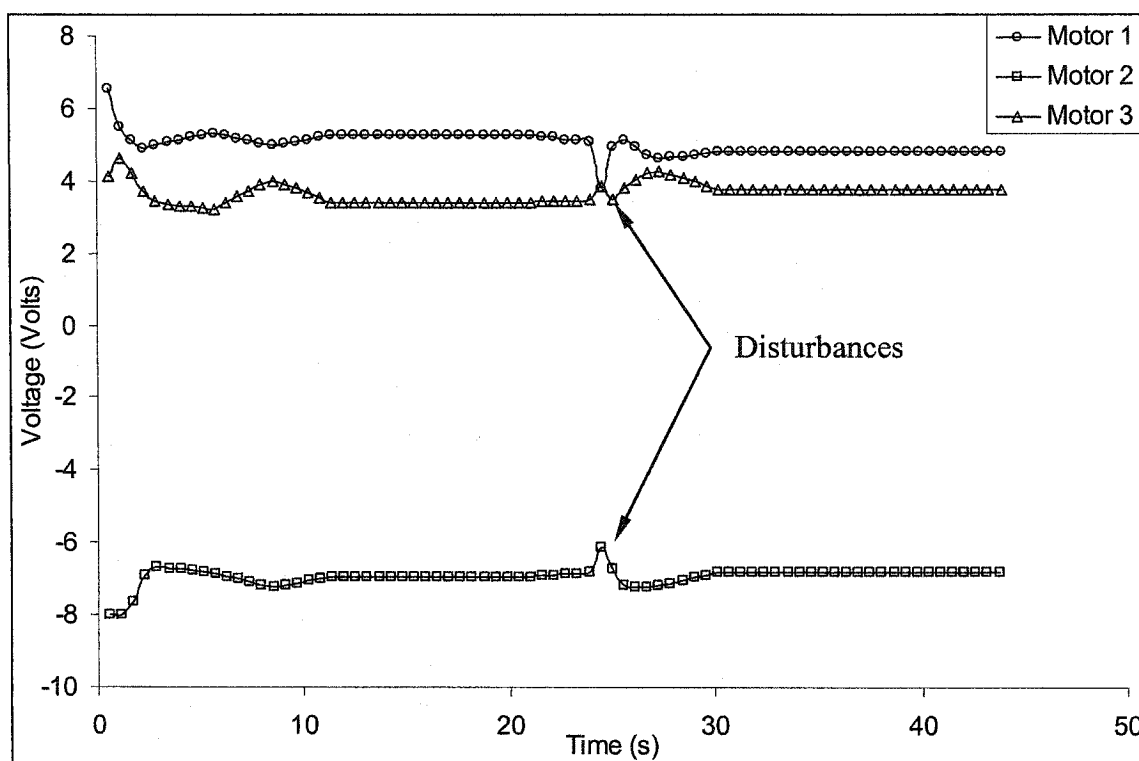
Figure 8.7 Records of the voltages applied on the three motors.

Fig. 8.7 shows the history of the voltages applied to the three T-motors during the control procedures. After the disturbance application, the voltages stabilized again. The voltage levels were however slightly different (<11%). This is possibly caused by the fact that the corrupted measurement of the small platform rotation φ was not fed back but instead, the φ feedback was set to zero.

8.2.2 Path control

A general path control (as opposed to PTP control) is comprised of two parts: a reference generator and a motion controller.

Figure 8.8 shows a block diagram for the path tracking control algorithm. The blocks A & B are the same as the corresponding blocks in Figure 8.5 for PTP control.
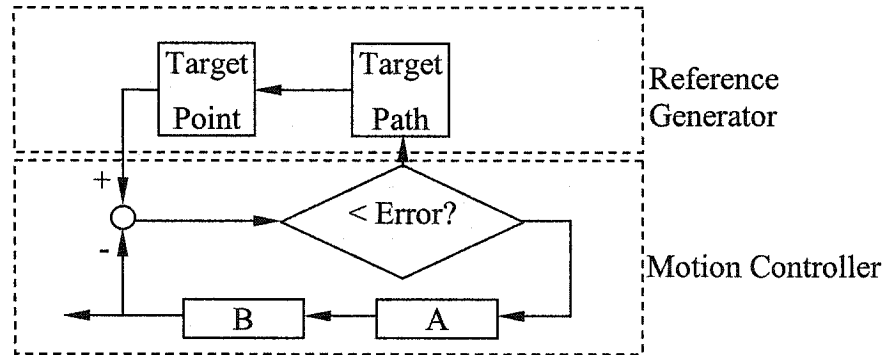
Figure 8.8 Block diagram for path tracking control.

To guarantee that the path tracking errors are smaller than the desired value, an error monitoring block is added to the control algorithm. Whenever a path tracking error exceeds the desired value, the position of the platform is being re-adjusted by the motion controller until the tracking error is small enough. The default criterion for the error correction was set to: $|\varepsilon_x|^2 + |\varepsilon_y|^2 < 0.5$ pixel^2, where ε_x and ε_y were the errors in the x and y directions, respectively. The procedure for the error correction uses the error vector information for fine tuning of the control.

Several paths were assigned to the manipulator during experiments. These paths include tracking straight lines, an ellipse and a four leaf clover.

The eight straight lines can be described by the following formula:

$$y = kx \qquad (8.3)$$

where $k = \pm 0.5, x \in [-10\mu m, 0]$ & $[0, 10 \mu m]$, and $k = \pm 2$, $x \in [-5 \mu m, 0]$, & $[0, 5 \mu m]$.

In order to track the lines smoothly, each line is divided into forty substeps. The three T-motors behave differently when they are required to produce a large rotation, which leads to motion asymmetry, for example, during the experiments, it was observed that it took from 80 to 270 seconds to follow the different line paths described by equation (8.3). The response record of path tracking in Figure 8.9 shows that the trace of the line, y = -0.5x, $x \in [0, 10 \mu m]$, especially when the target point is far away from the origin, is not as smooth as other traces which is caused mainly by the first motor's poor performance when approaching the limit of clockwise rotation (see Fig. 8.3).
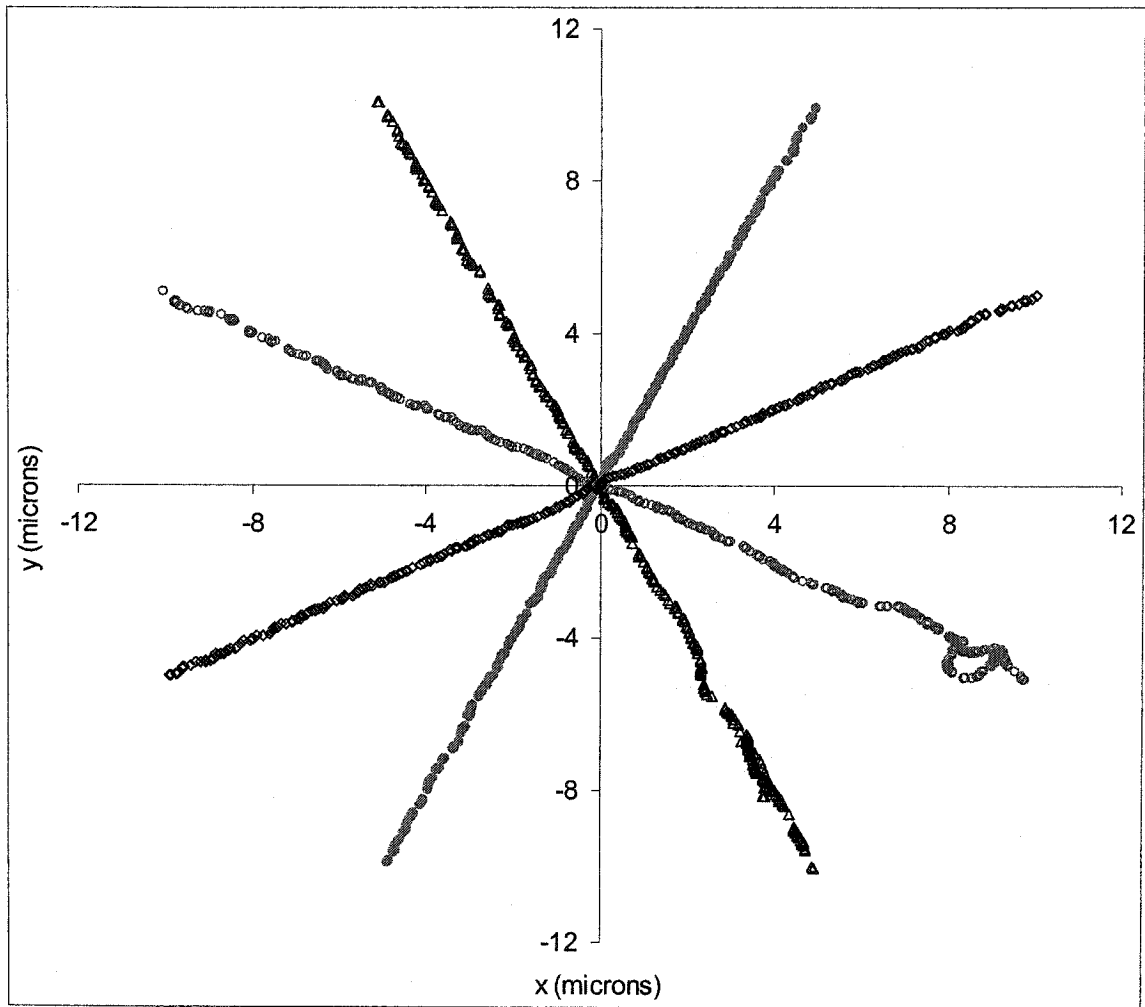
Figure 8.9 Response of tracking straight lines at different angles.

The formula for an ellipse is in the form of

$$\left(\frac{x}{a}\right)^2 + \left(\frac{y}{b}\right)^2 = 1,$$

(8.4)

where a = 3.3 μm, b = 5 μm were used.

The tracking response for the ellipse is presented in Figure 8.10. The whole path of the ellipse was divided into 360 points. The first point in the path is located in (3.3 μm, 0). Since the platform starts from the origin (which is the neutral position), the platform

has to reach a point on the ellipse first, and then start to trace the path. It takes about 360 seconds for the platform to go through all points.
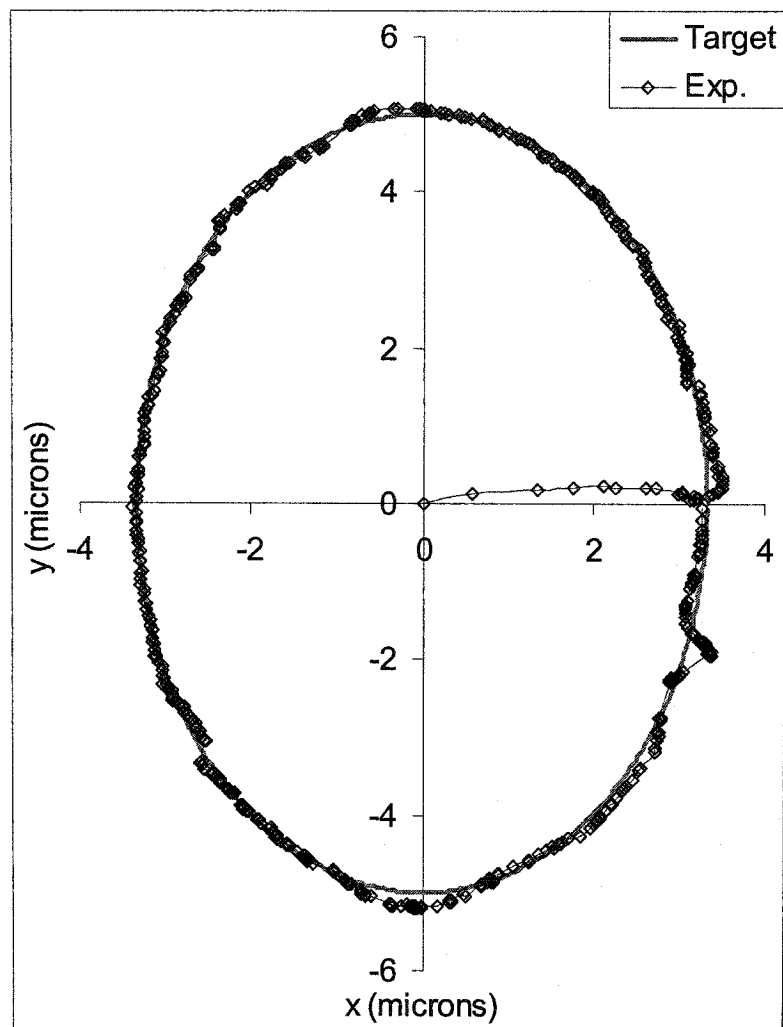
Figure 8.10 Response of tracking an ellipse.

The errors for tracking the ellipse are shown in Figure 8.11. After the platform reached the first point on the ellipse, the tracking errors in both the x and y directions decreased to less than 0.3 microns.
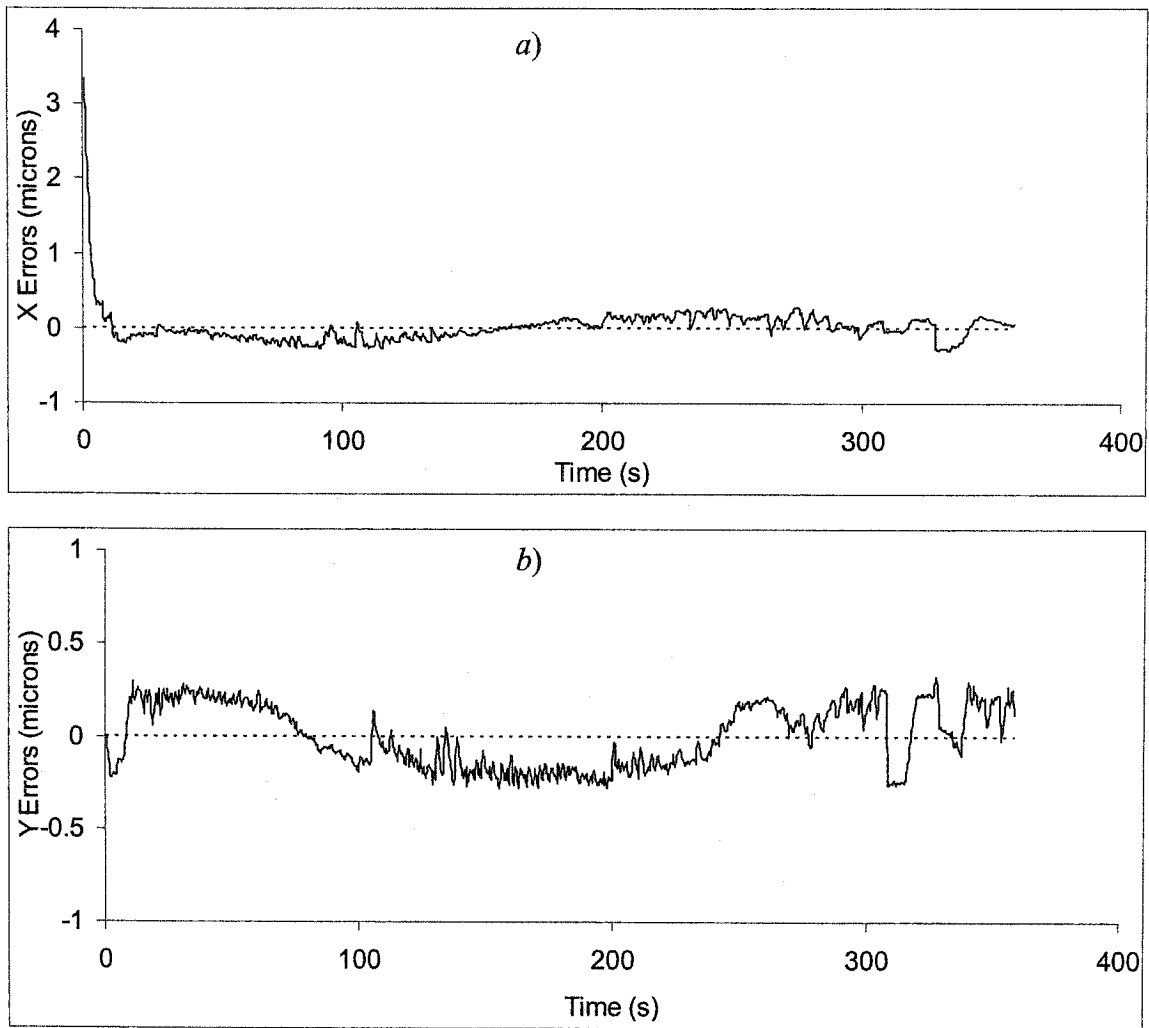
Figure 8.11 Path tracking errors for the ellipse: *a)* errors in the *x* direction, *b)* errors in the *y* direction.

The platform of the manipulator can trace more complicated paths using the same control scheme (Figure 8.8). Figure 8.12 shows a target path and an experimental path for the platform tracking a 5μm radius four-leaf-clover described by the function:

$$r = 5 \cdot \cos(2 \cdot \alpha) \tag{8.5}$$

where α is a parameter angle ranging from *(0+π/4)* to *(2π+π/4)*.

In this path tracking procedure, the criterion for the error correction was set to: $|\varepsilon_x|^2 + |\varepsilon_y|^2 < 0.8$ pixel².
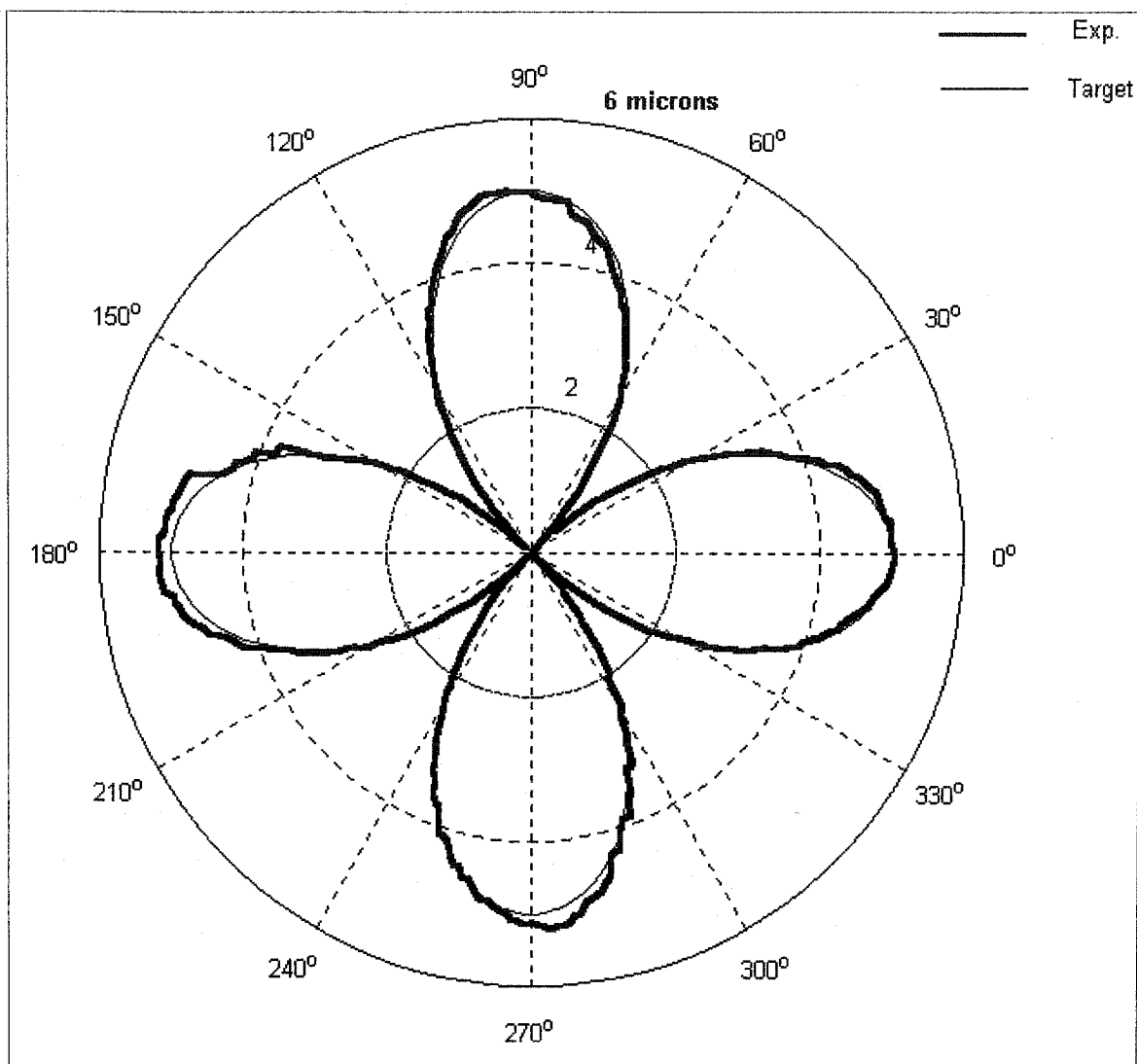
Figure 8.12 Path tracking results for a 5 μm radius four leaf clover.

The experimental results are very close to the target especially for small displacements. It took 430 seconds for the manipulator to follow through all 360 points in the target path within the desired error margin. An interval of more than 1 second was needed to reach adjacent points in the path. As noted before, the slow tracking speed is limited by the speed of capturing and digitalizing the image from the CCD camera.
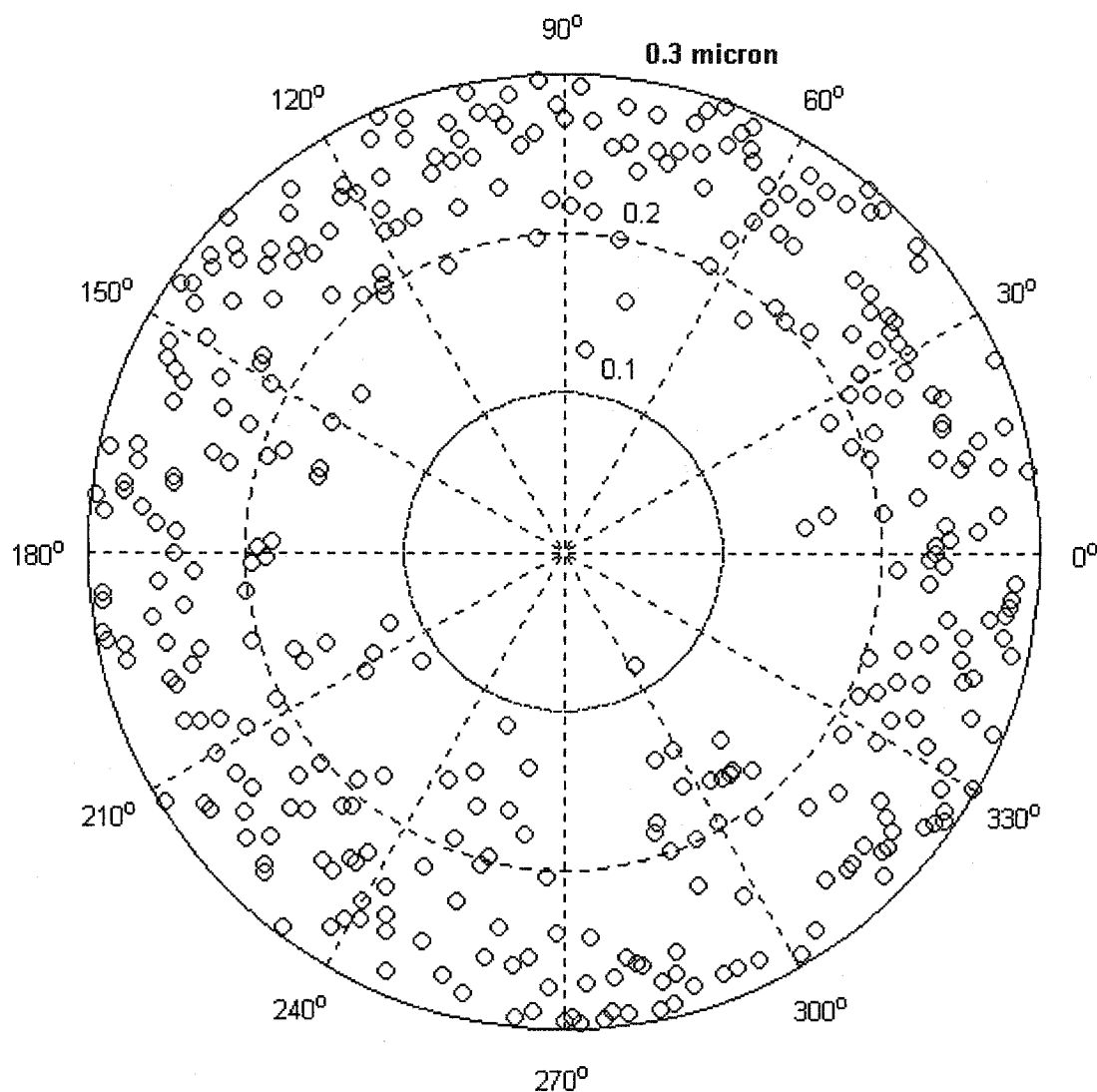
Figure 8.13 Path tracking results for a 5 μm radius four-leaf clover do not exceed 0.3 μm.

Figure 8.13 shows the tracking errors for the four leaf clover path. The magnitudes of the errors are less than 0.3 microns which is reasonable as compared to the 0.3 μm/pixel resolution of the optic system. It was observed that for a smaller motion range, the error criterion of the control algorithm could be set smaller which could reduce the tracking errors.

8.3 Conclusions

A rigid-link kinematic model of a microscopic planar three DOF manipulator was successfully applied for motion control. The objectives of using general purpose imaging software and hardware for gathering feedback information and executing control algorithms have been met. The achieved accuracy of path control was satisfactory, 0.3 μm, given the available resolution of the imaging system of 0.3 μm/pixel. The imaging software proved to be the slowest component of the feedback, resulting in about one second intervals for executing consecutive control steps.

9 Summary

This report includes the design, simulation and testing of micro manipulators.

Chapter 2 was dedicated to the investigation of designs of thermal actuators which are important components of micro manipulators. Several types of TAs, including sTA, dTA, sTA bank, Chevron TA, and rTA, were designed and tested. A sTA, at 5 volts, could develop 5 μN of force or 6 μm of displacement. A typical chevron actuator produced approximately 100 μN of force or 3 μm of displacement at most. Measured results confirmed that the flexures in the devices stored energy when they were deformed and decreased the output energy. The compromise designs are the rTAs or T-motors. They can produce output force larger than 15 μN and output displacements of more than 20 μm.

Chapter 3 reported the development of a rigid body model with 3 kinematic DOF for the micro manipulators studied. The work envelopes of the manipulators can be predicted using the kinematic model. The simulated investigations of work envelopes compared well with the measurements. The simulations based on this model showed that the strokes of the S-joints affect the size of a manipulator's work envelope.

Chapter 4 contains a Finite Element analysis of a fabricated micro manipulator using ANSYS. Up to 10 modes were produced by the FEA. Two kinds of modes were identified: in-phase modes and out-of-phase modes.

Chapter 5 developed two spring-mass modes, with 3 and 6 elastic DOF respectively, for the manipulator studied in chapter 4. The dynamic equations of the vibration system were achieved by different methods. The analytical results from models were solved and they agreed with FEM results. The derivation of the model's Jacobian matrix led to the development of the control algorithm in Chapter 8

Chapter 6 introduced the experimental setup for testing MEMS devices. It also contains a frequency spectrum simulation based on the analytical results from Chapter 5. The experimental results proved that the simulations were accurate.

Chapter 7 investigated control algorithms for 1DOF micro devices. A hybrid controller, including a proportional block, an integral block and an optimization block, has been successfully applied to several micro devices.

Chapter 8 reports the development of a control algorithm for point to point control and motion control, respectively. They are based on the rigid body model with 3 kinematic DOF. The path tracking control provided submicron accuracy.

10 Conclusions

10.1 Conclusions:

The objectives of the thesis have been met and the studies presented in the previous chapters lead to the following conclusions:

1. Planar micromanipulators with 3-DOF can be fabricated using MUMPs process. Several micromanipulators were designed and fabricated. Their work envelope reached a size of a circle of 20 μm in diameter.

2. A micromachined mechanism can be modeled by simple kinematic joints and rigid links. Kinematic models of designed planar micromanipulators can predict their work envelopes.

3. Both FEM and spring-mass models of micromanipulators can effectively predict their dynamic behavior. The results from these two models agreed with experimental results. The models revealed modes with repeated resonant frequencies and some other special properties, such as, in-phase modes and out-of-phase modes.

4. For a thermal actuator, its neutral position affects its performance. The closer its neutral configuration is to its toggle configuration, the larger displacement and less force it can produce. A departing-toggle TA is recommended when larger motion is required, while an approaching-toggle TA is recommended to provide large force.

5. TAs without cold arms, such as Chevron TAs and rTAs are recommended for higher efficiency operations.

6. It is practical to use image processing for control feedback. Motion control set-up for 1-DOF devices, point to point control and path tracking for a 3-DOF micromanipulator successfully achieved the control targets.

10.2 Recommendations for future work

The author believes that the presented research leads to several promising research projects either in academia or industry. The recommended research studies in the future are:

1. Application of the new bidirectional thermal actuators (rTAs and dTAs) should be further investigated, such as, performance under water, efficiency, etc.

2. The control speed of the manipulator in this study is slow. The investigation of high speed image processing was not included in the scope of the work. It is possible to process feedback information faster by shortening image processing time within the LabView program. That can be done by increasing the speed of control computer, improving image processing technique and its efficiency.

3. The control scheme, for the 3-DOF manipulator used in the studies, did not consider the feedback information about the rotation angle of the platform because the symmetrical shape of the platform made the IMAQ software unsuitable for measuring rotation angles. Further research on control scheme could provide better control response.

4. In this study, regardless of the number of actuators, control was applied to only a single manipulator. To manipulate micro objects, two or more collaborating manipulators could be considered.

5. The manipulators of this thesis are planar mechanisms. Their analysis should lead to a study of spatial micromanipulators.

Bibliography

1. R.T. M'Closkey, S. Gibson, J. Hui, "System identification of a MEMS gyroscope", Journal of Dynamic Systems, Measurement, and Control, ASME, Vol. 123, pp. 201-210, June 2001.

2. K.B. Brown, Y. Ma, A. Garcia, W. Allegretto, R.P.W. Lawson, F.E. Vermeulen, A.M. Robinson, "Pressure measurement using hysteresis effects in cantilever microstructures", Canadian Journal of Electronics & Computer Engineering, Vol. 25, No. 1, pp. 43-47, January 2000.

3. F. Arai, D. Andou, Y. Nonoda, T. Fukuda, H. Iwata, K. Itogawa, "Integrated microendeffector for micromanipulation", IEEE/ASME Transactions on Mechatronics, Vol. 3, No. 1, pp. 17-23, March 1998.

4. M. Madou, *Fundamentals of Microfabriction*, CRC Press, 1997.

5. D.A. Koester, R. Mahadevan, B. Hardy, and K.W. Markus, "MUMPs Design Handbook", revision 7.0, Cronos Integrated Microsystems, A JDS Uniphase Company, 3026 Cornwallis Rd. Research Triangle Park, NC 27709.

6. D. Clements, L.L. Howell, N. Master, B. Wight, "Floating pin joints fabricated from two layers of polysilicon at the micro level", 10th world congress on the theory of machines and mechanisms, pp 874-879, Oulu, Finland, June 20-24, 1999.

7. Z. Li, "Chaotic vibration sieve", Mech. Mach. Theory, Vol. 30, No. 4, pp. 613-618, 1995.

8. H. Fettig, "Design, Simulation and Testing of Micromachined Flexible Joints", 2001, Ph. D thesis at Dalhousie university, Halifax, B3J 2X4, Nova Scotia, Canada.

9. W.C. Tand, T.C.H. Nguyen, R.T. Howe, "Laterally driven polysilicon resonant microstructures," Sensors and Actuators, v. 20, pp. 25-32, 1989.

10. L. Que, J.-S. Park, Y.B. Gianchandani, "Bent-beam electrothermal actuators-Part I:Single beam and cascaded devices", Journal of Microelectromechanical Systems, Vol.10 Issue: 2, June 2001, pp. 247 -254.

11. J.H. Comtois, V.M. Bright, "Application for surface-micromachined polysilicon thermal actuators and arrays", Sensors and Actuators, A 58, pp.19-25, 1997.

12. W. Riethmuller, W. Benecke, "Thermally excited silicon microactuators", IEEE transactions on electron devices, vol. 35. No.6, pp. 758-763, June 1998.

13. R. Hickey, T. Hubbard, M. R. Kujath, "Analysis and optimization of two-beam micro-machined thermal actuators", J. of Vac. Sci. And Tech. A **20(3)**, pp. 971-974, May/June 2002.

14. R. Cragun, L.L. Howell, "A constrained thermal expansion micro-actuator", ASME, DSC-Vol. 66, Micro-Electro-Mechanical System (MEMS), pp. 365-371, 1998.

15. R. Cragun, L.L. Howell, "Linear Thermomechanical microactuators", ASME, MEMS-Vol.. 1, Microelectromechanical Systems (MEMS), pp. 181-188, 1999.

16. C.D. Lott, T.W. McLain, J.N. Harb, L.L. Howell, "Thermal modeling of a surface-micromachined linear thermomechanical actuator", Modeling and Simulation of Microsystems 2001, (www.cr.org), ISBN 0-9708275-0-4, pp. 370-373.

17. L.L. Howell, A. Midha, "A method for the design of compliant mechanisms with small-length flexural pivots", Transactions of the ASME, Vol. 116, pp. 280-290, March 1994.

18. J.M. Paros, and L. Weisbord, How to design flexure hinges, Machine Design, Novermber, 1965, pp. 151.

19. R.H Burns, F.F.E. Crossley, "Kinetostatic synthesis of flexible link mechanisms", ASME-Paper No. 68-Mech-36 1968.

20. L.L. Howell, and A. Midha, Parametric deflection approximations for end-loaded, large –deflection beams in compliant mechanisms, *ASME Journal of Mechanical Design*, **117(1)**, 156, 1995.

21. N. Lobontiu, et al., Design of symmetric conic-section flexure hinges based on closed-form compliance equations, *Mechanism and Machine Theory*, **37(5)**, 477, 2002.

22. S. Kota, J. Joo, Z. Li, S.M. Rodgers, and J. Sniegowski, Design of compliant mechanisms: applications to MEMS, *Analog Integrated Circuits and Signal Processing*, **29(1-2)**, 7, 2001.

23. N. Lobontiu, Compliant Mechanisms: Design of Flexure Hinges. CRC press, 2003.

24. O. Sigmund, "On the design of compliant mechanisms using topology optimization", Mech. Struct. & Mach., 25(4), pp. 493-524, 1997.

25. U.D. Larsen, O. Sigmund, S. Bouwstra, "Design and fabrication of compliant micromechanisms and structures with negative Poisson's ratio", Journal of Microelectromechanical Systems, Vol, 6, No. 2, pp. 99-106, June 1997.

26. S. Canfield, M. Frecker, "Topology optimization of compliant mechanical amplifiers for piezoelectric actuators", Struct. Multidisc Optim 20, pp. 269-279, Springer-Verlag 2000.

27. S. Kota, J. Hetrick, Z. Li, S. Rodgers, T. Krygowski, "Synthesizing high-performance compliant stroke amplification systems for MEMS", Proceedings IEEE Thirteenth Annual International Conference on Micro Electro Mechanical Systems (Cat. No.00CH36308) pp. 164-169, Jan. 23-27 2000.

28. X.T. Huang, M.T. Saif, N.C. MacDonald, "A micromotion amplifier", The Ninth Annual International Workshop on Micro Electro Mechanical Systems, 1996, MEMS '96, Proceedings. On Investigation of Micro Structures, Sensors, Actuators, Machines and Systems'. Pp. 424-428, Feb. 11-15, 1996.

29. H.L. Chen, C. Chang, K. Yen, H. Huang, J. Chio, C. Wu, P. Chang, "Fabrication of the planar angular rotator using the CMOS process", IEEE, 2000.

30. T. Akiyama, D. Collard, and H. Fujita, Scratch drive actuator with mechanical links for self-assembly of three-dimensional MEMS, *IEEE Journal of Microelectro-mechanical systems,* **6(1),** 10, 1997.

31. R.J. Linderman, and V.M. Bright, Nanometer precision positioning robots utilizing optimized scratch drive actuators, *Sensors and Actuators, Series A: Physical,* 91, 292, 2001.

32. L. Hunt, A. Belise, T. Hubbard, and M. Kujath, Investigation of Micro-Machined Scratch Drive Actuators, *the 3rd Canadian Workshop on MEMS (CWMEMS'03),* Ottawa, Canada, August, 2003.

33. F. Poltz, et al., A low-voltage torsional actuator for application in RF-microswitches, *Sensors and Actuators, Series A: Physical,* 92, 312, 2001.

34. S.K. Jericho, M.H. Jericho, M. Kujath, T. Hubbard, MEMS Microtweezers for the Manipulation of Micron Size Objects, *Canadian Workshop on MEMS '03,* Aug. 22, Ottawa ON.

35. T. Tanikawa and T. Arai, Development of a Micro-Manipulation System Having a Two-Fingered Micro-Hand, *IEEE Transactions on Robotics and Automation.* Vol., 15, No. 1, 1999, pp152-162.

36. M. Goldfarb, J.E. Speich, "Design of minimum surface-effect three degree-of-freedom micromanipulator", Proceedings of the 1997 IEEE, International Conference on Robotics and Automation, pp.1466-1471, Albuquerque, New Mexico-April 1997.

37. J. Zou, L.G. Watson, W.J. Zhang, S.S. Bi, G.H. Zong, "Kinematic Modeling and simulation of a 3DOF planar Micro-motion Stage", CSME form'2000, Montreal, May 17-19, 2000, pp. 32-39.

38. R. Yeh, E.J.J. Kruglick, and K.S.J. Pister, Surface-Micromachied Components for Articulated Microrobots, *Journal of MicroElectroMechanical Systems.* **5(1)**, March 1996, pp. 10-17.

39. B. Jokiel, L. Bieg, and G. Benavides, Planar and Spatial Three Degree-of-Freedom Micro-Stages in Silicon MEMS. Sandia National Laboratories, NM, March 2001, http://www.aspe.net/meetings/2001annual/short_abst/1160.pdf.

40. M. Gallant, and C. Gosselin, The effect of joint clearances on the singular configurations of planar parallel manipulators. *2003 CCToMM Symposium on Mechanisms, Machines, and Mechatronics.* Montreal, Quebec, M3-03-14.

41. M.L. Culpepper, G. Anderson, Design of a Low-cost Nano-manipulator which utilizes a monolithic, spatial compliant mechanism. *Journal of Precision Engineering*, 2002.

42. C. Kim, and Y. Kim, Micro xy-stage using silicon on a glass substrate. *J. Micromech. Microeng.* **12**, 2002, pp. 103-107.

43. C. Kim, H. Jeong, J. Jeon, and Y. Kim, Silicon Micro xy-stage with a large area shuttle and no-etching holes for spm-based data storage. *Journal of microelectromechanical system*, **12(4)**, 2003, pp. 470-478.

44. Y. Sun, B. J. Nelson, D. P. Potasek, and E., Enikov., A bulk microfabricated multi-axis capacitive cellular force sensor using transverse comb drives. *J. Micromech. Microeng.* **12(6)**, pp. 832-840.

45. J. Bernhard, L. Benavides, and J. Allen, Planar and Spatial Three-Degree-of-Freedom Micro-stages in Silicon MEMS. *Proceedings of the 16th Annual ASPE Meeting*, November, 2001.

46. N. Dagalakis, and E. Amatucci, Kinmatic Modeling of a 6 Degree of Freedom Tri-stage Micro-Positioner. *Proceedings of the 16th Annual ASPE Meeting*, November, 2001.

47. M.L. Culpepper, G. Anderson, and P. Petri, HexFlex: A planar mechanism for six-axis manipulation and alignment. *Proceedings of the 17th Annual ASPE Meeting*. November, 2002.

48. C. Gosselin, "Kinematic Analysis, Optimizatioin and Programming of Parallel Robotic Manipulators", June 1988, unpublished PhD thesis, Department of Mechanical Engineering, McGill University, Montreal, Canada.

49. C.M. Gosselin, and J. Wang, Singularity loci of planar parallel manipulators with revolute actuators. *Robotics and Autonomous Systems*. 21, 1997, pp. 377-398.

50. M. Gallant, and R. Boudreau, The synthesis of planar parallel manipulators with prismatic joints for an optimal, singularity-free workspace. *Journal of Robotic Systems*, 19(1), 2002, pp. 13-24.

51. M. Arsenault, and R. Boudreau, The synthesis of Three-Degree-of-Freedom Planar Manipulators with Revolute Joints (3-RRR) for an Optimal Singularity-Free Workspace. *2003 CCToMM Symposium on Mechanisms, Machines, and Mechatronics*. Montreal, Quebec, M3-03-19.

52. R. P. Feynman, "There's plenty of room at the bottom", Journal of microelectromechanical systems, Vol. 1, No. 1, March 1992.

53. B. Siciliano, "A closed-loop inverse kinematic scheme for on-line joint-based robot control", Robotica, Vol. 8, pp. 231-243, 1990.

54. J. Angeles, "On the numerical solution of the inverse kinematic problem", Intern. J. Robotics Research 4, No. 2, pp. 21-37, 1985.

55. A.A. Goldenberg, B. Benhabib, R.G. Fenton, "A complete generalized solution to the inverse kinematics of robots" IEEE J. Robotics and Automation RA-1, No. 1, pp. 14-20, 1985.

56. J.-J.E. Slotine, D.R. Yoerger, "A rule-based inverse kinematics algorithm for redundant manipulators" Intern. J. Robotics and Automation 2, No. 2, pp. 86-89, 1987.

57. P. Chiacchio, B. Siciliano, "A closed-loop Jacobian transpose scheme for solving the inverse kinematics of nonredundant and redundant writes" J. Robotic Systems 6, No. 5, pp. 601-630, 1989.

58. K. Ohnishi, M. Shibata, T. Murakami, "Motion control for advanced mechatronics", IEEE/ASME Transactions on mechatronics, Vol. 1, No. 1, pp. 56-67, March 1996.

59. S. Bhansali, A.L. Zhang, R.B. Zmood, P.E. Joines, D.K. Sood, "Prototype feedback-controlled bidirctional actuation system for MEMS applicaitons", Journal of microeletromechanical systems, Vol. 9, No. 2, pp. 245-251, June 2000.

60. A. Itoh, "Motion Control of Protozoa for Bio MEMS", IEEE/ASME Transactions on Mechatronics, Vol. 5, No. 2, June 2000.

61. R. Hickey, "Analysis and Optimization of Micro-Machined Thermal Actuators", Thesis of Master of Applied Science, May 2001, Dalhousie University, Halifax, Nova Scotia, Canada.

62. J. McDonald, "Micro Force Probe User's Manual", Internal project report of MEMS lab at Dalhousie University, Halifax, Nova Scotia, Canada, July 24, 2002.

63. M. Kujath, "Dynamic system II", class note, 2000 Fall term, Dalhousie University, Halifax, Nova Scotia, Canada.

64. Charles. E, Knight, *The finite element method in mechanical design,* 1995, PWS-KENT Publishing Company, Boston, USA.

65. ANSYS Online help document.

66. W.N, Sharpe, Y. Bin, R. Vaidyanathan, R.L. Edwards, "Measurement of Young's Modulus, Poisson's ratio, and Tensile Strength of Polysilicon", In Proceedings of MEMS'97-IEEE Tenth Workshop On MicroElectroMechanical Systems, Nagoya, Japan, January 1997. San Diego, CA: IEEE. 424-429.

67. J. Angeles, "The Kujath Parallel Manipulator: Derivation of the Jacobian Matrix", 2000, Technical Memorandum, McGill University.

68. R. C. Hibbeler, "Mechanics of Materials", 3rd version, 1997, Prentice Hall, ISBN 0-13-256983-3.

69. W.T. Thomson, M. Dahleh, "Theory of Vibration with Application", 5th edition, 1998, Prentice Hall, Upper Saddle River, NJ07458.

70. M. Kujath, K. Liu, U. Akpan, "Analysis of complex modes influence on modal correlation of space structures", A report prepared for the Ministry of Industry, Science and Technology, Canadian Space Agency, Directorate of Space Mechanics, May 18, 1998.

71.   H. Fettig, J. Wylde, T. Hubbard, M. Kujath, "Simulation, dynamic testing and design of micromachined flexible joints", J. Micromech. Microeng. 11 (2001) pp. 209-216.

72.   H. Zhang et al., "Viscous air damping in laterally driven microresonators", *MEMS'94, Proc. IEEE Workshop on MicroElectroMechanical Systems* (Oiso, Japan, 1994) pp. 199-204.

73.   H.W. Tang, X.Z. Qin, "Methods of Optimization", The press of Dalian University of Technology, ISBN 7-5611-0901-6, 1994.

74.   R. Hickey, "Analysis and Optimization of Micro-Machined Thermal Actuators", MASc thesis at Dalhousie University, Halifax, B3J 2X4, Nova Scotia, Canada, 2001.

75.   H. Fettig, Ted Hubbard, Marek Kujath, "Flexual Motion Amplifiers for Micro machined Thermal Actuators", Conference of CSME, Kingston, May 2002.

Appendix A: Derivation of Jacobian Matrix

A.1. Derivation of J_1

Point o in Figure 5.2 is the origin of the global coordinate system for the kinematic model. The velocity of the point P_3 can be obtained by differentiating equations (5.4) & (5.5) with respect to time. Their left hand side terms are:

$$\vec{v}_{p3} = \frac{d}{dt}(\overrightarrow{oP_3'}) \qquad \text{(Eq. A-1)}$$

Since point M_3 is the location of the base of motor 3, and it is fixed to the frame, the vector $\overrightarrow{oM_3}$ is constant. Differentiating equation (5.4) with respect to time, the velocity of the point P_3 will be in the following form:

$$\vec{v}_{p3} = \frac{d}{dt}(\overrightarrow{oP_3'}) = \frac{d}{dt}(\overrightarrow{oM_3}) + \frac{d}{dt}(\overrightarrow{M_3P_3'}) = \frac{d}{dt}(\overrightarrow{M_3P_3'}). \qquad \text{(Eq. A-2)}$$

Using equations (5.1) and (5.2), Eq. A-2 can be written as:

$$\vec{v}_{p3} = \frac{d}{dt}(\overrightarrow{M_3P_3'}) = \dot{l}_3 \cdot \vec{e}_{3r} + l_3 \cdot \dot{\theta}_3 \cdot E_r \cdot \vec{e}_{3r} \qquad \text{(Eq. A-3)}$$

Here $\dot{l}_3$ is the magnitude of the linear velocity along the vector M_3P_3'; l_3 is the magnitude of the vector M_3P_3'; and $\vec{e}_{3r}$ is the unit length vector in the radial direction (along the vector M_3P_3').

Similarly, the velocity of the point P_3 is obtained from equation (5.5):

$$\vec{v}_{p3} = \frac{d}{dt}(\overrightarrow{oP_3'}) = \frac{d}{dt}(\overrightarrow{oC'}) + \frac{d}{dt}(\overrightarrow{C'P_3'}) = \vec{v}_{c'} + \dot{r}_3 \cdot \vec{e}_{c'p_3} + r_3 \cdot \dot{\varphi}_p \cdot E_r \cdot \vec{e}_{c'p_3} \qquad \text{(Eq. A-4)}$$

Here the vector $\vec{v}_{c'}$ is the linear velocity of the platform center point o (c) which is $[\dot{x}_c, \dot{y}_c]^t$; the variable r_3 is the magnitude of the vector $C'P_3'$ which is constant; the vector $\vec{e}_{c'p_3}$ is the unit length vector in the direction of the vector $C'P_3'$; the variable $\dot{r}_3$ is the magnitude of the linear velocity along the vector $C'P_3'$, which is equal to zero due to the constant value of r_3.

Vector $\vec{e}_{3r}^{\perp}$ is defined as a unit vector perpendicular to the vector $\vec{e}_{3r}$, i.e.,

$(\vec{e}_{3r}^{\perp})^T \vec{e}_{3r} = 0$. Multiplied by the vector $(\vec{e}_{3r}^{\perp})^T$, Eqs. (A-3) and (A-4) become:

$$(\vec{e}_{3r}^{\perp})^T \vec{v}_{p3}$$
$$= \dot{l}_{3_3}(\vec{e}_{3r}^{\perp})^T (\vec{e}_{3r}) + l_3\dot{\theta}_3(\vec{e}_{3r}^{\perp})^T (E_r)(\vec{e}_{3r}) \qquad \text{(Eq. A-5)}$$
$$= l_3\dot{\theta}_3(\vec{e}_{3r}^{\perp})^T (E_r)(\vec{e}_{3r})$$

$$(\vec{e}_{3r}^{\perp})^T \vec{v}_{p3}$$
$$= (\vec{e}_{3r}^{\perp})^T \vec{v}_{c'} + \dot{r}_3(\vec{e}_{3r}^{\perp})^T \vec{e}_{c'p_3} + r_3\dot{\varphi}_p(\vec{e}_{3r}^{\perp})^T E_r\vec{e}_{c'p_3} \qquad \text{(Eq. A-6)}$$
$$= (\vec{e}_{3r}^{\perp})^T \vec{v}_{c'} + r_3\dot{\varphi}_p(\vec{e}_{3r}^{\perp})^T E_r(\vec{e}_{c'p_3})$$

The terms on the right hand side of Eqs (A-5) and (A-6) are equal. Therefore,

$$l_3\dot{\theta}_3(\vec{e}_{3r}^{\perp})^T (E_r)(\vec{e}_{3r})$$
$$= (\vec{e}_{3r}^{\perp})^T (\vec{v}_{c'}) + r_3\dot{\varphi}_p(\vec{e}_{3r}^{\perp})^T (E_r)(\vec{e}_{c'p_3}) . \qquad \text{(Eq. A-7)}$$

The vector $\vec{e}_{3r}$ is equal to $[\cos(\theta_{03}+\theta_3), \sin(\theta_{03}+\theta_3)]^t$; the vector $\vec{e}_{3r}^{\perp}$ is $[\sin(\theta_{03}+\theta_3),$

$-\cos(\theta_{03}+\theta_3)]^t$; the vector $\vec{e}_{c'p_3}$ is $[\cos(\varphi_{03}+\varphi_p), \sin(\varphi_{03}+\varphi_p)]^t$. Substituting these values

into Eq. (A-7), then equation will be written in the form of input variable θ_3, and output

variables x_c, y_c and φ_p. The term on the left hand side of the Eq. (A-7) is

$$l_3 \cdot \dot{\theta}_3 \cdot (\vec{e}_{3r}^{\perp})^T (E_r)(\vec{e}_{3r})$$
$$= l_3\dot{\theta}_3\begin{bmatrix}\sin(\theta_{03} +\theta_3) & -\cos(\theta_{03} +\theta_3)\end{bmatrix}\begin{pmatrix}0 & -1 \\ 1 & 0\end{pmatrix}\begin{bmatrix}\cos(\theta_{03} +\theta_3) \\ \sin(\theta_{03} +\theta_3)\end{bmatrix} \qquad \text{(Eq. A-8)}$$

$$= -l_3\dot{\theta}_3$$

The term on the right hand side of the Eq. (A-7) is equal to

$$(\vec{e}_{3r}^{\perp})^T (\vec{v}_{c'}) + r_3 \cdot \dot{\varphi}_p \cdot (\vec{e}_{3r}^{\perp})^T (E_r)(\vec{e}_{c'p_3})$$
$$= \begin{bmatrix}\sin(\theta_{03} +\theta_3) & -\cos(\theta_{03} +\theta_3)\end{bmatrix}\begin{bmatrix}\dot{x}_c \\ \dot{y}_c\end{bmatrix}$$
$$+ r_3\dot{\varphi}_p\begin{bmatrix}\sin(\theta_{03} +\theta_3) & -\cos(\theta_{03} +\theta_3)\end{bmatrix}\begin{pmatrix}0 & -1 \\ 1 & 0\end{pmatrix}\begin{bmatrix}\cos(\varphi_{03} +\varphi_p) \\ \sin(\varphi_{03} +\varphi_p)\end{bmatrix} \qquad \text{(Eq. A-9)}$$

$$= \dot{x}_c \sin(\theta_{03} + \theta_3) - \dot{y}_c \cos(\theta_{03} + \theta_3) - r_3\dot{\varphi}_p \cos(\theta_{03} + \theta_3 - \varphi_{03} - \varphi_p).$$

So the eventual relationship between θ_3 and $\dot{x}_c$, $\dot{y}_c$ and $\dot{\varphi}_p$ is

$$l_3\dot{\theta}_3$$

$$= -\dot{x}_c \sin(\theta_{03} + \theta_3) + \dot{y}_c \cos(\theta_{03} + \theta_3) + r_3\dot{\varphi}_p \cos(\theta_{03} + \theta_3 - \varphi_{03} - \varphi_p) \qquad \text{(Eq. A-10)}$$

Similar results can be obtained from studying the points P_1 and P_2.

$$l_1\dot{\theta}_1$$

$$= -\dot{x}_c \sin(\theta_{01} + \theta_1) + \dot{y}_c \cos(\theta_{01} + \theta_1) + r_1\dot{\varphi}_p \cos(\theta_{01} + \theta_1 - \varphi_{01} - \varphi_p) \qquad \text{(Eq. A-11)}$$

$$l_2\dot{\theta}_2$$

$$= -\dot{x}_c \sin(\theta_{02} + \theta_2) + \dot{y}_c \cos(\theta_{02} + \theta_2) + r_2\dot{\varphi}_p \cos(\theta_{02} + \theta_2 - \varphi_{02} - \varphi_p) \qquad \text{(Eq. A-12)}$$

Written in matrix form, Eqs. (A-10), (A-11) and (A-12) are changed to the following equation.

$$\begin{pmatrix} l_1 & 0 & 0 \\ 0 & l_2 & 0 \\ 0 & 0 & l_3 \end{pmatrix} \begin{bmatrix} \dot{\theta}_1 \\ \dot{\theta}_2 \\ \dot{\theta}_3 \end{bmatrix}$$

$$= \begin{pmatrix} -\sin(\theta_{01} + \theta_1) & \cos(\theta_{01} + \theta_1) & r_1\cos(\theta_{01} + \theta_1 - \varphi_{01} - \varphi_p) \\ -\sin(\theta_{02} + \theta_2) & \cos(\theta_{02} + \theta_2) & r_2\cos(\theta_{02} + \theta_2 - \varphi_{02} - \varphi_p) \\ -\sin(\theta_{03} + \theta_3) & \cos(\theta_{03} + \theta_3) & r_3\cos(\theta_{03} + \theta_3 - \varphi_{03} - \varphi_p) \end{pmatrix} \begin{bmatrix} \dot{x}_c \\ \dot{y}_c \\ \dot{\varphi}_p \end{bmatrix} \qquad \text{(Eq. A-13)}$$

$$\begin{bmatrix} \dot{\theta}_1 \\ \dot{\theta}_2 \\ \dot{\theta}_3 \end{bmatrix}$$

$$= \begin{pmatrix} \dfrac{-\sin(\theta_{01} + \theta_1)}{l_1} & \dfrac{\cos(\theta_{01} + \theta_1)}{l_1} & \dfrac{r_1\cos(\theta_{01} + \theta_1 - \varphi_{01} - \varphi_p)}{l_1} \\ \dfrac{-\sin(\theta_{02} + \theta_2)}{l_2} & \dfrac{\cos(\theta_{02} + \theta_2)}{l_2} & \dfrac{r_2\cos(\theta_{02} + \theta_2 - \varphi_{02} - \varphi_p)}{l_2} \\ \dfrac{-\sin(\theta_{03} + \theta_3)}{l_3} & \dfrac{\cos(\theta_{03} + \theta_3)}{l_3} & \dfrac{r_3\cos(\theta_{03} + \theta_3 - \varphi_{03} - \varphi_p)}{l_3} \end{pmatrix} \begin{bmatrix} \dot{x}_c \\ \dot{y}_c \\ \dot{\varphi}_p \end{bmatrix} \qquad \text{(Eq. A-14)}$$

The Jacobian matrix J_1 between the input variables θ_i and output variables x_c, y_c and φ_p is defined as the 3 by 3 matrix in the Eq.(A-14).

A.2. Derivation of J_2

Using the transposed vector of $\vec{e}_{3r}$ to multiply Eqs. (A-3) and (A-4), the right hand side terms of these two equations are still equal to each other. After some calculation and simplification, the following equation will be achieved.

$$\dot{l}_3 = \dot{x}_c \cdot \cos(\theta_{03} + \theta_3) + \dot{y}_c \cdot \sin(\theta_{03} + \theta_3) + r_3 \cdot \dot{\varphi}_p \cdot \sin(\theta_{03} + \theta_3 - \varphi_{03} - \varphi_p) \quad \text{(Eq. A-15)}$$

Similar results can be acquired for the other two motors.

$$\dot{l}_1 = \dot{x}_c \cdot \cos(\theta_{01} + \theta_1) + \dot{y}_c \cdot \sin(\theta_{01} + \theta_1) + r_1 \cdot \dot{\varphi}_p \cdot \sin(\theta_{01} + \theta_1 - \varphi_{01} - \varphi_p) \quad \text{(Eq. A-16)}$$

$$\dot{l}_2 = \dot{x}_c \cdot \cos(\theta_{02} + \theta_2) + \dot{y}_c \cdot \sin(\theta_{02} + \theta_2) + r_2 \cdot \dot{\varphi}_p \cdot \sin(\theta_{02} + \theta_2 - \varphi_{02} - \varphi_p) \quad \text{(Eq. A-17)}$$

Collected in a matrix form, equations (A-15), (A-16) & (A-17) are written as follows:

$$\begin{bmatrix} \dot{l}_1 \\ \dot{l}_2 \\ \dot{l}_3 \end{bmatrix} = \begin{pmatrix} \cos(\theta_{01} + \theta_1) & \sin(\theta_{01} + \theta_1) & r_1 \sin(\theta_{01} + \theta_1 - \varphi_{01} - \varphi_p) \\ \cos(\theta_{02} + \theta_2) & \sin(\theta_{02} + \theta_2) & r_2 \sin(\theta_{02} + \theta_2 - \varphi_{02} - \varphi_p) \\ \cos(\theta_{03} + \theta_3) & \sin(\theta_{03} + \theta_3) & r_3 \sin(\theta_{03} + \theta_3 - \varphi_{03} - \varphi_p) \end{pmatrix} \begin{bmatrix} \dot{x}_c \\ \dot{y}_c \\ \dot{\varphi}_p \end{bmatrix} \quad \text{(Eq. A-18)}$$

The Jacobian matrix J_2 between the velocity $\dot{l}_i$ and the velocities of the output variables x_c, y_c and φ_p is defined as the 3 by 3 matrix in the Eq. (A-18).

Appendix B: Elements for Finite Element Analysis [*]

The software being used for the finite element method is ANSYS (version 6.1). Different types of elements are selected for different purpose. The element BEAM4 is used for the modal analysis of S-joints; the element SHELL63 is used for delta actuators and platforms. Bending is the main motion for a S-joint beam. BEAM4 is a simple element with bending capability which meets the need of a S-joint simulation. Therefore, Beam4 is selected as S-joints elements in FEM.

Similarly, a manipulator and actuator have a high aspect ratio; these devices can be treated as shells. SHELL63 is a simple shell element with basic capabilities that are needed for modeling. The models based on these two elements provide precise results with acceptable calculating times.

BEAM4 is a three dimensional and uniaxial element with tension, compression, torsion, and bending capabilities. The element has six degrees of freedom at each node: translations in the nodal x, y, and z directions and rotations about the nodal x, y, and z axes. The element x-axis is oriented from node I toward node J (see Figure B.1).

For the two-node option, the default orientation of the element y-axis is automatically calculated to be parallel to the global X-Y plane. To define the element with two or three nodes, the cross-sectional area together with lateral dimensions of the area, two area moments of inertia I_{zz} & I_{yy}, an angle of orientation about the element x-axis, the torsional moment of inertia I_{xx}, and the material properties are required.

Global axes: $X, Y \& Z$
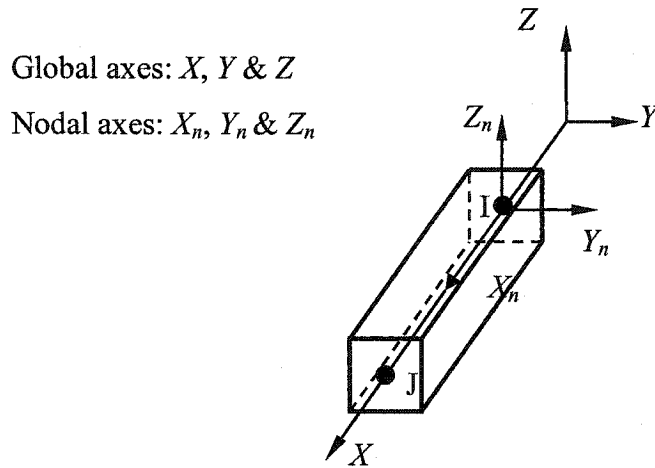
Nodal axes: $X_n, Y_n \& Z_n$

Figure B.0.1 3-D elastic beam (element beam4 in ANSYS).

SHELL63 has both bending and membrane capabilities. Both in-plane and normal loads are permitted. The element has six degrees of freedom at each node: translations in the nodal x, y, and z directions and rotations about the nodal x, y, and z-axes. Stress stiffening and large deflection capabilities are included. See the *ANSYS, Inc. Theory Reference* for more details about this element. The geometry, node locations, and the coordinate system for this element are shown in Figure B.2.
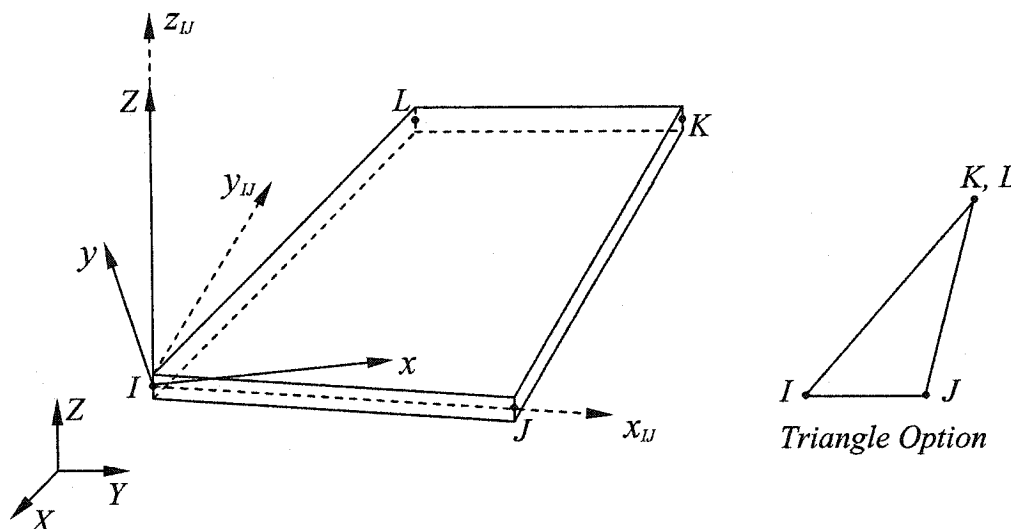
Figure B.0.2 Elastic shell element shell63.

The element is defined by four nodes (*I*, *J*, *K* & *L*), four thicknesses, elastic foundation stiffness, and the orthotropic material properties. The thickness is assumed to vary smoothly over the area of the element, with the thickness input at the four nodes. If the element has a constant thickness, only the thickness at node *I* needs to be inputted. If the thickness is not constant, all four thicknesses must be input. If the key option ESYS is supplied, the *x* axis of the element is set as x_{IJ}, otherwise, the global *x* axis is set as the element's *x* axis.

---

* See ANSYS help manual about Element: BEAM4 and SHELL63